frontiers | Research Topics

Prevention, mitigation, and relief of compound and chained natural hazards

Edited by
Chong Xu, Xiangli He, Wenwen Qi, Sansar Raj Meena, Qi Yao, Wentao Yang and Liam Taylor

Published in
Frontiers in Earth Science

ISSN 1664-8714
ISBN 978-2-8325-5212-4
DOI 10.3389/978-2-8325-5212-4

About Frontiers

Frontiers is more than just an open access publisher of scholarly articles: it is a pioneering approach to the world of academia, radically improving the way scholarly research is managed. The grand vision of Frontiers is a world where all people have an equal opportunity to seek, share and generate knowledge. Frontiers provides immediate and permanent online open access to all its publications, but this alone is not enough to realize our grand goals.

Frontiers journal series

The Frontiers journal series is a multi-tier and interdisciplinary set of open-access, online journals, promising a paradigm shift from the current review, selection and dissemination processes in academic publishing. All Frontiers journals are driven by researchers for researchers; therefore, they constitute a service to the scholarly community. At the same time, the *Frontiers journal series* operates on a revolutionary invention, the tiered publishing system, initially addressing specific communities of scholars, and gradually climbing up to broader public understanding, thus serving the interests of the lay society, too.

Dedication to quality

Each Frontiers article is a landmark of the highest quality, thanks to genuinely collaborative interactions between authors and review editors, who include some of the world's best academicians. Research must be certified by peers before entering a stream of knowledge that may eventually reach the public - and shape society; therefore, Frontiers only applies the most rigorous and unbiased reviews. Frontiers revolutionizes research publishing by freely delivering the most outstanding research, evaluated with no bias from both the academic and social point of view. By applying the most advanced information technologies, Frontiers is catapulting scholarly publishing into a new generation.

What are Frontiers Research Topics?

Frontiers Research Topics are very popular trademarks of the *Frontiers journals series*: they are collections of at least ten articles, all centered on a particular subject. With their unique mix of varied contributions from Original Research to Review Articles, Frontiers Research Topics unify the most influential researchers, the latest key findings and historical advances in a hot research area.

Find out more on how to host your own Frontiers Research Topic or contribute to one as an author by contacting the Frontiers editorial office: frontiersin.org/about/contact

Prevention, mitigation, and relief of compound and chained natural hazards

Topic editors

Chong Xu — National Institute of Natural Hazards, Ministry of Emergency Management, China

Xiangli He — National Institute of Natural Hazards, Ministry of Emergency Management, China

Wenwen Qi — National Institute of Natural Hazards, Ministry of Emergency Management, China

Sansar Raj Meena — University of Padua, Italy

Qi Yao — Institute of Earthquake Forecasting, China Earthquake Administration, China

Wentao Yang — University of Leeds, United Kingdom

Liam Taylor — University of Leeds, United Kingdom

Citation

Xu, C., He, X., Qi, W., Meena, S. R., Yao, Q., Yang, W., Taylor, L., eds. (2024). *Prevention, mitigation, and relief of compound and chained natural hazards*. Lausanne: Frontiers Media SA. doi: 10.3389/978-2-8325-5212-4

Table of contents

frontiers | Frontiers in Earth Science

TYPE Editorial
PUBLISHED 26 July 2024
DOI 10.3389/feart.2024.1462471

OPEN ACCESS

EDITED AND REVIEWED BY
Gordon Woo,
Risk Management Solutions, United Kingdom

*CORRESPONDENCE
Chong Xu,
xc11111111@126.com

RECEIVED 10 July 2024
ACCEPTED 11 July 2024
PUBLISHED 26 July 2024

CITATION
Xu C, Yao Q, He X, Qi W, Meena SR, Yang W and Taylor L (2024), Editorial: Prevention, mitigation, and relief of compound and chained natural hazards.
Front. Earth Sci. 12:1462471.
doi: 10.3389/feart.2024.1462471

Editorial: Prevention, mitigation, and relief of compound and chained natural hazards

Chong Xu[1,2]*, Qi Yao[3], Xiangli He[1,2], Wenwen Qi[1,2], Sansar Raj Meena[4], Wentao Yang[5] and Liam Taylor[6]

[1]National Institute of Natural Hazards, Ministry of Emergency Management of China, Beijing, China, [2]Key Laboratory of Compound and Chained Natural Hazards Dynamics, Ministry of Emergency Management, Beijing, China, [3]Institute of Earthquake Forecasting, China Earthquake Administration, Beijing, China, [4]Department of Geosciences, School of Sciences, University of Padua, Padua, Italy, [5]School of Soil and Water Conservation, Beijing Forestry University, Beijing, China, [6]School of Geography, University of Leeds, Leeds, United Kingdom

KEYWORDS

natural hazard, compound and chained relationship, formation and evolution mechanism, hazard assessment, early warning, database establishment

Editorial on the Research Topic
Prevention, mitigation, and relief of compound and chained natural hazards

Introduction

In the context of global climate warming and frequent earthquakes, extreme natural disasters have become increasingly common, posing significant threats to human life and property. Various types of natural disasters often overlap, interact, or trigger chain reactions. As a result, these natural disasters have a wide impact, long duration, and cause severe damage, exhibiting highly complex and interconnected characteristics. Therefore, the prevention, mitigation, and relief of compound and chained natural hazards have become critical issues we face today. Technological advancements are enhancing our ability to manage natural hazards, with artificial intelligence, big data, cloud computing, and space-based earth observation technologies providing valuable support in addressing compound and chained natural hazards. Against this backdrop, numerous scientists are dedicated to researching the mechanisms of natural disasters and developing technologies for disaster prevention, mitigation, and relief, yielding many outstanding results.

To advance the field of natural disaster prevention and control and promote communication among peers, we initiated a Research Topic titled "*Prevention, Mitigation, and Relief of Compound and Chained Natural Hazards*" on 4 March 2023. The goal was to collect both original research and review articles addressing state-of-the-art theories and methodologies in all types of natural hazards, with a particular emphasis on studies highlighting the compound and chained relationships between different natural hazards. Since its launch, this Research Topic has attracted widespread attention and received numerous submissions. Now that the Research Topic has closed, a total of nine papers have been accepted and published, successfully fulfilling the goals of this Research Topic. This preface provides an overview of the nine published papers, which primarily focus on earthquakes, geological hazards, and earthquake-triggered landslides. This Research Topic

has provided support for the advancement in the field of Prevention, Mitigation, and Relief of Compound and Chained Natural Hazards.

The monitoring of earthquakes and disaster assessment

Earthquakes are considered the foremost among natural disasters, with a single event potentially causing tens of thousands of fatalities (Xu et al., 2014; Yu et al., 2024). Research on earthquakes and their associated hazards has always been a prominent issue. This Research Topic publishes three papers in this field. Ahn et al. from the Korea Meteorological Administration designed a performance evaluation method for earthquake early warning systems in low seismic activity areas. This method considers the unique conditions of evaluating early warning systems in such regions and is significant for eliminating potential discrepancies from reviewers or nations. Efforts in earthquake early warning systems aid in disaster response and avoidance, while emergency shelters provide scientific reference for earthquake rescue and post-disaster emergency evacuation. Wang et al. from the National Institute of Natural Hazards, Ministry of Emergency Management of China using Xichang City in Sichuan Province, China as an example, conducted a spatial accessibility analysis of emergency shelters. They utilized data on emergency shelters and road networks, considering predicted strong ground motion and potential fault rupture characteristics in an earthquake scenario. This analysis improved the objectivity of the accessibility results for emergency shelters.

Earthquake-induced landslides are a significant type of earthquake disaster, especially in mountainous areas (Xu et al., 2014; Zhao et al., 2023). The evaluation of seismic landslide hazards is a popular research direction (Shao and Xu, 2022). Yang et al. from the Institute of Geomechanics, Chinese Academy of Geological Sciences, used the Newmark model to evaluate seismic landslide hazards based on peak ground acceleration, traditional Arias intensity, and an improved Arias intensity. They found that the results based on the improved Arias intensity were consistent with the spatial distribution of co-seismic landslides, indicating that this method is suitable for rapid assessment of earthquake-induced landslides, providing scientific support for emergency assessment of such events.

Slope geological hazards such as landslides and debris flows

The automatic identification of regional landslides has become a widely studied research direction in the context of advancements in machine learning technology (Qi et al., 2020; Yang et al., 2022; Yu et al., 2022). Ma et al. from the Institute of Geology and Geophysics, Chinese Academy of Sciences, proposed a landslide identification method based on a dual graph convolutional network. Using GeoEye-1 satellite imagery with a spatial resolution of 0.5 m, they conducted automatic landslide identification in a mountainous area of Xinyuan County, Xinjiang, achieving an accuracy of over 80%. Compared to traditional methods, this approach offers the ability to identify data over a larger area with higher efficiency, providing a reliable solution for the large-scale identification of landslides.

Landslide relics refer to areas where landslides have occurred or are occurring. Most landslide relics have undergone deformation, instability, movement, and accumulation, reaching a stable state. Some continue to deform without large-scale instability, or experience deformation again due to external factors such as earthquakes and rainfall after initial instability and accumulation. Landslide relics provide the only direct information for understanding the background of landslide development in a region. Some researchers have conducted specialized studies on landslide relics in various areas, revealing the background of landslide development in those regions (Wang W. et al., 2024; Feng et al., 2024; Sun et al., 2024; Zhang et al., 2024). Li et al. conducted a study on landslide relic identification in the boundary area between the Qinghai-Tibet Plateau and the Loess Plateau, specifically in Jianzha County, Qinghai Province, China, using high-resolution imagery from Google Earth platfrom for visual identification. They developed a comprehensive and detailed landslide relic database, which includes 713 landslide relics. The study analyzed the spatial distribution characteristics and area distribution of these landslide relics, providing support for analyzing landslide influencing factors, hazard assessment, and disaster prevention and mitigation efforts in the region.

Cai et al. from the Research Center of Applied Geology of the China Geological Survey studied the accumulation and movement patterns of potential source materials for debris flow disasters under conditions of extreme short-term heavy rainfall using numerical simulation methods. They revealed and analyzed the maximum movement speed, accumulation height, impact range, and evolution process of a debris flow in a mountainous area in southwestern China. This research provides support for debris flow risk assessment and disaster prevention and mitigation in mountainous regions. Wang et al. from the Institute of Geology and Geophysics, Chinese Academy of Sciences, determined the occurrence date of a historical debris flow in Qingyang Mountain, Qinghai Province, China as July 1982, using historical tree-ring data. They obtained the boundaries of the historical debris flow through remote sensing imagery before and after the event. Using a depth-integrated continuum model, they reconstructed the process of this debris flow. This study provides a reference for dating historical debris flows and reconstructing their movement processes.

Liu et al. from Beijing Forestry University combined Landsat 5 and Sentinel-2 imagery to construct a time series of deformation for the Beishan landslide in Lijie Town, northeastern Qinghai-Tibet Plateau, Gansu. They analyzed the relationship between landslide deformation and rainfall, revealing a significant correlation between recent deformation and precipitation levels. This work integrates Landsat 5 and Sentinel-2 imagery to trace landslide deformation over nearly 40 years, showcasing its profound value. It establishes a reliable technical framework for integrating comprehensive optical and radar deformation remote sensing data, including pixel offset tracking and InSAR techniques, for landslide deformation monitoring. Moreover, it provides scientific support for landslide monitoring and disaster prevention and mitigation under the backdrop of climate change.

Assessing landslide susceptibility and hazard based on machine learning is an important research direction, with numerous papers published in recent years (Zhao et al., 2021; Shao et al., 2024). Xia et al. from the Key Laboratory of Degraded and Unused Land Consolidation Engineering, Ministry of Natural Resources, employed four methods including Naive Bayes, J48 decision tree, and multilayer perceptron models to assess landslide susceptibility in Xiaojin County, Sichuan Province, China. They achieved a high accuracy rate of around 90%. This study serves as a beneficial case for applying machine learning models to assess landslide susceptibility.

Conclusions and prospects

Human understanding of natural laws is boundless, and the study of natural disasters remains an eternal topic crucial to human survival and development (Xu and Xu, 2021). The research outcomes of this Research Topic have furthered our profound understanding of the mechanisms and patterns of earthquakes and geological disasters. They have also advanced the development of technologies for disaster warning, assessment, and emergency response. This technological support is crucial for reducing the risks and losses associated with seismic and geological hazards. It is important to note that the theme of our Research Topic is "*Prevention, Mitigation, and Relief of Compound and Chained Natural Hazards*". We aimed to collect more research related to comprehensive natural hazards and disaster chains. However, the nine papers included in this Research Topic specifically focus on earthquakes and geological disasters. In reality, there are many types of natural disasters, such as meteorological events, floods, droughts, wildfires, and tsunamis. Against the backdrop of global warming, the risks associated with meteorological disasters and their chained interactions with floods and geological hazards are undoubtedly increasing. Therefore, considering this aspect, we have not concluded this topic with the completion of this Research Topic. Instead, we have opened Volume II of this Research Topic, samely titled "*Prevention, Mitigation, and Relief of Compound and Chained Natural Hazards II*." For more details, please visit https://www.frontiersin.org/research-topics/64578. We welcome continued submissions from colleagues, especially in directions beyond earthquakes and geological disasters, such as meteorological events, floods, droughts, wildfires, tsunamis, and their compound and chained hazards.

Author contributions

CX: Writing–review and editing, Writing–original draft. QY: Writing–review and editing. XH: Writing–review and editing. WQ: Writing–review and editing. SM: Writing–review and editing. WY: Writing–review and editing. LT: Writing–review and editing.

Funding

The author(s) declare that financial support was received for the research, authorship, and/or publication of this article. This study was supported by the National Institute of Natural Hazards, Ministry of Emergency Management of China (2023-JBKY-57).

Acknowledgments

We sincerely thank all the authors for their submissions to this Research Topic, all the reviewers for their valuable comments and suggestions, and the staff of "Frontiers in Earth Science" for their strong support in all phases of the realization of this Research Topic.

Conflict of interest

The authors declare that the research was conducted in the absence of any commercial or financial relationships that could be construed as a potential conflict of interest.

The author(s) declared that they were an editorial board member of Frontiers, at the time of submission. This had no impact on the peer review process and the final decision.

Publisher's note

References

Feng, L., Xu, C., Tian, Y., Li, L., Sun, J., Huang, Y., et al. (2024). Landslides of China's qinling. *Geoscience Data J.* doi:10.1002/gdj3.246

Qi, W., Wei, M., Yang, W., Xu, C., and Ma, C. (2020). Automatic mapping of landslides by the ResU-Net. *Remote Sens.* 12 (15), 2487. doi:10.3390/rs12152487

Shao, X., and Xu, C. (2022). Earthquake-induced landslides susceptibility assessment: a review of the state-of-the-art. *Nat. Hazards Res.* 2 (3), 172–182. doi:10.1016/j.nhres.2022.03.002

Shao, X., Xu, C., Li, L., Yang, Z., Yao, X., Shao, B., et al. (2024). Spatial analysis and hazard assessment of Large-scale ancient landslides around the reservoir area of Wudongde Hydropower Station, China. *Nat. Hazards* 120 (1), 87–105. doi:10.1007/s11069-023-06201-9

Sun, J., Xu, C., Feng, L., Li, L., Zhang, X., and Yang, W. (2024). The yinshan mountains record over 10,000 landslides. *Data* 9 (2), 31. doi:10.3390/data9020031

Wang, W., Huang, Y.-d., Xu, C., Shao, X.-y., Li, L., Feng, L.-y., et al. (2024). Identification and distribution of 13003 landslides in the northwest margin of Qinghai-Tibet Plateau based on human-computer interaction remote sensing interpretation. *China Geol.* 7 (2), 171–187. doi:10.31035/cg2023140

Xu, C., Xu, X., Yao, X., and Dai, F. (2014). Three (nearly) complete inventories of landslides triggered by the May 12, 2008 Wenchuan Mw 7.9 earthquake of China and their spatial distribution statistical analysis. *Landslides* 11 (3), 441–461. doi:10.1007/s10346-013-0404-6

Xu, X., and Xu, C. (2021). Natural Hazards Research: an eternal subject of human survival and development. *Nat. Hazards Res.* 1 (1), 1–3. doi:10.1016/j.nhres.2020.12.003

Yang, Z., Xu, C., and Li, L. (2022). Landslide detection based on ResU-net with transformer and CBAM embedded: two examples with geologically different environments. *Remote Sens.* 14 (12), 2885. doi:10.3390/rs14122885

Yu, B., Xu, C., Chen, F., Wang, N., and Wang, L. (2022). HADeenNet: a hierarchical-attention multi-scale deconvolution network for landslide detection. *Int. J. Appl. Earth Observation Geoinformation* 111, 102853. doi:10.1016/j.jag.2022.102853

Yu, X., Hu, X., Song, Y., Xu, S., Li, X., Song, X., et al. (2024). Intelligent assessment of building damage of 2023 Turkey-Syria Earthquake by multiple remote sensing approaches. *npj Nat. Hazards* 1 (1), 3. doi:10.1038/s44304-024-00003-0

Zhang, X., Xu, C., Li, L., Feng, L., and Yang, W. (2024). Inventory of landslides in the northern half of the taihang mountain range, China. *Geosciences* 14 (3), 74. doi:10.3390/geosciences14030074

Zhao, B., Su, L., Xu, Q., Li, W., Xu, C., and Wang, Y. (2023). A review of recent earthquake-induced landslides on the Tibetan Plateau. *Earth-Science Rev.* 244, 104534. doi:10.1016/j.earscirev.2023.104534

Zhao, Z., Liu, Z. Y., and Xu, C. (2021). Slope unit-based landslide susceptibility mapping using certainty factor, support vector machine, random forest, CF-SVM and CF-RF models. *Front. Earth Sci.* 9, 589630. doi:10.3389/feart.2021.589630

frontiers | Frontiers in Earth Science

TYPE Original Research
PUBLISHED 23 June 2023
DOI 10.3389/feart.2023.1187384

OPEN ACCESS

EDITED BY
Chong Xu,
Ministry of Emergency Management, China

REVIEWED BY
Himan Shahabi,
University of Kurdistan, Iran
Haijia Wen,
Chongqing University, China
Fatemeh Rezaie,
Korea Institute of Geoscience and Mineral Resources, Republic of Korea

*CORRESPONDENCE
Liheng Xia,
18092729601@163.com

RECEIVED 16 March 2023
ACCEPTED 02 June 2023
PUBLISHED 23 June 2023

CITATION
Xia L, Shen J, Zhang T, Dang G and Wang T (2023), GIS-based landslide susceptibility modeling using data mining techniques.
Front. Earth Sci. 11:1187384.
doi: 10.3389/feart.2023.1187384

GIS-based landslide susceptibility modeling using data mining techniques

Liheng Xia[1,2,3]*, Jianglong Shen[1,2,3], Tingyu Zhang[1,2,3], Guangpu Dang[4] and Tao Wang[4]

[1]Key Laboratory of Degraded and Unused Land Consolidation Engineering, Ministry of Natural Resources, Xi'an, China, [2]Shaanxi Provincial Land Consolidation Engineering Technology Research Center, Xi'an, China, [3]Land Engineering Technology Innovation Center, Ministry of Natural Resources, Xi'an, China, [4]Shaanxi Provincial Land Engineering Construction Group, Land Survey Planning and Design Institute, Xi'an, China

Introduction: Landslide is one of the most widespread geohazards around the world. Therefore, it is necessary and meaningful to map regional landslide susceptibility for landslide mitigation. In this research, landslide susceptibility maps were produced by four models, namely, certainty factors (CF), naive Bayes (NB), J48 decision tree (J48), and multilayer perceptron (MLP) models.

Methods: In the first step, 328 landslides were identified via historical data, interpretation of remote sensing images, and field investigation, and they were divided into two subsets that were assigned different uses: 70% subset for training and 30% subset for validating. Then, twelve conditioning factors were employed, namely, altitude, slope angle, slope aspect, plan curvature, profile curvature, TWI, NDVI, distance to rivers, distance to roads, land use, soil, and lithology. Later, the importance of each conditioning factor was analyzed by average merit (AM) values, and the relationship between landslide occurrence and various factors was evaluated using the certainty factor (CF) approach. In the next step, the landslide susceptibility maps were produced based on four models, and the effect of the four models were quantitatively compared by receiver operating characteristic (ROC) curves, area under curve (AUC) values, and non-parametric tests.

Results: The results demonstrated that all the four models can reasonably assess landslide susceptibility. Of these four models, the CF model has the best predictive performance for the training (AUC=0.901) and validating data (AUC=0.892).

Discussion: The proposed approach is an innovative method that may also help other scientists to develop landslide susceptibility maps in other areas and that could be used for geo-environmental problems besides natural hazard assessments.

KEYWORDS

landslide susceptibility, naive bayes classifier, J48 decision tree, multilayer perceptron, GIS

1 Introduction

Landslide is one of the most common geohazards around mountainous regions (Moayedi et al., 2019; Sharma and Mahajan, 2019; Xiong et al., 2019). Generally, the disaster-causing capacity of landslide hazards is particularly significant, causing enormous losses to houses, infrastructure, land resources, and human life (Corominas et al., 2014; Pourghasemi and Rahmati, 2018). China stands as one of the nations with a relatively high

frequency of geological hazards. In the year 2021, a total of 4,772 geological disasters occurred in China, resulting in the unfortunate loss of 80 lives, with 11 individuals reported missing, and inflicting direct economic losses of 3.2 billion dollars. Landslides, as a perilous geological hazard, prevail as the primary disaster type across China, predominantly afflicting the northwest and southwest regions of the country. Hence, the study and implementation of measures for geological hazard prevention and mitigation hold tremendous significance. Furthermore, the matter of geological hazard prediction demands urgent attention and resolutions.

In view of the severe consequences, the tasks of landslide control and prevention have attracted the attention of government organizations and scholars (An et al., 2016; Pham et al., 2016a; Wu et al., 2017). In this respect, landslide susceptibility assessment (LSA) is the research focus, and the results can guide landslide prevention engineering (Polykretis et al., 2015). Essentially, LSA is the work that is performed to find out whether landslide occurrence is intrinsically associated with conditioning factors, which can be used to predict the future spatial development of landslide hazards (Magliulo et al., 2008; Jaafari et al., 2014).

Currently, statistical models and machine learning (ML) models are the most popular approaches to build landslide susceptibility models (Huang and Zhao, 2018; Pourghasemi et al., 2018; Arabameri et al., 2019a). For the former, the probability and frequency of landslide occurrence are analyzed by conventional statistical approaches, such as the landslide susceptibility index model (Jamal and Mandal, 2016), frequency ratio model (Aditian et al., 2018), and weight of evidence model (Xu et al., 2012). However, when using conventional statistical methods, we have to first subjectively determine the statistical model, and it is hard to measure the relative importance among various conditioning factors (Elith et al., 2008). For the latter, a vast variety of landslide susceptibility models have been constructed by widely using ML approaches in recent years, and sequences of novel ML and ensemble learning algorithms have been proposed, for instance, random forest (Sun et al., 2021), alternating decision tree (Wu et al., 2020), kernel logistic regression (Chen and Chen, 2021), random subspace (Pham et al., 2018a), rotation forest, and decision tree (Hong et al., 2018; Pham et al., 2018b). It is considered that machine learning approaches are more suitable for large databases and can reveal the non-linear and complex linkage between landslide occurrence and each conditioning factor (Zare et al., 2013). Moreover, to acquire results with higher accuracy and a model with better generalization ability, numerous comparative studies of machine learning algorithms have been conducted (Akgun, 2012; Zhu et al., 2018; Juliev et al., 2019; Lei et al., 2020a; Li et al., 2021).

As known, landslides are a very complex natural phenomenon that cause severe loss of human lives and properties worldwide. An accurate assessment of the occurrence of these extreme events is needed in order to understand their spatial correlations with the landslides. An effective method is to map the areas that are susceptible to landslide occurrence. In recent years, various machine learning techniques have been applied for landslide susceptibility mapping. However, we cannot conclude which model is the best universally. Moreover, even a small increment of the prediction accuracy may control the resulting landslide susceptibility zones. Therefore, many more case studies must be performed to reach a reasonable conclusion.

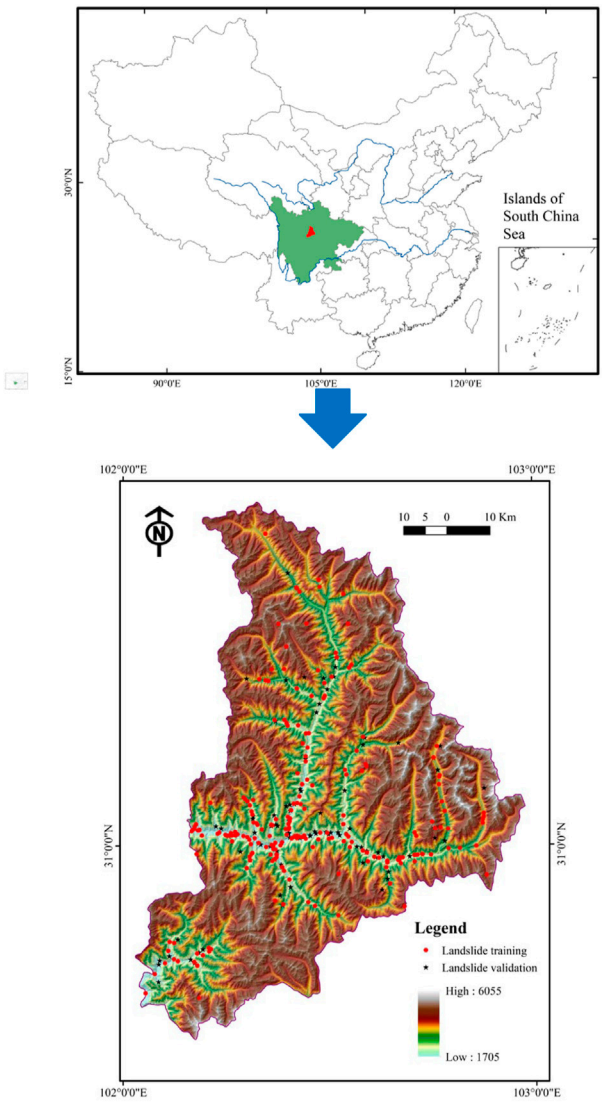

Figure. 1 Study area

FIGURE 1
Study area.

In this paper, we employed the naive Bayes, J48 decision tree, and multilayer perceptron models to predict landslide occurrence in Xiaojin County, Sichuan Province, China. The contents of this paper are as follows: 1) The contribution of conditioning factors to three used ML models are investigated; 2) the CF bivariate model is integrated with ML methods for the spatial prediction of landslides; 3) CF illuminates a superior reliable model that is far ahead of the state-of-the-art ML in landslide susceptibility assessment; 4) the model performance is considered based on their discrimination capacity and reliability. The primary difference here between this study and the literature mentioned is that the approaches in this paper are seldom used and compared in landslide susceptibility assessment. Another point is that four models were first applied in

Xiaojin County, and statistical models and machine learning models possess superior interpretability compared to deep learning models, and they can be trained using smaller datasets, which aim to improve the accuracy of the results in the study area. The performance of the models was quantitatively evaluated and comprehensively compared, and the proposed approach is an innovative method that may also help other scientists to develop landslide susceptibility maps in other areas and that could be used for geo-environmental problems other than natural hazard assessments.

2 The study area

Xiaojin County is located in Sichuan Province, China (Figure 1). The study area is between longitude 102°01′E and 102°59′E and latitude 30°35′N and 31°43′N. The area is dominated by a subtropical monsoon climate. However, the climate vertical differentiation is extremely distinct due to the dramatic changes of altitudes. Generally, the annual average temperature is 12.2°C, and the average annual rainfall is 613.9 mm (http://www.xiaojin.gov.cn/). Hydrologically, the Fubian River and Xiaojin River are the main rivers in this area. The length of these two rivers are 83 km and 150 km, respectively (Xie et al., 2021).

Xiaojin County presents a distinctive topography, with higher elevations in the northwest and lower ones in the southeast, characterized by a modest mountainous terrain. Historical landslides in Xiaojin County encompass both rockslides and soil slides, with rockslides constituting the majority and soil slides being relatively scarce. In terms of magnitude, the study area primarily exhibits small to medium-sized landslides, with a lesser occurrence of large-scale landslides. Due to its location within a high mountainous and hilly terrain, situated along the Circum-Pacific Mediterranean Fault Zone, Xiaojin County experiences frequent and intense tectonic movements. It represents a typical high-risk zone for geological hazards in southwestern China, particularly noteworthy for its proximity of a mere 100 km to Wenchuan City in Sichuan Province. On 12 May 2008, Wenchuan City was struck by a severe earthquake measuring over a magnitude of 8, which severely impacted Xiaojin County as well. This event triggered numerous slope instability incidents. Compounded by the concentrated population and the predominant construction of buildings and public facilities in mountainous areas, the potential landslide risks pose a significant threat to the social security of Xiaojin County. Furthermore, up until now, there has been a dearth of research on landslide susceptibility specific to Xiaojin County, which serves as the rationale for selecting it as the study area.

3 Data preparation

Through collection of historical data, satellite image interpretation, and field investigation, 328 landslides in total were extracted from this area. The average dimension of a landslide is about 6.9×10^3 m^2, and the average volume is 4.3×10^4 m^3, respectively. Due to the relatively diminutive size of landslide areas within the study area, the centroid method was employed to generate landslide points. Additionally, an equivalent number of non-landslide points was randomly generated within regions where the slope angle is non-zero. For establishing a landslide susceptibility model, these landslides and non-landslides were randomly divided into two datasets, the training dataset (accounting for 70%) and validating dataset (accounting for 30%) (Figure 1).

Afterwards, slope angle, slope aspect, altitude, plan curvature, profile curvature, topographic wetness index (TWI), distance to rivers, distance to roads, normalized difference vegetation index (NDVI), land use, soil, and lithology were selected as conditioning factors for landslide susceptibility mapping according to the existing literature (Althuwaynee et al., 2012; Felicísimo et al., 2013; Conforti et al., 2014; Ada and San, 2018), and the corresponding thematic maps were acquired (Figure 2). In the process of producing thematic maps, the DEM image, obtained from the website http://www.gscloud.cn/, was adopted to extract regional values of the slope angle, slope aspect, altitude, plan curvature, profile curvature, and TWI. The buffer zones of rivers and roads can be generated by regional water system and traffic maps. The NDVI was obtained by Landsat 8 OLI images (http://www.gscloud.cn/). Land use, soil, and lithology were extracted from land use, soil, and geological maps with scales of 1:100000, 1:1000000, and 1:500000, respectively. All the thematic maps were rasterized with a resolution of 20 m × 20 m. The data source is shown in Table 1.

The slope angle is a necessary conditioning factor in this task (Eiras et al., 2021). The slope stability and failure modes usually vary with slope angle values (Dai et al., 2001). Here, the slope angle values were reclassified into nine categories with an interval of 10°, <10°, 10°–20°, 20°–30°, 30°–40°, 40°–50°, 50°–60°, 60°–70°, 70°–80°, and >80°.

The slope aspect has a prominent influence on temperature and humidity around slopes (Ercanoglu and Gokceoglu, 2002). Therefore, the slope aspect is related to the slope stability. In this paper, the slope aspects were divided into nine directions, namely, flat, north, northeast, east, southeast, south, southwest, west, and northwest.

It is clear that the degree of vegetation coverage, freezing, thawing, and moisture changes dramatically with the variety of altitude (Ding et al., 2017). With an interval of 500 m, nine groups were generated, namely, <2000 m, 2000–2500 m, 2500–3000 m, 3000–3500 m, 3500–4000 m, 4000–4500 m, 4500–5000 m, 5000–5500 m, and >5500 m.

Plan curvature and profile curvature are two indexes that are employed to measure slope shapes, which always affect the stress distribution of slopes (Aghdam et al., 2016). Moreover, the curvature values have impacts on surface runoff (Chen et al., 2017). In this study, curvature values were derived from DEM using the ArcGIS toolbox (ESRI, 2014). The plan curvature values were reclassified as (−32.95)-(−1.70) (−1.70)-(-0.65) (−0.65)-0.14, 0.14-1.19, and1.19-34.02, while the profile curvature values were (−44.22)-(-2.24) (−2.24)-(-0.80), (−0.80)-0.28, 0.28-1.73, and 1.73-48.04.

The topographic wetness index (TWI) is employed to quantitatively evaluate the control function of topography on hydrological characteristics (Moore et al., 1991). In this way, five categories of TWI values were formed by the natural break method: 0.14-1.55, 1.55-2.26, 2.26-3.20, 3.20-4.78, and 4.78-15.12.

Rivers can affect the hydrogeology characteristics of slopes and usually corrode the toe of a slope, which may decrease the anti-slide force (Nsengiyumva et al., 2018). By analyzing buffer zones, eight buffer zones of rivers were produced, namely, <200 m, 200–400 m, 400–600 m, 600–800 m, and >800 m.

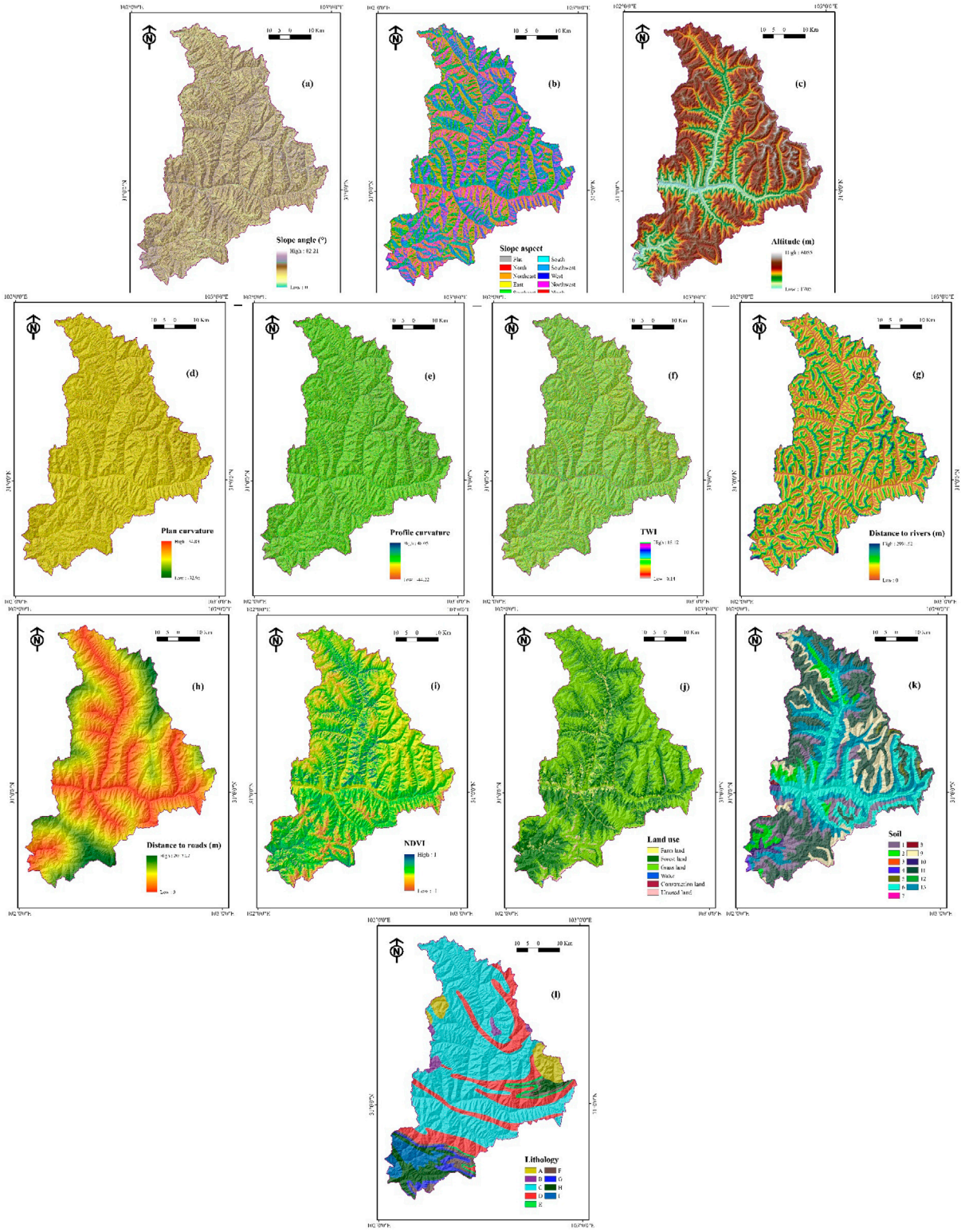

FIGURE 2
Thematic maps. **(A)** slope angle; **(B)** slope aspect; **(C)** altitude; **(D)** plan curvature; **(E)** profile curvature; **(F)** TWI; **(G)** distance to rivers; **(H)** distance to roads; **(I)** NDVI; **(J)** land use; **(K)** soil; **(L)** lithology.

In mountainous areas, it is common that numerous landslide hazards are triggered by road construction (Vuillez et al., 2018). Hence, the distance to roads was regarded as a conditioning factor in this study and reclassified into five buffer zones: <300 m, 300–600 m, 600–900 m, 900–1200 m, and >1200 m.

TABLE 1 Data source.

Conditioning factors	Source	Resolution/scale
Slope angle	Extracting from DEM image	20 m × 20 m
Slope aspect	Extracting from DEM image	20 m × 20 m
Altitude	Extracting from DEM image	20 m × 20 m
Plan curvature	Extracting from DEM image	20 m × 20 m
Profile curvature	Extracting from DEM image	20 m × 20 m
Topographic wetness index (TWI)	Extracting from DEM image	20 m × 20 m
Distance to rivers	Generating from regional water system maps	Vector
Distance to roads	Generating from regional traffic maps	Vector
Normalized difference vegetation index (NDVI)	Generating from Landsat 8 OLI images	Vector
Land use	Extracting from landuse maps	1:100000
Soil	Extracting from soil maps	1:1000000
Lithology	Extracting from lithology maps	1:500000

The normalized difference vegetation index (NDVI) is used to reflect the degree of vegetation coverage on a slope surface (Han et al., 2019). Thus, the NDVI values of the study area were arranged into five classes (−1.00)-(−0.16) (−0.16)-(-0.01), (−0.01)-0.01, 0.01-0.16, and 0.16-1.00.

It has been proved that landslide occurrence is indeed connected with land-use type (Leventhal and Kotze, 2008). In the study area, a total of six land-use types were identified, namely, farmland, forestland, grassland, water, construction land, and unused land.

Soil type and lithology, which affect the physical and mechanical texture of soil and rock mass, determine slope stability (Yalcin et al., 2011). Based on the soil map of the study area, thirteen soil types were classified. The outcrops in the study area formed in several geological ages, which include the Sinian period, Ordovician period, Silurian period, Devonian period, Carboniferous period, Permian period, Triassic period, and Quaternary period. The main lithologies are marble, quartzite, phyllite, limestone, sandstone, and soil. Correspondingly, nine lithology groups were reclassified.

4 Modeling approach

4.1 Selection of landslide conditioning factors

It is usually considered that the selection of conditioning factors has significant effects on the certainty and outcome of landslide predictive models (Lei et al., 2020a). These important instructions point to the need to take the optimal combination of conditioning factors into consideration as part of the criteria of raising the accuracy of landslide susceptibility models. In this case, we compared the relative importance of various conditioning factors by a chi-square test based on the Weka workbench (Frank et al., 2016).

4.2 Certainty factors

The certainty factors method, which was proposed by Buchanan and Shortliffe in 1984 (Buchanan and Shortliffe, 1984), has been extensively represented in tasks of LSA (Kanungo et al., 2011; Devkota et al., 2013). In this process, each conditioning factors can generate a corresponding data layer. Then, the weights of all the pixels in different data layers can be figured out by Eq. 1:

$$CF = \begin{cases} \dfrac{HH_a - HH_s}{HH_a\left(1 - HH_s\right)}, HH_a \geq HH_s \\ \dfrac{HH_a - HH_s}{HH_s\left(1 - HH_a\right)}, HH_s < HH_a \end{cases} \tag{1}$$

where HH_a is the conditional probability of landslide occurrence in a class, and HH_s is the prior probability of landslide events in the whole study area (Devkota et al., 2013).

4.3 Naive bayes

The naive Bayes classifier is based on the Bayes theorem and independence assumption, and it has been popular in various domains in recent decades (Lee, 2018; Sun et al., 2018; Berrar et al., 2019; He et al., 2019). In terms of the naive Bayes algorithm, the training data are used to calculate the prior probability of various classifications. Then, the classification results can be determined by the posteriori probability and conditional probability density function. Assuming that X is the vector of new observation data, and x_i denotes the ith observation value, for a certain class c_j, the conditional probability p $(X|c_j)$ can then be figured out through the following equation:

$$p\left(X|c_j\right) = \prod_{i=1} p\left(\frac{x_i}{c_j}\right) \tag{2}$$

In the tasks of landslide susceptibility, assuming that y_j (i = landslide, non-landslide) represents the classification results, the

final prediction results can be identified through the following equation:

$$y_j = argmax p(y_j) \prod_{i=1} p\left(\frac{x_i}{y_j}\right) \quad (3)$$

4.4 J48 decision tree

The J48 decision tree (C4.5) is a type of decision tree algorithm, and it presents an improvement on the ID3 decision tree (Hong et al., 2018). In terms of the J48 decision tree, the information gain ratio is introduced to select splitting attributions, and the information gain ratio can be calculated by Eq. 4:

$$Information\ Gain\ Ratio = \frac{Information\ Gain}{-\sum_{i=1}^{m} \frac{n_i}{N} \square log\left(\frac{n_i}{N}\right)} \quad (4)$$

where the information gain is calculated by entropy or the Gini value, m is the number of sub-nodes, and N represents the data quantity of a parent node when n_i denotes that of the ith sub-node.

When constructing a decision tree, overfitting may occur under the effects of noisy data (Sathyadevan et al., 2015). Therefore, tree pruning techniques are employed to avoid overfitting occurrence and simplify the construction of a decision tree. Generally, there are two pruning approaches, namely, prepruning and postpruning. The postpruning approaches can be further divided into reduced error pruning, pessimistic error pruning, cost-complexity pruning, and error-based pruning (Sathyadevan et al., 2015).

4.5 Multilayer perceptron

Multilayer perceptron (MLP) is a typical perceptron learning algorithm. Compared with traditional neural networks, MLP consists of one input layer, one output layer, and multiple hidden layers. The training data are input into MLP through the input layer, and the mapping between the input data and output data is established by hidden layers. Because there is no restriction on the hidden function types and number of neurons of the output layer, MLP is more suitable for non-linear data multi-classification problems (Manaswi and Manaswi, 2018). In the process of MLP training, according to the back-propagation regulation, the weights of various hidden layers are optimized by the following loss function:

$$E = \frac{1}{2} \sum_{j \in L_k} \left(t^{(j)} - y_k^{(j)}\right)^2 \quad (5)$$

where E is the loss, L_k represents all the neurons of the output layer, $y(j)$ k means the output of the jth node of L_k, and $t^{(j)}$ is the corresponding label of the input data.

4.6 Receiver operating characteristic (ROC) curve

The receiver operating characteristic (ROC) curve has been understood as the standard method for measuring classifier performance (Amiri et al., 2019; Arabameri et al., 2019b; Lei et al., 2020b). Taking the "1-specificity" as the transverse axis and the "sensitivity" as the longitudinal axis, the ROC curve can be obtained by connecting the coordinate points, which are drawn under various classification threshold values (Chen W. et al., 2021; Chen et al., 2021b). Based on the ROC curve, the optimal classification threshold value can be easily found, and the model performance is obviously reflected by the shape of curve. Furthermore, to quantitatively assess model performance with the ROC curve, a higher value of area under the ROC curve (AUC) embodies a better classification performance (Chen et al., 2021c).

5 Results and analysis

This section reports the results from an interpretative framework of both predictors' effects and model performance in terms of different perspectives.

5.1 Selection of landslide conditioning factors

The average merit (AM) values of the twelve conditioning factors were figured out and are shown in Figure 3. Among these factors, altitude has the highest AM value (NB and J48 of 0.329; MLP of 0.322). The second highest AM value (NB of 0.307; J48 and MLP of 0.305) is for soil type, which is followed by distance to roads (NB, J48, MLP AM = 0.272, 0.275, 0.265) and distance to rivers (NB, J48, MLP AM = 0.233, 0.232, 0.231). For the NB model, the AM values are lithology = 0.098, slope angle = 0.091, TWI = 0.087, profile curvature = 0.07, land use = 0.066, plan curvature = 0.061, NDVI = 0.044, and slope aspect = 0.043. For the J48 model, the AM values are lithology = 0.095, TWI = 0.084, slope angle = 0.083, land use = 0.064, plan curvature = 0.05, profile curvature = 0.048, NDVI = 0.036, and slope aspect = 0.031. For the MLP model, the AM values are lithology = 0.088, slope angle = 0.082, TWI = 0.081, profile curvature = 0.063, land use = 0.055, plan curvature = 0.045, slope aspect = 0.035, and NDVI = 0.032. Moreover, it is observed that the NB model has the greatest contribution. Therefore, the NB model should be considered as better than the other models.

Moreover, there may exist a multicollinearity problem among the conditioning factors, and severe multicollinearity can have an impact on the model by increasing the variance of regression coefficients and rendering them unstable. To assess the potential multicollinearity problem among the conditioning factors, we verified it by calculating the variance inflation factor (VIF) and tolerance (TOL) of the conditioning factors. From Table 2, it can be observed that the VIF values of all the conditioning factors are less than 10, and the TOL values are greater than 0.1, indicating the absence of multicollinearity among the conditioning factors. Hence, all the conditioning factors were retained in the subsequent modeling process.

5.2 Correlation analysis using CF model

In this study, the different response relationship between the fitting models and each conditioning factor was analyzed by the CF model (Figure 4). In terms of the slope angle, the highest CF value

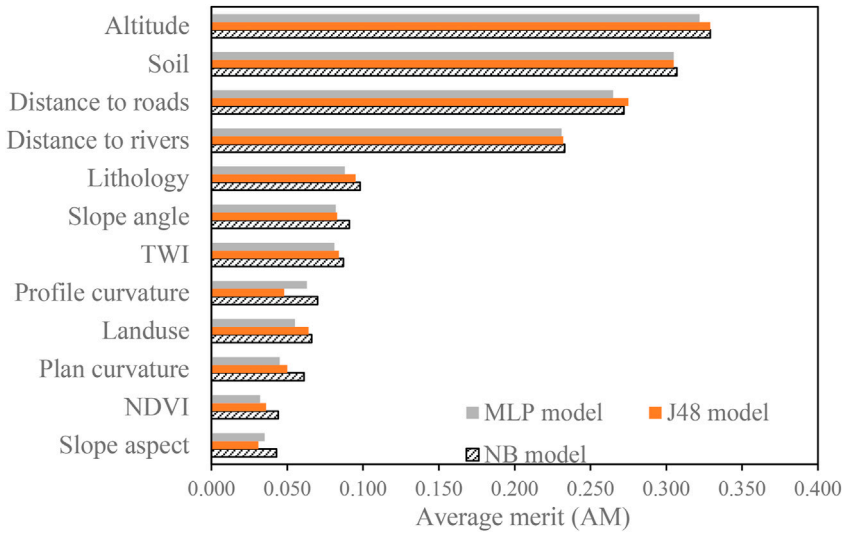

FIGURE 3
Importance of conditioning factors.

TABLE 2 Verification result of potential multicollinearity problem among the conditioning factors.

Conditioning factors	VIF	Tolerances (TOL)
Altitude	1.493	0.670
Soil	1.232	0.812
Distance to roads	1.261	0.793
Distance to rivers	1.474	0.678
Lithology	1.003	0.997
Slope angle	1.525	0.656
TWI	1.178	0.849
Profile curvature	1.319	0.758
Land use	1.233	0.811
Plan curvature	1.409	0.710
NDVI	1.175	0.851
Slope aspect	1.226	0.816

(0.717) belongs to the class of <10°, which indicates that most landslides occur in regions with lower slope angles. For altitude, the regions in which altitudes are less than 3500 m have promoting effects on landslide occurrence, and the CF value is the highest (0.961) when altitudes are 2000 m–2500 m. For plan curvature, there are only two positive CF values of .117 and 0.187, which belong to the classes of (−0.65)-0.14 and 0.14-1.19, respectively. For profile curvature, the class of 0.28–1.73 has the highest CF value of 0.190, followed by the class of (−0.80)-0.28 (0.125). It can be observed that the CF values significantly rise with the increase of the TWI values, and the CF value is the highest for the class of 4.78–15.12 (0.859). For the distance to rivers, the highest CF value is the only positive value, which is observed for <200 m. As obvious from the results of distance to roads, landslide occurrence density decreases with the lengthening of the distance to roads. Thus, there is no doubt that rivers and road construction generally trigger landslide hazards. For NDVI, the CF value is the highest (0.350) for the class of (−0.16)-(−0.01), followed by the class of (−0.01)-0.01 (0.263). The results show that vegetation on a slope surface can prevent landslide occurrence. For the influence situation of land use, construction land, farmland, and unused land have higher CF values of 0.984, 0.810, and 0.027, respectively, indicating that human activities play a critical role in landslide distribution. In terms of soil type, the highest CF value of 0.866 is found in group 8, followed by group 10 (0.861). Moreover, for lithology, group C and group I have the positive CF values of 0.232 and 0.416, respectively.

5.3 Application of models

After determining the most effective conditioning factors, based on the CF analysis result of correlation, LSI analyses were performed following the formula below (Eq. 5). The factors first had to be reclassified to calculate the landslide distribution for each class shown in pixel amount. The final LSM was determined by the superposition of the results of the twelve factor maps using the Raster Calculator Module. The output values were reclassified into five categories, namely, very low, low, moderate, high, and very high, according to geometrical interval method (Pham et al., 2016b) (Figure 5A).

$$LSI_{CF} = Altitude_{CF} + Slope\ angle_{CF} + Slope\ aspect_{CF} + Plan\ curvature_{CF} + Profile\ curvature_{CF} + TWI_{CF} + NDVI_{CF} + Distance\ to\ rivers_{CF} + Distance\ to\ roads_{CF} + Landuse_{CF} + Soil_{CF} + Lithology_{CF} \quad (6)$$

It is evident that a large drawback of bivariate models, such as the CF mode, is that they only consider a single factor, that is,

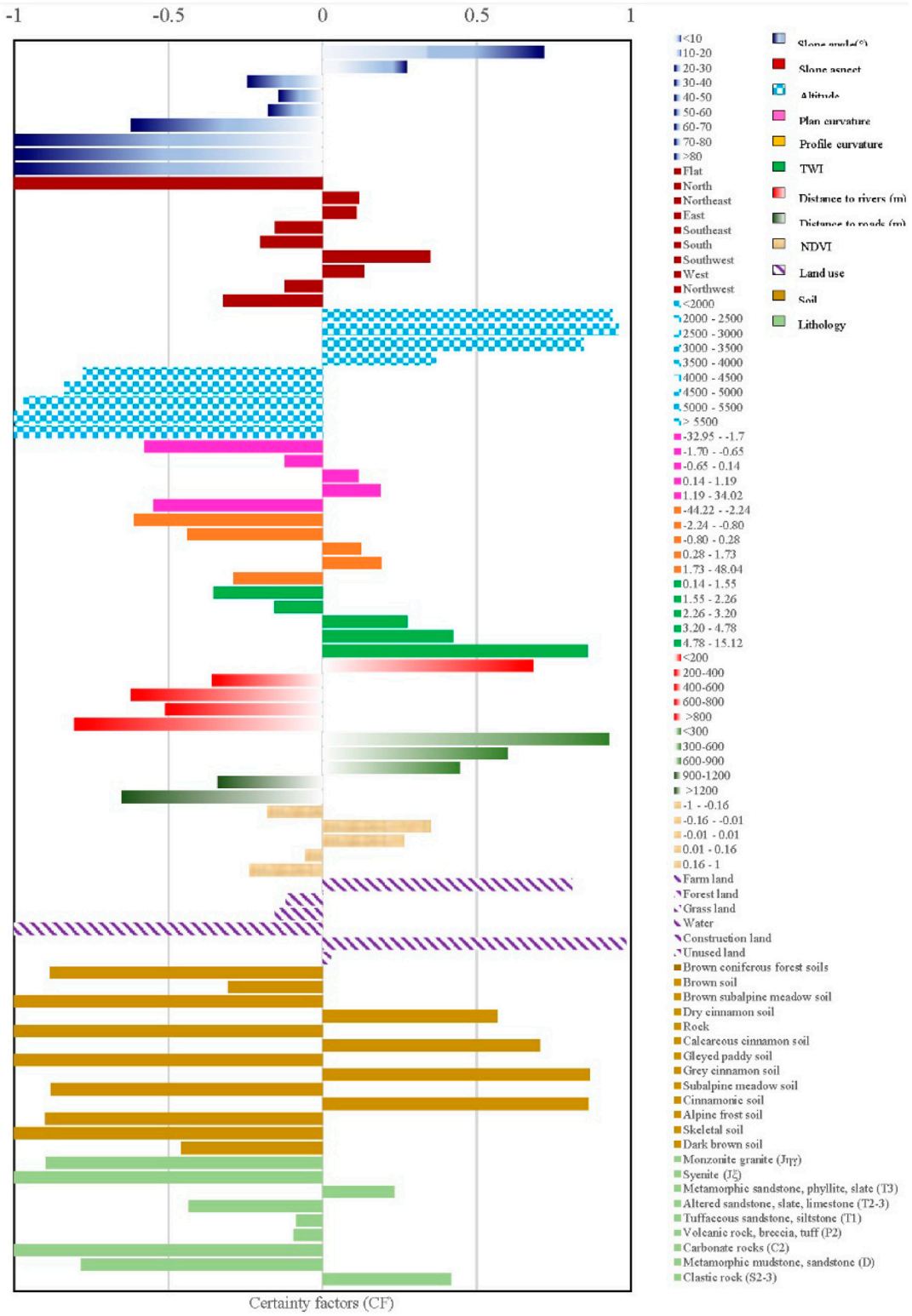

FIGURE 4
Correlation between landslides and factors by CF.

sub-factors weights. A CF and ML model coupling pattern that can augment the result of the ML models can thus be envisaged. We denoted landslide (328) and non-landslide (328) pixels by value 1 or value 0 in this study using 656 input variables. Input variables must be split into two parts: 70% training and 30% validation. After the CF model was successfully established, these data were pretreated with

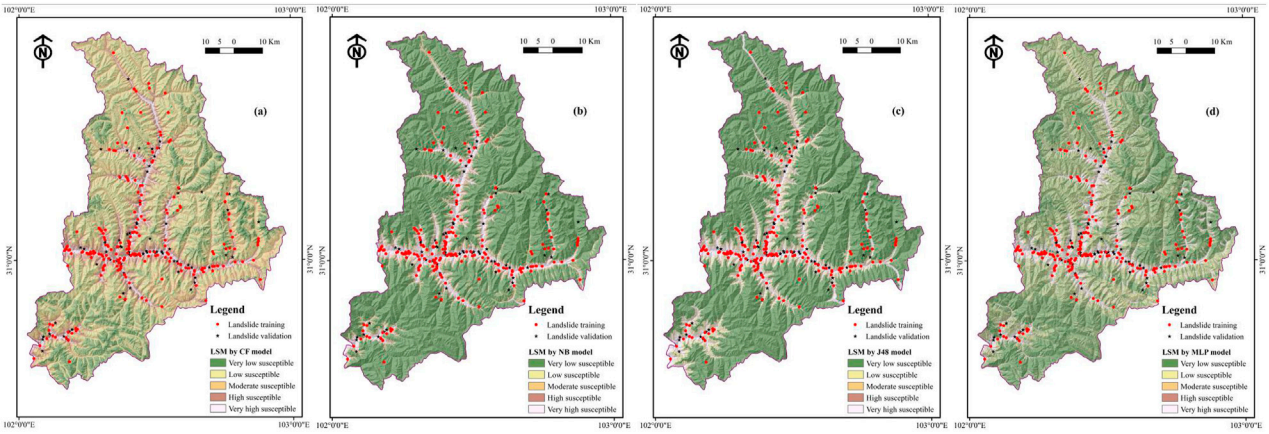

FIGURE 5
Landslide susceptibility map: **(A)** CF model, **(B)** NB model, **(C)** J48 model, **(D)** MLP model.

the CF value as the input of the NB model. The NB model was implemented in the Weka software to output the LSI value of each pixel in the full study area. The range of output values was from 0 to 1, which reflects the probability of landslide occurrence of this pixel position. Along these lines, all the LSI values were converted to ArcGIS, and the spatial mapping process was performed. Similarly to the CF classification, the NB classification model was established, in which each category area indicates the different intensity of the landslide. Then, the validating data were input into the trained model to test the accuracy of the trained network. The final LSM was presented by the machine learning NB model (Figure 5B).

In the present study, Weka software was employed to form landslide susceptibility with the J48 model. When running the J48 program, we chose the confidence factor as 0.25, which is the threshold to determine whether there shall be pruning or not. The minimum number of objects of each leave is 2, and the number of folds is 3. The pruning scheme is a reduced error pruning approach. Finally, the landslide susceptibility index (LSI) values were calculated, and the corresponding landslide susceptibility map (Figure 5C) was generated using ArcGIS software. Similarly, the LSI values were arranged into five classes.

For the MLP algorithm, the BP learning approach and auto hidden layer were adopted to model highly non-linear functions. Every layer consists of a number of neurons, which independently process information, and these neurons connect with the other layers of neurons by the weight. Then, the output values were imported into ArcGIS software to produce a landslide susceptibility map (Figure 5D). Through reclassification based on the geometrical interval method, five different susceptibility classes were obtained.

As suggested from the four visual inspections of Figures 5A–D, there is a similar pattern of susceptibility distribution, which exhibit an obvious rule. All the very high categories are distributed along national road G350 and provincial road S210 and the river and valley. In addition, very high categories are also located in the calcareous cinnamon soil-type area, which is the cause of highly weathered soil damage slope stability. Different susceptibility maps have the same total number of pixels, but the pixels for each category of susceptibility are different. The comparison of area pixels for each category of the four maps is shown in Figure 6, and the accuracy of these maps shown in Figures 7, 8. Although the four models yield high accuracy, the four LSMs highlight significant differences. CF and NB depict reasonable patterns, whereas the very high area only has a few pixels, and the categories of "low and very low" have the majority of pixels. By contrast, J48 and MLP encounter an unreasonable problem. As the very high category occupies more pixels, some of them appear in flat areas.

5.4 Validation and comparison of models

In this section, the performance study of various models with training data and validating data would make great progress by the evaluation and comparison of the ROC curves, AUC values, and non-parametric testing approaches.

In this study, the general performance of a bivariate model and three ML models has been assessed by the ROC curves and AUC values. For the training data (Table 3), the CF bivariate model has the best fit quality, and the AUC value is as high as 0.901 with a correspondingly perfect confidence interval of 0.872–0.931. In the three ML models, NB is the highest reached (0.893), and the 95% confidence interval is from 0.863 to 0.923. The AUC value of the MLP model is 0.835 with a confidence interval of 0.797–0.872. The performance of the J48 model is inferior to the other models, and the AUC value of the MLP model is 0.798 with a confidence interval of 0.754–0.843.

In the more important case of validating data (Table 4), the CF model remains stable at first place in model performance in terms of AUC with a value of 0.892, and NB model remains stable at first place in the three ML models, thus presenting the best AUC with a value of 0.887. The MLP and J48 models also exhibit good predictive ability with AUC values of 0.831 and 0.804. In addition, the CF and NB models possess the lowest standard errors and confidence intervals, with standard error values of 0.023 and 0.024 and 95% confidence intervals of 0.847–0.937 and 0.84 to 0.935, respectively. The predictive performance of the J48 and MLP models seems poor compared that of the other models.

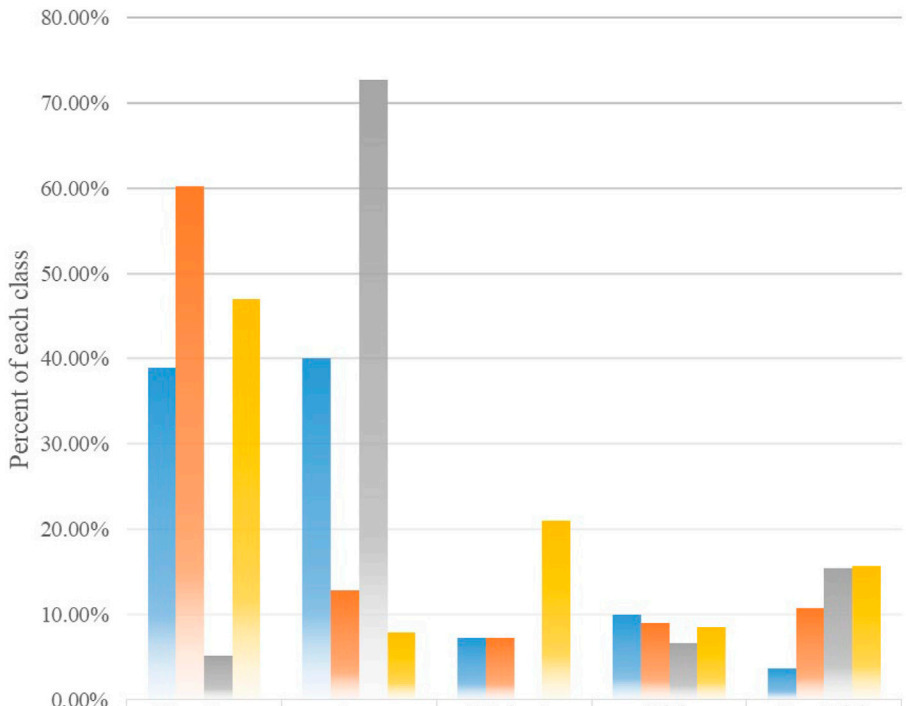

	Very Low	Low	Moderate	High	Very High
CF	38.99%	40.06%	7.29%	9.99%	3.67%
NB	60.20%	12.88%	7.22%	9.02%	10.68%
J48	5.15%	72.79%	0.03%	6.64%	15.39%
MLP	46.94%	7.91%	21.04%	8.49%	15.62%

FIGURE 6
Percentages of landslide susceptibility classes.

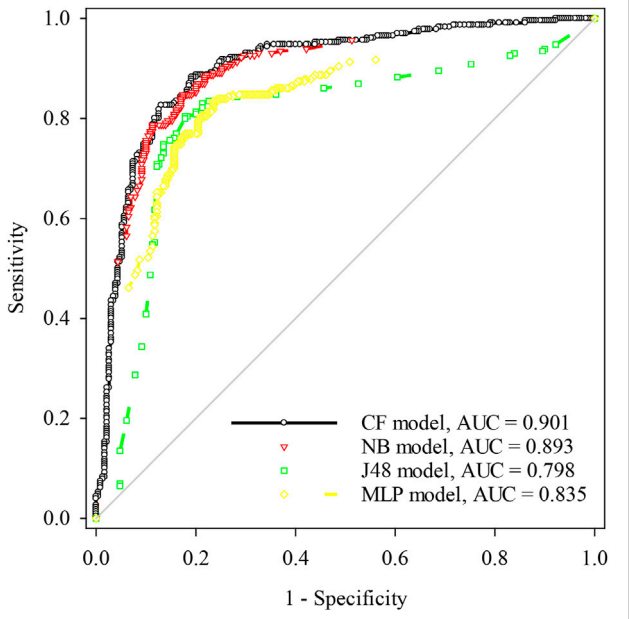

FIGURE 7
ROC curves of the models using training dataset.

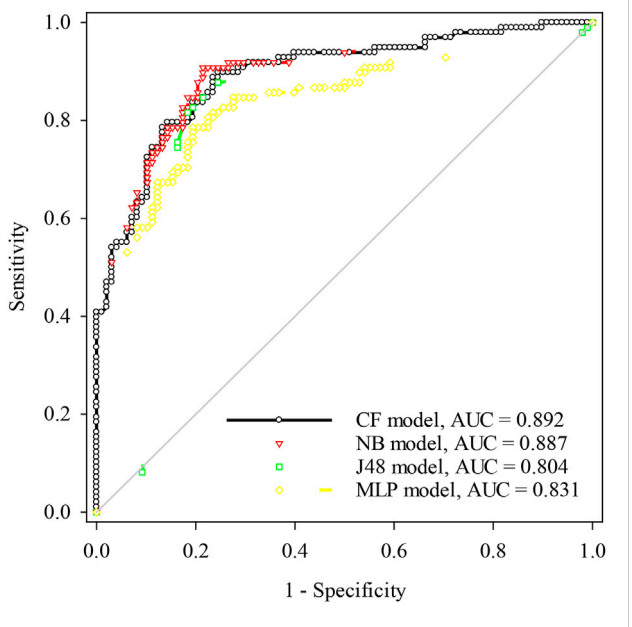

FIGURE 8
ROC curves of the models using validation dataset.

TABLE 3 Parameters of ROC curves using training dataset.

Models	AUC	Standard error	95% confidence interval	P
CF	0.901	0.015	0.872 To 0.931	<0.0001
NB	0.893	0.015	0.863 To 0.923	<0.0001
J48	0.798	0.023	0.754 To 0.843	<0.0001
MLP	0.835	0.019	0.797 To 0.872	<0.0001

TABLE 4 Parameters of ROC curves using validation dataset.

Models	AUC	Standard error	95% confidence interval	P
CF	0.892	0.023	0.847 To 0.937	<0.0001
NB	0.887	0.024	0.840 To 0.935	<0.0001
J48	0.804	0.034	0.737 To 0.870	<0.0001
MLP	0.831	0.030	0.773 To 0.890	<0.0001

TABLE 5 Pairwise comparison for the four models using the validation dataset based on chi-square.

Pairwise comparison	Chi-square	*p*-Value	Significance
CF vs. NB	0.496	0.481	No
CF vs. J48	11.670	0.000	Yes
CF vs. MLP	8.945	0.003	Yes
NB vs. J48	10.450	0.001	Yes
NB vs. MLP	7.625	0.006	Yes
J48 vs. MLP	0.816	0.367	No

Determining the effective identify among the models, whether or not there exist significant differences, has been a critical step in the LSA tasks. In the session, the chi-square was adopted, and the results are listed in Table 5. It can be seen that the *p* values (0.481 and 0.367) exceed the significant level (0.05). Hence, it can be inferred that the performance of CF is similar to NB statistically, and J48 is similar to the MLP model statistically. Furthermore, in terms of the quantitative difference of the models, it is clear seen from the calculated chi-square values that there is no significant difference between the CF and NB models and the MLP and J48 models as the value does not exceed 3.841. The two sets of models have no significant difference compared to other model sets, because both of these values are below the threshold, and the other model sets only have a low significance level because these values are slightly higher than the threshold.

6 Discussion

Based on the field survey information, the CF, J48, MLP, and NB models were implemented to produce landslide susceptibility maps of the study area. The AUC values and a series of statistical indexes were used to measure the accuracy of four maps. The results obviously demonstrate that four models have excellent performance in landslide susceptibility mapping, and a similar outcome appears both for the training and validation subsets. Among them, the CF and NB models have a superior effect, while the performance of the other two models has no significant difference. In terms of the present study, the initial data best accord with the pre-assumptions of the CF models, and this model naturally has a solid mathematical foundation. Thus, the landslide susceptibility map generated by the CF and NB models exhibits better accuracy and rationality. It seems preferable to select CF and NB as the susceptibility model over the study area. It is striking that the actual validation subset of J48 received better performance than the training set, especially for decision trees. It is very rare that it produces an overfit for within-sample models and loses much predictive power when predicting an out-of-sample situation (Schaffer, 1993), as is well known. This uncommon result may be explained due to the randomness of the sampling. This relationship shows that the original landslide data exhibit low internal variability, regardless of the sampling scheme. In turn, this allows us to consider the resulting susceptibility maps as a reliable tool to predict landslides in Xiaojin County. In addition, the parameters of the classifiers and the correlation among the conditioning factors determine the classification results to some degree. It can be believed that the comprehensive performance of the MLP and J48 models may be further improved by parameter optimization and conditioning factor selection. Therefore, due to the uncertainties in landslide susceptibility modeling, there is more than one approach to generate satisfying results, and the optimized approach is hard to determine.

For the twelve conditioning factors mentioned above, the importance of altitude is the highest, followed by soil type, distance to roads, and distance to rivers. Generally, lower altitude areas have a higher probability of landslide occurrence (Polykretis et al., 2015; Hong et al., 2019). Landslide susceptibility delineation depends on the selected conditioning factors and the weight of each

variable. If the modeling's objective is to improve the process performance measures rather than just surveillance and prediction, the thorough understanding of the causes leading to this result is of great value. Being able to show the relative importance of the variables using different models may pique the interest of the model utility. In the present analysis, the J48, NB, MLP, and three ML models were used to calculate the relative contribution of each variable to the three models themselves. A total of 12 selected conditioning factors were tested (Figure 3), and according to results, we can confirm that the top four conditioning factors are the most significant in all the models. This result is consistent with the visual inspection of the LSM analyzed in Section 5.3. The LSM and the four most significant factor maps obey a similar spatial pattern. Even if all four factor maps have this feature, as can be intuitively seen, the contribution percentage to models (in descending order) was: altitude, soil, distance to roads, and distance to river. For the remaining eight non-significant conditioning factors, the contribution of slope aspect occupies the lowest percentages for the NB and J48 models, while for the MLP model, NDVI reveals the lowest percentages; moreover, the profile curvature factor importance value is lower than that of land use and plan curvature for the J48 model but not for NB and MLP. All in all, different factors have different importance values due to different evaluation models (Tien Bui et al., 2016). Finally, we provide a hypothesis that there may be factor overestimation and underestimation presence.

In this study area, most landslides spread in areas in which altitudes are less than 3000 m. The main reason is that human activities are always more severe in lower altitude areas, which is one of the most critical landslide-triggering factors in Xiaojin County. Normally, areas covered by loose deposits are prone to cause landslides (Cui et al., 2019; Huang et al., 2019; Zhang et al., 2019), which has been proved by this study as well. Moreover, the results showed that the density of landslide points basically decreases as the distance to rivers and roads increases. This is because the incidence of river erosion and road construction disturbance is usually finite (Dang et al., 2019). In the case of the slope angle, areas with low slope angles have a higher possibility of landslide occurrence, which does not conform to conventional cognition. The basic reason is that areas with gentle terrain are generally suitable for land development activities such as farming, irrigation, and construction. The land use–landslide susceptibility relationship also indicates that farmland and construction land have positive effects on landslide occurrence. Therefore, it can be inferred that landslide occurrence in Xiaojin County has firm connections with human activities. Meanwhile, the slope aspect is regarded as a useless conditioning factor, indicating that the influence of this factor can be neglected to raise the computing efficiency of classifiers. For the other conditioning factors, the correlation between them and landslide occurrence is relatively reasonable according to the relevant literature (Hong et al., 2017a; Hong et al., 2017b). Considering the model construction and overall performance, the conclusion obtained in this paper is that the CF bivariate model proved best because it performed excellently and with stable classification ability in predicting landslides in Xiaojin County. This is a unique conclusion of the predictive studies: traditional statistical computing models are far ahead of intelligent ML models. Moreover, CF could greatly improve time efficiency as it eliminates the lengthy modeling process of ML. Therefore, future studies should not only pursue state-of-the-art algorithms. The final recommendation is centered on combining data analysis with GIS applications as framework templates so that this could become more widely used.

7 Conclusion

In this study, the CF, NB, J48, and MLP models were applied to evaluate landslide susceptibility in Xiaojin County, China. The information of regional geology and landslide points was obtained by a field survey and aerial photographs interpretation. To establish the set of conditioning factors regarding landslide occurrence, a total of twelve initial conditioning factors were determined. Furthermore, the importance of various conditioning factors was assessed using AM values, and slope aspect was removed from the landslide susceptibility modeling process. Moreover, the interaction between landslide occurrence and each conditioning factor was analyzed by the CF method. As a result, it was found that the negative synergy that forms high landslide susceptibility consists of 0°–10° slopes, 2000–2500 m altitude, 0.14–1.19 interval in plan curvature, 0.28–1.73 interval in profile curvature, 4.78 < TWI <15.12, distance <200 m from rivers, distance <300 m from roads, −0.16 < NDVI < −0.01, construction land in land use, group 8 of soil types, and group I of lithology types. Additionally, the comprehensive performance of the four models in landslide susceptibility mapping was compared by statistic indexes, ROC curves, and AUC values. It can be concluded that the CF bivariate model has the best predictive capacity with an AUC value of 0.892 AUC, and the NB model also has a better predictive capacity with an AUC value of 0.887, followed by the MLP model (AUC=0.831) and J48 model (AUC=0.804). Based on the results of the Wilcoxon signed-rank test (two-tailed), it is clear that the performance of NB model is significantly similar to the CF model and likewise for the J48 and MLP models. Finally, four landslide susceptibility maps were reclassified into five categories, and all the produced landslide susceptibility maps were found to have profound applicability and practical significance on landslide prevention in Xiaojin County. The obtained landslide susceptibility map can inform local authorities in their endeavors to undertake disaster prevention and mitigation measures, effectively reducing the scope of landslide investigations. In the event of a landslide occurrence, it enables the judicious selection of appropriate refuge sites.

Data availability statement

The original contributions presented in the study are included in the article/Supplementary material, further inquiries can be directed to the corresponding author.

Author contributions

Conceptualization, LX; methodology, LX and JS; software, JS; validation, JS, GD, and TZ; formal analysis, GD; investigation, LX; resources, TZ; data curation, GD; writing—original draft preparation, LX; writing—review and editing, LX, GD, and TW; visualization, JS; supervision, TW; project administration, LX;

funding acquisition, TW. All authors contributed to the article and approved the submitted version.

Funding

This research was funded by the Shaanxi Province Natural Science Basic Research Program (2022JQ-457), Shaanxi Land Construction-Xi'an Jiaotong University Land Engineering and Human Settlement Environment Technology Innovation Center Open Fund Project (2021WHZ0089). The authors declare that this study received funding from the Inner Scientific Research Project of Shaanxi Land Engineering Construction Group (DJNY-ZD-2023-1, DJNY-YB-2023-18, DJNY-YB-2023-28, DJNY2022-16, DJNY2022-36). The funder was not involved in the study design, collection, analysis, interpretation of data, the writing of this article, or the decision to submit it for publication.

Conflict of interest

Authors GD and TW were employed by the company Shaanxi Provincial Land Engineering Construction Group.

The remaining authors declare that the research was conducted in the absence of any commercial or financial relationships that could be construed as a potential conflict of interest.

Publisher's note

References

Ada, M., and San, B. T. (2018). Comparison of machine-learning techniques for landslide susceptibility mapping using two-level random sampling (2lrs) in alakir catchment area, antalya, Turkey. *Nat. Hazards* 90, 237–263. doi:10.1007/s11069-017-3043-8

Aditian, A., Kubota, T., and Shinohara, Y. (2018). Comparison of gis-based landslide susceptibility models using frequency ratio, logistic regression, and artificial neural network in a tertiary region of ambon, Indonesia. *Geomo* 318, 101–111. doi:10.1016/j.geomorph.2018.06.006

Aghdam, I. N., Varzandeh, M. H. M., and Pradhan, B. (2016). Landslide susceptibility mapping using an ensemble statistical index (wi) and adaptive neuro-fuzzy inference system (anfis) model at alborz mountains (Iran). *Environ. Earth Sci.* 75, 553. doi:10.1007/s12665-015-5233-6

Akgun, A. (2012). A comparison of landslide susceptibility maps produced by logistic regression, multi-criteria decision, and likelihood ratio methods: A case study at İzmir, TTurkey *Landslides* 9, 93–106. doi:10.1007/s10346-011-0283-7

Althuwaynee, O. F., Pradhan, B., and Lee, S. (2012). Application of an evidential belief function model in landslide susceptibility mapping. *Comput. Geosci.* 44, 120–135. doi:10.1016/j.cageo.2012.03.003

Amiri, M., Pourghasemi, H. R., Ghanbarian, G. A., and Afzali, S. F. (2019). Assessment of the importance of gully erosion effective factors using boruta algorithm and its spatial modeling and mapping using three machine learning algorithms. *Geoderma* 340, 55–69. doi:10.1016/j.geoderma.2018.12.042

An, H., Viet, T. T., Lee, G., Kim, Y., Kim, M., Noh, S., et al. (2016). Development of time-variant landslide-prediction software considering three-dimensional subsurface unsaturated flow. *Environ. Model. Softw.* 85, 172–183. doi:10.1016/j.envsoft.2016.08.009

Arabameri, A., Pradhan, B., Rezaei, K., and Lee, C.-W. (2019a). Assessment of landslide susceptibility using statistical- and artificial intelligence-based fr–rf integrated model and multiresolution dems. *Remote Sens.* 11, 999. doi:10.3390/rs11090999

Arabameri, A., Rezaei, K., Cerdà, A., Conoscenti, C., and Kalantari, Z. (2019b). A comparison of statistical methods and multi-criteria decision making to map flood hazard susceptibility in northern Iran. *ScTEn* 660, 443–458. doi:10.1016/j.scitotenv.2019.01.021

Berrar, D. (2019). "Bayes' theorem and naive bayes classifier," in *Encyclopedia of bioinformatics and computational biology*. Editors S. Ranganathan, M. Gribskov, K. Nakai, and C. Schönbach (Oxford: Academic Press), 403–412.

Buchanan, B., and Shortliffe, E. (1984). *Rule-based expert systems*, 571–588.

Chen, X., and Chen, W. (2021). Gis-based landslide susceptibility assessment using optimized hybrid machine learning methods. *CATENA* 196, 104833. doi:10.1016/j.catena.2020.104833

Chen, W., Pourghasemi, H. R., Panahi, M., Kornejady, A., Wang, J., Xie, X., et al. (2017). Spatial prediction of landslide susceptibility using an adaptive neuro-fuzzy inference system combined with frequency ratio, generalized additive model, and support vector machine techniques. *Geomorphology* 297, 69–85. doi:10.1016/j.geomorph.2017.09.007

Chen, W., Lei, X., Chakrabortty, R., Chandra Pal, S., Sahana, M., and Janizadeh, S. (2021a). Evaluation of different boosting ensemble machine learning models and novel deep learning and boosting framework for head-cut gully erosion susceptibility. *J. Environ. Manage.* 284, 112015. doi:10.1016/j.jenvman.2021.112015

Chen, Y., Chen, W., Chandra Pal, S., Saha, A., Chowdhuri, I., Adeli, B., et al. (2021b). Evaluation efficiency of hybrid deep learning algorithms with neural network, decision tree and boosting methods for predicting groundwater potential. *Geo. Inter.* 37, 5564–5584. doi:10.1080/10106049.2021.1920635

Chen, Y., Chen, W., Janizadeh, S., Bhunia, G. S., Bera, A., Pham, Q. B., et al. (2021c). Deep learning and boosting framework for piping erosion susceptibility modeling: Spatial evaluation of agricultural areas in the semi-arid region. *Geo. Inter.* 37, 4628–4654. doi:10.1080/10106049.2021.1892212

Conforti, M., Pascale, S., Robustelli, G., and Sdao, F. (2014). Evaluation of prediction capability of the artificial neural networks for mapping landslide susceptibility in the turbolo river catchment (northern calabria, Italy). *Catena* 113, 236–250. doi:10.1016/j.catena.2013.08.006

Corominas, J., van Westen, C., Frattini, P., Cascini, L., Malet, J. P., Fotopoulou, S., et al. (2014). Recommendations for the quantitative analysis of landslide risk. *Bull. Eng. Geol. Environ.* 73, 209–263.

Cui, Y., Jiang, Y., and Guo, C. (2019). Investigation of the initiation of shallow failure in widely graded loose soil slopes considering interstitial flow and surface runoff. *Landslides* 16, 815–828. doi:10.1007/s10346-018-01129-9

Dai, F. C., Lee, C. F., Li, J., and Xu, Z. W. (2001). Assessment of landslide susceptibility on the natural terrain of lantau island, Hong Kong. *Environ. Geol.* 40, 381–391. doi:10.1007/s002540000163

Dang, V.-H., Dieu, T. B., Tran, X.-L., and Hoang, N.-D. (2019). Enhancing the accuracy of rainfall-induced landslide prediction along mountain roads with a gis-based random forest classifier. *Bull. Eng. Geol. Environ.* 78, 2835–2849. doi:10.1007/s10064-018-1273-y

Devkota, K. C., Regmi, A. D., Pourghasemi, H. R., Yoshida, K., Pradhan, B., Ryu, I. C., et al. (2013). Landslide susceptibility mapping using certainty factor, index of entropy and logistic regression models in gis and their comparison at mugling–narayanghat road section in Nepal himalaya. *Nat. Hazards* 65, 135–165. doi:10.1007/s11069-012-0347-6

Ding, Q., Chen, W., and Hong, H. (2017). Application of frequency ratio, weights of evidence and evidential belief function models in landslide susceptibility mapping. *Geocarto Int.* 32, 1–21. doi:10.1080/10106049.2016.1165294

Eiras, C., Souza, J., Freitas, R., Barella, C. F., and Pereira, T. M. (2021). Discriminant analysis as an efficient method for landslide susceptibility assessment in cities with the scarcity of predisposition data. *Nat. Hazards* 107, 1427–1442. doi:10.1007/s11069-021-04638-4

Elith, J., Leathwick, J. R., and Hastie, T. (2008). A working guide to boosted regression trees. *J. Animal Ecol.* 77, 802–813. doi:10.1111/j.1365-2656.2008.01390.x

Ercanoglu, M., and Gokceoglu, C. (2002). Assessment of landslide susceptibility for a landslide-prone area (north of yenice, nw Turkey) by fuzzy approach. *Environ. Geol.* 41, 720–730. doi:10.1007/s00254-001-0454-2

ESRI (2014). *Arcgis desktop: Release 10.2 redlands, ca*. Environmental systems research institute.

Felicísimo, Á. M., Cuartero, A., Remondo, J., and Quirós, E. (2013). Mapping landslide susceptibility with logistic regression, multiple adaptive regression splines, classification and regression trees, and maximum entropy methods: A comparative study. *Landslides* 10, 175–189. doi:10.1007/s10346-012-0320-1

Frank, E., Hall, A., M., and Witten, H., I. (2016). "The weka workbench," in *Online appendix for "data mining: Practical machine learning tools and techniques"*. fourth edition (morgan kaufmann).

Han, J.-C., Huang, Y., Zhang, H., and Wu, X. (2019). Characterization of elevation and land cover dependent trends of ndvi variations in the hexi region, northwest China. *J. Environ. Manag.* 232, 1037–1048. doi:10.1016/j.jenvman.2018.11.069

He, Q., Shahabi, H., Shirzadi, A., Li, S., Chen, W., Wang, N., et al. (2019). Landslide spatial modelling using novel bivariate statistical based naïve bayes, rbf classifier, and rbf network machine learning algorithms. *ScTEn* 663, 1–15. doi:10.1016/j.scitotenv.2019.01.329

Hong, H., Tsangaratos, P., Ilia, I., Chen, W., Xu, C., and Mikos, M. (2017a). "Comparing the performance of a logistic regression and a random forest model in landslide susceptibility assessments. The case of wuyaun area, China," in *Advancing culture of living with landslides*. Editors B. Tiwari, Y. Yin, and K. Sassa (Cham: Springer International Publishing), 1043–1050.

Hong, H., Ilia, I., Tsangaratos, P., Chen, W., and Xu, C. (2017b). A hybrid fuzzy weight of evidence method in landslide susceptibility analysis on the wuyuan area, China. *Geomorphology* 290, 1–16. doi:10.1016/j.geomorph.2017.04.002

Hong, H., Liu, J., Bui, D. T., Pradhan, B., Acharya, T. D., Pham, B. T., et al. (2018). Landslide susceptibility mapping using j48 decision tree with adaboost, bagging and rotation forest ensembles in the guangchang area (China). *CATENA* 163, 399–413. doi:10.1016/j.catena.2018.01.005

Hong, H., Shahabi, H., Shirzadi, A., Chen, W., Chapi, K., Ahmad, B. B., et al. (2019). Landslide susceptibility assessment at the wuning area, China: A comparison between multi-criteria decision making, bivariate statistical and machine learning methods. *Nat. Hazards* 96, 173–212. doi:10.1007/s11069-018-3536-0

Huang, Y., and Zhao, L. (2018). Review on landslide susceptibility mapping using support vector machines. *Catena* 165, 520–529. doi:10.1016/j.catena.2018.03.003

Huang, H., Song, K., Yi, W., Long, J., Liu, Q., and Zhang, G. (2019). Use of multi-source remote sensing images to describe the sudden shanshucao landslide in the three gorges reservoir, China. *Bull. Eng. Geol. Environ.* 78, 2591–2610. doi:10.1007/s10064-018-1261-2

Jaafari, A., Najafi, A., Pourghasemi, H. R., Rezaeian, J., and Sattarian, A. (2014). Gis-based frequency ratio and index of entropy models for landslide susceptibility assessment in the caspian forest, northern Iran. *Int. J. Environ. Sci. Technol.* 11, 909–926. doi:10.1007/s13762-013-0464-0

Jamal, M., and Mandal, S. (2016). Monitoring forest dynamics and landslide susceptibility in mechi–balason interfluves of darjiling himalaya, West Bengal using forest canopy density model (fcdm) and landslide susceptibility index model (lsim). *Model. Earth Syst. Environ.* 2, 1–17. doi:10.1007/s40808-016-0243-2

Juliev, M., Mergili, M., Mondal, I., Nurtaev, B., Pulatov, A., and Hübl, J. (2019). Comparative analysis of statistical methods for landslide susceptibility mapping in the bostanlik district, Uzbekistan. *Sci. Total Environ.* 653, 801–814. doi:10.1016/j.scitotenv.2018.10.431

Kanungo, D. P., Sarkar, S., and Sharma, S. (2011). Combining neural network with fuzzy, certainty factor and likelihood ratio concepts for spatial prediction of landslides. *Nat. Hazards* 59, 1491–1512. doi:10.1007/s11069-011-9847-z

Lee, C.-H. (2018). An information-theoretic filter approach for value weighted classification learning in naive bayes. *Data and Knowl. Eng.* 113, 116–128. doi:10.1016/j.datak.2017.11.002

Lei, X., Chen, W., and Pham, B. T. (2020a). Performance evaluation of gis-based artificial intelligence approaches for landslide susceptibility modeling and spatial patterns analysis. *ISPRS Int. J. Geo-Information* 9, 443. doi:10.3390/ijgi9070443

Lei, X., Chen, W., Avand, M., Janizadeh, S., Kariminejad, N., Shahabi, H., et al. (2020b). Gis-based machine learning algorithms for gully erosion susceptibility mapping in a semi-arid region of Iran. *Remote Sens.* 12, 2478. doi:10.3390/rs12152478

Leventhal, A. R., and Kotze, G. P. (2008). Landslide susceptibility and hazard mapping in Australia for land-use planning — With reference to challenges in metropolitan suburbia. *Eng. Geol.* 102, 238–250. doi:10.1016/j.enggeo.2008.03.021

Li, Y., Chen, W., Rezaie, F., Rahmati, O., Davoudi Moghaddam, D., Tiefenbacher, J., et al. (2021). Debris flows modeling using geo-environmental factors: Developing hybridized deep-learning algorithms. *GeoIn* 37, 5150–5173. doi:10.1080/10106049.2021.1912194

Magliulo, P., Di Lisio, A., Russo, F., and Zelano, A. (2008). Geomorphology and landslide susceptibility assessment using gis and bivariate statistics: A case study in southern Italy. *Nat. Hazards* 47, 411–435. doi:10.1007/s11069-008-9230-x

Manaswi, N. K. (2018). "Multilayer perceptron," in *Deep learning with applications using python: Chatbots and face, object, and speech recognition with tensorflow and keras*. Editor N. K. Manaswi (Berkeley, CA: Apress), 45–56.

Moayedi, H., Mehrabi, M., Mosallanezhad, M., Rashid, A. S. A., and Pradhan, B. (2019). Modification of landslide susceptibility mapping using optimized pso-ann technique. *Eng. Comput.* 35, 967–984. doi:10.1007/s00366-018-0644-0

Moore, I. D., Grayson, R. B., and Ladson, A. R. (1991). Digital terrain modelling: A review of hydrological, geomorphological, and biological applications. *HyPr* 5, 3–30. doi:10.1002/hyp.3360050103

Nsengiyumva, J. B., Luo, G., Nahayo, L., Huang, X., and Cai, P. (2018). Landslide susceptibility assessment using spatial multi-criteria evaluation model in Rwanda. *Int. J. Environ. Res. Public Health* 15, 243–255. doi:10.3390/ijerph15020243

Pham, B. T., Pradhan, B., Tien Bui, D., Prakash, I., and Dholakia, M. B. (2016a). A comparative study of different machine learning methods for landslide susceptibility assessment: A case study of uttarakhand area (India). *Environ. Model. Softw.* 84, 240–250. doi:10.1016/j.envsoft.2016.07.005

Pham, B. T., Bui, D. T., Prakash, I., and Dholakia, M. B. (2016b). Evaluation of predictive ability of support vector machines and naive bayes trees methods for spatial prediction of landslides in uttarakhand state (India) using gis. *J. Geomatics* 10, 71–79.

Pham, B. T., Prakash, I., and Tien Bui, D. (2018a). Spatial prediction of landslides using a hybrid machine learning approach based on random subspace and classification and regression trees. *Geomorphology* 303, 256–270. doi:10.1016/j.geomorph.2017.12.008

Pham, B. T., Shirzadi, A., Tien Bui, D., Prakash, I., and Dholakia, M. B. (2018b). A hybrid machine learning ensemble approach based on a radial basis function neural network and rotation forest for landslide susceptibility modeling: A case study in the himalayan area, India. *Int. J. Sediment Res.* 33, 157–170. doi:10.1016/j.ijsrc.2017.09.008

Polykretis, C., Ferentinou, M., and Chalkias, C. (2015). A comparative study of landslide susceptibility mapping using landslide susceptibility index and artificial neural networks in the krios river and krathis river catchments (northern peloponnesus, Greece). *Bull. Eng. Geol. Environ.* 74, 27–45. doi:10.1007/s10064-014-0607-7

Pourghasemi, H. R., and Rahmati, O. (2018). Prediction of the landslide susceptibility: Which algorithm, which precision? *CATENA* 162, 177–192. doi:10.1016/j.catena.2017.11.022

Pourghasemi, H. R., Teimoori Yansari, Z., Panagos, P., and Pradhan, B. (2018). Analysis and evaluation of landslide susceptibility: A review on articles published during 2005–2016 (periods of 2005–2012 and 2013–2016). *Arabian J. Geosciences* 11, 193. doi:10.1007/s12517-018-3531-5

Sathyadevan, S., Nair, R. R., Jain, L. C., and Behera, H. S. (2015). "Comparative analysis of decision tree algorithms: Id3, c4.5 and random forest," in *Computational intelligence in data mining*. Editors J. K. Mandal and D. P. Mohapatra (New Delhi: Springer India), 1, 549–562.

Schaffer, C. (1993). Overfitting avoidance as bias. *Mach. Learn.* 10, 153–178. doi:10.1007/bf00993504

Sharma, S., and Mahajan, A. K. (2019). A comparative assessment of information value, frequency ratio and analytical hierarchy process models for landslide susceptibility mapping of a himalayan watershed, India. *Bull. Eng. Geol. Environ.* 78, 2431–2448. doi:10.1007/s10064-018-1259-9

Sun, N., Sun, B., Lin, J., and Wu, M. Y.-C. (2018). Lossless pruned naive bayes for big data classifications. *Big Data Res.* 14, 27–36. doi:10.1016/j.bdr.2018.05.007

Sun, D., Shi, S., Wen, H., Xu, J., and Wu, J. (2021). A hybrid optimization method of factor screening predicated on geodetector and random forest for landslide susceptibility mapping. *Geomorphology* 379, 107623. doi:10.1016/j.geomorph.2021.107623

Tien Bui, D., Tuan, T. A., Klempe, H., Pradhan, B., and Revhaug, I. (2016). Spatial prediction models for shallow landslide hazards: A comparative assessment of the efficacy of support vector machines, artificial neural networks, kernel logistic regression, and logistic model tree. *Landslides* 13, 361–378. doi:10.1007/s10346-015-0557-6

Vuillez, C., Tonini, M., Sudmeier-Rieux, K., Devkota, S., Derron, M.-H., and Jaboyedoff, M. (2018). Land use changes, landslides and roads in the phewa watershed, Western Nepal from 1979 to 2016. *Appl. Geogr.* 94, 30–40. doi:10.1016/j.apgeog.2018.03.003

Wu, Z., Wu, Y., Yang, Y., Chen, F., Zhang, N., Ke, Y., et al. (2017). A comparative study on the landslide susceptibility mapping using logistic regression and statistical index models. *Arabian J. Geosciences* 10, 187. doi:10.1007/s12517-017-2961-9

Wu, Y., Ke, Y., Chen, Z., Liang, S., and Hong, H. (2020). Application of alternating decision tree with adaboost and bagging ensembles for landslide susceptibility mapping. *CATENA* 187, 104396. doi:10.1016/j.catena.2019.104396

Xie, W., Li, X., Jian, W., Yang, Y., Liu, H., Robledo, L. F., et al. (2021). A novel hybrid method for landslide susceptibility mapping-based geodetector and machine learning cluster: A case of xiaojin county, China. *ISPRS Int. J. Geo-Inf.* 10, 93. doi:10.3390/ijgi10020093

Xiong, S., Yao, W., and Li, C. (2019). Stability evaluation of multilayer slopes considering runoff in the saturated zone under rainfall. *Eur. J. Environ. Civ. Eng.* 25, 1718–1732. doi:10.1080/19648189.2019.1600038

Xu, C., Xu, X., Lee, Y. H., Tan, X., Yu, G., and Dai, F. (2012). The 2010 yushu earthquake triggered landslide hazard mapping using gis and weight of evidence modeling. *Environ. Earth Sci.* 66, 1603–1616. doi:10.1007/s12665-012-1624-0

Yalcin, A., Reis, S., Aydinoglu, A. C., and Yomralioglu, T. (2011). A gis-based comparative study of frequency ratio, analytical hierarchy process, bivariate statistics and logistics regression methods for landslide susceptibility mapping in trabzon, ne Turkey. *CATENA* 85, 274–287. doi:10.1016/j.catena.2011.01.014

Zare, M., Pourghasemi, H. R., Vafakhah, M., and Pradhan, B. (2013). Landslide susceptibility mapping at vaz watershed (Iran) using an artificial neural network model: A comparison between multilayer perceptron (mlp) and radial basic function (rbf) algorithms. *Arabian J. Geosci.* 6, 2873–2888. doi:10.1007/s12517-012-0610-x

Zhang, M., Wu, L., Zhang, J., and Li, L. (2019). The 2009 jiweishan rock avalanche, wulong, China: Deposit characteristics and implications for its fragmentation. *Landslides* 16, 893–906. doi:10.1007/s10346-019-01142-6

Zhu, A. X., Miao, Y., Yang, L., Bai, S., Liu, J., and Hong, H. (2018). Comparison of the presence-only method and presence-absence method in landslide susceptibility mapping. *CATENA* 171, 222–233. doi:10.1016/j.catena.2018.07.012

frontiers | Frontiers in Earth Science

TYPE Original Research
PUBLISHED 12 September 2023
DOI 10.3389/feart.2023.1268064

OPEN ACCESS

EDITED BY
Chong Xu,
Ministry of Emergency Management, China

REVIEWED BY
Iunio Iervolino,
University of Naples Federico II, Italy
Yuandong Huang,
Ministry of Emergency Management, China
Xiaoyi Shao,
China Earthquake Administration, China

*CORRESPONDENCE
Woo-Hyun Baek,
geoback@seoultech.ac.kr

RECEIVED 27 July 2023
ACCEPTED 05 September 2023
PUBLISHED 12 September 2023

CITATION
Ahn J-K, Cho S, Hwang E-H and Baek W-H (2023), Assessing network-based earthquake early warning systems in low-seismicity areas.
Front. Earth Sci. 11:1268064.
doi: 10.3389/feart.2023.1268064

Assessing network-based earthquake early warning systems in low-seismicity areas

Jae-Kwang Ahn[1], Seongheum Cho[1], Eui-Hong Hwang[2] and Woo-Hyun Baek[3]*

[1]Earthquake and Volcano Technology Team, Korea Meteorological Administration, Seoul, Republic of Korea, [2]Earthquake and Volcano Research Division, Korea Meteorological Administration, Seoul, Republic of Korea, [3]Department of Civil Engineering, Seoul National University of Science and Technology, Seoul, Republic of Korea

Earthquake early warning (EEW) technology, designed to alert the public of earthquake risks after initial P-wave detection but before the onset of strong tremors, has developed rapidly. Methodologies from various fields are combined in EEW systems to estimate earthquake locations, magnitudes, and expected intensities based on the initial P-wave data. These systems operate automatically because prompt responses are required. However, as no common evaluation framework for EEW system verification exists, potentially divergent evaluations from reviewers or countries could ensue. Moreover, evaluating EEW systems is more complicated when the target area does not experience frequent earthquakes. We aimed to establish a guidance review process for low-seismicity areas to ensure reliable and stable integrated EEW system operation. We incorporated management aspects through actual system operator surveillance and designed an EEW assessment process based on feedback from our surveys. Using this approach, we created a comprehensive and well-informed evaluation process that considers the diverse perspectives of experts involved in EEWs. Our proposed assessment method allows for a uniform and consistent evaluation process, regardless of changes in the methods or technologies used by EEW systems. The method aims to guide EEW system assessments in low-seismicity areas.

KEYWORDS

warning assessment, analytic hierarchy process, earthquake early warning, lowseismicity area, public services, seismic hazard

1 Introduction

For rapid mitigation against seismic hazards, automated alerting technology based on seismic networks EEWs is used, with automated event estimation employed to facilitate the issuing of timeous public alerts (Allen and Melgar, 2019; Velazquez et al., 2020). Such systems operate at national or local government levels, as their fundamental technology requires 24 h monitoring (Mayer et al., 2008). Several countries have implemented EEW systems as public services, including Japan (Hoshiba and Ozaki, 2014), Republic of Korea (Lee et al., 2022), Taiwan (Hsiao et al., 2009), and the United States (Kohler et al., 2018). Among these countries, Republic of Korea experiences the lowest occurrence frequency of medium-to large-scale earthquakes.

After the introduction of EEW in Republic of Korea in 2015 (KMA, 2018), public awareness remained low until two earthquakes occurred (local magnitude [M_L] = 5.8 on

12 September 2016, and M_L = 5.4 on 15 November 2017). The low level of public awareness could be ascribed to the occurrence and recording of only ten earthquakes exceeding $M_L > 5.0$ since instrumental observations started in 1980. However, the two events of 2016–2017 were a timely reminder of the importance of EEW, and EEW technology has since developed rapidly in the country. Initially, a cell broadcasting service (CBS) was intended for governmental use, but the Korea Meteorological Administration (KMA, 2017) has extracted and applied relevant parts of the service for earthquake, tsunami, and volcano warnings (KMA, 2018). The network-based EEW system was optimized further to suit domestic observation environments, estimation of magnitudes (Sheen et al., 2018), and detection of initial P-waves (Cho et al., 2022).

KMA EEW progress relies on warning time reduction, as it is crucial to warn people as quickly as possible in the case of an earthquake (Bostrom et al., 2022; Ahn et al., 2023). Warning time is a critical factor in assessing preparedness for an earthquake and a vital consideration from a risk management perspective (Allen et al., 2009). The evaluation of EEWs is often based on lead time, i.e., the time between an alert is received and the arrival of tremors or shaking (Cremen et al., 2022). A primary method to reduce EEW lead time is decreasing the number of stations (nS) used for detecting earthquakes in the initial analysis version of the event. However, the likelihood of prediction errors increases when fewer stations are involved in earthquake determination and analysis.

Although Republic of Korea has not experienced social disruption induced by false earthquake alarms for KMA, such incidents could cause substantial social issues. On 5 January 2018, a false alarm occurred when an EEW mistakenly identified two small earthquakes as one large earthquake in Japan, causing temporary public panic (BBC News, 2018). The head of the Japan Meteorological Administration was forced to apologize publicly for the error. Owing to a computer error, a warning of a large-scale earthquake off the coast of California (United States) was issued on 22 June 2017, 92 years after it had actually occurred. This warning caused widespread public confusion (BBC News, 2017). Another notable example is a false alert issued in Mexico on 28 July 2014, by Sky Alert, a popular smartphone application, prompting response from numerous people. This incident triggered a social issue in Mexico, invoking Aesop's fable "The Boy Who Cried Wolf" (Reddy, 2020). Although SkyAlert is not a public service, the consequences of the false alarm emphasized the importance of proper EEW management.

While the fact that Republic of Korea experiences fewer earthquakes and alerts may be considered a positive aspect, it has also led to many Koreans being unaware of EEWs. According to a 2020 survey by Ahn (2021), only 84 (approximately 44%) of 192 general public respondents (i.e., non-seismologists and non-civil engineers) were aware of EEWs. As a result of the limited number of alert cases and the lack of public awareness, obtaining public evaluations of these services remains a challenge.

Owing to these limitations, EEWs are generally evaluated by experts rather than the public. Past studies have either assessed the point source or alert accuracy. Point source assessments verify EEW algorithms for magnitude and hypocenter accuracy (e.g., Cua et al., 2009; Chen et al., 2015; Massin et al., 2021). Alert assessments are performed to prevent errors during operations or simulations (e.g., Chen et al., 2019; Chung et al., 2019; Zuccolo et al., 2021). However, management aspects require a comprehensive review of the overall EEW. Cochran et al. (2018) proposed a framework for a Testing and Certification Platform (TCP) that assesses the performance of the overall system alerts issued by the decision module and those generated by individual algorithms. The TCP assessment consists of both point-source alert elements (i.e., magnitude, epicentral location, origin time, and alert latency) and ground-motion prediction accuracy. TCP is evaluated on the basis of alerts, and the more earthquakes available for evaluation, the better. Unfortunately, in countries with low earthquake frequency and relatively few strong motions, the Cochran et al. (2018) platform is limited.

Expert assessments vary based on the knowledge and interests of the individual conducting the evaluation (Binger et al., 2012; May et al., 2016). Additionally, the evaluator must make a minimum number of decisions for the assessment, which could be challenging. Experts tend to be cautious during decision-making because their decisions ultimately affect the public services provided to citizens (Meijer and Grimmelikhuijsen, 2020). For KMA EEW, the public is informed of earthquake risks for events with $M_L > 3.5$. However, since 2010, there have been only five events of $M_L \geq 5.0$. As a result, evaluations often include earthquakes with slight magnitudes which was events of $M_L \geq 2.5$ (Cho et al., 2022). These issues raise concerns regarding the appropriate magnitude target for assessment, review area, and acceptable accuracy standard. Answers from the experts could differ, i.e., it is crucial to recognize that even experts could hold different perspectives on related issues.

The fundamental goal of an EEW is achieving promptness and accuracy (Allen et al., 2009; Kamigaichi et al., 2009; Satriano et al., 2011; Finazzi, 2020) However, balancing these two aspects is challenging, and performance scores could vary depending on the criteria and the reviewer. Therefore, as regards the decision-making process in assessing EEW, it is essential to integrate expert opinion with the goal of providing an effective public service, as different people could have different values and priorities, even when working toward a common mission. Therefore, we aimed to establish an EEW review method that incorporates management aspects through actual system operator surveillance. We designed an EEW assessment process based on the feedback received from our surveys, such as criteria for analysis, pairwise comparison, and so on. Our approach was to create a comprehensive and well-informed evaluation process that considers the diverse perspectives of the experts involved in EEWs.

2 Criteria and methods

2.1 Alert criteria and EEW service

Conservative alert standards are in place in the KMA EEW service. The Korean Peninsula is an area of low seismicity; therefore, even a small tremor could unnerve citizens. Furthermore, considering that the country hosts semiconductor factories, high-speed rails, and nuclear facilities, alert services are conducted with sensitivity preparation. In the event of an earthquake of $M_L \geq 3.5$, seismic information is disseminated within 5–10 s after the initial detection.

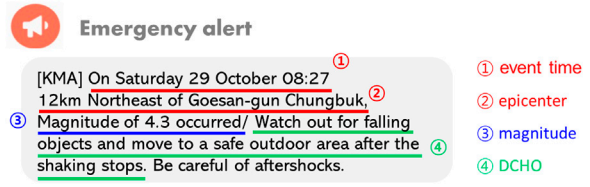

FIGURE 1
Warning messages delivered to end-users in Republic of Korea to "drop, cover, and hold on" (DCHO).

The KMA EEW uses at least four stations for optimal performance (Cho et al., 2022), aiming to make decisions on alerts about 5 s after the first observation when an earthquake occurs on the Korean Peninsula. In EEW, the theoretical minimum number of stations (nS) for hypocenter determination is three (Yamada et al., 2021), but relying on the assessment accuracy can be challenging. Low accuracy is particularly associated with earthquakes occurring outside the observation network. Based on these settings, when an earthquake with $M_L > 3.5$ (or > 4.0, if occurring over the sea) occurs, a warning message is automatically propagated to the public. If an earthquake with an $M_L > 5.0$ occur, warnings with a stronger alert sound are disseminated. These alert criteria were designed as a policy decision in Republic of Korea. Therefore, the EEW alert decisions might differ in other countries.

Additionally, the KMA operates a network-based EEW that incorporates the algorithms ElarmS-3.0 (Chung et al., 2019), RTLoc (Satriano et al., 2008), and Maxwell–Hertz electrostatic potential theory (Sheen, 2016). These algorithms have been optimized for the Korean Peninsula by KMA and are used simultaneously for monitoring earthquakes. The KMA EEW is based on the mutual interaction and automatic collaborative decision making of the algorithms, and produces an alert when two or more algorithms detect an earthquake. In principle, if two logically distinct algorithms working concurrently sound an alert, the likelihood of an actual earthquake occurrence is higher.

By combining three algorithms, we achieve analysis accuracy as well as 24 h service stability. This approach has been instrumental in overcoming occasional system failures experienced by the KMA, including bugs, delays, and network issues. However, owing to the complexity of the algorithm, which involves the integration of multiple systems, it becomes sensitive to minor enhancements.

2.2 Disaster communications to the public

The KMA EEW alerts, determined by a combination of technology and policy, are issued to citizens in the event of an earthquake through the CBS. Using CBS technology, a warning is sent to numerous users in the vicinity of base stations (Doi, 2011; Wu et al., 2022). Alarm is transmitted to mobile phones in approximately 3 s (Minson et al., 2018), and the public receives messages shortly after earthquake detection. Alerts are forcibly sent to individual mobile phones in the form of emergency text messages. Figure 1 shows an example of earthquake warning information delivered to the public. The message provides information on the epicenter, event time, and magnitude of the earthquake, along with guidelines to "drop, cover, and hold on" (DCHO) (Porter, 2016).

Following alert dissemination, evaluations from citizens regarding the system's effectiveness could be gathered. Speediness, as perceived by the citizens, is the time difference between receiving the alert and feeling the earthquake vibrations. It is challenging for citizens to quantitatively assess promptness, as the warning and the shaking occur within a very short time frame. However, as regards source information (i.e., location, magnitude, and event time), people judge the warning accuracy by comparing it to subsequent earthquake information released through news broadcasts. Collecting feedback is vital for understanding the needs of the public with respect to the DCHO advice, which is a crucial aspect of emergency preparedness. However, intermediate and large earthquakes do not occur frequently in the Korean Peninsula, and assessing KMA EEW might be difficult for the general public. Consequently, only people who manage and develop the system can evaluate the KMA EEW.

2.3 Assessment survey and design

Operator or manager assessments may vary depending on the expertise of the reviewer (Cooke and Goossens, 2004). Here, evaluations conducted from the perspective of a small group of developers could lead to serious issues in the future. To address this concern, we gathered opinions from individuals with relevant experience and field knowledge. We surveyed 18 KMA employees who operated EEW from July 14–16, 2021. The survey research was designed and conducted in the following order 1) assessment parameter selection, 2) relational questionnaire development based on assessment parameters and pairwise analysis questionnaires for the factors, 3) operator interviews, 4) questionnaire criteria determination, analytic hierarchy process (AHP) analysis, and weight function designation, and 5) EEW operational aspect assessment.

2.3.1 Aspect-based assessment parameter selection

To select appropriate assessment parameters for EEW, two aspects were considered, namely, operations and management, which are distinct but interrelated. Operation refers to the day-to-day activities and tasks of a system (Whipple and Frankel, 2000). In EEWs, operations focus on the reliability of alert production (Medina-Cetina and Nadim, 2008). In contrast, management involves EEW planning and control to achieve high performance (Ittner and Lacker, 1997), considering alert reliability and seismic information accuracy (Ruhl et al., 2019; Esposito et al., 2022). Managers are responsible for overseeing objective reviews and implementing improvements, ensuring that a balance is maintained between safety, effectiveness, and sustainability (Too and Weaver, 2014). Figure 2 shows the EEW algorithm analysis process with both aspects. The assessment steps are shown in the EEW flow, considering algorithm analysis based on simulations.

As regards the operational aspects, system behavior was categorized into three steps. Step 1 is the evaluation preparation stage, comprising input of the earthquake scenario and setting the minimum targeted nS. Step 2 is the detection phase of the analysis

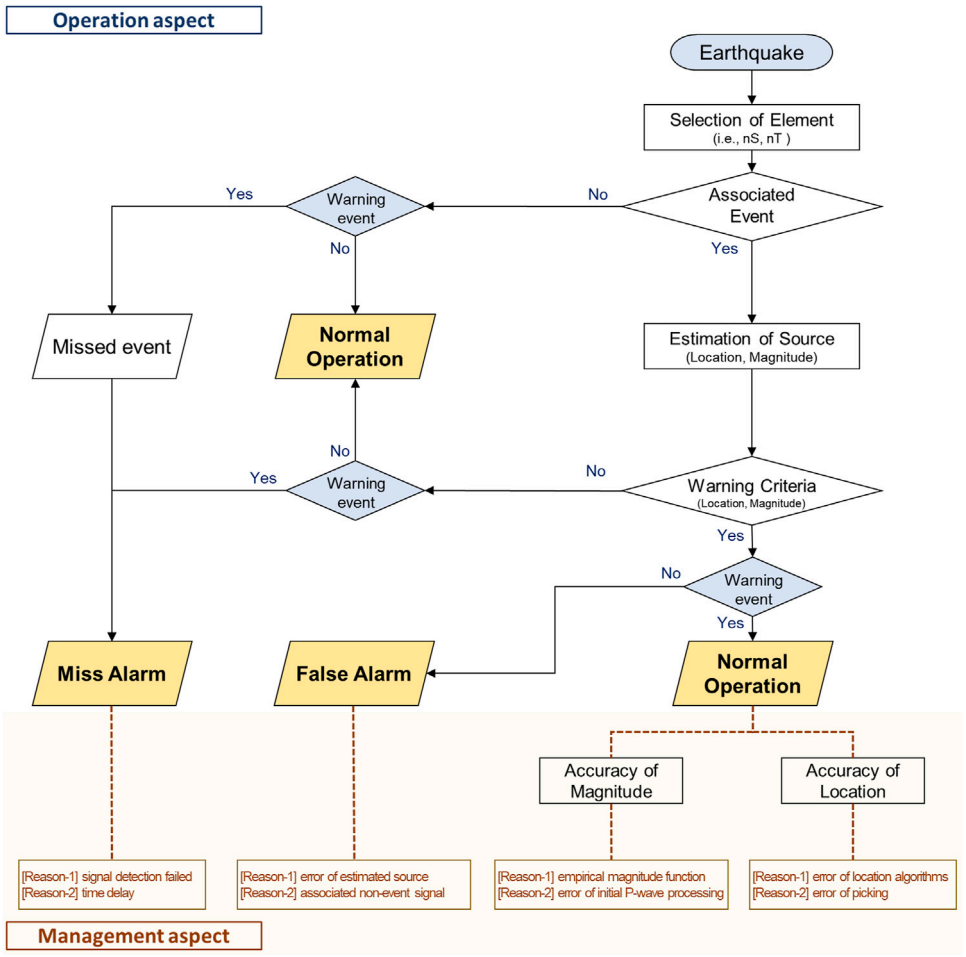

FIGURE 2
Flowchart of assessment parameter calculation process. nS, number of stations; nT, number of trigger sensors.

process [i.e., short-time-average over long-time-average trigger (Allen, 1982)] or the filter picker (Lomax et al., 2012). If the nS condition is satisfied, it is verified to determine whether it becomes an associated event (Cho et al., 2022). If the alarm fails to generate an event, verification is required whether this event was alarm worthy. Verification allows the determination of the alarm being operationally a false alarm or normal operation. Step 3 comprises predicting the source and assessing the alarm based on associated event information (Weyrich et al., 2021). Alarms can be produced by EEWs based on the predicted source information, which is termed decision making of warning (DMW).

As regards the management aspect, it is essential to verify the success of the alert and the source information that influenced the decision to issue an early warning. By considering all the parameters that impacted the final alert, it could be ensured that the algorithm and system were free of issues. Figure 2 presents representative error sources that could be easily identified from an administrator viewpoint. However, various errors could occur in operations, and this procedure is only applicable to natural earthquakes.

In the review of EEW assessment, we ignored the associate event time, which depends on the nS. Additionally, waveform data used in KMA seismic stations are applied only to locations that pass strict criteria for latency, background noise, and trigger rate (KMA, 2017; Ahn et al., 2021). Consequently, data lagging or failed equipment rarely occur for KMA EEW in real-time operations. However, from a management perspective, a station detection rate review within a certain time frame could be performed separately, because of trigger checking at the observatory.

We selected four parameters for this study based on aspects. 1) The first parameter is “prevent missed alerts (PM)” in the system, i.e., confirming whether a targeted earthquake alert was missed. Alerts in normal operations are issued when the national observation network detects a warning event using n stations. 2) The second parameter is “prevent false alerts (PF)” in the system, which determines whether a targeted earthquake alert is incorrect. This involves checking alarms that are normal operations, non-earthquakes, or source errors when EEW alerts occur. 3) The third parameter is the accuracy of magnitude (AM), and 4) is the accuracy of location (AL). These four parameters were reviewed from operational and administrative perspectives and represent all the information that the public sees when an alert is triggered.

2.3.2 Assessment criteria preparation

To help respondents better understand the assessment parameters, we provided training before conducting the research. During the training, we introduced various existing analytical examples, explained the unique features of the criteria, and received approval for ethical review surveys involving human participants. Further, we discussed the EEW technical and theoretical limitations. These are 1) Inability to fully understand the underground geological structure, implying that seismic information is subject to uncertainty at source (Iervolino et al., 2009; Tidlund et al., 2022; Murray et al., 2023; Ni et al., 2023). 2) Detection accuracy varies depending on the observation network because of wave propagation attenuation (Jackson and Anderson, 1970; Vipin and Sitharam, 2011; Goda et al., 2023). 3) Accuracy limitations of source detection in coastal earthquakes (Angove et al., 2019; Lim et al., 2020; Takabatake and Kojima, 2023), and the difficulty of installing seismometers in the seabed (Podolskiy et al., 2021). The system operators understood and agreed with these EEW limitations. In addition, we emphasized understanding of the characteristics of earthquakes in the Korean Peninsula, as well as the psychological conditions of the public. Given the infrequent occurrence of seismic events in the Korean Peninsula, even weak shaking could elicit feelings of surprise and unease among the general population (Kwon et al., 2020; Yeon et al., 2020). Therefore, unlike other countries, the KMA issues warning criteria from even slight magnitudes (M_L 3.5 and over).

Considering KMA policy and technology characteristics, we designed a questionnaire for the EEW assessment. In the criteria establishment stage of the survey, we created five response items to establish the assessment criteria. We classified the criteria between inland areas and outside (i.e., ocean, outside the country) of the seismic observation network. Both groups 1) within the seismic observation network (= inside seismic network, ISN) and 2) outside the seismic observation network (= outside seismic network, OSN) were considered. Categorization by observation network was included in all five questions.

The survey questions were:

Q.1: "What is the minimum magnitude of an earthquake to be analyzed for performance assessment?" We needed to establish a baseline progression for our evaluation, considering the margin of error in our prediction scale. However, detecting initial waveforms from slight magnitude earthquakes is complicated owing to their small amplitudes and poor observation environments. The EEW performance results could, therefore, vary depending on the criteria and magnitude, with greater sensitivity for weaker events than larger ones.

Q.2: "Compared with $M_L \geq 5.0$, how important is an earthquake of $M_L < 5.0$?" This item was included in the questionnaire, as the level of ensuing damage could differ according to the magnitude of the event. While seismic intensity is important from a damage perspective, the basic information transmitted is magnitude and location. Therefore, we investigated the relativity of magnitude. The initial standard for early warnings of earthquakes in Republic of Korea was $M_L > 5$.

Q.3: "How important is the comparison of earthquake locations, both inside and outside the observation network?" This question was included because it is associated with the observation network conditions, and the current criteria classify inland and outside events (i.e., teleseismic or occurring outside the country). These criteria represent the KMA strategy for considering the impact of earthquake detection relative to the observation network. Inland earthquakes can be detected rapidly and analyzed as they occur between observation networks, but oceanic analysis could likely be inaccurate in relation to the source owing to biased and sparse observation networks.

Q.4: "What is the maximum allowable error range when evaluating the accuracy of the magnitude?"

Q.5: "What is the maximum allowable error range when evaluating the accuracy of the epicenter?" The fourth and fifth questions are related to accuracy, as accuracy could affect missed and false alarms. Additionally, if the difference between the predicted information and precise information analyzed afterward is significant, an operating system check could be required.

In the criteria establishment stage of our survey, we analyzed the results based on the five questionnaires and collected the majority opinion regarding operational recommendations. Table 1 shows a summary of the established criteria from the questionnaire. The criteria in Q.1 allowed us to define the analysis object range. We established the range for earthquakes to be considered by ISN and OSN, i.e., 0.5 smaller than the magnitude of the alert criteria.

We set the weight for event sources based on Q.2 and Q.3. From an operational side, all earthquakes are valued equally because the evaluation pertains only to whether an alert should be issued. For instance, in a point-source assessment by Cochran et al. (2018), all earthquakes were also valued equally. However, the damage caused by an earthquake depends on the location and magnitude of the event. Therefore, we proposed weighing of the source effects. The score for each earthquake event was:

$$\text{Event Value } (EV) = \delta M \times \delta L \tag{1}$$

where EV is event value, which is the judgment of earthquakes from a management perspective. δM is the weight for magnitude, and δL is the weight for the source location (i.e., ISN, OSN) of the earthquake. For example, if an earthquake of M_L 5.5 occurred inland, the event value would be 1. Conversely, if an earthquake with magnitude M_L 3.2 occurred inland near the coast, the event value would be 0.18.

The criteria for an EEW false alarm was selected based on answers to Q.4 and Q.5. The criteria set for a false alarm were assessed based on the estimated source information produced by EEWs. In practice, the results of both source location and magnitude of EEWs depend on the nS (Lim et al., 2020). The more stations are involved in collecting information, the better would be the accuracy of epicenter analysis. From a management perspective, the criteria for a false alarm could be a crucial factor for planning system improvements.

2.3.3 Assessment parameter scoring

Assessments of EEWs must consider both the appropriateness of the alerts and the accuracy of earthquake source estimates. The source estimates in EEWs are updated rapidly as they increase because of a higher number of nS. However, we do not recommend reviewing all the steps that are updated over time, because the public responds to the first warning message (Lassa, 2008; Vihalemm et al., 2012); therefore, the information at the moment the alarm occurs is the only concern. Alert time depends on

TABLE 1 Performance assessment criteria based on questionnaire responses.

Assessment criteria		Criteria	
		ISN	OSN
(Q.1)	Minimum magnitude of assessment	3.0	3.5
(Q.2)	Weight of magnitude (δM)	1.0 (5.0 ≤ M)	1.0 (5.0 ≤ M)
		0.7 (3.5 ≤ M < 5.0)	0.7 (4.0 ≤ M < 5.0)
		0.3 (2.0 ≤ M <3.5)	0.3 (2.0 ≤ M <3.5)
(Q.3)	Weight of epicenter (δL)	1.0	0.6
(Q.4)	Maximum allowable magnitude error (ΔM)	0.4	0.6
(Q.5)	Maximum allowable epicenter error (ΔL)	10 km	30 km

nS, which is the most important factor in EEW alarm decision making. Our proposed assessment is designed to evaluate performance according to the target nS.

The first step was to score alert appropriateness (AA). We designed the scoring to include only events where the alert was a normal operation under the target nS conditions. If an earthquake required an alert but resulted in a false or missed alarm, we scored it as zero. This allowed us to determine if the system has effective controls for false or non-alarms. Consequently, our assessment could result in a low score if the system failed to control alarms for multiple cases. The formula for this is:

$$\text{Prevent false alerts } (PF) = EV \times AA \tag{2}$$

$$\text{Prevent Miss alerts } (PM) = EV \times AA \tag{3}$$

where EV is the event value by Eq. 1, AA is scoring of alert appropriateness (only 1 or 0). Therefore, a normal alert is 1, and false and missed alarms are 0.

The second step is to score the accuracy of an estimated source. By default, we designed the accuracy calculation to be based only on positive cases (normal alerts). The basic framework is similar to that of the Cochran et al. (2018) model. The expression is:

$$\text{Accurate of magnitude } (AM) = EV \times \left(1 - \frac{M_{No} - M_{EEW}}{\Delta M}\right) \times AA \tag{4}$$

$$\text{Accurate of location } (AL) = \text{EV} \times \left(1 - \frac{L_{No} - L_{EEW}}{\Delta L}\right) \times AA \tag{5}$$

where M_{NO} and L_{NO} are the notified magnitude and epicenter of the earthquake according to the KMA. The notified earthquake information is calculated through manual analysis by seismic analysts at the KMA. The M_{EEW} and L_{EEW} are the calculated source information (i.e., magnitude and epicenter) according to the target nS in the EEW. The maximum allowable error values, ΔM and ΔL, are based on the answers to Q.4 and Q.5. The accuracy value is close to 1 for a small error and close to 0 for a large error.

2.3.4 Pairwise analysis and assessment parameter weight

We assumed that different experts would place different values on the four parameters; therefore, we performed a relative comparison of the four parameters to obtain their values. For the weights of the four assessment parameters, we used the Analytic Hierarchy Process (AHP) that involves pairwise comparison, weight calculation, and consistency verification, as described by Saaty et al. (1990). The AHP process could be used as a rational decision-making tool for risk assessment to stratify, simplify, and systematize multiple criteria (Wen, 2015; Thaker et al., 2018; Providakis et al., 2022). This survey aimed to identify the most important parameters for operators by employing relative comparability.

During the pairwise comparison process, the study assessed the relative importance of the four assessment parameters using a nine-point scale, as shown in Figure 3. Following this step, the results were subjected to consistency verification to ensure their reliability. The consistency index (CI) used to assess the reliability of the responses was calculated through the maximum Eigenvalue operation of the comparison matrix. A lower CI value indicated higher reliability. For this study, an average weight of 11 questionnaires with a consistency index of 0.2 or less was used for the analysis. A summary of the results of these weights is presented in Table 2.

In pairwise analysis, the most important factor from the perspective of managers and operators is controlling false alarms. This factor is crucial because the issuing of a warning and the level of the warning depend on the accuracy of magnitude and location. Although the algorithm itself does not reveal this, operators consider the activation of a warning without an actual earthquake a significant problem. Therefore, false alarm control was allocated the highest weight, followed by non-alarm control, location accuracy, and magnitude accuracy.

To determine the assessment of the overall score (OS), we used the weights and assessment points of the four parameters. The final score was obtained by multiplying the score of each element by its weight, as follows:

$$\text{Overall Score } (OS) = \alpha \cdot PM + \beta \cdot PF + \gamma \cdot AM + \kappa \cdot AL \tag{6}$$

where PM, PF, AM, and AL refer to parameters such as prevent missed alerts, prevent false alerts, accuracy of magnitude, and accuracy of location, with α, β, γ, and κ as their respective weights (Table 2).

3 Results

3.1 Assessment preparation

We verified the proposed assessment of results in EEWs using past earthquake data. We analyzed 58 domestic earthquakes that

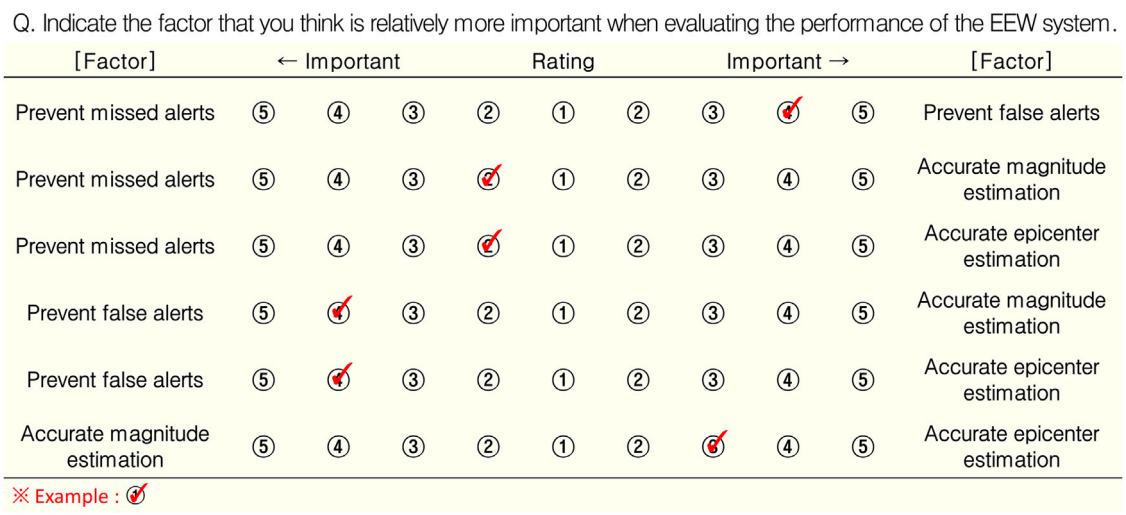

FIGURE 3
Questionnaire example for pairwise assessment parameter comparison. EEW, earthquake early warning.

TABLE 2 Weighting of four assessment parameters based on questionnaire answers received from Korean Metrological Administration (KMA).

Section	PM (α)	PF (β)	AM (γ)	AL (κ)	Consistency index
SR-1	0.073	0.475	0.125	0.327	0.159
SR-2	0.264	0.527	0.123	0.087	0.05
SR-3	0.237	0.189	0.361	0.212	0.68
SR-4	0.533	0.272	0.13	0.065	0.26
SR-5	0.125	0.625	0.125	0.125	0.00
SR-6	0.351	0.351	0.109	0.189	0.00
SR-7	0.28	0.553	0.083	0.083	0.03
SR-8	0.076	0.484	0.304	0.136	0.11
SR-9	0.523	0.272	0.089	0.117	0.14
SR-10	0.056	0.546	0.159	0.239	0.09
SR-11	0.092	0.495	0.206	0.206	0.05
SR-12	0.248	0.62	0.066	0.066	0.12
SR-13	0.202	0.558	0.087	0.154	0.07
Weight	0.208	0.501	0.134	0.157	

SR, survey respondents.

occurred between January 2015 and August 2021, with $M_L \geq 3.0$ and ≥ 3.5 for the ISN and OSN, respectively. The details of the events are shown in Figure 4 and summarized in Table 3. In this analysis, the operational decisions for checking the appropriateness of the alerts are shown in Table 4 using the criteria of Cho et al. (2022). However, differing from the Cho et al. (2022) study, the current assessment imposed stricter criteria for matching source information based on the survey result.

We assessed the performance of the initial P-wave trigger criteria in the ElarmS-3 algorithm, which was proposed by Chung et al. (2019) and include minPa, Range-Post Trigger (RP), NEtoZ, and Zero-Crossing (ZC). MinPa is the criterion for the initial P-wave, representing the minimum amplitude of acceleration during 4 s. Noise signals (i.e., boxcars, spikes) and block S-waves are removed using RP and NEtoZ, respectively. The validity of the signal is determined by ZC by counting the number of samples based on zero. Ultimately, we designed five simulation matrices based on the study by Cho et al. (2022). The configuration of each module is summarized in Table 5.

We assessed the effectiveness of the EEWs by simulating past earthquake events. Although past earthquake simulations cannot completely replicate real-time data delays, simulation analyses based

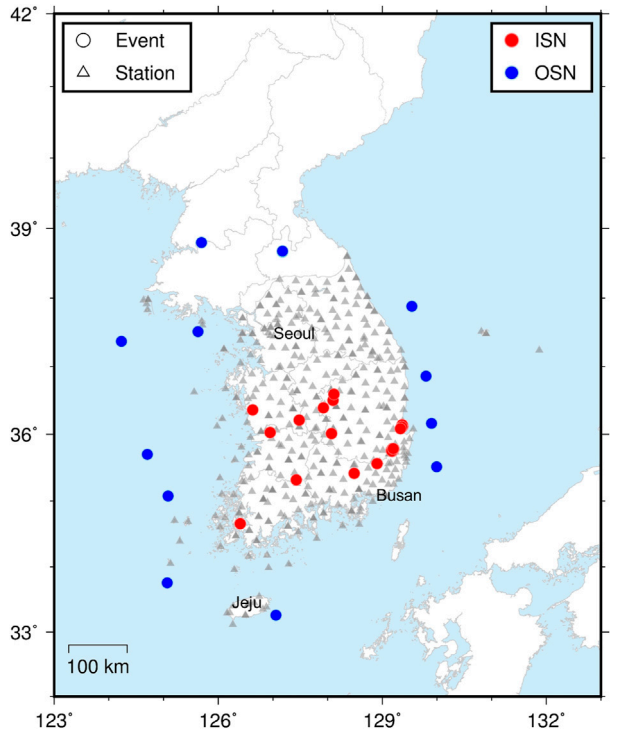

FIGURE 4
Distribution of events based on performance assessment. ISN, inside seismic network; OSN, outside seismic network.

on recorded data could produce reliable results similar to those of real-time operations (Lim et al., 2020). The simulation method used in this study does not allow for the delay of telecommunication time, and time-related errors were not surveyed, which is a limitation of the study. We assumed that the processing of observation data was conducted without delay.

Figure 5 shows an instance of simulation results for an earthquake. Here, we observed that the analysis results differed each time the simulation was executed, despite using identical simulation environments. The recording values of several observatories were transmitted simultaneously to the algorithm, and the buffer order changed owing to differences in micro-small system time. These issues were also found in a couple of pairs of a real-time system. However, as they do not significantly affect the overall analysis, we decided to tolerate the problem and considered it in this study. We conducted 20 repetitive simulations for all events to consider any unspecified deviations that could arise during simulation reproduction.

3.2 Performance assessment case

We conducted a performance evaluation of the actual EEW algorithm using the *OS*. The accuracy of the network-based EEWs increased along with an increase in the nS (Ruhl et al., 2019; Cho et al., 2022), as shown in Figure 5. Accordingly, the *OS* should receive higher scores as the nS increases. To verify this finding, we examined the evaluation results for condition 1, as shown in Figure 6. The figure shows that as the nS increased, the *OS* also increased, and the deviations in the 20 simulation cases declined.

We conducted performance assessment of the actual EEW algorithm by applying the assessment process developed for OS. This was intended to review the suitability of the assessment process and evaluate the algorithmic condition algorithm performance. The simulation analysis results for five algorithmic conditions and 58 earthquakes were obtained for this performance assessment. In this study, the five algorithmic conditions were termed A1–A5.

As four is the minimum nS for the KMA EEW, we compared the OS under five conditions with the evaluation results shown in Figure 7. As the proposed OS could calculate a score based on a single earthquake, the overall results are presented in a box and whisker plot to show the mean and median values. The results in Figure 7 indicate that A1–2 without the RP condition was more stable than A3–5.

We had to determine the reason for the addition of the RP condition resulting in relatively low scores; therefore, we determined the number of points each parameter earned. Figure 8 shows the average scores obtained in the parameter domain. Compared with A3–5, A1–2 exhibited a slight increase in the AM and a significant increase in the PF. We expected that using the RP condition would be effective for controlling false alarms; however, the results were not satisfactory.

In the case of A1–2 without the RP condition, we found that the analysis of A2 was more stable than that of A1. The criterion for minPa in A2 is the optimization proposed by Cho et al. (2022). Ultimately, the optimized amplitude criterion could secure EEW stability. In addition, the optimization criterion proposed in the study by Cho et al. (2022) was A5. However, in the current study, A2 was found to ensure EEW stability. This finding indicates that using minPa alone was more effective than using both conditions.

4 Limitation

To address earthquake hazards and establish strategies in various countries, EEWs are currently subjected to various research initiatives (e.g., Minson et al., 2018; Santos-Reyes, 2019; McBride et al., 2020; Ahn, 2021; Bostrom et al., 2022; Dallo et al., 2022; Sumy et al., 2022; Sutton et al., 2022). Similar strategies for earthquake responses are evolving to suit the characteristics of each country. Accordingly, the KMA needed to develop network-based EEW assessment strategies for Republic of Korea, a low-seismicity area.

The KMA evaluation method proposed in this study could potentially be adopted by other countries to assess stability during minor earthquakes. However, its applicability might vary depending on the disparities in the network-based EEW algorithms employed by each country and the perspectives of the network managers.

The EEWs are not only network based but also include other types, such as performance-based EEW (Convertito et al., 2008), OnSite EEW, and hybrid methods (Iervolino et al., 2006). The performance-based EEWs have focused on Intensity Measures (IM) and damage estimation for specific structures (Iervolino et al., 2009; Iervolino, 2011). The OnSite EEW issues an alert based on IM in a small area. The IM-based EEW could be tied

TABLE 3 Assessment target event list.

YYMMDD (UTC)		M_L	Location	YYMMDD (UTC)		M_L	Location
‘150108	11:15	3.5	OSN	`161212	08:53	3.3	ISN
‘150803	01:11	3.7	OSN	`161214	08:20	3.3	ISN
‘151221	19:31	3.9	ISN	`170105	20:31	3.3	ISN
‘160106	11:39	3.0	ISN	`170331	04:46	3.3	ISN
‘160210	20:57	3.1	ISN	`170415	02:31	3.1	ISN
‘160602	19:53	3.0	ISN	`170505	14:16	3.0	ISN
‘160705	11:33	5.0	OSN	`171115	05:29	5.4	ISN
‘160912	10:44	5.1	ISN	`171115	05:32	3.6	ISN
‘160912	10:48	3.1	ISN	`171115	06:09	3.5	ISN
‘160912	11:10	3.1	ISN	`171115	07:49	4.3	ISN
‘160912	11:32	5.8	ISN	`171116	00:02	3.6	ISN
‘160912	11:34	3.6	ISN	`171119	14:45	3.5	ISN
‘160912	11:36	3.4	ISN	`171119	21:05	3.6	ISN
‘160912	11:38	3.0	ISN	`171225	07:19	3.5	ISN
‘160912	11:39	3.0	ISN	`180210	20:03	4.6	ISN
‘160912	11:40	3.0	ISN	`190108	18:10	3.7	OSN
‘160912	14:18	3.0	ISN	`190210	03:53	4.1	OSN
‘160912	14:52	3.1	ISN	`190419	02:16	4.3	OSN
‘160912	15:37	3.1	ISN	`190421	20:45	3.8	OSN
‘160912	23:24	3.2	ISN	`190627	06:19	3.9	OSN
‘160913	05:31	3.0	ISN	`190721	02:04	3.9	ISN
‘160913	15:48	3.0	ISN	`190921	06:11	3.5	OSN
‘160919	11:33	4.5	ISN	`191027	06:37	3.4	ISN
‘160921	02:53	3.5	ISN	`191229	15:32	3.5	ISN
‘160928	07:34	3.1	ISN	`200129	15:52	3.2	ISN
‘161002	11:53	3.0	ISN	`200503	13:07	3.1	ISN
‘161010	13:59	3.3	ISN	`200511	10:45	3.8	OSN
‘161105	21:26	3.5	OSN	`210419	05:20	3.7	OSN
‘161113	12:52	3.5	ISN	`210821	00:40	4.0	OSN

TABLE 4 Performance assessment criteria comparison.

Section	Cho et al. (2022)	Survey results	
		ISN	OSN
Normal operation	$\Delta L \leq 100$	$\Delta L \leq 10$	$\Delta L \leq 30$
		$\Delta M \leq 0.4$	$\Delta M \leq 0.6$
False alert	$\Delta L > 100$	$\Delta L > 10$	$\Delta L > 30$
		$\Delta M > 0.4$	$\Delta M > 0.6$
Missed alert	Non-associated event (= missing earthquake)		

TABLE 5 Assessment configurations of five conditions in early earthquake warning (EEW) algorithms.

Algorithmic condition	minPa	RangePostTrig (RP)	
	log (Pa)	Rv	Ra
A 1	−2.5	OFF	OFF
A 2	−2.7	OFF	OFF
A 3	Off	0.000013	0.00074
A 4	−2.5	0.000013	0.00074
A 5	−2.7	0.000013	0.00074

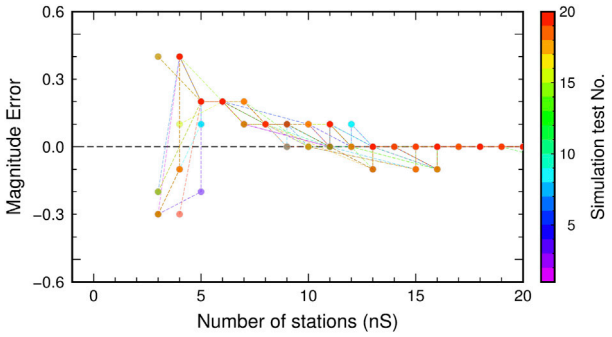

FIGURE 5
Differences between simulation results performed with the same system environment parameters of a magnitude 3.4 earthquake on 27 October 2019, in the Korean Peninsula.

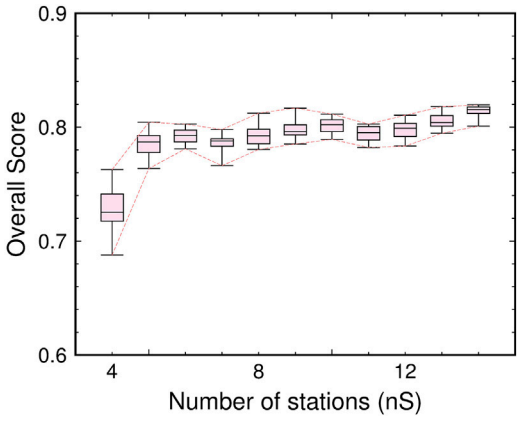

FIGURE 6
Box and whisker plot for overall score (OS) of algorithmic condition 1 for earthquake early warnings (EEW).

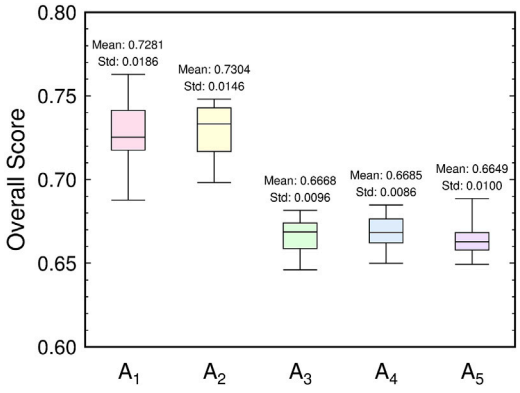

FIGURE 7
Box and whisker plot for overall score (OS) of algorithmic condition at number of stations, (nS) = 4.

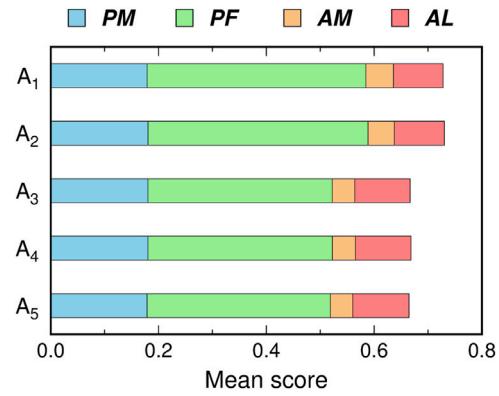

FIGURE 8
Mean score of four parameters for algorithmic condition at number of stations (nS) = 4. PM, prevent missed alerts; PF, prevent false alerts; AM, accuracy of magnitude; AL, accuracy of location.

to a strategic alerting strategy to consider damage. We believe that developing a damage-based strategic evaluation technique holds practical significance (Iervolino et al., 2011; Papadopoulos et al., 2023). The KMA is also engaged in the development and experimentation of on-site EEW systems based on IM (Ahn et al., 2023). However, these methods differ from network-based EEWs.

The current study concentrated on alerts disseminated in the public domain. Given the widespread use of smartphones, CBS stands out as the most efficient means of conveying alerts to individuals. However, to guarantee the reliability of alerts in the public sphere, this study defined successful, false, and missed alarms from an administrator standpoint. However, we note that this viewpoint could contrast with the that of the public receiving the service.

5 Conclusion

We developed an assessment for EEWs based on management aspects. While promptness is an integral factor in EEW assessment, we considered that reducing warning time based on nS could result in less accurate information. Therefore, the proposed performance assessment could comprehensively review EEW services from multiple aspects.

Surveys involving experts were conducted to establish standards for assessment criteria consistent with KMA EEW operational management. The proposed weights sufficiently addressed the preferences of operators with EEW technical system knowledge and the managers of the systems. These experts selected operational impact factors according to their operational principles, with most operators expressing a desire to minimize EEW false alerts.

The comprehensive review was scored by assigning weights to each element based on the AHP analysis. Accordingly, a quantitative assessment method was developed that could replace the conventional method, which only considers warnings. The established assessment equation reflected performance improvement based on accuracy.

Performance assessments can be conducted with changes in algorithms or parameters.

Our method could be appropriate for regions that are new to EEW in low-seismicity areas. However, our study is limited in that it only surveyed operators who were familiar with EEW technology. They responded with answers characterized by 1) imagining end-user satisfaction, 2) considering only technical aspects, and 3) summarizing all perspectives. Therefore, we note that the criteria could change depending on the survey responses, as individuals have various perspectives, backgrounds, and types of thinking.

The proposed EEW system assessment offers a quantitative approach that takes into account operational aspects. This method would be also expected the quantitative values of factors during actual operational periods, such as delays and anomalies arising from issues at the observation stations. Given the range of potential scenarios, it is imperative that this method undergoes further refinements for future operations.

Data availability statement

The original contributions presented in the study are included in the article, further inquiries can be directed to the corresponding author.

Author contributions

J-KA: Conceptualization, Data curation, Formal Analysis, Methodology, Supervision, Writing–original draft, Writing–review and editing. SC: Formal Analysis, Visualization, Writing–original draft. E-HH: Funding acquisition, Project administration, Supervision, Writing–original draft. W-HB: Conceptualization, Methodology, Writing–original draft, Writing–review and editing.

Funding

The authors declare financial support was received for the research, authorship, and/or publication of this article. This work was supported by the (grant number KMA 2022-02121: Development of Earthquake Information Production Technology).

Acknowledgments

The authors gratefully acknowledge the assistance received from the staff of the KMA Earthquake and Volcano Research Division.

Conflict of interest

The authors declare that the research was conducted in the absence of any commercial or financial relationships that could be construed as a potential conflict of interest.

Publisher's note

References

Ahn, J. K., Kwak, D. Y., and Kim, H. S. (2021). Estimating VS30 at Korean peninsular seismic observatory stations using HVSR of event records. *Soil Dyn. Earthq. Eng.* 146, 106650. doi:10.1016/j.soildyn.2021.106650

Ahn, J. K., Park, E., Kim, B., Hwang, E. H., and Hong, S. (2023). Stable operation process of earthquake early warning system based on machine learning: trial test and management perspective. *Front. Earth Sci.* 11, 1157742. doi:10.3389/feart.2023.1157742

Ahn, J. K. (2021). *Study on the preparation of disaster communication strategy: Focusing on the dissemination of early earthquake warnings*, Master's thesis. Seoul: Joongang University

Allen, R. M. (1982). Automatic phase pickers: their present use and future prospects. *BSSA* 72 (6B), S225–S242. doi:10.1785/bssa07206b0225

Allen, R. M., Gasparini, P., Kamigaichi, O., and Bose, M. (2009). The status of earthquake early warning around the world: an introductory overview. *Seismol. Res. Lett.* 80, 682–693. doi:10.1785/gssrl.80.5.682

Allen, R. M., and Melgar, D. (2019). Earthquake early warning: advances, scientific challenges, and societal needs. *Annu. Rev. Earth Planet. Sci.* 47, 361–388. doi:10.1146/annurev-earth-053018-060457

Angove, M., Arcas, D., Bailey, R., Carrasco, P., Coetzee, D., Fry, B., et al. (2019). Ocean observations required to minimize uncertainty in global tsunami forecasts, warnings, and emergency response. *Front. Mar. Sci.* 6, 350. doi:10.3389/fmars.2019.00350

BBC News (2017). California earthquake alarm sounded - 92 Years late. Available at: https://www.bbc.com/news/technology-40366816 (Accessed June 22, 2017).

BBC News (2018). False earthquake warning panics Japan. Available at: https://www.bbc.com/news/world-asia-42582113 (Accessed January 5, 2018).

Binger, C., Ball, L., Dietz, A., Kent-Walsh, J., Lasker, J., Lund, S., et al. (2012). Personnel roles in the AAC assessment process. *AAC* 28, 278–288. doi:10.3109/07434618.2012.716079

Bostrom, A., McBride, S. K., Becker, J., Goltz, J. D., de Groot, R. M., Peek, L., et al. (2022). Great expectations for earthquake early warnings on the United States West Coast. *Int. J. Disaster Risk Reduct.* 82, 103296. doi:10.1016/j.ijdrr.2022.103296

Chen, D. Y., Hsiao, N. C., and Wu, Y. M. (2015). The earthworm based earthquake alarm reporting system in Taiwan. *Bull. Seismol.* 105 (2A), 568–579. doi:10.1785/0120140147

Chen, D. Y., Lin, T. L., Hsu, H. C., Hsu, Y. C., and Hsiao, N. C. (2019). An approach to improve the performance of the earthquake early warning system for the 2018 Hualien earthquake in Taiwan. *Terr. Atmos. Ocean. Sci.* 30, 423–433. doi:10.3319/TAO.2018.12.23.02

Cho, S., Ahn, J. K., and Hwang, E. H. (2022). Optimization of network-based earthquake early warning systems on the Korean Peninsula. *IEEE Access* 10, 83931–83939. doi:10.1109/access.2022.3197661

Chung, A. I., Henson, I., and Allen, R. M. (2019). Optimizing earthquake early warning performance: elarmS-3. *Seismol. Res. Lett.* 90 (2A), 727–743. doi:10.1785/0220180192

Cochran, E. S., Kohler, M. D., Given, D. D., Guiwits, S., Andrews, J., Meier, M. A., et al. (2018). Earthquake early warning ShakeAlert system: testing and certification platform. *Seismol. Res. Lett.* 89 (1), 108–117. doi:10.1785/0220170138

Convertito, V., Iervolino, I., Manfredi, G., and Zollo, A. (2008). Prediction of response spectra via real-time earthquake measurements. *Soil Dyn. Earthq. Eng.* 28, 492–505. doi:10.1016/j.soildyn.2007.07.006

Cooke, R. M., and Goossens, L. H. (2004). Expert judgement elicitation for risk assessments of critical infrastructures. *J. Risk Res.* 7, 643–656. doi:10.1080/1366987042000192237

Cremen, G., Galasso, C., and Zuccolo, E. (2022). Investigating the potential effectiveness of earthquake early warning across Europe. *Nat. Commun.* 13, 639. doi:10.1038/s41467-021-27807-2

Cua, G., Fischer, M., Heaton, T., and Wiemer, S. (2009). Real-time performance of the virtual seismologist earthquake early warning algorithm in Southern California. *Seismol. Res. Lett.* 80, 740–747. doi:10.1785/gssrl.80.5.740

Dallo, I., Marti, M., Clinton, J., Böse, M., Massin, F., and Zaugg, S. (2022). Earthquake early warning in countries where damaging earthquakes only occur every 50 to 150 years – the societal perspective. *Int. J. Disaster Risk Reduct.* 83, 103441. doi:10.1016/j.ijdrr.2022.103441

Doi, K. (2011). The operation and performance of earthquake early warnings by the Japan Meteorological Agency. *Soil Dyn. Earthq. Eng.* 31, 119–126. doi:10.1016/j.soildyn.2010.06.009

Esposito, M., Palma, L., Belli, A., Sabbatini, L., and Pierleoni, P. (2022). Recent advances in internet of things solutions for early warning systems: A review. *Sensors* 22, 2124. doi:10.3390/s22062124

Finazzi, F. (2020). The earthquake network project: A platform for earthquake early warning, rapid impact assessment, and search and rescue. *Front. Earth Sci.* 8, 243. doi:10.3389/feart.2020.00243

Goda, K., Rimando, J., Peace, A. L., Sirous, N., Rosset, P., and Chouinard, L. (2023). Regional seismic loss estimation and critical earthquake scenarios for the western Quebec seismic zone. *Georisk*, 1–20. doi:10.1080/17499518.2023.2201246

Hoshiba, M., and Ozaki, T. (2014). Earthquake early warning and tsunami warning of the Japan Meteorological Agency, and their performance in the 2011 off the Pacific Coast of Tohoku earthquake (M 9.0). Early Warning for Geological Disasters. *Adv. Technol. Earth Sci.*, 1–28. doi:10.1007/978-3-642-12233-0_1

Hsiao, N. C., Wu, Y. M., Shin, T. C., Zhao, L., and Teng, T. L. (2009). Development of earthquake early warning system in Taiwan. *Geophys. Res. Lett.* 36, L00B02. doi:10.1029/2008gl036596

Iervolino, I., Convertito, V., Giorgio, M., Manfredi, G., and Zollo, A. (2006). Real time risk analysis for hybrid earthquake early warning systems. *J. Earthq. Eng.* 10, 867–885. doi:10.1142/S1363246906002955

Iervolino, I., Giorgio, M., Galasso, C., and Manfredi, G. (2009). Uncertainty in early warning predictions of engineering ground motion parameters: what really matters? *Geophys. Res. Lett.* 36, L00B06. doi:10.1029/2008gl036644

Iervolino, I. (2011). Performance-based earthquake early warning. *Soil Dyn. Earthq. Eng.* 31, 209–222. doi:10.1016/j.soildyn.2010.07.010

Iervolino, I., Zollo, A., and Erdik, M. (2011). Foreword to: prospects and applications of Earthquake Early Warning for real-time earthquake engineering, risk management and loss mitigation. *Soil Dyn. Earthq. Eng.* 31, 105. doi:10.1016/j.soildyn.2010.11.001

Ittner, C. D., and Larcker, D. F. (1997). Quality strategy, strategic control systems, and organizational performance. *Acc. Organ. Soc.* 22, 293–314. doi:10.1016/s0361-3682(96)00035-9

Jackson, D. D., and Anderson, D. L. (1970). Physical mechanisms of seismic-wave attenuation. *Rev. Geophys.* 8, 1–63. doi:10.1029/rg008i001p00001

Kamigaichi, O., Saito, M., Doi, K., Matsumori, T., Tsukada, S. Y., Takeda, K., et al. (2009). Earthquake early warning in Japan: warning the general public and future prospects. *Seismol. Res. Lett.* 80, 717–726. doi:10.1785/gssrl.80.5.717

Kohler, M. D., Cochran, E. S., Given, D., Guiwits, S., Neuhauser, D., Henson, I., et al. (2018). Earthquake early warning ShakeAlert system: west Coast wide production prototype. *Seismol. Res. Lett.* 89, 99–107. doi:10.1785/0220170140

Korea Meteorological Administration (2018). Government publications registration. Avaialble at: https://www.kma.go.kr/download_01/Annual_Report_2018.pdf.

Korea Meteorological Administration (2017). Seismic observation data quality report. *KMA, Seoul. Korea Rep.*, 279–288 (in Korean). Avaialble at: http://lod.nl.go.kr/resource/CNTS-00107278365.

Kwon, H. R., Eoh, Y., and Park, S. H. (2020). The mediating role of catastrophizing in the relationship between emotional clarity and posttraumatic stress symptoms among earthquake survivors in Korea: A cross-sectional study. *Front. Psychol.* 11, 1114. doi:10.3389/fpsyg.2020.01114

Lassa, J. (2008). Measuring the sustainability of tsunami early warning systems: an interdisciplinary research agenda. *Georisk* 2, 187–194. doi:10.1080/17499510802369140

Lee, J., Lee, D. K., and Ahn, J. K. (2022). Automatic fault plane solution for the provision of rapid earthquake information in South Korea. *Sustainability* 15, 520. doi:10.3390/su15010520

Lim, D., Ahn, J. K., and Lee, J. (2020). Comparative analysis of past earthquake simulation and test operation. *J. Korean Soc. Hazard Mitig.* 20, 281–290. doi:10.9798/kosham.2020.20.5.281

Lomax, A., Satriano, C., and Vassallo, M. (2012). Automatic picker developments and optimization: filterPicker—a robust, broadband picker for real-time seismic monitoring and earthquake early warning. *Seismol. Res. Lett.* 83, 531–540. doi:10.1785/gssrl.83.3.531

Massin, F., Clinton, J., and Böse, M. (2021). Status of earthquake early warning in Switzerland. *Front. Earth Sci.* 9, 707654. doi:10.3389/feart.2021.707654

May, P. J., Koski, C., and Stramp, N. (2016). Issue expertise in policymaking. *J. Public Policy.* 36, 195–218. doi:10.1017/s0143814x14000233

Mayer, R., Plank, C., Bohner, A., Kollarits, S., Corsini, A., Ronchetti, F., et al. (2008). Monitor: hazard monitoring for risk assessment and risk communication. *Georisk* 2, 195–222. doi:10.1080/17499510802506139

McBride, S. K., Bostrom, A., Sutton, J., de Groot, R. M., Baltay, A. S., Terbush, B., et al. (2020). Developing post-alert messaging for ShakeAlert, the earthquake early warning system for the West Coast of the United States of America. *Int. J. Disaster Risk Reduct.* 50, 101713. doi:10.1016/j.ijdrr.2020.101713

Medina-Cetina, Z., and Nadim, F. (2008). Stochastic design of an early warning system. *Georisk* 2, 223–236. doi:10.1080/17499510802086777

Meijer, A., and Grimmelikhuijsen, S. (2020). *Responsible and accountable algorithmization: How to generate citizen trust in governmental usage of algorithms.* LONDON: The Algorithmic Society.

Minson, S. E., Meier, M. A., Baltay, A. S., Hanks, T. C., and Cochran, E. S. (2018). The limits of earthquake early warning: timeliness of ground motion estimates. *Sci. Adv.* 4, eaaq0504. doi:10.1126/sciadv.aaq0504

Murray, J. R., Crowell, B. W., Murray, M. H., Ulberg, C. W., McGuire, J. J., Aranha, M. A., et al. (2023). Incorporation of real-time earthquake magnitudes estimated via peak ground displacement scaling in the ShakeAlert Earthquake Early Warning System. *Bull. Seismol. Soc. Am.* 113, 1286–1310. doi:10.1785/0120220181

Ni, C. F., Chung, C. C., Zhang, L., Wang, Y., and Dong, J. J. (2023). Preface of the special issue on 'geological uncertainty and its impact on geohazards and water resources assessments and infrastructure design. ' *Eng. Geol.* 313, 106981. doi:10.1016/j.enggeo.2022.106981

Papadopoulos, A. N., Böse, M., Danciu, L., Clinton, J., and Wiemer, S. (2023). A framework to quantify the effectiveness of earthquake early warning in mitigating seismic risk. *Earthq. Spectra* 39, 938–961. doi:10.1177/87552930231153424

Podolskiy, E. A., Murai, Y., Kanna, N., and Sugiyama, S. (2021). Ocean-bottom and surface seismometers reveal continuous glacial tremor and slip. *Nat. Commun.* 12, 3929. doi:10.1038/s41467-021-24142-4

Porter, K. A. (2016). *How many injuries can be avoided through earthquake early warning and drop, cover, and hold on?* Boulder, Colorado: Structural Engineering and Structural Mechanics Program.

Providakis, S., Rogers, C. D., and Chapman, D. N. (2022). 3D Spatiotemporal risk assessment analysis of the tunnelling-induced settlement in an urban area using analytical hierarchy process and BIM. *Georisk* 16, 251–266. doi:10.1080/17499518.2021.1952607

Reddy, E. A. (2020). Crying 'crying wolf': how misfires and Mexican engineering expertise are made meaningful. *Ethnos* 85, 335–350. doi:10.1080/00141844.2018.1561489

Ruhl, C. J., Melgar, D., Chung, A. I., Grapenthin, R., and Allen, R. M. (2019). Quantifying the value of real-time geodetic constraints for earthquake early warning using a global seismic and geodetic data set. *J. Geophys. Res. Solid Earth.* 124, 3819–3837. doi:10.1029/2018jb016935

Saaty, T. L. (1990). How to make a decision: the analytic hierarchy process. *Eur. J. Oper. Res.* 48, 9–26. doi:10.1016/0377-2217(90)90057-i

Santos-Reyes, J. (2019). How useful are earthquake early warnings? The case of the 2017 earthquakes in Mexico city. *Int. J. Disaster Risk Reduct.* 40, 101148. doi:10.1016/j.ijdrr.2019.101148

Satriano, C., Elia, L., Martino, C., Lancieri, M., Zollo, A., and Iannaccone, G. (2011). PRESTo, the earthquake early warning system for southern Italy: concepts, capabilities and future perspectives. *Soil Dyn. Earthq. Eng.* 31, 137–153. doi:10.1016/j.soildyn.2010.06.008

Satriano, C., Lomax, A., and Zollo, A. (2008). Real-time evolutionary earthquake location for seismic early warning. *Bull. Seismol. Soc. Am.* 98, 1482–1494. doi:10.1785/0120060159

Sheen, D. H. (2016). Determination method for location and origin time of earthquake using arrival time of primary wave: KR patents KR101635791B1. Avaialble at: https://patents.google.com/patent/KR101635791B1/en. Accessed February 27, 2015.

Sheen, D. H., Kang, T. S., and Rhie, J. (2018). A local magnitude scale for South Korea. *Bull. Seismol. Soc. Am.* 108, 2748–2755. doi:10.1785/0120180112

Sumy, D. F., Jenkins, M. R., McBride, S. K., and de Groot, R. M. (2022). Typology development of earthquake displays in free-choice learning environments, to inform earthquake early warning education in the United States. *Int. J. Disaster Risk Reduct.* 73, 102802. doi:10.1016/j.ijdrr.2022.102802

Sutton, J., Wood, M. M., Crouch, S., and Waugh, N. (2022). Public perceptions of U.S. Earthquake early warning post-alert messages: findings from focus groups and interviews. *Int. J. Disaster Risk Reduct.* 84, 103488. doi:10.1016/j.ijdrr.2022.103488

Takabatake, T., and Kojima, T. (2023). Impact of rising sea levels on future nankai–tonankai earthquake tsunamis: A case study of osaka, Japan. *Georisk* 17, 595–611. doi:10.1080/17499518.2022.2119256

Thaker, T. P., Savaliya, P. J., Patel, M. D., and Patel, K. (2018). "GIS based seismic risk analysis of Ahmedabad City, India," in *Proceedings of the GeoShanghai 2018 international conference: Geoenvironment and geohazard. GSIC 2018* (Singapore: Springer). doi:10.1007/978-981-13-0128-5_13

Tidlund, M., Spross, J., and Larsson, S. (2022). Observational method as risk management tool: the hvalfjörður tunnel project, Iceland. *Icel. Georisk.* 17, 346–360. doi:10.1080/17499518.2022.2046784

Too, E. G., and Weaver, P. (2014). The management of project management: A conceptual framework for project governance. *Int. J. Proj. Manag.* 32, 1382–1394. doi:10.1016/j.ijproman.2013.07.006

Velazquez, O., Pescaroli, G., Cremen, G., and Galasso, C. (2020). A review of the technical and socio-organizational components of earthquake early warning systems. *Front. Earth Sci.* 8, 533498. doi:10.3389/feart.2020.533498

Vihalemm, T., Kiisel, M., and Harro-Loit, H. (2012). Citizens' response patterns to warning messages. *J. Contingencies Crisis Manag.* 20, 13–25. doi:10.1111/j.1468-5973.2011.00655.x

Vipin, K. S., and Sitharam, T. G. (2011). Multiple source and attenuation relationships for evaluation of deterministic seismic hazard: logic tree approach considering local site effects. *Georisk* 5, 173–185. doi:10.1080/17499518.2010.532015

Wen, H. (2015). A susceptibility mapping model of earthquake-triggered slope geohazards based on geo-spatial data in mountainous regions. *Georisk* 9, 25–36. doi:10.1080/17499518.2015.1005634

Weyrich, P., Ruin, I., Terti, G., and Scolobig, A. (2021). Using serious games to evaluate the potential of social media information in early warning disaster management. *Int. J. Disaster Risk Reduct.* 56, 102053. doi:10.1016/j.ijdrr.2021.102053

Whipple, J. M., and Frankel, R. (2000). Strategic alliance success factors. *J. Supply Chain Manag.* 36, 21–28. doi:10.1111/j.1745-493x.2000.tb00248.x

Wu, W. N., Chang, S. M., and Wang, Y. W. (2022). Assessment of taiwan public warning cell broadcast service: insights from an expert focus group and citizens. *Public Adm. Q.* 46, 406–428. doi:10.37808/paq.46.4.6

Yamada, M., Tamaribuchi, K., and Wu, S. (2021). The extended integrated particle filter method (IPFx) as a high-performance earthquake early warning system. *Bull. Seismol. Soc. Am.* 111, 1263–1272. doi:10.1785/0120210008

Yeon, D. H., Chung, J. B., and Im, D. H. (2020). The effects of earthquake experience on disaster education for children and teens. *Int. J. Environ. Res. Public Health.* 17, 5347. doi:10.3390/ijerph17155347

Zuccolo, E., Cremen, G., and Galasso, C. (2021). Comparing the performance of regional earthquake early warning algorithms in Europe. *Front. Earth Sci.* 9, 686272. doi:10.3389/feart.2021.686272

frontiers | Frontiers in Earth Science

TYPE Methods
PUBLISHED 22 September 2023
DOI 10.3389/feart.2023.1248340

OPEN ACCESS

EDITED BY
Chong Xu,
Ministry of Emergency Management, China

REVIEWED BY
Mohammad Azarafza,
University of Tabriz, Iran
Danqing Song,
South China University of Technology, China
Zheng Han,
Central South University, China

*CORRESPONDENCE
Shouding Li,
lsdlyh@mail.iggcas.ac.cn

RECEIVED 27 June 2023
ACCEPTED 11 September 2023
PUBLISHED 22 September 2023

CITATION
Ma S, Li S, Bi X, Qiao H, Duan Z, Sun Y, Guo J and Li X (2023), Automatic landslide identification by Dual Graph Convolutional Network and GoogLeNet model-a case study for Xinjiang province, China.
Front. Earth Sci. 11:1248340.
doi: 10.3389/feart.2023.1248340

Automatic landslide identification by Dual Graph Convolutional Network and GoogLeNet model-a case study for Xinjiang province, China

Shiwei Ma[1,2,3,4], Shouding Li[1,2,3]*, Xintao Bi[5], Hua Qiao[6], Zhigang Duan[7], Yiming Sun[1,2,3], Jingyun Guo[1,2,3] and Xiao Li[1,2,3]

[1]Key Laboratory of Shale Gas and Geoengineering, Institute of Geology and Geophysics, Chinese Academy of Sciences, Beijing, China, [2]Innovation Academy for Earth Science, Chinese Academy of Sciences, Beijing, China, [3]College of Earth and Planetary Sciences, University of Chinese Academy of Sciences, Beijing, China, [4]China Institute of Geo-Environment Monitoring, Technical Guidance Center for Geo-Hazards Prevention of MNR, Beijing, China, [5]Shengli Oil Field Exploration and Development Research Institute, Shandong, China, [6]Geological Environment Monitoring Institute of Xinjiang Uygur Autonomous Region, Urumchi, Xinjiang, China, [7]Naval Research Academy, Beijing, China

Landslides are a natural disaster that exists widely in the world and poses a great threat to human life and property, so it is of great importance to identify and locate landslides. Traditional manual interpretation can effectively identify landslides, but its efficiency is very low for large interpreted areas. In this sense, a landslide recognition method based on the Dual Graph Convolutional Network (DGCNet) is proposed to identify the landslide in remote sensing images quickly and accurately. The remote sensing image (regional remote sensing image) of the northern mountainous area of Tuergen Township, Xinyuan County, Xinjiang Province, was obtained by GeoEye-1 (spatial resolution: 0.5 m). Then, the DGCNet is used to train the labeled images, which finally shows good accuracy of landslide recognition. To show the difference with the traditional convolutional network model, this paper adopts a convolution neural network algorithm named GoogLeNet for image recognition to carry out a comparative analysis, the remote sensing satellite images (single terrain image) of Xinyuan County, Xinjiang Province is used as the data set, and the prediction accuracy is 81.25%. Compared with the GoogLeNet model, the DGCNet model has a larger identification range, which provides a new method for landslide recognition of large-scale regional remote sensing images, but the performance of DGCNet is highly dependent on the quality and characteristics of the input image. If the input data quality is poor or the image structure is unclear, the model's performance may decline.

KEYWORDS

geological disaster, landslide identification, GoogLeNet model, Dual Graph Convolutional Network, model

1 Introduction

In recent years, the identification of geological disasters using remote sensing images has become a prominent research area within the realm of natural disasters. Landslide geological disasters are widespread across the globe and pose a severe threat to human life and property. In 2021, a total of 367 severe natural disasters occurred worldwide, including 11 significant landslides. These landslides

TABLE 1 List of machine learning techniques practiced for landslide susceptibility analysis (Breiman, 1996; Wan, 2013; Alimohammadlou et al., 2014; Bien Bui et al., 2016; Tien Bui et al., 2016; Wang et al., 2016; Kavzoglu et al., 2019; Du et al., 2020; Mohan et al., 2020; Chen et al., 2023).

Methods	Category	Purpose	Advantage	Disadvantage
Random Forest	Tree-based	Feature selection, regression, classification	Limited samples can be fully applied	Overfitting on some noisy problems
			Advantage of versatility and accuracy	
			Highly adaptable	
Rotation Forest	-	Generation of accurate and diverse classifiers	Training is faster	Sensitive to noise data
Functional Tree	-	To develop a decision tree for separating two classes from the training set	Advantage of versatility and accuracy	Overfitting on some noisy problems
Logistic Model tree	-	-	Advantage of versatility and accuracy	Overfitting on some noisy problems
Decision Tree	-	Description of structural pattern in data without having relation with input variable to objective variable	Low complexity	Overmatching issues may arise
			Insensitive to missing intermediate values	
			Can handle uncorrelated feature data	
Bagging	-	Classification and regression	Has a very high accuracy rate	On certain sample sets that are relatively noisy, the model tends to fall into overfitting
			Can handle very high dimensional data without feature selection	
SVM	Kernel-based	Find optimal hyperplane	Low generalization error rate	Sensitive to parameter tuning and choice of kernel function
			Low computational overhead	Raw classifiers unmodified are suitable for dealing with two-class problems
			Results are easy to interpret	
Kernel Logistic Regressor	Kernel-based	Find discriminant function for separating discriminating classes	Can be applied to continuous and categorical independent variables	Sensitive to multicollinearity of independent variables in the model Can be applied to continuous and categorical independent variables
Self-organizing map	Neural network	Dimensionality reduction	The final clustering results produced have a relatively high level of visualization and interpretability	Without a defined objective function, it is not easy to compare different clustering results
Fuzzy Clustering	Fuzzy-based	Arrange objects with similarity in a group	Will calculate the affiliation of each sample to all classes, has a sample classification results reliability of the calculation method	Higher computational volume
			Sample categorization is more accurate	
Deep Learning	-	By combining low-level features to form more abstract high-level representations of attribute categories or features, one can discover distributed feature representations of the data	Highly adaptable	Time-consuming training, model validation is complex and troublesome
			Strong learning ability and wide coverage	Poor portability and high hardware cost
Artificial Neural Network	-	Simulating biological neural networks	High accuracy; High learning ability	Need a large number of parameters
				Cannot observe the learning process, the results are difficult to interpret
				Long learning time
Logistic Regression	-	To develop a regression formula for classification borders based on existing data	Computationally inexpensive	Easy to underfit
			Easy to understand and implement	Classification accuracy may not be high
			Not very complex	

impacted 12 countries or regions, predominantly in Asia and South America, resulting in a tragic loss of 224 lives, affecting the livelihoods of 56,600 people, and causing direct economic damages totaling $250 million (Beijing Normal University, 2021). Therefore, timely and accurate identification of landslide locations and the implementation of corresponding prevention and control measures are of paramount importance. As artificial intelligence continues to advance, the integration of artificial intelligence with remote sensing imagery for the identification of geological disasters is gradually evolving. In recent years, numerous studies have been conducted on landslides using deep learning algorithms (Hu et al., 2019; Piralilou et al., 2019; Ye et al., 2019; Prakash et al., 2020; Yu et al., 2020; Zhu et al., 2020). For instance, Cheng et al. (2013) introduced a new scenario classification method for automatic landslide detection based on remote sensing images. Danneels et al. (2007) presented a landslide recognition method utilizing the maximum likelihood classification (MLC) approach for multispectral remote sensing images. Zhan et al. (2022) devised a method for extracting landslide trails using the Fire Extinguishing Model. Shao et al. (2021); Shao et al. (2022) proposed the Novel Multiscale Decision Fusion approach for unsupervised change detection in high-resolution images, as well as an unsupervised change detection method using Fuzzy Topology-Based Majority Voting. Fu et al. (2022) introduced the Novel Higher-Order Clique Conditional Random Field for unsupervised change detection in remote sensing images. Zhang et al. (2001) employed a support vector machine (SVM) for hyperspectral data classification. Nikoobakht et al. (2022) conducted a landslide susceptibility assessment using convolutional neural networks, and Azarafza et al. (2021) presented a deep learning-based approach for landslide susceptibility mapping. Each of these AI algorithms applied to landslide identification possesses distinct properties, as summarized in Table 1.

A general convolutional neural network operates on an Euclidean structure so that the data from the convolutional operation shows a very neat matrix. However, most of the data are irregular, such data usually do not follow obvious patterns or rules and are characterized by diversity, complexity, and uncertainty. The data interact with each other to form the shape of the graph in the data structure. The Dual Graph Convolutional Network (DGCNet) is characterized by its ability to operate on graph-structured data, treating nodes and their connections as fundamental elements. DGCNet employs dual graph convolution layers, allowing it to capture both local and global structural information efficiently. It can integrate diverse data sources, adapt to graph data, and excel in tasks involving spatial relationships and complex networks, making it particularly suitable for applications such as social network analysis, geospatial data, and recommendation systems. DGCNet offers a powerful framework for addressing problems with graph-based data. Zhang et al. (2019) used the model for semantic segmentation and achieved good results.

In this study, we employed two different network models to identify landslide geological disasters in remote sensing images from Xinyuan County. Firstly, the regional remote sensing images of Tuergen town (a mountainous area in Xinyuan County) are annotated, which was trained and predicted by the DGCNet model. To show the difference between the DGCNet model and the traditional convolutional network model, one of the traditional convolutional network models named GoogLeNet is used to identify the landslide geological disaster of remote sensing image (single terrain image) in Xinyuan County. Compared with the GoogLeNet model, the DGCNet model has a wider recognition range. The identification of landslides requires the consideration of various data sources such as geographical information, topography, vegetation, and more. DGCNet allows the integration of these diverse data sources into a unified graph structure, making it more suitable for this type of task. It can effectively amalgamate multi-source information, account for spatial relationships, adapt to graph data, and offer novel, advanced approaches for landslide recognition. This will contribute to improving the accuracy and timeliness of landslide identification, thereby safeguarding human lives and property. The DGCNet model is introduced into the field of landslide recognition, which provides a new method for landslide recognition of large-scale regional remote sensing images.

2 Geological background and data selection

Xinjiang province is located in the northwestern part of China, with a vast territory of rolling mountains, wide topographic height difference, strong neotectonic movement, and a complex and changeable climate and natural environment. The underground cavities formed by underground projects (underground mining and air defense work) have led to ground collapse geological disasters to some extent. Therefore, the geological disasters in this region are characterized by many types, high frequency, wide affected areas, and serious hazards. Due to the frequency and severity of landslides, it was decided to use Xinjiang province as the study area. The location of Xinjiang Province and the study area of the DGCNet model are shown in Figure 1.

Geological disasters in Xinjiang Province are of significant concern, as they have consistently posed severe threats to the safety of towns, critical engineering facilities, and the lives and properties of residents. A statistical analysis conducted during the investigation of geological hazards in Xinjiang Province revealed that out of the 90 counties (cities) examined, 81 of them have experienced geological hazards. A total of 4791 geological disasters have occurred in Xinjiang province, resulting in 541 deaths, and $65 million of direct economic losses. Among the geological disasters that occurred in this area, according to the classification and grading standards for geological hazards issued by the China Association of Geological Hazard Prevention and Control Engineering (T/CAGHP 018-2016) (China Association of Geological Hazard Prevention and Control Engineering, 2016), there are 10 super large disasters, 9 large disasters, 79 medium disasters, and 4693 small disasters (Xinjiang Geological Environment Monitoring Institute, 2014).

Xinyuan County is situated at the eastern end of the Yili River Valley in the northern region of Xinjiang Province. This area falls within the North Temperate Continental Semi-Arid climate zone, characterized by mild winters and cool summers, owing to the influence of moist air currents moving from west to east. The average annual temperature stands at 8.5°C, with the coldest month (January) averaging −14.4°C, and the hottest month (July)

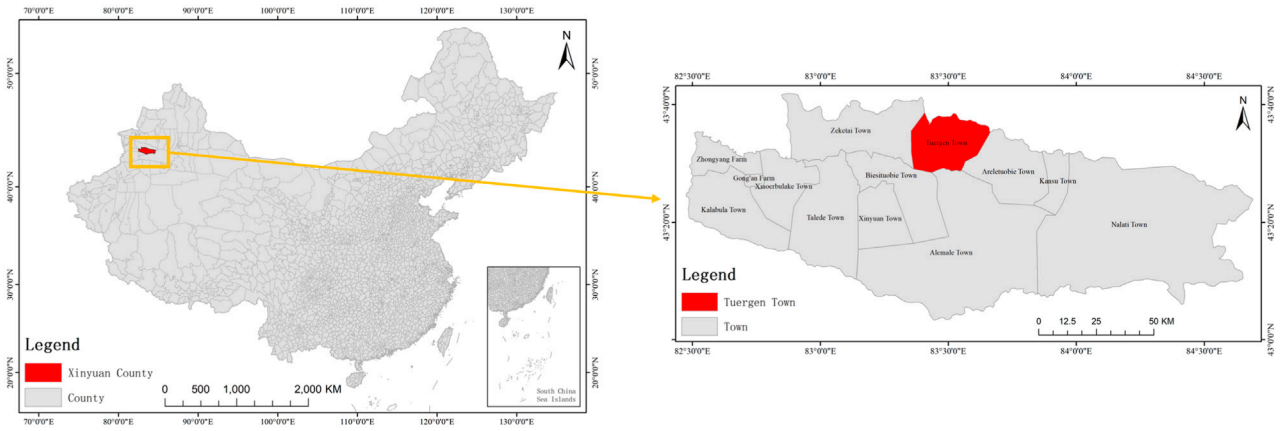

FIGURE 1
The study area of the DGCNet model (Tuergen Township, Xinyuan County, Xinjiang province).

registering an average of 27.95°C. Extreme temperature fluctuations have been observed, ranging from a minimum of −27.7°C to a maximum of 39.8°C. Annual precipitation ranges between 270 and 880 mm, while water evaporation levels vary from 1300 to 2000 mm. Rainwater infiltrates through cracks at the rear edge of slopes, causing erosion at the front edge, ultimately leading to landslide occurrences. Different types of landslides occur under the influence of various rock mass structures, which can be classified into the following six types.

(1) When the upper part of the slope is the slope deposit and the lower part is the bedrock structure type, the main groundwater type is mainly pore water, and the deformation characteristics are the overall surface sliding. The landslide type is shallow sliding landslides.
(2) When the upper part of the slope is aeolian deposit loess and the lower part is bedrock structure type, the main groundwater type is fissure water and the deformation characteristic is the overall surface sliding collapse. The landslide type is collapse landslide.
(3) When the upper part of the slope body is aeolian deposit loess, the middle part is the terrace, and the lower part is bedrock structure type, the main groundwater type is fissure water, and the formation of cracks at the back edge of the slope. The landslide type is a fluid landslide.
(4) When the upper part of the slope body is the terrace, and the lower part is the bedrock structure type, the main groundwater type is fissure water and the deformation characteristic is collapse. The landslide type is collapse landslide.
(5) When the slope is a deep gully structure of loess, the main groundwater type is mainly pore water, and the deformation characteristic is slope creep, resulting in lateral diffusion or flow landslide.
(6) In the case of high and steep fracture rock mass structures, the main groundwater type is fissure water, and the deformation characteristics are mainly rock fracture expansion. The landslide type is collapse landslide.

To solve the identification problem of geological disasters in Xinyuan County, the DGCNet model is used to identify landslides, because it is suitable for the identification in a large area. Based on the remote sensing image data of Tuergen Township in Xinyuan County, three remote sensing images in the northern mountainous area of Tuergen Township were selected for labeling and training, and another one for testing and identification. The labeling was done with Labelme software, which is a graphical interface image labeling software. The first step is to import the image into the software, select the landslide area to label as a landslide, and then save and export the file. The remote sensing images of Tuergen Township used are GeoEye-1 image data (spatial resolution: 0.5 m) from Google Earth, and the location area is shown in Figure 1. The training set is shown in Figure 2.

On the other hand, the GoogLeNet model is selected to identify and classify landslide terrain images. A total of 102 landslides and 152 other topographic images from satellite images were selected based on known landslides in several areas throughout Xinyuan County. The images used are GeoEye-1 image data (spatial resolution: 0.5 m), Figure 3 and Figure 4 show some landslides and other topographic images in the sample set respectively. The sample is divided into two parts: the training set and the test set. 80% of the images of landslide terrain and other terrain are selected as the training set, and the other 20% are selected as the test set for analysis.

The process of data and model application is shown in Figure 5.

3 Model introduction

3.1 ResNet network model

The ResNet50 is used as the basic network for training. It was proposed by four Chinese scholars, including Kaiming of Microsoft Research Institute (He et al., 2016). By using residual units, a 50-layer deep neural network was successfully trained with an error rate of 3.57%. At the same time, the number of parameters is lower than the Visual Geometry Group Network (VGGNet), and the effect is very prominent. The structure of the ResNet 50 model can accelerate the training of the ultra-deep neural network, and the accuracy of the model is also greatly improved. Assuming that a shallow neural

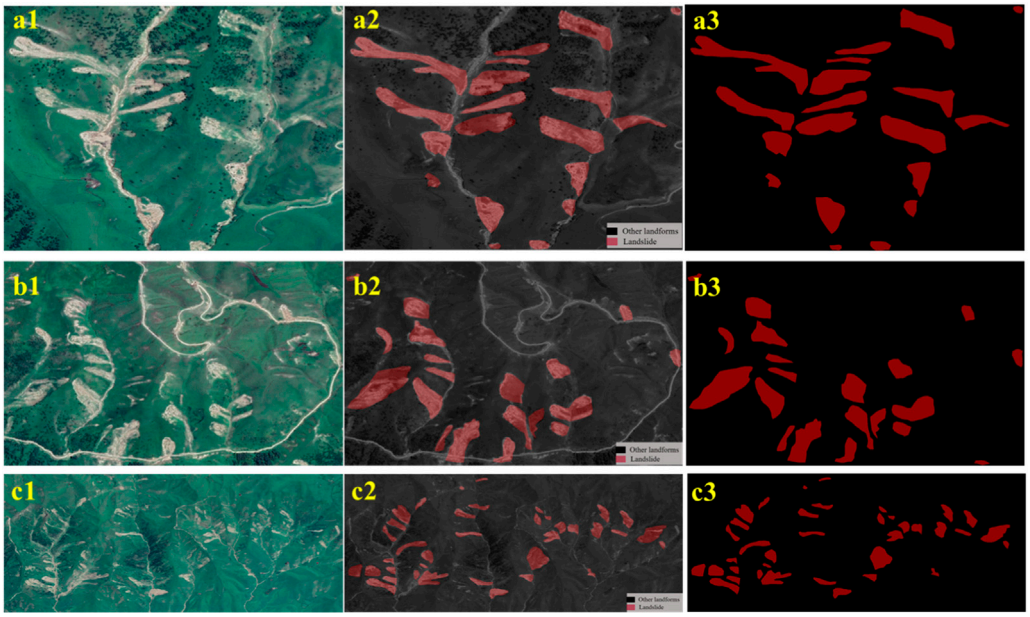

FIGURE 2
Schematic diagram of training set: **(a1, b1, c1)** remote sensing images, **(a2, b2, c2)** landslide labeling, **(a3, b3, c3)** landslide areas.

FIGURE 3
The terrain images of landslides in the sample set.

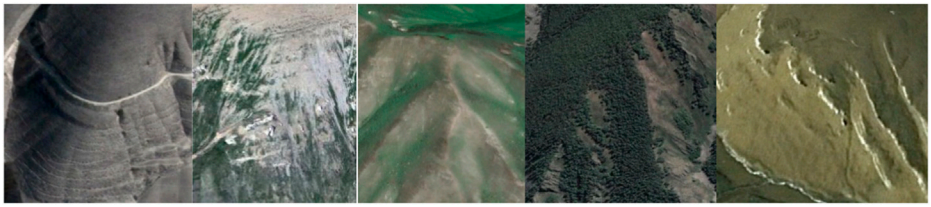

FIGURE 4
The other terrain images of the sample set.

network has reached the saturated accuracy, then add several congruent mapping layers of y = x, at least the error will not increase, that is, a deeper network should not lead to an increase in the error on the training set. Assuming that the input of a neural network is x and the expected output is H (x) if we directly transfer the input x to the output as the initial result, then the goal we need to learn is f (x) = H (x) - X. The ResNet is equivalent to changing the learning goal. Since it is no longer learning a complete output H (x), the difference between output and input H (x) - x, is the residual.

The residual block is implemented using a shortcut connection, where the input and output of the block overlap with the shortcut. This straightforward addition does not introduce additional parameters or computational overhead to the network. Simultaneously, it significantly enhances training speed and

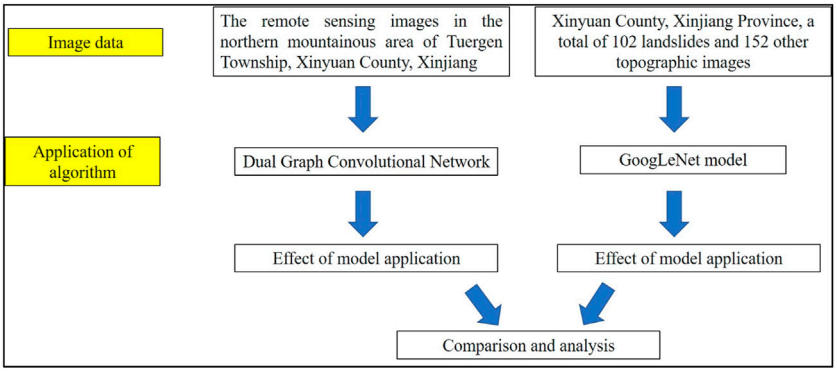

FIGURE 5
Data and model application process.

improves the model's training effectiveness. This simple structure can effectively address the degradation problem that arises when deepening the layers of the model. In traditional convolutional or fully connected layers, issues like information loss can occur. ResNet partially addresses this problem by directly bypassing input information to the output, thus preserving the integrity of the information. Consequently, the entire network only needs to learn the differences between input and output, simplifying the learning objectives and reducing complexity.

3.2 DGCNet model framework

3.2.1 Principle

The DGCNet models the global context of the input feature by modeling two orthogonal graphs in a single framework. The first component models spatial relationships between pixels in the image, whilst these cond model interdependencies along the channel dimensions of the network's feature map. This is done efficiently by projecting the feature into a new, lower-dimensional space where all pairwise interactions can be modeled, before reprojecting into the original space (Zhang et al., 2019).

It consists of two branches, each consisting of a graph convolutional network (GCN) to model contextual information in the spatial and channel dimensions in a convolutional feature map. The model has the following main components, the specific model structure explanation refers to the Reference (Zhang et al., 2019).

3.2.1.1 Input graph data

The input to DGCNet is a graph data representation, consisting of nodes and edges. Each node represents an element of data, and edges indicate relationships between nodes. This forms the foundational data structure for DGCNet.

3.2.1.2 Graph convolutional layers

DGCNet employs graph convolutional layers to process the input graph data. These layers perform convolution operations to capture relationships between nodes and facilitate feature propagation.

3.2.1.3 Dual graph convolution layers

A distinguishing feature of DGCNet is the presence of dual graph convolution layers, typically comprising two parallel graph convolution operations. These layers simultaneously capture local and global structural information.

3.2.1.4 Feature propagation

Within each convolutional layer, features propagate from one node to its neighboring nodes, facilitating the capture of inter-node relationships and information dissemination. This is crucial for feature extraction.

3.2.1.5 Pooling layers

Pooling operations are often applied after each convolutional layer to reduce the graph's size and extract the most salient features. This helps in reducing computational complexity.

3.2.1.6 Fully connected layers

Following the convolutional layers, one or more fully connected layers can be included to map the extracted features to the desired output space, such as classification or regression.

3.2.1.7 Activation functions

Between layers, activation functions are commonly used to introduce non-linearity and enhance the model's expressive power. Common activation functions include ReLU, Sigmoid, and Tanh.

These components collectively form the basic structure of a DGCNet model, enabling it to effectively handle semi-supervised learning tasks on graph-structured data.

3.2.2 Model structure

The model used in this paper consists of two branches:

1) The GCN of coordinate space models the spatial relationships of pixels, enabling the network to produce continuous predictions and consider all objects in the graph.
2) The feature space GCN captures the correlation among more abstract features. The features of the two parts of the inference

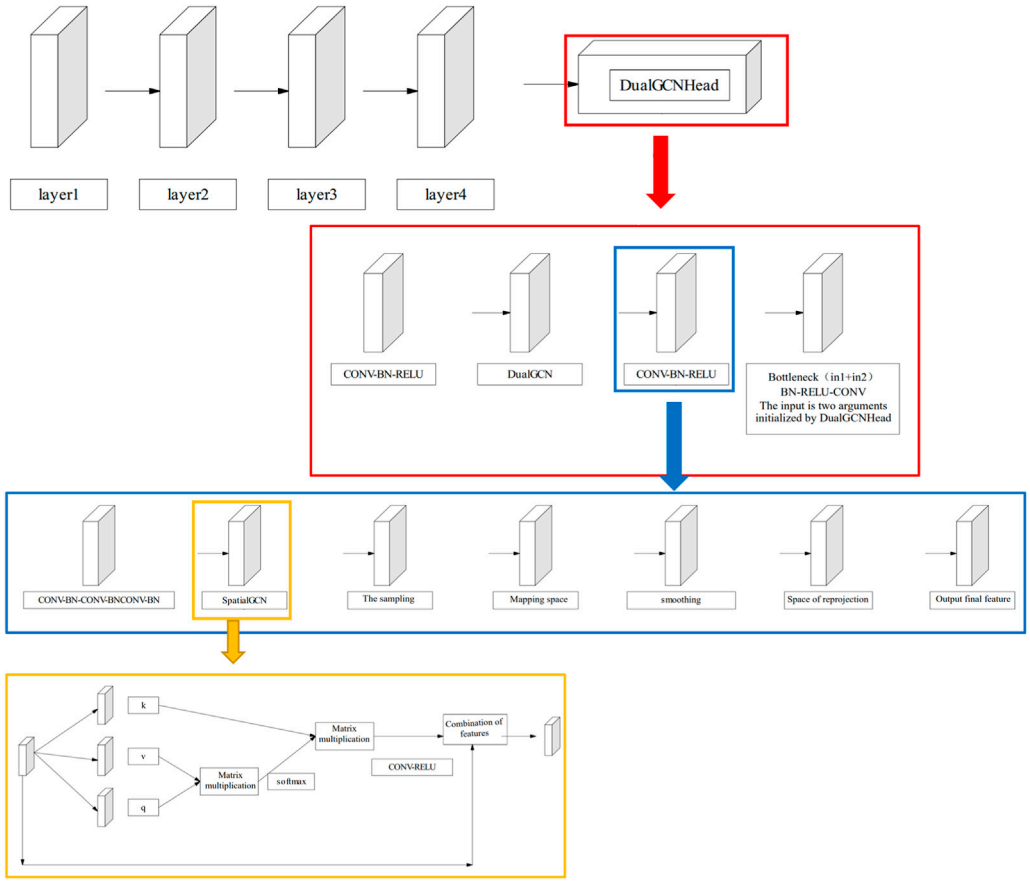

FIGURE 6
Schematic diagram of the model structure.

are mapped to the original coordinate space and added to the original features.

The backbone of the model is a ResNet series. The ResNet series is connected to the DGCNHead. DGCNHead consists of coordinate branches and channel branches. The input features are first learned in the coordinate branch, the original input features are mapped into new dimensions and convolution learning is carried out. Then, the feature map is combined with some features of the channel to output the final feature result.

As is shown in Figure 6.

The overall process is as follows:

1) Training stage: The supervision loss function of training is the cross-entropy loss function.
2) In the training process, the results of the last round will be verified in each training, and the relevant loss value will be printed.
3) The trained model is used to test the accuracy of the test set.

PASCAL-VOC represents the sample dataset.

As is shown in Figure 7.

3.3 GoogLeNet model

GoogLeNet is a Convolutional Neural Network (CNN) architecture introduced by Christian Szegedy and his team at Google, which secured the championship in the Imagenet competition in 2014. The GoogLeNet model consists of 22 layers in total, featuring 9 inception structures. Despite its depth of 22 layers and 5 million parameters, the number of parameters is significantly lower than that of both the AlexNet and VGG models. In fact, GoogLeNet has only 1/12 of the parameters of AlexNet and 1/36 of those in VGG. Therefore, when facing limitations in memory or CPU and GPU resources, GoogLeNet emerges as the preferable choice.

The standout characteristic of GoogLeNet lies in its utilization of the inception module. This module is designed to create a network with a robust local topology. It achieves this by performing multiple convolution and pooling operations on input images and then combining all the output results into a deep feature map. As various convolution and pooling operations, such as 1×1, 3×3, or 5×5, capture different information from the input images, processing these operations in parallel and merging the results yields a superior image representation. For a detailed explanation of the specific model structure, please refer to Reference (Szegedy et al., 2015).

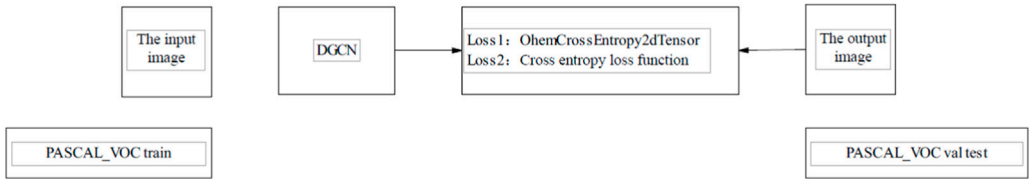

FIGURE 7
Schematic diagram of the process.

The model has the following characteristics.

(1) It can integrate feature information from different scales and retain more input information. Before this, most other commonly used convolutional neural networks improved the performance of the network by stacking more and more convolutional layers.
(2) A 1 × 1 convolution kernel is used for reduction and mapping processing. Compared with AlexNet and VGGNet, there is only one output layer.
(3) Two auxiliary classifiers are added in the middle of the network to help with training, with a total of three output layers, the problem of gradient disappearance in the training process is solved.
(4) The average pooling is used instead of the fully connected layer, which greatly reduces the number of model parameters.

3.3.1 Inception structure

The Inception structure is a crucial component of the GoogLeNet model, and its core idea is to approximate or directly replace the optimized local sparse component structure with a dense component structure. This structure retains the original Inception design, consisting of four convolutional branches:

Branch 1 employs a 1 × 1 convolutional layer with a step size of 1. The convolution kernel does not alter the length and width of the feature map but directly modifies its depth.

Branch 2 utilizes a 3 × 3 convolutional layer with a step size of 1 and padding of 1, aimed at extracting feature maps of varying sizes.

Branch 3 incorporates a 5 × 5 convolutional layer with a step size of 1 and padding of 2, also intended to extract feature maps of different sizes.

Branch 4 is a max-pooling layer with a pool core size of 3 × 3, a step size of 1, and padding of 1. This layer suppresses non-maximal information in the original image, replacing it with the most significant neighborhood information while preserving the image's size.

When the feature matrix is input, all four branches can simultaneously apply convolutional or pooling operations, resulting in four parallel outputs. As the step size for all branches is 1, the convolution or pooling dimensions remain unchanged. This allows them to be concatenated in the same dimension to produce the final output. Compared to the series-structured models like AlexNet and VGGnet, GoogLeNet alters the input into a parallel structure. It combines inputs after various operations and then proceeds to the subsequent layers. In contrast to other convolutional neural network architectures, where the next convolutional layer can only process the feature map from the preceding layer, GoogLeNet's approach helps prevent information loss from the earlier stages, ensuring it can still be accessed in subsequent layers.

3.3.2 Auxiliary classification structure

The GoogLeNet model incorporates two auxiliary classifiers and structures to facilitate training. The first level comprises a 5 × 5 average pooling layer with a step size of 3. The second level consists of a 1 × 1 convolutional layer with a step size of 1, featuring a total of 128 convolution kernels. The third and fourth levels consist of fully connected layers with 1024 and 1000 nodes, respectively. It is important to note that the auxiliary classifier is solely utilized during training and not during testing. It is introduced into the overall network loss with a weight of 0.3 to counteract gradient vanishing and provide regularization.

4 Training process and recognition results

4.1 Recognition result of landslide by DGCNet model

The training set consists of three remote sensing satellite images. The verification set consists of one remote sensing image, and the test set consists of one remote sensing image. The number of training epochs is set to 20, the batch size is set to 8, and the input picture size is set to 600. In the training process, the loss value will be displayed in the window, the Excel data generated in the training process will be saved as pictures, and the network model generated in the training will be saved at the same time. The device model used in this work is NVIDIA Geforce GTX 3080 GPU (8 GB memory) on the Windows system, which applies Pycharm editor, and uses Python for programming. The curves of training accuracy, training loss, training precision, DSC, F1, and M-IOU are shown in the figure. Ideally, the training loss value should decrease rapidly in the first few epochs. When 20 epochs are trained, the accuracy of the training set tended to the maximum, the loss rate tended to the minimum. The results are shown in Figure 8.

Similarly, the verification accuracy, verification loss, verification precision, and verification M-IOU curves of this work are shown in Figure 9. As can be seen in Figure 9, the lowest value of the loss is found at the 20 epochs, the DSC is 0.8815, the M-IOU is 0.77, the precision is 0.82, the F1 is 0.86, and the accuracy is 0.96.

The test set results are shown in Figure 10, it can be seen from Figure 10 that the landslide identification accuracy using this

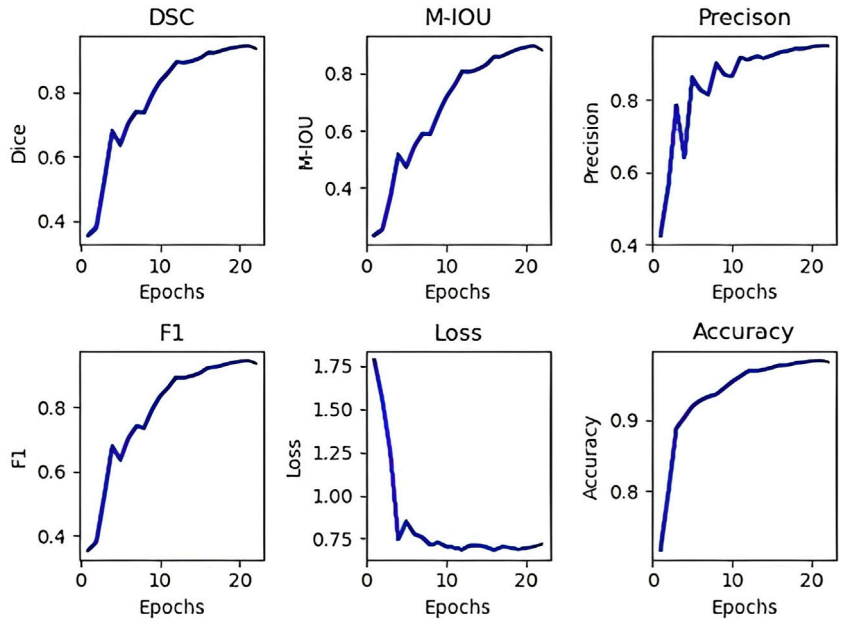

FIGURE 8
Line chart of the DSC, M-IOU, accuracy, loss, precision, and F1 in the training data set experiment.

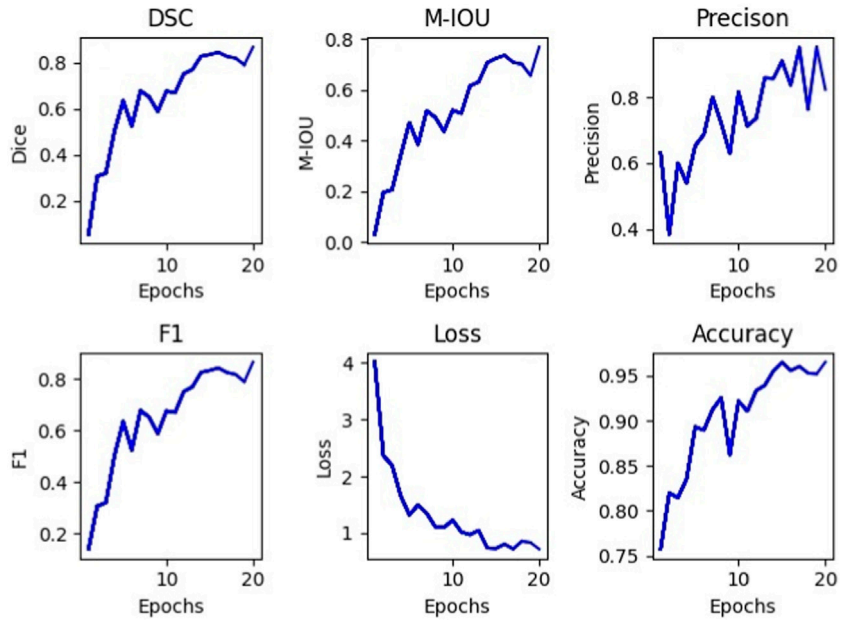

FIGURE 9
Line chart of the DSC, M-IOU, accuracy, loss, precision, and F1 in the validation data set experiment.

method is high. Large-scale landslides can be identified. The unrecognized area is mainly the landslide boundary, and the incorrectly identified area is mainly the exposed area on the top of the mountain, but the area is small. Because this model training uses fewer training sets, which may have a certain impact on the results, the training sets can be added later to improve the accuracy of the model.

4.2 Recognition result of landslide by GoogLeNet model

During the process of model training, optimizing parameters to minimize the loss function is a crucial parameter-tuning step. The optimizer's task is to compute the gradient of the loss function in each epoch and consequently update the parameters. The Adam

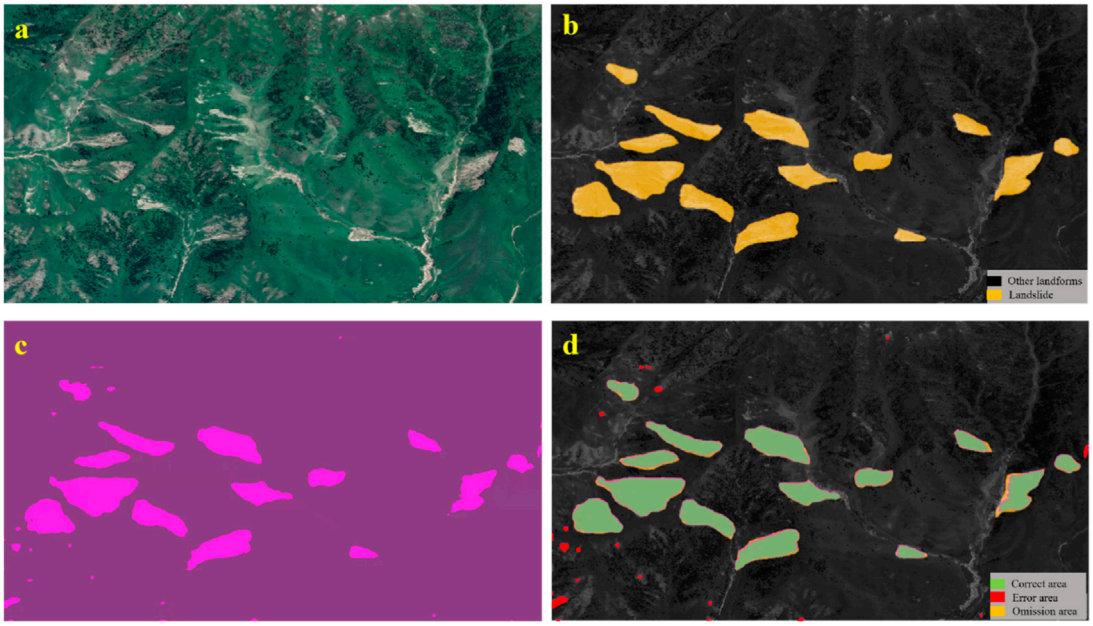

FIGURE 10
The test set prediction results: **(A)** the sample to be tested; **(B)** manual interpretation area; **(C)** model identification area; **(D)** identification area distribution characteristics.

optimizer, developed by Kingma and Ba in 2014, amalgamates the strengths of the AdaGrad and RMSProp optimization algorithms. It takes into account both first-moment and second-moment estimations of the gradient to determine the update step.

An image is an array of pixels organized in a specific sequence, with colors represented by the three primary channels of red, green, and blue. These pixels assume values ranging from 0 to 255; for instance, (0, 0, and 0) represents black. When employing a convolutional neural network for image recognition, pixel values are transformed into an array. The values within this array represent the image's features, and any changes in the image result in corresponding alterations in these pixel values. Furthermore, it is essential to preserve the spatial arrangement of images as much as possible when feeding image features into a neural network. In the process of identifying images of landslides and other topographic features through convolution layers, distinct convolutional kernels are utilized to generate corresponding output values, determining which one best characterizes the landslide features. When a convolution kernel yields high output values for landslide features and low output values for non-landslide terrain, it effectively extracts the desired features from the image. The optimal convolution kernel is then passed through a pooling layer after multiplication with the image's corresponding feature matrix. This step serves to reduce the number of trainable parameters, retain the most pertinent landslide information from the terrain images, and mitigate the risk of overfitting.

For the training process when the image data is small, when there are a small number of incorrect labels in the sample, the incorrect labels will have an impact on the accuracy of the prediction. Therefore, label smoothing is adopted to reduce overfitting and improve the model's generalization ability. Weight_ Decay can adjust the complexity of the model and reduce the impact on the loss function. With a smaller weight, the complexity of the network is lower, and the fitting of the data will be better. Picture size through img = cv2 Resize [img, (224)] is scaled to the size format of 224 pixels * 224 pixels. The parameter batch size is 32, the optimizer is Adma, the learning rate is 0.0001, and the weight_decay is 0.001.

During the training of the model, the loss rate and accuracy of the training set and validation set are used to evaluate the model. A total of 100 epochs were trained. After training 20 epochs, the curves of the loss rate and accuracy rate of the training set tended to be flat. After 60 epochs, the accuracy rates of the training and validation sets become close to the peak Figure 11 and Figure 12 show the images of the change in loss rate and accuracy of the training and validation sets during the training process.

The loss and accuracy rates of the training set and validation set after 100 epochs of training iteration were saved as a document file. The accuracy of the validation set fluctuates between 78.125% and 81.25%, with the highest prediction accuracy of 81.25%.

Also, the trained optimal model was saved and applied to predict the label of the input picture. Some prediction results are shown in Figure 13.

The GoogLeNet model used in this paper has the highest prediction accuracy of 81.25%, while Zhang et al. (2020) proposed a model for seismic landslide recognition based on deep learning, and the accuracy of this model on the validation set is 88.15%. It is 6.9% higher than the GoogLeNet model. It can be seen from Figure 9 that the accuracy of the DGCNet Model is also higher than that of the GoogLeNet model. In addition, the two models have different applicable situations, the DGCNet model can identify and label landslides in a satellite remote sensing image that contains dozens of slopes, while the GoogLeNet model can only classify whether a single slope in a remote sensing satellite image is a

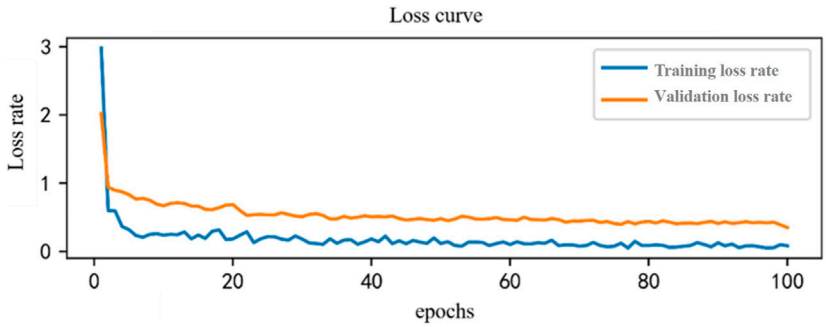

FIGURE 11
Epoch loss curve of the training set and validation set.

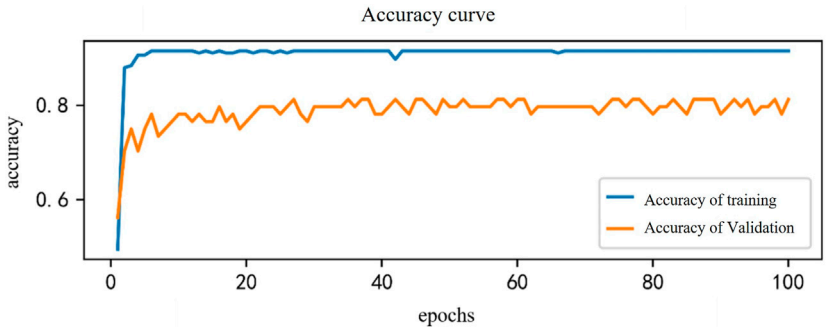

FIGURE 12
Epoch Accuracy curve of the training set and validation set.

landslide, which is relatively inefficient. Therefore, the DGCNet model has a better recognition effect and plays a good reference role in landslide identification, which can quickly identify large-scale landslides and provide a basis for emergency rescue and disposal in the later stage of landslide disasters.

5 Discussion

DGCNet typically demands some data for training to achieve optimal performance. In the context of landslide image recognition, when datasets are limited in size, the model may face challenges related to overfitting or decreased performance. The effectiveness of DGCNet is highly dependent on the choice of hyperparameters, including the number of convolutional layers, kernel sizes, and learning rates. Fine-tuning these parameters for different applications can be time-consuming and computationally intensive. DGCNet may require significant computational resources, including high-performance GPUs, especially when dealing with large graph-based data. This can be impractical in resource-constrained environments. DGCNet is a deep learning model with complex internal mechanisms, making it challenging to interpret. In applications where decision explainability is crucial, the model's lack of interpretability may be a limitation.

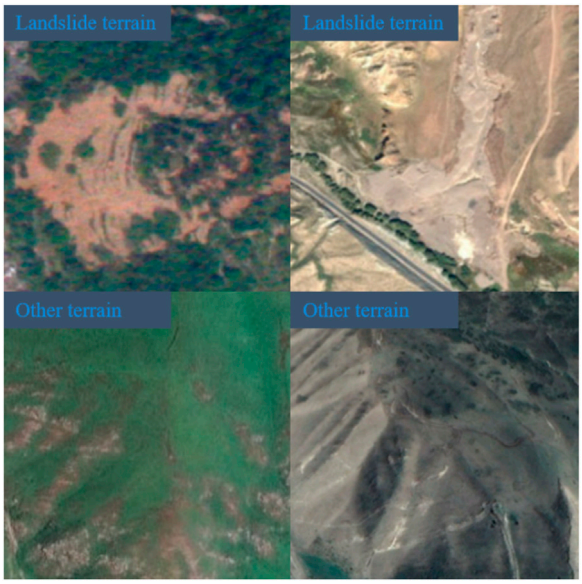

FIGURE 13
Prediction results of some topographic images.

DGCNet excels at integrating diverse data sources, such as topography, vegetation information, *etc.* This capability enables a comprehensive analysis of landslide image recognition. DGCNet can capture spatial correlations between nodes (representing geographical locations) within the graph, emphasizing the importance of geographical context, thereby enhancing the accuracy of landslide image recognition. Landslide data is often represented as a graph, where locations and their interconnections constitute nodes and edges. DGCNet is purpose-built for handling graph-based data, making it well-suited for such tasks. Employing DGCNet for landslide image recognition represents a relatively novel approach. It offers the potential to introduce fresh research perspectives and technological advancements to the field, ultimately improving the efficiency and accuracy of landslide recognition assessment.

In summary, DGCNet shows promise in landslide image recognition but also presents certain limitations. Addressing issues related to data requirements, hyperparameter tuning, and computational complexity, while enhancing model interpretability, will facilitate its broader adoption and utility in landslide recognition analysis.

6 Conclusion

The identification and location of landslides are of paramount importance due to their significant threat to human life and property worldwide. Traditional manual interpretation methods, while effective, are inefficient for large areas. In response to this challenge, this study introduced a landslide recognition method based on the Dual Graph Convolutional Network for quick and accurate identification of landslides in remote sensing images. The results demonstrated the efficacy of the DGCNet model in accurately identifying landslides within the regional remote sensing images of Tuergen Township, Xinyuan County, Xinjiang Province. A comparative analysis was conducted with the traditional convolutional network model, GoogLeNet, using single terrain images from Xinyuan County. The DGCNet model exhibited a broader recognition range, making it a valuable tool for large-scale regional remote sensing image analysis. However, it is important to note that the performance of the DGCNet model is highly dependent on the quality and characteristics of the input graph data. Poor data quality or unclear graph structures can lead to a decline in performance. Therefore, data preprocessing and quality assurance remain essential aspects of landslide recognition using DGCNet. In the future, other landslide databases can be used to train the model to improve the accuracy of the model. DGCNet has stronger learning and transmission ability than other methods and can handle more data types. This research contributes to the growing body of knowledge in this field, offering a new approach to address the challenges associated with landslide recognition in large-scale regional remote sensing images.

Data availability statement

The original contributions presented in the study are included in the article/Supplementary Material, further inquiries can be directed to the corresponding author.

Author contributions

Data resources, HQ and ZD; The research methods, SM, XB, and SL; writing–original draft preparation, SM and SL; editing, SM, YS, JG, and XL; All authors contributed to the article and approved the submitted version.

Funding

This research was financially supported by the National Natural Science Foundation of China (42077440, 41202217), the second Tibet Plateau Scientific Expedition and Research (2019QZKK0904), the project (Grant Nos. BJH16J030, BJH16J032), the National Key Research and Development Program of China (2018YFC1505503), the Key Developing Program of the Chinese Academy of Sciences (Grant Nos. ZDRW-ZS-2021-3-1, ZDBS-LY-DQC003), the Scientific Research and Technology Development Project of China National Petroleum Corporation (No. 2022DJ5503) and CAS Key Technology Talent Program.

Conflict of interest

The authors declare that the research was conducted in the absence of any commercial or financial relationships that could be construed as a potential conflict of interest.

Publisher's note

References

Alimohammadlou, Y., Najafi, A., and Gokceoglu, C. (2014). Estimation of rainfall-induced landslides using ANN and fuzzy clustering methods: a case study in saeen slope, Azerbaijan province, Iran. *Catena* 120, 149–162. doi:10.1016/j.catena.2014.04.009

Azarafza, M., Azarafza, M., Akgün, H., Atkinson, P. M., and Derakhshani, R. (2021). Deep learning-based landslide susceptibility mapping. *Sci. Rep.* 11 (1), 24112. doi:10.1038/s41598-021-03585-1

Beijing Normal University (2021). *Global natural disaster assessment report-EN*. Beijing: Beijing Normal University.

Bien Bui, D., Tuan, T. A., Klempe, H., Pradhan, B., and Revhaug, I. (2016). Spatial prediction models for shallow landslide hazards: a comparative assessment of the efficacy of support vector machines, artificial neural networks, kernel logistic regression, and logistic model tree. *Landslides* 13 (2), 361–378. doi:10.1007/s10346-015-0557-6

Breiman, L. (1996). Bagging predictors. *Mach. Learn* 24 (2), 123–140. doi:10.1007/bf00058655

Chen, Z., Song, D., Du, Y., and Dong, L. (2023). Investigation on the spatial distribution of landslides in Sichuan Province, southwest China. *Geomatics, Nat. Hazards Risk* 14 (1), 2232085. doi:10.1080/19475705.2023.2232085

Cheng, G., Guo, L., Zhao, T. Y., Han, J. W., Li, H. H., and Fang, J. (2013). Automatic landslide detection from remote-sensing imagery using a scene classification method based on BoVW and pLSA. *Int. J. Remote Sens.* 34 (1), 45–59. doi:10.1080/01431161.2012.705443

China Association of Geological Hazard Prevention and Control Engineering (2016). *T/CAGHP 018-2016 standard of classification for geological hazard*. WuHan: China University of Geosciences Press.

Danneels, P., Pirard, E., and Havenith, H. B. (2007). "Automatic landslide detection from remote sensing images using supervised classification methods," in Proceedings of the 2007 IEEE International Geoscience and Remote Sensing Symposium, Barcelona, Spain, 23-28 July 2007.

Du, H., Song, D., Chen, Z., Shu, H., and Guo, Z. (2020). Prediction model oriented for landslide displacement with step-like curve by applying ensemble empirical mode decomposition and the PSO-ELM method. *J. Clean. Prod.* 270, 122248. doi:10.1016/j.jclepro.2020.122248

Fu, W. Q., Shao, P., Dong, T., and Liu, Z. W. (2022). Novel higher-order Clique conditional random field to unsupervised change detection for remote sensing images. *Remote Sens.* 14, 3651. doi:10.3390/rs14153651

He, K. M., Zhang, X. Y., Ren, S. Q., and Sun, J. (2016). "Deep residual learning for image recognition," in 2016 IEEE Conference on Computer Vision and Pattern Recognition (CVPR), Las Vegas, NV, USA, 27-30 June 2016.

Hu, Q., Zhou, Y., Wang, S., Wang, F., and Wang, H. (2019). Improving the accuracy of landslide detection in"off-site" area by machine learning model portability comparison: a case study of jiuzhaigou earthquake, China. *Remote Sens.* 11, 2530. doi:10.3390/rs11212530

Kavzoglu, T., Colkesen, I., Sahin, E. K., and Sahin, E. K. (2019). "Machine learning techniques in landslide susceptibility mapping: A survey and a case study," in *Landslides: Theory, practice and modelling. Advances in natural and technological hazards research*. Editors S. Pradhan, V. Vishal, and T. Singh (Cham, Switzerland: Springer), 50.

Mohan, A., Singh, K. A., Kumar, B., and Dwivedi, R. (2020). Review on remote sensing methods for landslide detection using machine and deep learning. *Trans. Emerg. Telecommun. Technol.* 32 (7). doi:10.1002/ett.3998

Nikoobakht, S., Azarafza, M., Akgün, H., and Derakhshani, R. (2022). Landslide susceptibility assessment by using convolutional neural network. *Appl. Sci.* 12 (12), 5992. doi:10.3390/app12125992

Piralilou, S., Shahabi, H., Jarihani, B., Ghorbanzadeh, O., Blaschke, T., Gholamnia, K., et al. (2019). Landslide detection using multi-scale image segmentation and different machine learning models in the Higher Himalayas. *Remote Sens.* 11, 2575. doi:10.3390/rs11212575

Prakash, N., Manconi, A., and Loew, S. (2020). Mapping landslides on EO data: performance of deep learning models vs. traditional machine learning models. *Remote Sens.* 12, 346. doi:10.3390/rs12030346

Shao, P., Shi, W., Liu, Z., and Dong, T. (2021). Unsupervised change detection using fuzzy topology-based majority voting. *Remote Sens.* 13, 3171. doi:10.3390/rs13163171

Shao, P., Yi, Y., Liu, Z., Dong, T., and Ren, D. (2022). Novel Multiscale decision fusion approach to unsupervised change detection for high-resolution images. *IEEE Geoscience Remote Sens. Lett.* 19, 1–5. Art no. 2503105. doi:10.1109/LGRS.2022.3140307

Szegedy, C., Liu, W., Jia, Y. Q., Sermanet, P., Reed, S., Anguelov, D., et al. (2015). "Going deeper with convolutions," in 2015 IEEE Conference on Computer Vision and Pattern Recognition (CVPR), Boston, MA, USA, 07-12 June 2015, 1–9. doi:10.1109/CVPR.2015.7298594

Tien Bui, D., Ho, T. C., Pradhan, B., Pham, B. T., Nhu, V. H., and Revhaug, I. (2016). GIS-based modeling of rainfall-induced landslides using data mining-based functional trees classifier with AdaBoost, Bagging, and MultiBoost ensemble frameworks. *Environ. Earth Sci.* 75 (14), 1101–1122. doi:10.1007/s12665-016-5919-4

Wan, S. (2013). Entropy-based particle swarm optimization with clustering analysis on landslide susceptibility mapping. *Environ. Earth Sci.* 68 (5), 1349–1366. doi:10.1007/s12665-012-1832-7

Wang, L. J., Guo, M., Sawada, K., Lin, J., and Zhang, J. (2016). A comparative study of landslide susceptibility maps using logistic regression, frequency ratio, decision tree, weights of evidence and artificial neural network. *Geosci. J.* 20 (1), 117–136. doi:10.1007/s12303-015-0026-1

Xinjiang Geological Environment Monitoring Institute (2014). *The mechanics of landslide in Yili, Xinjiang county*. Urumqi: Xinjiang Geological Environment Monitoring Institute.

Ye, C., Li, Y., Cui, P., Liang, L., Pirasteh, S., Marcato, J., et al. (2019). Landslide detection of hyperspectral remote sensing data based on deep learning with constrains. *IEEE J. Sel. Top. Appl. Earth Obs. Remote Sens.* 12, 5047–5060. doi:10.1109/jstars.2019.2951725

Yu, B., Chen, F., and Xu, C. (2020). Landslide detection based on contour-based deep learning framework in case of national scale of Nepal in 2015. *Comput. Geosci.* 135, 104388. doi:10.1016/j.cageo.2019.104388

Zhan, Z., Shi, W., Zhang, M., Liu, Z., Peng, L., Yu, Y., et al. (2022). Landslide trail extraction using Fire extinguishing model. *Remote Sens.* 14, 308. doi:10.3390/rs14020308

Zhang, J. P., Zhang, Y., and Zhou, T. X. (2001). "Classification of hyperspectral data using support vector machine," in Proceedings of the 2001 International Conference on Image Processing (Cat. No.01CH37205), Thessaloniki, Greece, 07-10 October 2001.

Zhang, L., Li, X., Arnab, A., Yang, K. Y., Tong, Y. H., and Philip, H. S. (2019). *Dual graph convolutional network for semantic segmentation*. arXiv preprint arXiv:1909.06121.

Zhang, P., Xu, C., Ma, S., Shao, X., Tian, Y., and Wen, B. (2020). Automatic extraction of seismic landslides in large areas with complex environments based on deep learning: an example of the 2018 iburi earthquake, Japan. *Remote Sens.* 12, 3992. doi:10.3390/rs12233992

Zhu, L., Huang, L., Fan, L., Huang, J., Huang, F., Chen, J., et al. (2020). Landslide susceptibility prediction modeling based on remote sensing and a novel deep learning algorithm of a cascade-parallel recurrent neural network. *Sensors* 20, 1576. doi:10.3390/s20061576

frontiers | Frontiers in Earth Science

TYPE Original Research
PUBLISHED 11 October 2023
DOI 10.3389/feart.2023.1273352

OPEN ACCESS

EDITED BY
Wentao Yang,
University of Leeds, United Kingdom

REVIEWED BY
Yiding Bao,
Key Laboratory of Mountain Hazards and Surface Processes, Institute of Mountain Hazards and Environment, Chinese Academy of Sciences (CAS), China
Chaojun Ouyang,
Institute of Mountain Hazards and Environment, Chinese Academy of Sciences (CAS), China

*CORRESPONDENCE
Xueliang Wang,
wangxueliang@mail.iggcas.ac.cn

RECEIVED 06 August 2023
ACCEPTED 21 September 2023
PUBLISHED 11 October 2023

CITATION
Wang X, Sun J, Zhang Y, Jiao Q, Qi S, Wang R, Liu H and Zhang M (2023), Energetic impact of reconstructed debris flow on the intensity and duration of growth disturbances in tree rings. *Front. Earth Sci.* 11:1273352. doi: 10.3389/feart.2023.1273352

Energetic impact of reconstructed debris flow on the intensity and duration of growth disturbances in tree rings

Xueliang Wang[1,2,3]*, Juanjuan Sun[1,2,3], Yong Zhang[4], Qisong Jiao[5], Shengwen Qi[1,2,3], Ran Wang[6], Haiyang Liu[7] and Mengjie Zhang[1,2,3]

[1]Key Laboratory of Shale Gas and Geoengineering, Institute of Geology and Geophysics, Chinese Academy of Sciences, Beijing, China, [2]Innovation Academy for Earth Sciences, Chinese Academy of Sciences, Beijing, China, [3]College of Earth and Planetary Sciences, University of Chinese Academy of Sciences, Beijing, China, [4]Key Laboratory of Land Surface Pattern and Simulation, Institute of Geographic Sciences and Natural Resources Research, Chinese Academy of Sciences, Beijing, China, [5]National Institute of Natural Hazards, MEMC, Beijing, China, [6]Research Center of Applied Geology of China Geological Survey, Chengdu, China, [7]China Aero Geophysical Survey and Remote Sensing Center for Natural Resources, Beijing, China

A rare study on the quantitative relationship between the energetic impact of debris flows on the intensity and duration of growth disturbances of tree rings was carried out, partly due to a lack of feasible approaches and detailed field evidence. In this study, we first used a dendrogeomorphic technique to determine the age of a recent debris flow derived from historic landslide deposits at Qingyang Mountain (QYM) on the northeastern Tibet plateau. We acquired the quantitative data on the annual widths of tree rings in history and confirmed the influence of the debris flow rather than other factors (e.g., climatic events and inset outbreaking) in disturbing the growth of tree rings in a specific year. Using this approach, we determined that the age of the debris flow at QYM occurred in 1982, which was speculated to be triggered by the high monthly precipitation registered during July 1982. Subsequently, based on the boundaries of historic debris flow identified on remote sensing images before and after 1982 and the depth-integrated continuum model, we reconstructed the process of the 1982 debris flow and obtained the kinematic energy of the debris flow impacting the sampled trees. Based on the study, we observed that two growth disturbance patterns of tree rings influenced by the reconstructed 1982 debris flow were revealed, including growth suppression and asymmetric growth. We obtained a raw logarithm relationship between duration (i.e., lasting time for the disturbed tree rings to recover the initial width) and intensity of growth disturbances (i.e., growth suppression ratio of disturbed tree rings). We concluded that there is a negative exponential relationship between the simulated kinematic energy of debris flow impacting the disturbed trees and the time to recover the initial width of corresponding tree rings.

KEYWORDS

debris flow simulation, remote sensing, tree ring, mass flow, northeastern Tibet

1 Introduction

Different kinematic energy of debris flow impacting trees can lead to different failure characteristics and growth disturbances (Wistuba et al., 2013). Previous studies mostly focused on the relationships of kinematic energy of rockfall with morphological characteristics of trees (e.g., diameter at breast height and stand density) (Perret et al., 2004; Dorren and Berger, 2006; Woltjer et al., 2008). A rare study on the quantitative relationship between the impact of debris flows and the intensity and duration of growth disturbances in tree rings was carried out. For such a study, first, large amounts of tree ring samples disturbed by the same debris flow event are needed, but it is difficult for many trees to remain well preserved on-site for a long period. Second, the criterion to quantify the growth suppression or other disturbed characteristics in tree rings of different tree species influenced by debris flow is still limited for clarifying such a relationship. The last and most difficult factor is how to monitor or acquire the kinematic energy of debris flow impacting different disturbed trees. Recent studies that focus on dynamic process and kinematic energy of landslides and debris flow have been carried out with the help of the development of simulation approaches (Ouyang et al., 2019a; Ouyang et al., 2019b; Wu and ping-Hsuan Hsieh, 2021; Bao et al., 2023a; Bao et al., 2023b). For example, Ouyang et al. (2019a) adopted a depth-integrated continuum method to analyze the dynamic process of two large sequential landslides that occurred in Baige village along the Jinsha River. The authors concluded that the evaluation of potentially landslide-prone areas simulated by the method is feasible. Wu and Ping-Hsuan Hsieh (2021) applied three-dimensional (3D) numerical modeling code 3DEC to numerically model the debris movement and deposition of the Chiu-fen-erh-shan landslide under the impact of the Chi-Chi earthquake, showing that post-failure configuration generated by the 3DEC simulations is similar to that observed in the field. Focusing on the same Baige village landslide, Bao et al., 2023a; Bao et al., 2023b) used a three-dimensional model based on the finite-discrete element method-smoothed particle hydrodynamics (FDEM-SPH) coupling approach to reconstruct the dynamic process of the landslide. The results of the landslide deposit area and the impulse wave-affected area were consistent with the results of field investigations. In this study, considering the characteristics of debris observed in the field and others simulated by previous studies (Ouyang et al., 2019a; Sun et al., 2021; Bao et al., 2023a), kinematic energy of debris flow was simulated through the numerical approach of mass flow that was used for debris flow dynamic propagation process modeling (Ouyang et al., 2013).

Although new geochronological methods increase the number of dated geohazards (e.g., landslides and debris flows), absolute dating methods (e.g., cosmic ray exposure, optically stimulated luminescence, thermoluminescence, and uranium-series (^{234}U/^{230}Th) dating) are still less developed for geohazards occurred on the centennial or millennial timescales (Crosta and Clague, 2009; Pánek, 2015). The dendrogeomorphic technique (tree ring-based) has been developed to constrain the ages of geohazards that were recorded as growth disturbances in tree rings on a centennial or millennial scale (Butler et al., 1986; Stoffel et al., 2005; Stoffel, 2006; Šilhán et al., 2016; Noguchi et al., 2021). Frequent geohazards impact local trees, leading to growth disturbances in tree rings (e.g., wider or narrower rings, and missing rings), which are used to determine the time and frequency of geohazards (Stoffel et al., 2005; Schneuwly and Stoffel, 2008; Lopez Saez et al., 2012; Šilhán, 2017; Zhang et al., 2019; Šilhán, 2021). However, there are also some other factors, such as earthquakes, temperature, precipitation, and inset outbreaking, that lead to growth disturbances in tree rings, which hinder the identification of landslide events (Carrara and O'Neill, 2003; Ciervo et al., 2017; Zhang et al., 2019). Meanwhile, random events around a tree, such as single block hitting and water flowing around tree roots, could also disturb the growth of a tree. Until now, studies of specific characteristics and index values of growth disturbances in tree rings of different tree species influenced by geohazards, especially debris flows, are still limited, impeding the timing of debris flows by dendrogeomorphic techniques.

With the development of remote sensing, images and the Digital Elevation Model (DEM) obtained by satellite methods, unmanned aerial vehicles (UAV), and terrestrial lidar systems were used to identify debris flows and to analyze the geometric characteristics of debris flows (Loye et al., 2009; Ma et al., 2019; Wang et al., 2021). Regional spatial distribution of geohazards has been widely mapped using the images obtained by satellite methods (Qi et al., 2010; Wang et al., 2021). One of the obvious merits of satellite methods is that satellite images provide clear visible evidence of debris flows that occurred in a location during a period. However, because of their strict application conditions for acquiring images (e.g., available satellite, suitable weather conditions, and acritical data acquiring setting), time series of past global satellite images rarely continue yearly or monthly focusing on an area, limiting the application of satellite images for reconstructing the evolution process of geohazards.

In a previous study, Zhang et al. (2019) reconstructed the centennial-scale process activity of landslides at QYM using dendrogeomorphic techniques. They mainly focused on an approach to determine the time series of landslides. Here, we further explore an approach to determine the age of a landslide by combining the dendrogeomorphic technique with remote sensing because the evidence to define the occurrence of a landslide or debris flows solely by dendrogeomorphic technique is not sufficient due to uncertain complex factors. More importantly, after determining the age, we studied the specific characteristics and index values of growth disturbance in tree rings (e.g., growth suppression ratio and lasting time for tree rings to recover their normal width) in the year of the debris flow. Furthermore, to reveal the kinematic energy of debris flows impacting the disturbed trees at QYM and their rarely studied relationship, we attempted to use numerical simulation of a depth-integrated continuum model and remote sensing images to reconstruct the evolution process, including spatial distribution of kinematic energy of the dated debris flow.

2 Materials and methods

2.1 Study area and field investigation

Qingyang Mountain (QYM) is located in the northeastern Qilian Shan range. Because of tectonic faults and long-term weathering, landslides and rockfalls occurred frequently with widely distributed landslide deposits on the mountains (Figure 1). There were small landslides that occurred in the

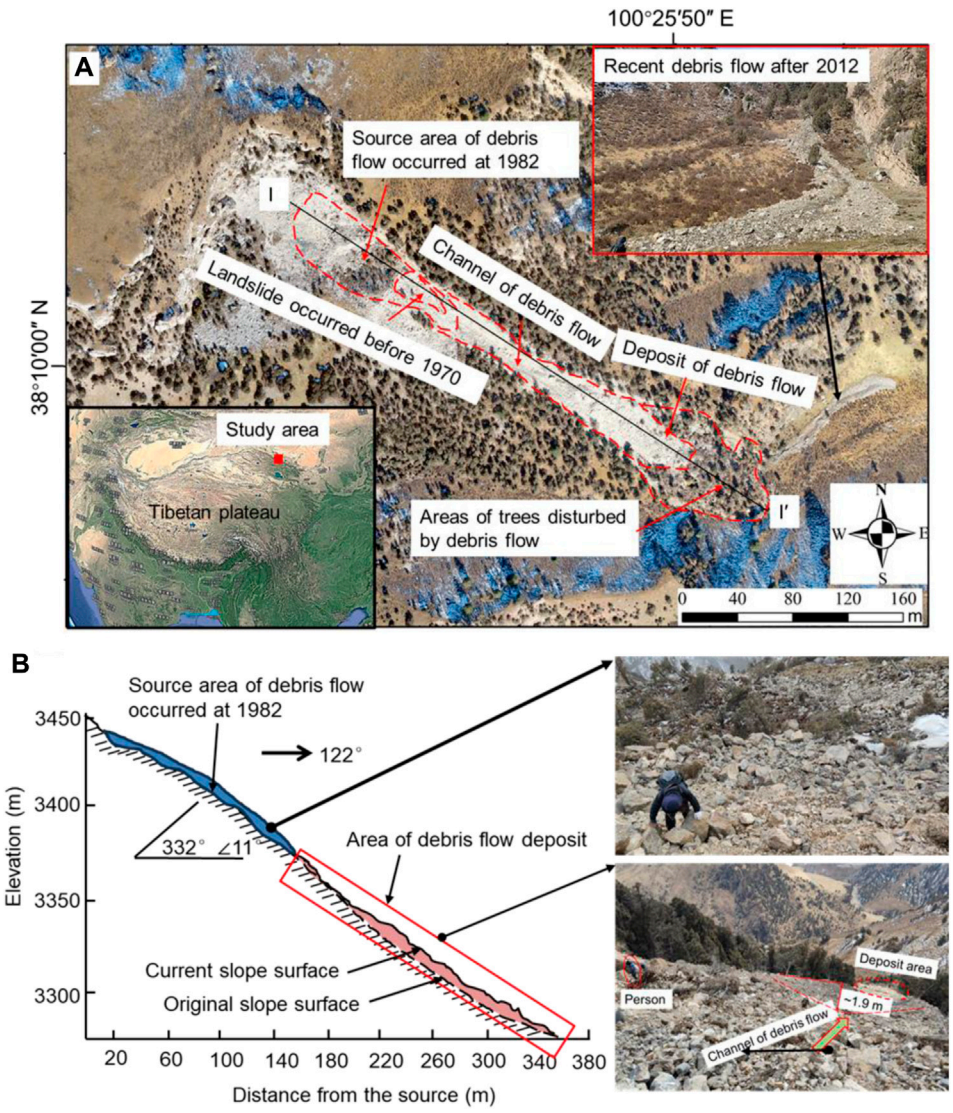

FIGURE 1
(A) Location of the landslide and debris flow in Qingyang Mountain and **(B)** topographic profile of I-I′ in Figure 1A.

middle section of QYM before 1970 (Zhang et al., 2019). The landslides were located at elevations ranging from 3,375 to 3,450 m a.s.l. (Figure 1B). Through fieldwork, we observed that historical landslide deposits were transformed as the initiation zone of typical debris flow, followed by the channel of propagation (with a channel depth of ~1.9 m) and accumulation zone (Figure 1). After the debris flow, recent smaller debris flows have been occurring on-site since 2012 (Figure 1A), which partly verifies the dynamic evolution of historic debris flows in the study area. The grain size of the deposits mostly ranges from 0.001 to 0.04 m^3, which falls into the small rock blocks class according to the International Society for Rock Mechanics (ISRM, 1979). Based on topographic analysis and field investigation, it was estimated that the total volume of the deposits of the accumulation zone is 4.9×10^4 m^3, with an average depth of 5.5 m.

The trees of Qilian junipers mostly grow on sunny slopes at elevations from 3,000 to 3,600 m a.s.l. at QYM (Zhang et al., 2019). The debris flow destroyed some trees that grew on the slope. Based on the site work, we noticed that more than 20 trees were hit (i.e., disturbed) by the debris on the accumulation zone, which was demonstrated by tree scars, injuries on the stem, and inclined trees on the deposit (Figure 2).

2.2 Geospatial data processing and analysis

We collected 1970 satellite images from the KH4B satellite (number DS1108-2184DA088) with a resolution of 1.83 m (Figure 3A), which was the oldest source of imagery with high resolution in the study area. With the most advanced cameras on board, the KH4A and KH4B satellites (imagery resolution of 2.74 and 1.83 m) collected global-scale, high-resolution imagery as one important part of the CORNOA program from 1960 to 1972 (Casana, 2020). The images in 2012 (Figure 3B) and 2019

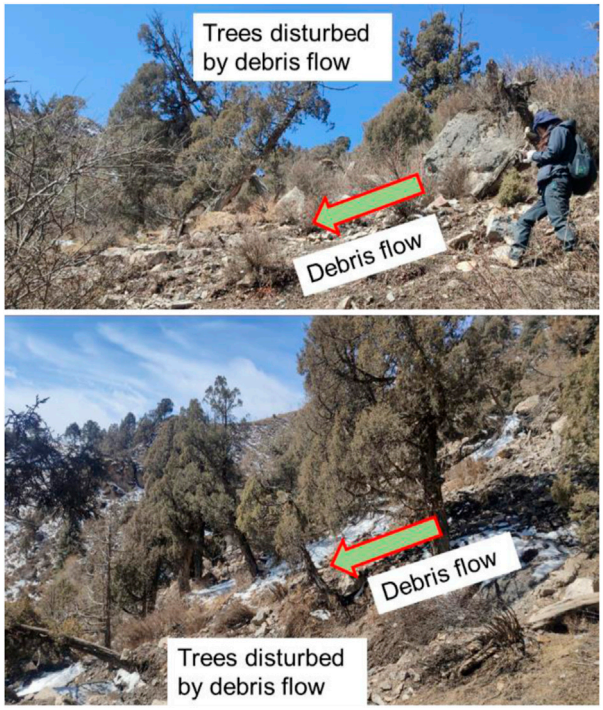

FIGURE 2
Trees disturbed by debris flow on the accumulation zone in QYM.

(Figure 1A) were obtained from Google Earth and UAV. We obtained 476 photographs taken over an area of approximately 10 km^2 by UAV in 2019, which was used to create a 0.3-m-resolution DEM with the structure from the motion photogrammetry technique (Johnson et al., 2014). The images and DEM were used to analyze the temporal evolution of landslides in QYM and to simulate the debris flow as basic data by numerical modeling.

Although the boundaries of landslides and former debris flows occurred before 1970 (i.e., the year of the imagery obtained) on KH4B satellite imagery were difficult to exactly check on-site, we could still roughly verify the identification by comparing the white color boundary on the imagery (Figure 3A) and the exposure of rock mass on-site. In contrast, the clear image from 2012 and the currently well-preserved boundary and characteristics of deposits on-site helped us to easily verify the boundary of recent debris flow (Figure 3B).

2.3 Width measurement of core samples

To collect the core samples of tree rings, we chose the trees with obvious injuries or trees that were inclined on or near the debris flow deposit. A total of two or three increment cores were extracted per tree using increment borers from two directions including the scar direction (i.e., the direction of debris flowing) and the opposite one (Stoffel et al., 2013). If there were no obvious scars on the trees, we collected cores in the supposed direction of the debris flow movement (i.e., upslope and downslope cores) (Stoffel et al., 2005). We sampled all Qilian junipers on the deposit body with diameters at breast height exceeding 20 cm (the highest measured 110 cm) with increment borers. We marked the locations of the core samples on the topographic map created from our 0.3-m-resolution DEM. Ultimately, a total of 52 increment cores were extracted from 23 Qilian juniper trees.

In reference to previous studies (Stokes and Smiley, 1968; Stoffel et al., 2013), we dealt with the collected samples in a lab based on standard dendrogeomorphical techniques. First, the samples were left to air dry, and then we used glue to attach the dried samples to wood grooves. The firmed samples were polished using fine sandpaper to make the cells of increment cores clear to be observed by microscope. Finally, we measured the annual widths of tree rings using a LINTAB™ instrument (Figure 4) whose maximum resolution was 1/1,000 mm (http://www.rinntech.de/content/view/16/47/lang,english/index.html). The measured data were automatically recorded by the TSAP-Win™ software platform for tree ring analyses (http://www.rinntech.de/content/view/17/48/lang,english/index.htm).

After measuring the annual widths of tree rings, we used a previously built reference chronology in the same area for precise cross-dating and age corrections of the core samples disturbed by the debris flow using COFECHA (Cook and Kairiukstis, 1990; Zhang et al., 2019). The verification of cross-dating accuracy was based on the value of the correlation coefficient between the measured annual width of tree rings and reference chronology larger than 0.4 (Grissino-Mayer, 2001).

2.4 Numerical simulation of debris flow

The mass flow was based on the depth-integrated continuum model, transforming the 3D description of the dynamic process of debris flow into a simple 2D problem by integrating the Navier–Stokes equations in the depth direction (Iverson and Ouyang, 2015). Under the depth integral condition, Leibniz's law and dynamic boundary conditions were used to simplify the mass and momentum conservation equations as follows (Ouyang et al., 2019a; Sun et al., 2021):

$$\frac{\partial(\bar{\rho}h)}{\partial t}+\frac{\partial(\bar{\rho}h\bar{v}_x)}{\partial x}+\frac{\partial(\bar{\rho}h\bar{v}_y)}{\partial y}=0 \tag{1}$$

$$\frac{\partial(\bar{\rho}h\bar{v}_x)}{\partial t}+\frac{\partial\left(\beta_{v_xv_x}\bar{\rho}h\bar{v}_x^2\right)}{\partial x}+\frac{\partial\left(\beta_{v_xv_y}\bar{\rho}h\bar{v}_x\bar{v}_y\right)}{\partial y}=\bar{\rho}g_xh-k_{ap}\bar{\rho}g_zh\frac{\partial(h+z_b)}{\partial x}-(\tau_{zx})_b \tag{2}$$

$$\frac{\partial\left(\bar{\rho}h\bar{v}_y\right)}{\partial t}+\frac{\partial\left(\beta_{v_xv_y}\bar{\rho}h\bar{v}_x\bar{v}_y\right)}{\partial x}+\frac{\partial\left(\beta_{v_yv_y}\bar{\rho}h\bar{v}_y^2\right)}{\partial y}=\bar{\rho}g_yh-k_{ap}\bar{\rho}g_zh\frac{\partial(h+z_b)}{\partial y}-\left(\tau_{zy}\right)_b \tag{3}$$

where ρ is the mass density; h is the flow height; t is the time; β is the momentum distribution coefficient; v_x and v_y represent the components of the velocity vector on the x and y-axes, respectively; g_x, g_y, and g_z represent the components of the acceleration of gravity on the x, y, and z-axes, respectively; and k_{ap} is the lateral Earth pressure coefficient. The calculation expression of k_{ap} is presented in Eq. 4, dominantly controlled by

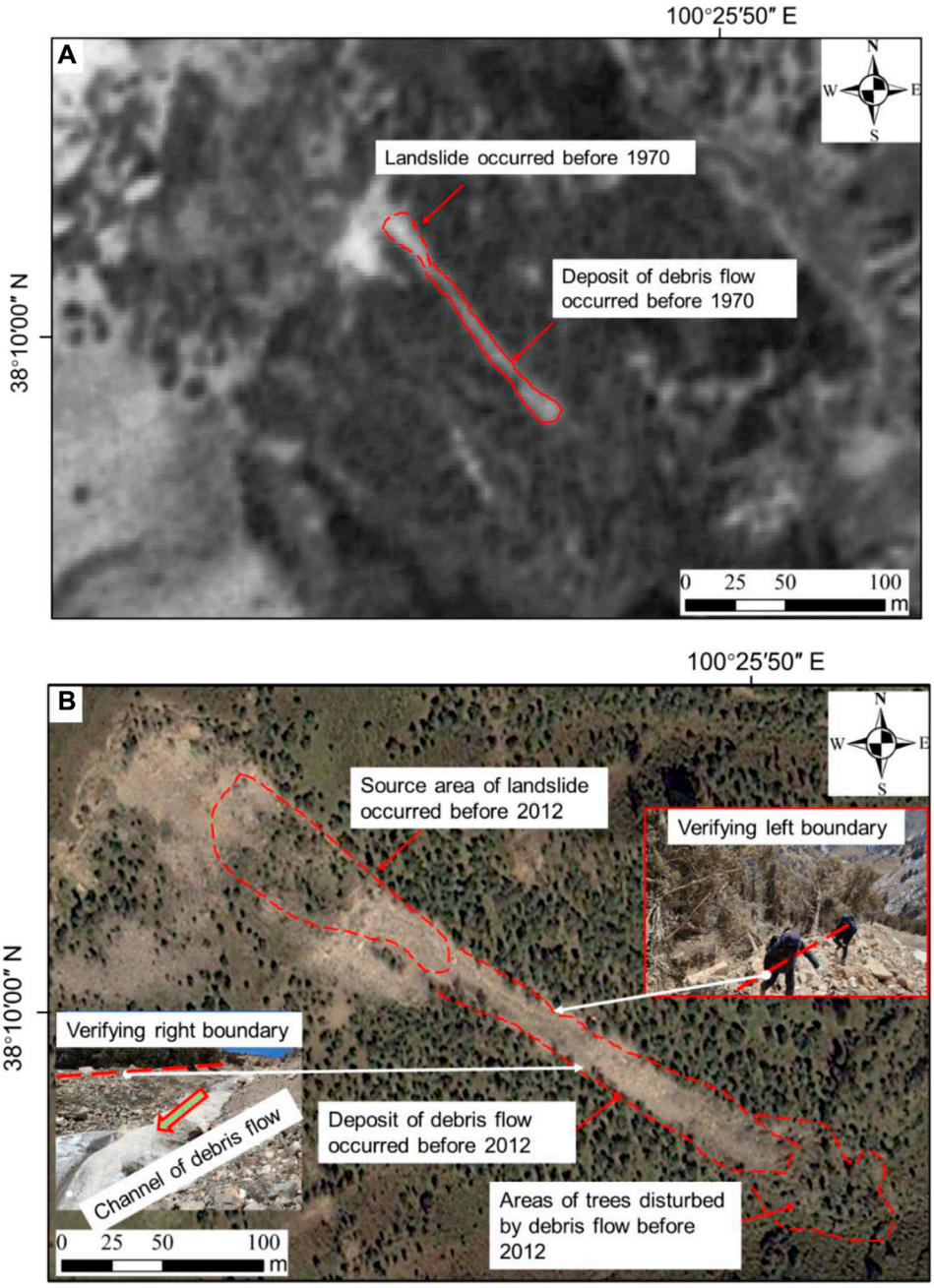

FIGURE 3
(A) Distribution of the landslide and debris flow occurred before 1970 from imagery obtained by the KH4B satellite in 1970; **(B)** Distribution of the landslide and debris flow that occurred before 2012 from imagery obtained by Google Earth in 2012.

the strain rate of the moving material; here, $(\tau_{zy})_b$ and $(\tau_{zx})_b$ are the basal resistance components.

$$k_{ap} = \frac{2}{\cos^2\varphi} \times \left[1 \pm \sqrt{1 - (1 + \tan^2\delta)\cos^2\varphi}\right] - 1 \qquad (4)$$

where φ and δ represent the internal friction angle and basal friction angle of the moving material, respectively.

The basal friction stress of debris flow was assumed to obey the Coulomb failure criterion (Eq. 5). For the Coulomb friction model available in mass flow, three dominant parameters were needed for simulation, namely, cohesion, friction angle, and pore water pressure parameters. Usually, it is difficult or even impossible in some cases to carry out field tests to obtain the values of parameters used for debris flow simulation. Hence, the parameters used in mass flow simulation are commonly obtained from back analysis of historic events (Ouyang et al., 2013; Sun et al., 2021). Luckily, the historic debris flow event in QYM provided us with a good chance to back analyze the parameters by optimizing the simulated

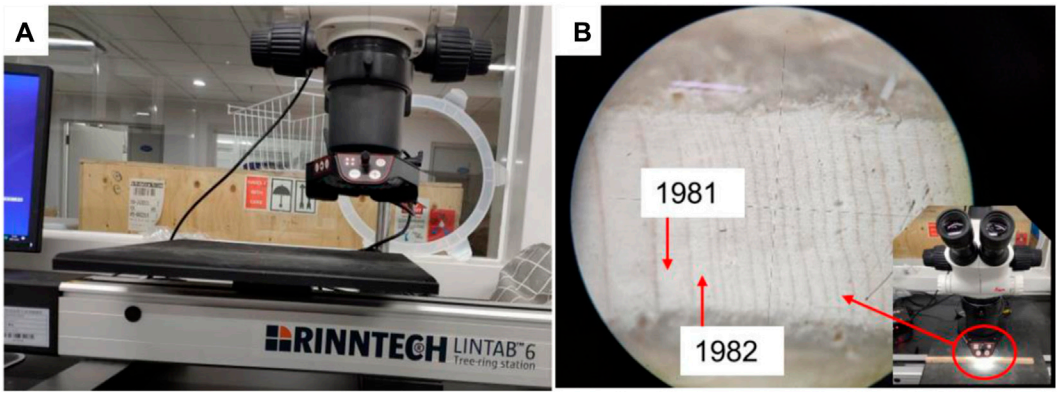

FIGURE 4
(A) The LINTAB™-6 instrument used for measuring the annual width of the tree rings; **(B)** The image of increment core observed with LINTAB™-6.

debris flow characteristics to fit the occurred ones (e.g., the farthest range and depth of the debris flow deposit).

$$\tau = c + \rho g h \cdot tan(\psi) \quad (5)$$

where c and ψ are the cohesion and friction angle of the mass, respectively.

Based on the 1970 satellite image, we plotted the boundary of the debris flow that occurred once or more times before 1970 (Figure 3A), which was used as the comparable characteristics with the simulated ones for back analysis. To simulate the dynamic propagation process of debris flow by mass flow, the source area and its thickness should be calculated first, including three dominant steps as follows:

(1) Build the current DEM of the calculation area. We clipped the specific area of DEM for calculation from the whole DEM of QYM, which was obtained before.
(2) Reconstruct the pre-slide topographic lines of the calculation area. Based on the field investigation and the 1970 satellite image, we adjusted the current topographic lines according to the contour lines of the surrounding terrain to build the approximately original topographic lines before the debris flow in ArcMAP.
(3) Create the area and thickness files of the debris flow source area. Using the two DEMs of the original and current ones, we created the source area using the tool of grid subtraction in ArcMAP. Hence the area and thickness of the source area could be extracted directly.

Using the source area data and given parameters, we simulated debris flow in the mass flow platform.

3 Results

3.1 Age of debris flow

Using the satellite images from 1970 to 2012, we obtained in ArcGIS the different boundaries of the debris flows at different stages. The boundary in 1970 was small, indicating that a small debris flow of approximately 6.1×10^3 m^3 occurred at that time or before (Figure 3A). The length and width of the debris flow presented in the image from 2012 were approximately 288 and 31 m (Figure 3B), both of which were about twice the measurement of the 1970 debris flow. Hence, a large debris flow occurred during the period from 1970 to 2012. The geometric features of the debris flow after 2012 do not have significant differences (e.g., from the debris flow image from 2019 in Figure 1A), indicating a relatively stable state of the debris flow body on the whole in the last 10 years (i.e., from 2013 to 2022).

Considering the possibility that the debris flow occurred between 1970 and 2012 and disturbed the annual width of tree rings, we analyzed the variation of annual widths of sampled tree rings (Figure 5). From the trees collected on the debris flow deposit, we observed 19 trees with synchronous growth disturbance in tree rings occurring in 1982. The growth disturbance included two patterns. One pattern was the growth suppression of width in tree rings in 1982, which was demonstrated by 13 trees (Figure 5A). Another pattern was the asymmetric growth of rings in 1982, as demonstrated by 6 trees (Figure 5B). For the second pattern, two core samples collected on opposite sides grew almost equally before a sudden disturbance. After the disturbance, one side grew faster or slower, while the other side did not grow synchronously. Hence, the difference in widths on the two opposite sides became larger and was influenced by the disturbance in the second pattern.

Two patterns of growth disturbance in tree rings, namely, growth suppression and asymmetric growth, could be observed not only from 19 trees, as occurring in 1982, but also from growth disturbances in the history of a single tree. For example, the annual widths of tree rings in samples QYG2314A and QYG2314B revealed several significant growth disturbance events (e.g., rockfall or landslide) in 1710 (i.e., asymmetric growth), 1860 (i.e., growth suppression), and 1982 (i.e., growth suppression) (Figure 10A). Meanwhile, the annual widths of tree rings of samples QYG2324A and QYG2324B revealed growth disturbance events in different years: 1742 (i.e., asymmetric growth) and 1810 (i.e., growth suppression) besides the same year of the 1982landslide (i.e., growth suppression) (Figure 10B). Hence, besides the synchronous growth disturbance in tree rings by the same large debris flow event, there were also some random growth disturbances

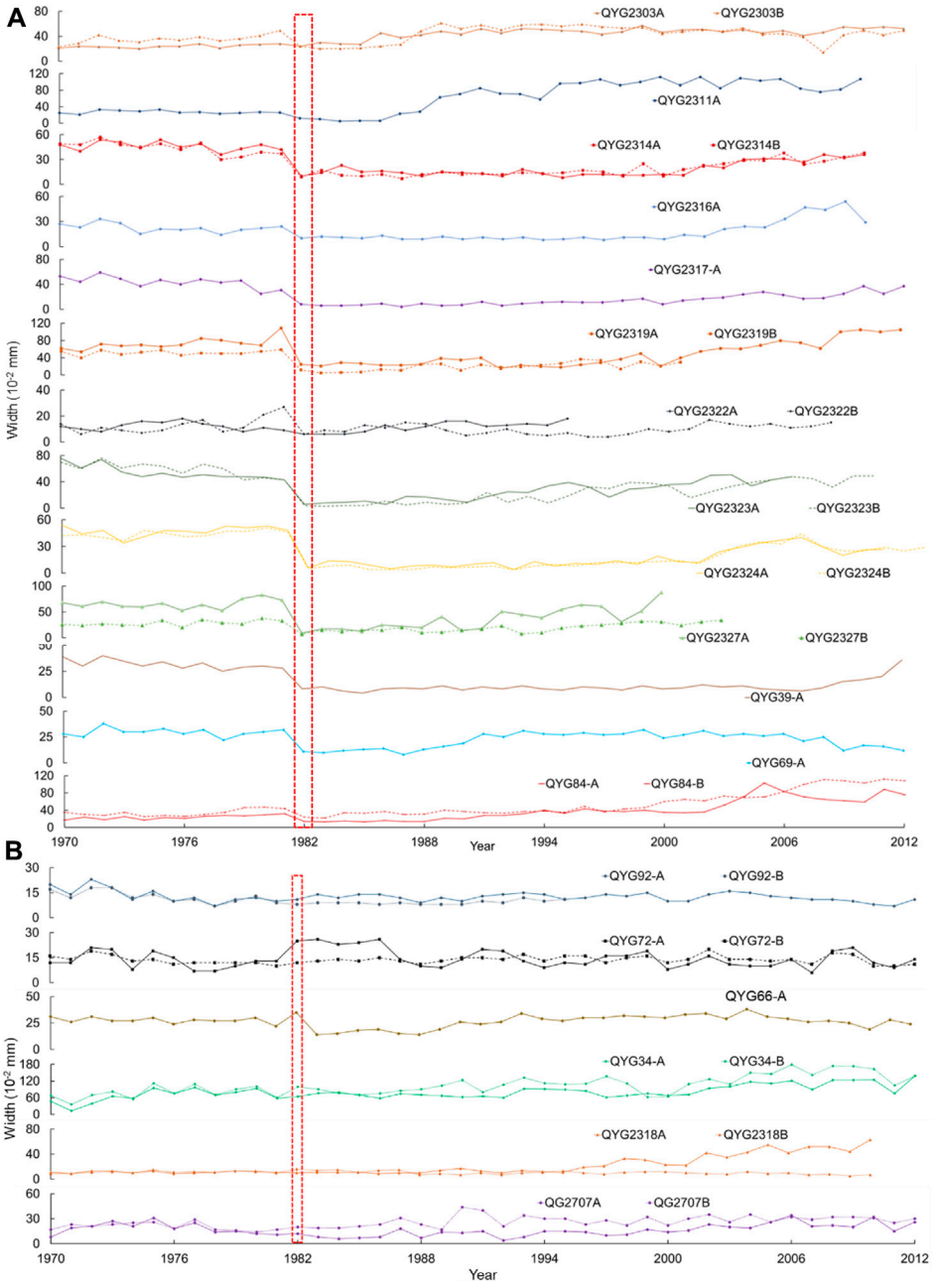

FIGURE 5
Tree-ring annual widths of sampled Qilian junipers demonstrating growth suppression **(A)** and asymmetric growth **(B)** in 1982 as a result of debris flow (red dotted box).

of different trees. Meanwhile, there were random growth disturbances in some specific tree rings rather than in all of them, as seen in Figure 5 (e.g., reduction in 2007 of QYG2303B and increment in 2000 of QYG2707A). The missing width data of some tree rings (e.g., QYG 2322A after the year 1996, QYG2324A after the year 2000, and QYG2324A after the year 2003) is due to artificial causes destroying the core samples. We did not note the obvious effect of the positions of samples on the patterns of growth disturbance.

Hence, considering the same debris flow event disturbing the growth of trees at the same time, we attributed the synchronous disturbance in 1982 of the width of 32 tree rings to a large debris flow. Combining the visible evidence, provided by satellite images, that a debris flow occurred between 1970 and 2012 with the data revealed by the synchronous growth disturbance in 1982 in tree rings, we determined the age of the debris flow in QYM as having occurred in 1982.

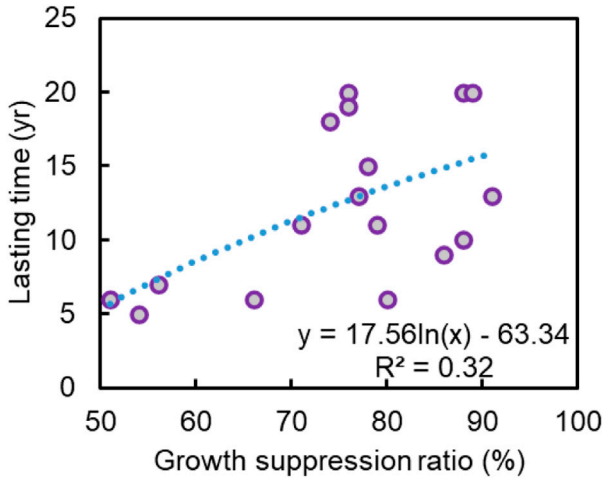

FIGURE 6
The relationship between lasting time and growth suppression ratio of tree rings disturbed by the 1982 debris flow.

3.2 Index values of growth disturbance in tree rings by the 1982 debris flow

By comparing the annual widths of tree rings in 1981 and 1982, we calculated the index of growth suppression ratio to be equal to the width of the disturbed tree rings in a year (i.e., 1982) divided by the width of undisturbed tree rings on the year before (i.e., 1981) using the data with obvious growth suppression pattern in our study (Figure 5A and Figure 6). Meanwhile, previous studies proposed that if the width of a tree ring in year t is reduced by more than 40% or 50% (i.e., growth suppression ratio in our study) of the width in year t-1, and the reduction of width lasts more than 5 years, year t is defined as the year of debris flow (Carrara and O'Neill, 2003; Zhang et al., 2019). Similarly, in our study, the maximum growth suppression ratio was 91% (QYG2323B), while the minimum was 51% (QYG2303B), with an average value of 73% (σ=0.16). The lasting time of growth suppression is an important index to reveal the influence of debris flow on the growth of tree rings (Van Den Eeckhaut et al., 2009). Based on our data, the lasting time for the disturbed tree rings to recover the initial width by the 1982 debris flow in QYM ranges from 5 to 26 years, with an average of 12 (σ=0.46) years. We observed that the larger the growth suppression ratio influenced by debris flow, the longer the lasting time for tree rings to recover, which is consistent with previous studies (Carrara and O'Neill, 2003; Van Den Eeckhaut et al., 2009). Meanwhile, a raw logarithm relationship between lasting time (y) (i.e., time to recover the initial width) and growth suppression ratio (x) (y=17.56ln(x)-63.34,σ=0.32) was obtained in our study (Figure 6).

3.3 Effect of precipitation in triggering the 1982 debris flow

Precipitation is important in triggering geohazards, especially debris flows (Ouyang et al., 2013; Ouyang et al., 2019a; Zhang et al., 2019). To analyze the effect of precipitation on the 1982 debris flow in QYM, we obtained monthly precipitation data from 1957 to 1982. We observed that the precipitation in July was the highest in the whole year averaged by the data of the last 25 years (Figure 7A), while the value in July 1982 (i.e., 1,299 mm) was 1.34 times that of the average value (i.e., 972 mm). Meanwhile, the monthly precipitation in July 1982 was the third highest of the previous 26 years, followed by that of 1981 (i.e., 1,374 mm) (Figure 7B). However, we also know that debris flows are commonly triggered by intense short-term precipitation events, sometimes preceded by high antecedent moisture conditions. Hence, because of a lack of more acute hourly precipitation in QYM, we just speculated that the high monthly precipitation observed in July 1982 played an important role in the evolution of the 1982 debris flow.

3.4 Kinematic energy of debris flow impacting the sampled trees

3.4.1 Parameters obtained by back analysis of the debris flow before 1970

To calibrate the parameters, we simulated the debris flow that occurred before 1970 for a series of scenarios with different values of

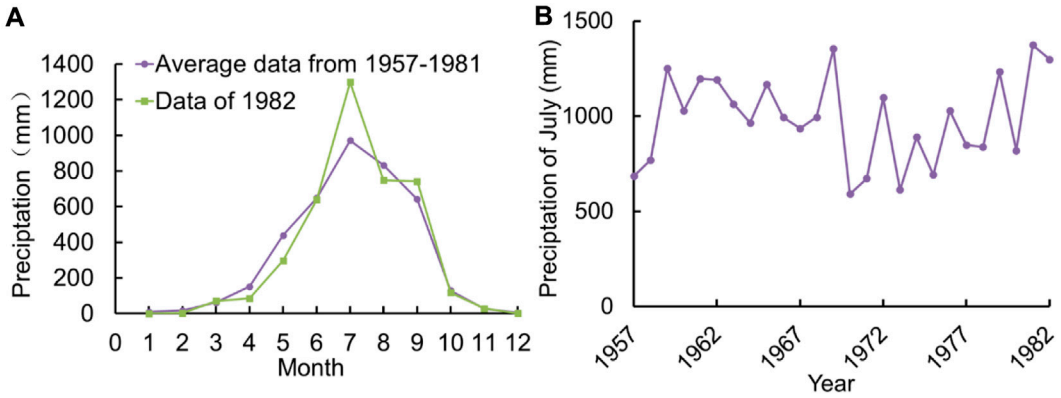

FIGURE 7
(A) Average monthly precipitation from 1957 to 1981 and monthly data in 1982 for the QYM region. **(B)** Monthly precipitation of July from 1957 to 1981 for the QYM region.

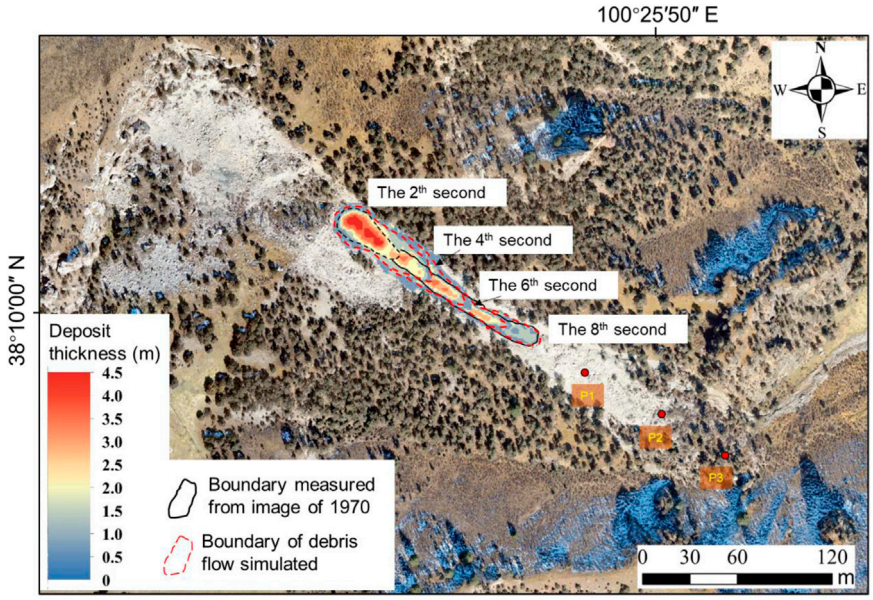

FIGURE 8
The evolution of debris flow depositing occurred before 1970, as calculated by numerical simulation.

coefficient, friction angle, and pore water pressure coefficients. Meanwhile, we collected parameters by back analysis from previous similar studies so that our results were more accurate (Ouyang et al., 2013; Ouyang et al., 2019b; Sun et al., 2021). Based on post-debris flow and reconstructed pre-debris flow 1x1 m topography DTMs, ~6,130 m^3 of mass was estimated as being detached from the source area (i.e., pre-occurred landslide) before 1970. The results obtained using the cohesion of 8 kPa, the friction coefficient of 0.43, and the pore water pressure coefficient of 0.3 showed relatively good consistency with the farthest range of the real debris flow deposit in 1970 (Figure 8).

The deposit thickness contours of the debris flow before 1970 at times t = 2, 4, 6, and 8 s are shown in Figure 8. Based on the simulated results, we observed that the debris flow moved fast forward from the source area from the beginning to the fourth second. The debris flow material deposited more in the back and front areas than in the middle area, forming a long-strip shape deposit. From the fourth to the eighth second, the debris flow extended further and finished moving during this second period, controlled by the reduction of material supplied from the source area and the frictional resistance of the deposited material. Eventually, the debris flow deposited as presented in the simulation map (Figure 9). As seen in the image, the farthest range is consistent with the real range observed in the satellite image from 1970, considering the effect of the resolution of the satellite image (Figure 3A).

3.4.2 Kinematic energy of the 1982 debris flow impacting the sampled trees

We simulated the evolution of the 1982 debris flow by mass flow, obtaining the spatial distribution and kinematic energy of the debris flow deposit (Figure 9). Because of large amounts of materials detached from the source area, the debris flow was transported farther than those before 1970. The debris flow arrived at the top of the current dominant deposit area at the 10th second (Figure 9A). From the 10th to the 14th second, the material started to spread to a wider range and reached the area of the disturbed trees. From the 14th to the 18th second, the blocks involved in the debris hit the trees (Figure 9B), causing them to become injured, fall, and be destroyed. Lastly, the material was deposited with a final depth of 2–6 m in the front area.

In addition to the deposit depth varying spatially, the impacts were responsible for decreasing the kinematic energy of the debris flow. To analyze the energy variation after impacting the disturbed trees, three monitoring points (Figure 8 and Figure 9B) were set up along the debris flow transport direction during the simulation. The result shows that the kinematic energy was reduced from more than 630.3 KJ (P1) to ~503.4 KJ (P2) before hitting the trees on the debris flow deposit. After hitting the sampled trees, the mass kinematic energy reduced spatially along the runout path, with the largest monitored value of 495.3 KJ located at QYG2323 and the smallest value of 9.1 KJ located at QYG2316.

4 Discussion

4.1 Relationship between impact energy and recovery time of disturbed tree rings

It is very important to quantitatively obtain the dynamic growth process of trees (i.e., tree rings) disturbed by debris flows. Based on the relationship, we could predict the possible disturbance degree of trees by potential debris flows, which provides a reference for designing and maintaining bioengineering in debris flow-prone areas (Brang, 2001). Second, building the relationship provides us an additional approach to back analyze the evolution process and kinematic energy of historically

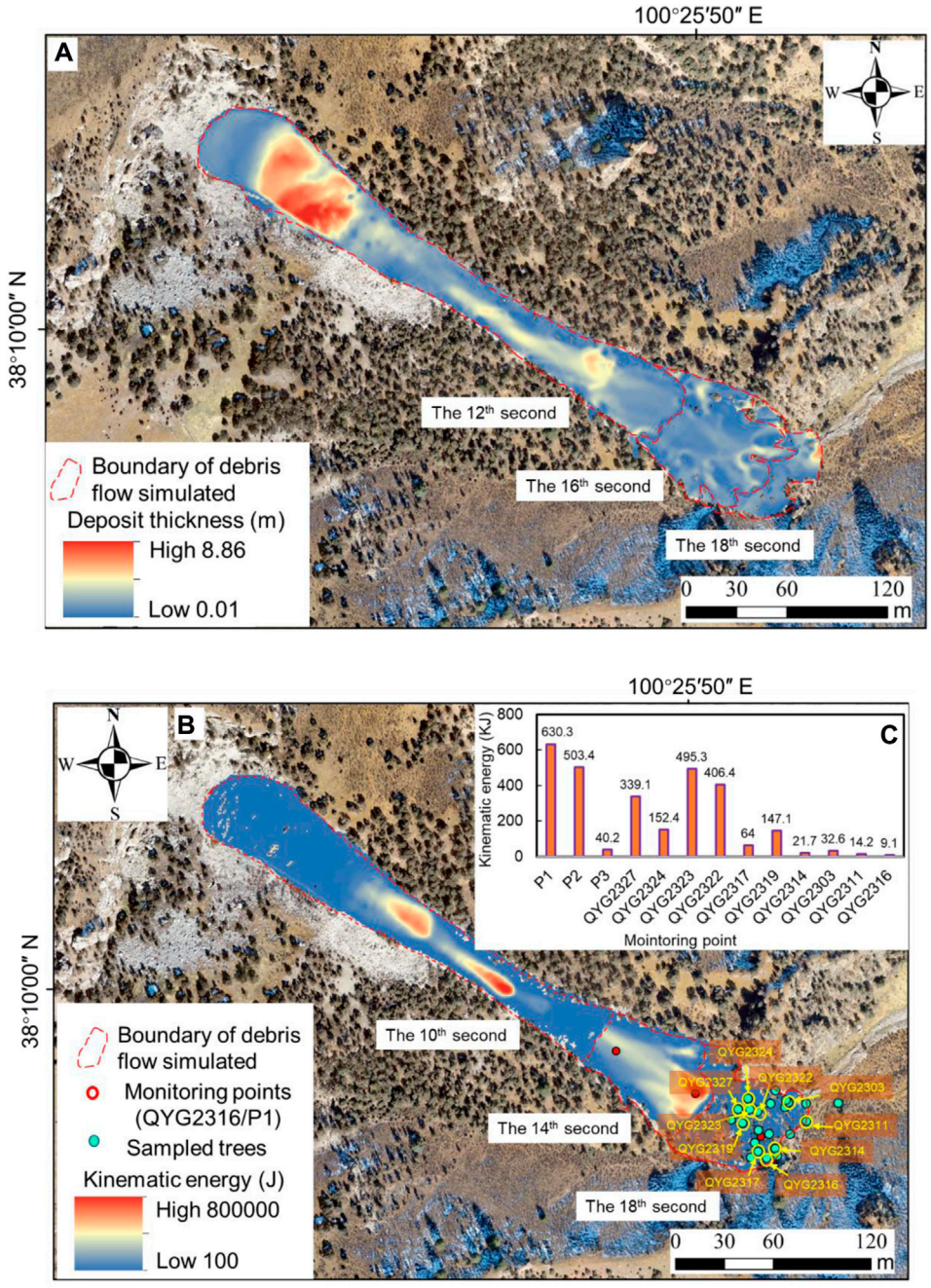

FIGURE 9
(A) The evolution of debris flow depositing and **(B)** kinematic energy of debris flow occurred in 1982 as calculated by numerical simulation. The locations of monitoring points for kinematic energy of debris flow impacting the sampled trees **(C)** are presented in **(B)**.

occurred debris flows using the measurable growth disturbance in tree rings. Hence, based on the data, we attempted to build a relationship between the impact kinematic energy of debris flows and the time to recover the initial width in tree rings.

Although there was a lack of a real record of the debris flow process impacting the sampled trees in QYM, we used numerical simulation to reconstruct the evolution process including the kinematic energy of the 1982 debris flow. We observed a raw negative exponential function (R^2=0.46) between the recovery time of disturbed tree rings (y, yr) and kinematic energy of debris flow (x, KJ) larger than 50 KJ in QYM (Figure 10A). This means that higher impact kinematic energy of debris flow leads to a larger growth suppression ratio and a longer recovery time. Meanwhile, we also noted that the growth suppression ratio almost remained constant with increasing kinematic energy after reaching the threshold value of ~300 KJ (Figure 10B), which was the value inferred to the trees that were completely destroyed, with no more records of tree rings after that energy value.

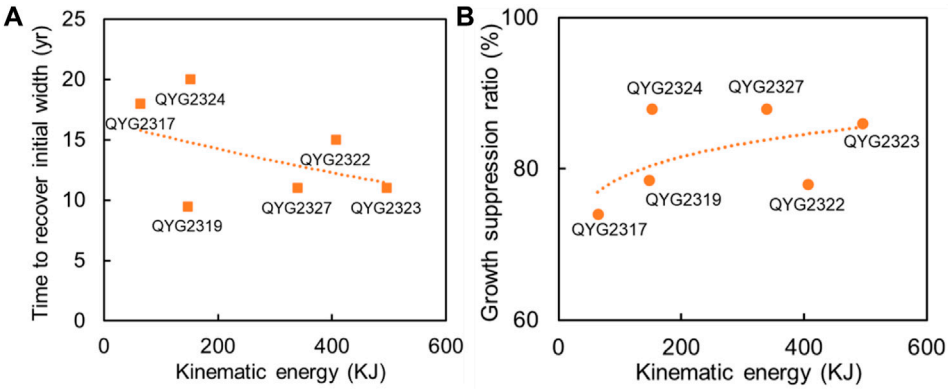

FIGURE 10
The relationship between the recovery time of disturbed tree rings **(A)** and the growth suppression ratio **(B)** and kinematic energy of debris flow (KJ) impacting the disturbed trees.

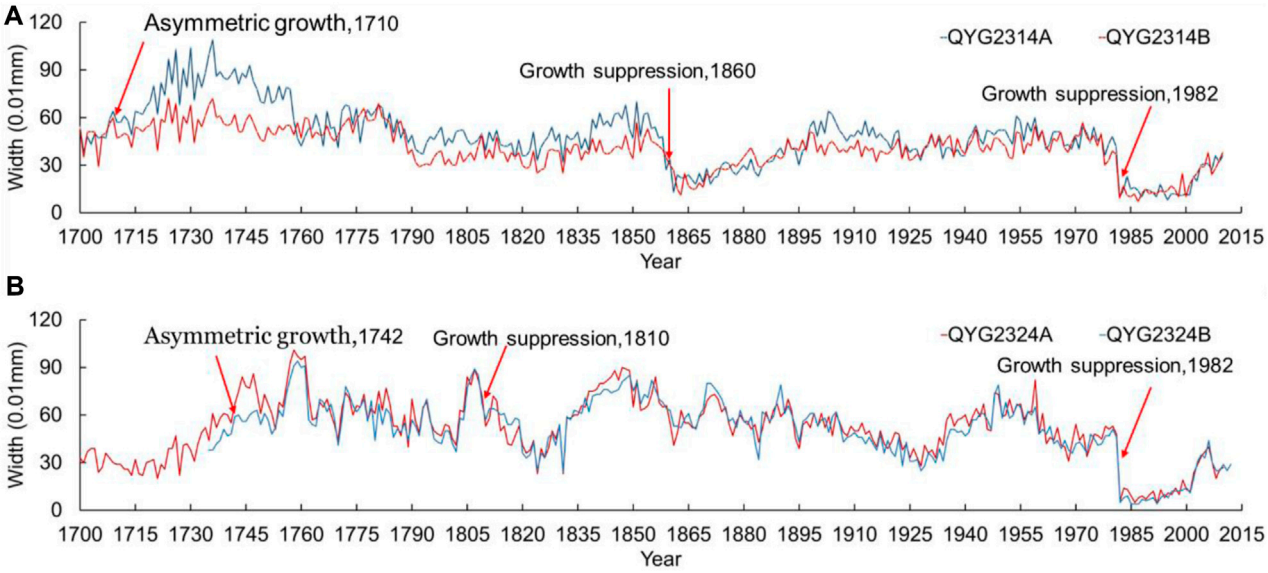

FIGURE 11
Tree-ring annual widths of sampled Qilian junipers QYG2314 **(A)** and QYG2324 **(B)**. Red arrows point to the segments with abnormal growth (growth suppression and asymmetric growth) as a result of landslides, single block hitting, or some other factor.

4.2 Uncertainty analysis

It is normal for tree rings to have one random growth disturbance pattern (growth suppression or asymmetric growth) influenced by water flow destroying the root systems or even local inset outbreaking (Figure 5 and Figure 11), rather than synchronous two patterns of growth disturbance as those influenced by the 1982 debris flow (Carrara and O'Neill, 2003; Ciervo et al., 2017; Zhang et al., 2019). Meanwhile, the influence of climatic events on the growth disturbance in tree rings should cover all the local trees rather than only the trees on the debris flow path. Hence, combined with satellite images, the growth disturbance in trees on the debris flow deposit from 1970 to 2012 was used to identify the debris flow that occurred in 1982.

The disturbance of 19 trees in 1982 was attributed to a relatively large debris flow. Considering several random growth disturbances occurred in specific years (i.e., the years 1710 and 1860 in QYG2314 in contrast to the years 1742 and 1810 in QYG2324) and their similar characteristics with those of 1982 (Figure 4), we suggest that the hitting of small blocks on the trees (or so-called rockfall) probably played an important role in those random disturbances because no large debris flow was observed around the sampled trees from the satellite image from 1970. However, we noted that there were some other random growth disturbances without typically identified characteristics in the sampled trees (e.g., 32 tree rings from 1970 to 2012 in Figure 5 and some unlabeled in Figure 11). We do not have enough confidence to attribute all of the growth disturbance events to rockfalls or landslides, instead of the fact possibly demonstrating that complex factors control the growth

disturbance of tree rings in natural slopes (Carrara and O'Neill, 2003; Ciervo et al., 2017; Zhang et al., 2019). Research on the characteristics of growth disturbance controlled by different factors (e.g., geohazard, climatic forcing, or insect outbreaks) is a worthwhile future endeavor.

Our main objective in the study of the relationship between time to recover the initial width of disturbed tree rings and kinematic energy was to reveal the possible pattern of the relationship. Possible errors in the relationship dominate uncertainties in our numerical simulation of debris flow because we lacked precise topography data before 1982, which significantly controls the simulation results of debris flow. We tried to reduce the uncertainty by checking the 1970 satellite images and adjusting the current high-resolution DEM data from the surrounding terrains based on our previous experience (Sun et al., 2021). In addition, the errors due to uncertainties in debris flow simulation likely have more influence on the specific exponent value than the relationship pattern of the negative power function (Figure 11A). Accordingly, the degree of uncertainty in the numerical simulation of debris flow does not alter our conclusions about the possible coupling pattern of growth disturbance in tree rings and the kinematic energy of debris flow. Furthermore, because it is difficult to obtain sufficient data on disturbed tree rings to build a more convincing relationship, the negative power function obtained in this study is raw. This means that the relationship is full of so-called epistemic uncertainty compared with the real one (Wang et al., 2014).

5 Conclusion

In this study, we applied an approach for dating debris flow by a dendrogeomorphic technique and evidence of occurrence on remote sensing images, which was applied to identify the debris flow in QYM that occurred in 1982 in northeastern Tibet. Using clear boundaries of debris flow on remote sensing images before and after 1982 and a depth-integrated continuum model, we reconstructed the process of the 1982 debris flow and obtained the kinematic energy of the debris flow.

1. We observed two growth disturbance patterns in tree rings influenced by the 1982 debris flow, including growth suppression and asymmetric growth. By quantitative measurement of annual widths of tree rings in 1981 and 1982 from Qilian junipers, the maximum growth suppression ratio of tree rings influenced by the 1982 debris flow was 91%, while the minimum was 51%, with an average value of 73% (σ=0.16). The lasting time for disturbed tree rings by the 1982 debris flow to recover their initial width was from 5 to 26 years, with an average of 12 (σ=0.46) years.
2. Using simulated kinematic energy of the 1982 debris flow impacting the sampled trees, we obtained a raw negative exponential relationship between the kinematic energy of debris flow and time to recover the initial width of disturbed tree rings. The negative exponential relationship could be used to roughly estimate the time for specific trees to recover their initial state after an energy-calculated debris flow hazard.

By combining numerical simulation and remote sensing, the present study allows us to clarify the relationship between time to recover the initial width of disturbed tree rings and the kinematic energy of debris flows. However, field tests of how debris flow impacts trees and long-term monitoring of growth disturbance in tree rings are needed to build a more reliable relationship and revise the conclusion in our study in the future. Meanwhile, the monthly and annual resolution of precipitation data does not allow for a satisfactory explanation of the debris flow triggering conditions. More precise data on precipitation are needed to explore the effect of precipitation on the debris flow in QYM.

Data availability statement

The raw data supporting the conclusion of this article will be made available by the authors, without undue reservation.

Author contributions

XW: Conceptualization, Data curation, Formal Analysis, Funding acquisition, Investigation, Methodology, Supervision, Writing–original draft, Writing–review and editing. JS: Data curation, Formal Analysis, Investigation, Methodology, Visualization, Writing–original draft, Writing–review and editing. YZ: Data curation, Investigation, Methodology, Software, Writing–original draft. QJ: Data curation, Investigation, Methodology, Writing–original draft. SQ: Funding acquisition, Resources, Supervision, Validation, Writing–original draft. RW: Data curation, Investigation, Methodology, Software, Writing–original draft. HL: Data curation, Investigation, Methodology, Software, Writing–original draft. MZ: Data curation, Project administration, Visualization, Writing–original draft.

Funding

The author(s) declare financial support was received for the research, authorship, and/or publication of this article. This research was supported by the Strategic Priority Research Program of the Chinese Academy of Sciences (Grant No. XDA23090402), the China Natural Science Foundation (Grant Nos 42172304 and 41977392), and the Second Tibetan Plateau Scientific Expedition and Research Program (STEP) (Grant No. 2019QZKK0904).

Acknowledgments

We thank Wenling An and Chenxi Xu for their help with the dendrogeomorphic technique.

Conflict of interest

The authors declare that the research was conducted in the absence of any commercial or financial relationships that could be construed as a potential conflict of interest.

Publisher's note

References

Bao, Y., Zhang, Y., Chen, J., Su, L. J., Li, Y. C., Zhang, X. D., et al. (2023b). Numerical investigation of river blocking process of Gangda paleolandslide at the upstream reaches of the Jinsha River, Tibentan Plateau. *Landslides* 20, 1865–1882. doi:10.1007/s10346-023-02078-8

Bao, Y. D., Su, L. J., Chen, J. P., Ouyang, C. J., Yang, T., Lei, Z. H., et al. (2023a). Dynamic process of a high-level landslide blocking river event in a deep valley area based on FDEM-SPH coupling approach. *Eng. Geol.* 319, 107108. doi:10.1016/j.enggeo.2023.107108

Brang, P. (2001). Resistance and elasticity: promising concepts for the management of protection forests in the European Alps. *For. Ecol. Manag.* 145, 107–119. doi:10.1016/S0378-1127(00)00578-8

Butler, D. R., Oelfke, J. G., and Oelfke, L. A. (1986). Historic Rockfall Avalanches, Northeastern Glacier National Park, Montana, U.S.A. *U.S.A. Mt. Res. Dev.* 6, 261. doi:10.2307/3673396

Carrara, P. E., and O'Neill, J. M. (2003). Tree-ring dated landslide movements and their relationship to seismic events in southwestern Montana, USA. *Quat. Res.* 59, 25–35. doi:10.1016/S0033-5894(02)00010-8

Casana, J. (2020). Global-Scale Archaeological Prospection using CORONA Satellite Imagery: automated, Crowd-Sourced, and Expert-led Approaches. *J. Field Archaeol.* 45, S89–S100. sup1. doi:10.1080/00934690.2020.1713285

Ciervo, F., Rianna, G., Mercogliano, P., and Papa, M. N. (2017). Effects of climate change on shallow landslides in a small coastal catchment in southern Italy. *Landslides* 14, 1043–1055. doi:10.1007/s10346-016-0743-1

Cook, E. R., and Kairiukstis, L. A. (1990). *Methods of dendrochronology: applications in the environmental Sciences*. Dorefrecht: Kluwer Academic Publishers.

Crosta, G. B., and Clague, J. J. (2009). Dating, triggering, modelling, and hazard assessment of large landslides. *Geomorphology* 103, 1–4. doi:10.1016/j.geomorph.2008.04.007

Dorren, L. K. A., and Berger, F. (2006). Stem breakage of trees and energy dissipation during rockfall impacts. *Tree Physiol.* 26, 63–71. doi:10.1093/treephys/26.1.63

Grissino-Mayer, H. D. (2001). Evaluating crossdating accuracy-a manual and tutorial for the computer program COFECHA. *Tree-Ring Res.* 2, 205–221.

ISRM (1979). Suggested methods for the quantitative description of discontinuities in rock masses. *Int. J. Rock Mech. Min. Sci. Geomechanics Abstr.* 16, 22. doi:10.1016/0148-9062(79)91476-1

Iverson, R. M., and Ouyang, C. (2015). Entrainment of bed material by Earth-surface mass flows: review and reformulation of depth-integrated theory. *Rev. Geophys.* 53, 27–58. doi:10.1002/2013RG000447

Johnson, K., Nissen, E., Saripalli, S., Arrowsmith, J. R., McGarey, P., Scharer, K., et al. (2014). Rapid mapping of ultrafine fault zone topography with structure from motion. *Geosphere* 10, 969–986. doi:10.1130/GES01017.1

Lopez Saez, J., Corona, C., Stoffel, M., Astrade, L., Berger, F., and Malet, J.-P. (2012). Dendrogeomorphic reconstruction of past landslide reactivation with seasonal precision: the Bois Noir landslide, southeast French Alps. *Landslides* 9, 189–203. doi:10.1007/s10346-011-0284-6

Loye, A., Jaboyedoff, M., and Pedrazzini, A. (2009). Identification of potential rockfall source areas at a regional scale using a DEM-based geomorphometric analysis. *Nat. Hazards Earth Syst. Sci.* 9, 1643–1653. doi:10.5194/nhess-9-1643-2009

Ma, S., Xu, C., Shao, X., Zhang, P., Liang, X., and Tian, Y. (2019). Geometric and kinematic features of a landslide in Mabian Sichuan, China, derived from UAV photography. *Landslides* 16, 373–381. doi:10.1007/s10346-018-1104-z

Noguchi, K., Tsou, C.-Y., Ishikawa, Y., Higaki, D., and Wu, C.-Y. (2021). Tree-Ring Based Chronology of Landslides in the Shirakami Mountains, Japan. *Water* 13, 1185. doi:10.3390/w13091185

Ouyang, C., An, H., Zhou, S., Wang, Z. W., Su, P. C., Wang, D. P., et al. (2019a). Insights from the failure and dynamic characteristics of two sequential landslides at Baige village along the Jinsha River, China. *Landslides* 16, 1397–1414. doi:10.1007/s10346-019-01177-9

Ouyang, C., He, S., Xu, Q., Luo, Y., and Zhang, W. (2013). A MacCormack-TVD finite difference method to simulate the mass flow in mountainous terrain with variable computational domain. *Comput. Geosciences* 52, 1–10. doi:10.1016/j.cageo.2012.08.024

Ouyang, C., Wang, Z., An, H., Liu, X., and Wang, D. (2019b). An example of a hazard and risk assessment for debris flows—A case study of Niwan Gully, Wudu, China. *Wudu, China, Eng. Geol.* 263, 105351. doi:10.1016/j.enggeo.2019.105351

Pánek, T. (2015). Recent progress in landslide dating. *Prog. Phys. Geogr. Earth Environ.* 39, 168–198. doi:10.1177/0309133314550671

Perret, S., Dolf, F., and Kienholz, H. (2004). Rockfalls into forests: analysis and simulation of rockfall trajectories ? considerations with respect to mountainous forests in Switzerland. *Landslides* 1. doi:10.1007/s10346-004-0014-4

Qi, S., Xu, Q., Lan, H., Zhang, B., and Liu, J. (2010). Spatial distribution analysis of landslides triggered by 2008.5.12 Wenchuan Earthquake, China. *Eng. Geol.* 116, 95–108. doi:10.1016/j.enggeo.2010.07.011

Schneuwly, D. M., and Stoffel, M. (2008). Spatial analysis of rockfall activity, bounce heights and geomorphic changes over the last 50 years – A case study using dendrogeomorphology. *Geomorphology* 102, 522–531. doi:10.1016/j.geomorph.2008.05.043

Šilhán, K. (2021). A new tree-ring-based index for the expression of spatial landslide activity and the assessment of landslide hazards. *Geomatics, Nat. Hazards Risk* 12 (1), 3409–3428. doi:10.1080/19475705.2021.2011790

Šilhán, K. (2017). Evaluation of growth disturbances of Picea abies (L.) Karst. to disturbances caused by landslide movements. *Geomorphology* 276, 51–58. doi:10.1016/j.geomorph.2016.10.005

Šilhán, K., Prokešová, R., Medveďová, A., and Tichavský, R. (2016). The effectiveness of dendrogeomorphic methods for reconstruction of past spatio-temporal landslide behaviour. *CATENA* 147, 325–333. doi:10.1016/j.catena.2016.07.035

Stoffel, M. (2006). A Review of Studies Dealing with Tree Rings and Rockfall Activity: the Role of Dendrogeomorphology in Natural Hazard Research. *Nat. Hazards* 39, 51–70. doi:10.1007/s11069-005-2961-z

Stoffel, M., Butler, D. R., and Corona, C. (2013). Mass movements and tree rings: A guide to dendrogeomorphic field sampling and dating. *Geomorphology* 200, 106–120. doi:10.1016/j.geomorph.2012.12.017

Stoffel, M., Schneuwly, D., Bollschweiler, M., Lièvre, I., Delaloye, R., Myint, M., et al. (2005). Analyzing rockfall activity (1600–2002) in a protection forest—a case study using dendrogeomorphology. *Geomorphology* 68, 224–241. doi:10.1016/j.geomorph.2004.11.017

Stokes, M. A., and Smiley, T. L. (1968). *An introduction to tree-ring dating*. China: University of Arizona Press.

Sun, J., Wang, X., Liu, H., and Yuan, H. (2021). Effects of the attitude of dominant joints on the mobility of translational landslides. *Landslides* 18, 2483–2498. doi:10.1007/s10346-021-01668-8

Van Den Eeckhaut, M., Muys, B., van Loy, K., Poesen, J., and Beeckman, H. (2009). Evidence for repeated re-activation of old landslides under forest. *Earth Surf. Process. Landforms* 34, 352–365. doi:10.1002/esp.1727

Wang, X., Frattini, P., Crosta, G. B., Zhang, L., Agliardi, F., Lari, S., et al. (2014). Uncertainty assessment in quantitative rockfall risk assessment. *Landslides* 11, 711–722. doi:10.1007/s10346-013-0447-8

Wang, X., Liu, H., and Sun, J. (2021). A new approach for identification of potential rockfall source areas controlled by rock mass strength at a regional scale. *Remote Sens.* 13 (5), 938. doi:10.3390/rs13050938

Wistuba, M., Malik, I., Gärtner, H., Kojs, P., and Owczarek, P. (2013). Application of eccentric growth of trees as a tool for landslide analyses: the example of Picea abies Karst. in the Carpathian and Sudeten Mountains (Central Europe). *Catena111* 111, 41–55. doi:10.1016/j.catena.2013.06.027

Woltjer, M., Rammer, W., Brauner, M., Seidl, R., Mohren, G. M. J., and Lexer, M. J. (2008). Coupling a 3D patch model and a rockfall module to assess rockfall protection in mountain forests. *J. Environ. Manage* 87, 373–388. doi:10.1016/j.jenvman.2007.01.031

Wu, J. H., and Ping-Hsuan Hsieh, P. H. (2021). Simulating the postfailure behavior of the seismically-triggered Chiu-fen-erh-shan landslide using 3DEC. *Eng. Geol.* 287, 106113. doi:10.1016/j.enggeo.2021.106113

Zhang, Y., Stoffel, M., Liang, E., Guillet, S., and Shao, X. (2019). Centennial-scale process activity in a complex landslide body in the Qilian Mountains, northeast Tibetan Plateau, China. *CATENA* 179, 29–38. doi:10.1016/j.catena.2019.03.036

frontiers | Frontiers in Earth Science

TYPE Original Research
PUBLISHED 27 December 2023
DOI 10.3389/feart.2023.1257440

OPEN ACCESS

EDITED BY
Chong Xu,
Ministry of Emergency Management, China

REVIEWED BY
Danqing Song,
South China University of Technology, China
Yiding Bao,
Chinese Academy of Sciences (CAS), China
Xiaoyi Shao,
Institute of Geology, China Earthquake Administration, China
Jiewei Zhan,
Chang'an University, China

*CORRESPONDENCE
Wenjie Huang,
hwenjie@mail.cgs.gov.cn

RECEIVED 12 July 2023
ACCEPTED 30 October 2023
PUBLISHED 27 December 2023

CITATION
Cai J, Huang W and Yang Q (2023), Detailed investigation and analysis of the dynamic evolutionary process of rainstorm debris flows in mountain settlements: a case study of Xiangbizui Gully.
Front. Earth Sci. 11:1257440.
doi: 10.3389/feart.2023.1257440

Detailed investigation and analysis of the dynamic evolutionary process of rainstorm debris flows in mountain settlements: a case study of Xiangbizui Gully

Jiajun Cai[1,2,3], Wenjie Huang[2,3,4]* and Quanzhong Yang[5]

[1]Research Center of Applied Geology of China Geological Survey, Chengdu, China, [2]Institute of Exploration Technology, Chinese Academy of Geological Sciences, Chengdu, China, [3]Technical Center for Geological Hazard Prevention and Control, Chinese Academy of Geological Sciences, Chengdu, China, [4]Chengdu Huajian Geological Engineering Technology Co Ltd., Chengdu, China, [5]Sichuan Province Geological Engineering Co Ltd., Chengdu, China

Short-term heavy rainfall often causes large-scale rainstorm debris flows in mountainous areas of Southwest China. Aiming to investigate the accumulation and movement of potential source material for the formation of debris flow hazards under extreme short-term heavy rainfall, this paper takes the Xiangbizui debris flow gully, Southwest China, as a case study. A detailed field engineering and geological investigation was carried out on the valley characteristics, formation conditions, provenance types, distribution range, loose solid material reserves that can be transformed into debris flows, and characteristics showing the variation in the grain size of the accumulated solids along the gully to further explore the characteristics of rainstorm-induced debris flow movement. The dynamic processes of debris flow movement and accumulation are numerically simulated to analyze the maximum velocity, accumulation height, range of influence, and evolutionary process based on the theory of continuous media of the approximate Voellmy solution and a high-precision three-dimensional model. The results indicated that rainstorms and steep terrain are the main factors stimulating debris flows. The amount of loose solid material in the channel is approximately 1550.61 × 10^4 m^3, and the dynamic material reserves are approximately 396.41 × 10^4 m^3. The maximum flow depth and velocity are approximately 3.5 m/s and 13 m/s, respectively, which mainly occur in the upper and middle reaches of the channel and in the accumulation fan at the outlet of the channel. The evolutionary process of the debris flow includes four stages: a 0–1,500 m initial acceleration stage, a 1,500–2,200 m fast forward movement stage, a 2,200–3,400 m acceleration stage in the middle and lower reaches, and a 3,400–4,300 m deceleration and end of accumulation stage. The research findings can provide a scientific basis and strong support for risk assessment and avoidance, as well as prevention and control of debris flows in mountainous areas with severe climate change.

KEYWORDS

rainstorm debris flow, numerical analysis, process of accumulation movement, numerical simulation, field investigation

1 Introduction

Debris flows, which are sudden hazards in mountainous areas, are characterized by a fast flow, high flow, intense energy for carrying solid materials, and high destructive force, making them one of the primary categories of geohazards in Southwest China and worldwide (Tang et al., 2012; Hu et al., 2014; Ni et al., 2014; Gao and Sang, 2017; Liu et al., 2020; Chen and Song, 2021; Chen et al., 2023; Chen and Song, 2023). With recent global climate change, rainfall-induced debris flow disasters feature high volumes and concentrations of rainfall, extreme solid rainfall, a unimodal shift in rain patterns, and short durations. Debris flow frequently lead to severe impacts and significant losses to the economic production and lives of residents (Chen and Song, 2021; Chen et al., 2023; Chen and Song, 2023). Examples include the multiple outbreaks of debris flows in the Xiangbizui gully in Southwest China on 23 October 2017, 26 June 2018, 11 July 2018, and 18 May 2019. Among these, the larger-scale debris flow on 18 May 2019, flushed out approximately 1.3×10^4 m^3 of solid material at once, causing a road blockage, a river blockage, and blockage of a road culvert under construction, which led to direct economic loss. Thus, analyzing debris flow hazards and predicting the debris flow distance and flooding extent to propose prevention and control measures are of great importance for national road access as well as human safety in the study area (Collins, 2008; Jakob et al., 2012; Thouret et al., 2020).

The general approach to examining debris flows is a statistical evaluation and dynamic analysis based on data from regional surveys of water sources, physical sources, and circulation conditions. Such approaches have high confidence in the results but are costly and cumbersome, and numerical simulations with parameter correction can also provide a rational analysis (Canuti et al., 1999; Thiebes, 2012). Utilizing a new generation of geographic information systems (GISs) combined with theoretical modeling of two-phase fluid analysis of debris flows to simulate the debris flow movement and accumulation process, as well as providing critical parameters for the later evaluation of debris flow hazard zoning and prevention, are the current research areas and difficulties in the theoretical study of debris flows, as well as the design of engineering prevention and control (Xu et al., 2021; Chen et al., 2023). As a nonhomogeneous mixed medium, debris flows have complex physical processes and kinetic characteristics. With the development and maturity of computer technology, numerical algorithms, and intrinsic models, numerical simulation has been the primary way to characterize debris flow motion (Harris et al., 2009; Fischer-Kowalski et al., 2011; Ciurean et al., 2017). By establishing numerical models of debris flows with numerical analysis methods, the initiation, flow, and accumulation processes of debris flows are simulated. The obtained results reveal the movement process of debris flows with the help of data and graphics, which can be used as references for debris flow disaster prevention and planning and design of controlling measures (Christen et al., 2010; Zhou et al., 2013; Gan and Zhang, 2019; Zhang et al., 2019; Musumeci et al., 2021).

Dynamic modeling is one of the current research approaches to predicting debris flow movement and accumulation; it generally employs numerical techniques to simulate debris flow transport and accumulation processes using energy and motion conversion laws (Kang et al., 2022; Wang et al., 2022). For different debris flow dynamics issues, Bao et al. (2021) compared and investigated the Eulerian method, the CEL method, and the FEM-SPH method based on the Abaqus software in landslide barrage simulation by applying the method of fluid-solid coupling a coupled fluid-solid coupling (Bao et al., 2021). Liu et al. (2021a) proposed a complex fluid-particle-structure interaction impact estimation model a coupled fluid-particle-structure numerical model for predicting debris flow propagation and building structural damage using the coupled SPH-DEM-FEM method (Liu et al., 2021). Bao et al. (2023a) proposed a new SPH integrated 3D numerical method for quantitatively evaluating and solving the problem of 3D debris flow dynamic simulation process (Bao et al., 2023a). Kong et al. (2022) used a coupled physically based computational fluid dynamics (CFD) and discrete element method (CFD-DEM) to numerically analyse the different blocking mechanisms of flexible, slit and rigid blocking two-phase geophysical flows (Kong et al., 2022). Bao et al. (2023b) used a coupled finite discrete element method-smoothed particle hydrodynamics (FDEM-SPH) approach to reconstruct a three-dimensional model of a weir landslide and simulate its dynamic process and proposed an evolutionary mechanism of high level flow-like landslide-induced waves in a deep valley (Bao et al., 2023b).

The constant medium dynamic model is based on hydrodynamics and uses the material–motion–energy dissipation conversion equation to describe the dynamic process of a debris flow. Therefore, the continuum model can more rationally portray the kinematic properties of the solid material of a debris flow and is thus widely used (Tang et al., 2023). Massflow adopts a depth integral-based numerical analysis method of continuous medium mechanics, which can reveal the whole process of the temporal and spatial evolution of landslides, debris flows, flash floods, and other mountain hazards and simplifies the three-dimensional computational problem into two dimensions, effectively improving the computational efficiency (Huang et al., 2022). In particular, it has been applied in debris flow research, featuring a fast speed, large scale, and scalability (Hungr et al., 1984; Ouyang, 2021; Li et al., 2022). Related applications have been used in dam failure debris flow simulation, risk assessment, and calculation of parameters, such as the maximum rise height, impact force, flow depth, and flow velocity, to enable debris flow simulation and prediction of movement characteristics under complex terrain conditions (Ouyang et al., 2015; Wu and Lan, 2020; Zhu et al., 2023).

Despite extensive research on the mechanism of debris flow movement, fluidization and accumulation characteristics, as well as numerical simulation, owing to the relative lack of basic geological and research data, detailed investigations on the characteristics of channel siltation and accumulation of material sources during the process of debris flow movement have not been carried out. Moreover, the simulated movement of debris flows has relatively poor accuracy due to complicated topographic conditions at the sites where debris flows develop and the inability to conduct large-scale and high-precision topographic mapping in the whole basin area. Therefore, we identify the detailed source conditions of debris flow formation based on indoor data collection and field investigation in this paper, including the source type, distribution range, storage of loose solids that can be transformed into debris flows, and the changes in the solid accumulation size of debris flows along the channel. In addition, the 1:50,000 high-resolution topographic data

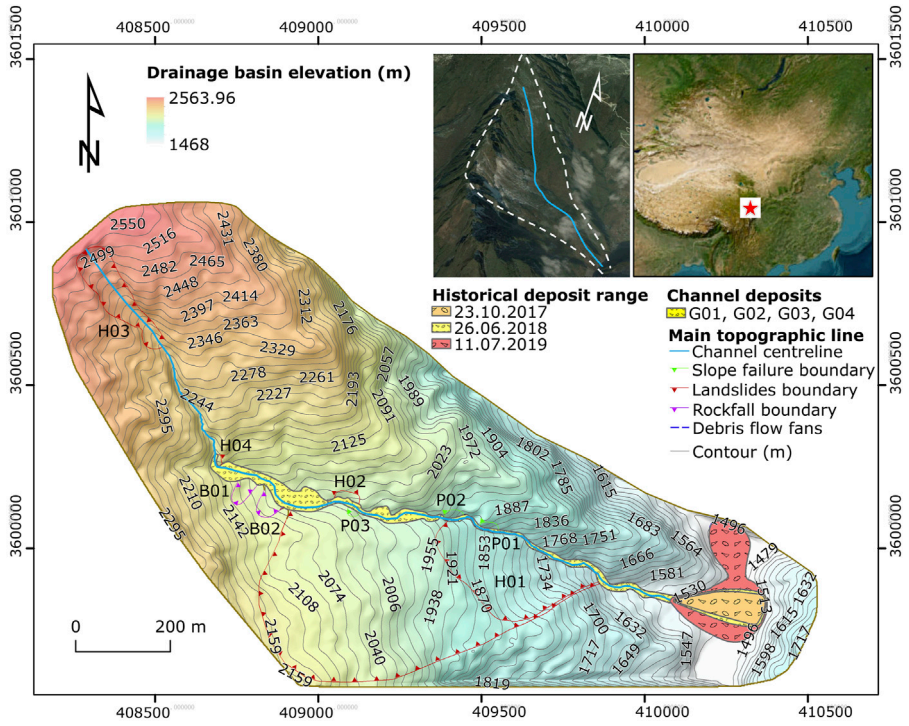

FIGURE 1
Regional location and basic developmental characteristics of the debris flow channel in Xiangbizui Gully, Southwest China (1:50,000 watershed topographic data derived from high-resolution UAV (Phantom 4 RTK) photogrammetry. The coordinate system uses the China Geodetic Coordinate System 2000).

of the Nose Mouth Gully are combined with the Voellmy numerical analysis model to conduct numerical simulations of the movement characteristics of a storm-type debris flow, revealing the dynamics of the debris flow accumulation process, flooding extent, and accumulation thickness. The research results can not only provide a reference for debris flow disaster prevention and control in mountainous areas affected by climate change but also supply computational methods for in-depth research on storm-induced debris flows in the future.

2 Background

The Xiangbizui gully is located in Pingwu County, Sichuan Province, Southwest China. The geographic coordinates of the mouth of the ditch are 104° 2′41.93“E, 32° 31′7.76“N (Figure 1). The drainage area is 2.55 km^2, and it is mainly 4.45 km in length, with a maximum elevation of approximately 3,145 m and an outlet elevation of 1,484.6 m. Intersecting the main Tiger River, the relative height difference reaches 1,660 m, and the average slope drop of the main ditch is 358.9‰.

The topography of the upper part of the gully is steeply inclined, the middle and lower parts of the gully are narrow, and steep local canyons are present. Following the characteristics showing each stage of movement of the gully and the topography, the gully channel mainly consists of three parts: the material source area, circulation area, and accumulation area. The material source area primarily comprises medium alpine landslides; the area is prone to landslides, channel blockages during rainfall and channel scouring due to the loose material structure. The channel of the flow area is narrower compared to that in the source area, with a greater slope and less vegetation on both sides of the channel, which quickly causes undercutting of the channel and increases the scale of the debris flow disaster. Finally, the accumulation area is located in the outlet channel, where the debris flow washed out of the outlet and deposited itself in the area, forming a large-scale debris flow accumulation fan.

2.1 Geological environment

The research area lies on the eastern edge of the high mountain–valley zone in the transition from the Qinghai-Tibet Plateau to the Sichuan Basin; the area is doubly influenced by the southeast and southwest monsoons and the cold air of the Tibetan Highlands, and the climate elements are vertically distributed according to the change in altitude. Consequently, the precipitation is highly variable, with an average annual rainfall of 806.0 mm, and is unevenly distributed, with May to September accounting for 80% of the annual rainfall within the region.

The central river valleys and valley slopes have widely distributed loose accumulations of the Quaternary system. They have experienced multiperiod glacial activities in the Quaternary period, with glacial geomorphic relics, moraines, and ice-water

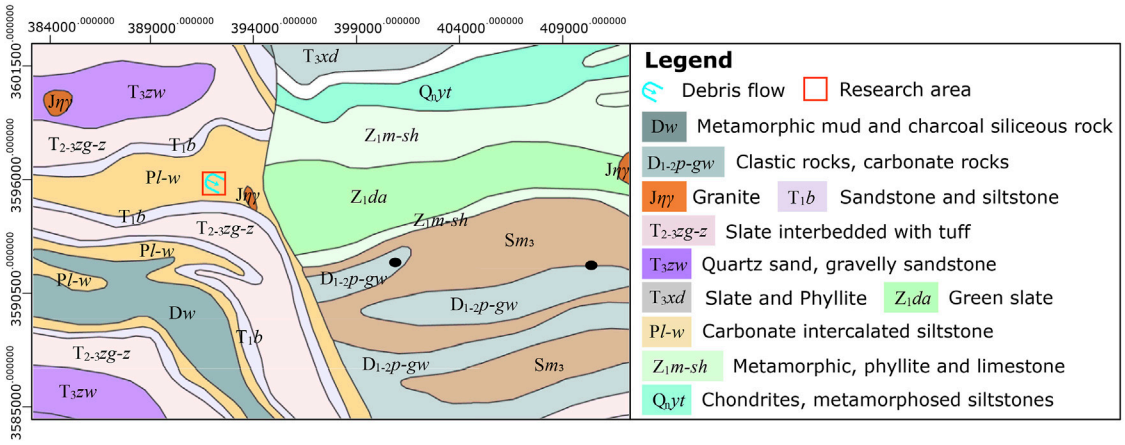

FIGURE 2
Regional stratigraphic background of the Xiangbizui debris flow gully (The coordinate system uses the China Geodetic Coordinate System 2000).

deposits. The types of Quaternary deposits in the riverbeds and terraces of the main channel and its tributaries is complex and include alluvial deposits, flood deposits, moraines, ice and water deposits, and crumbling slope deposits. The most widely distributed metamorphic rocks in the area are mainly metamorphic sandstone and sandy slate, followed by crystalline greywacke and migmatite. In the river valleys and valley slopes, there are loos Quaternary accumulations caused by metamorphic rock weathering and accumulation. The causes of Quaternary accumulations in channels, riverbeds and terraces are complicated, and these accumulations include alluvial and floodplain types (Figure 2).

2.2 Historical development

The debris flow ditch erupted on 23 October 2017, 26 June 2018, 11 July 2018, and 18 May 2019. On 23 October 2017, a large-scale burst occurred as a slide, and the one-off volume of material washed out by the debris flow was approximately 1.3×10^4 m^3, causing road blockage, river blockage, and under-construction road culvert blockage, resulting in direct economic losses of approximately 800,000 yuan. On 26 June 2018, Pingwu County, Hu Ya Tibetan Township, experienced a heavy rainfall that lasted approximately 4 h. Then, the debris flow ditch once again initiated the debris flow, which washed out approximately 1.0×10^4 m^3 of material, resulting in the blockage of roads and river channels, and buried roads, overwater culverts and retaining walls. As of 11 July 2018, the area again suffered from a heavy rainstorm, which continued for approximately 6 h, and precipitation exceeded 100 mm, triggering the breakdown of a debris flow in this debris flow channel and creating a pile-up of approximately 1.5×10^4 m^3 material at the ditch outlet. Initiating large-scale debris flows on 18 May 2019, the channel again flushed out nearly 50,000 square meters of solid material, destroying high-voltage line pylons, burying farmhouses, and washing away 600 m of road. In addition, an extensive debris flow jammed the Tiger River, posing a threat to the Tiger Township field town approximately 1.5 km downstream.

3 Methods

3.1 Detailed investigation of field engineering geology

Combining the emergency field investigation of typical debris flow cases in Xiangbizui with relevant regional geological background and related literature, field geological survey statistics and unmanned aerial vehicles (UAVs) were used. The UAV equipment model and postprocessing software were Phantom 4 RTK and PhotoScan, respectively. The specific processing flow included image import, alignment (estimation of the camera position and overlap position), creation of point clouds, 3D models, DEMs, and orthophotos. To observe, record, and describe the internal structural characteristics of the flow phase in a typical profile of the primary channel and determine the topographic, geomorphic and water source conditions of debris flow formation, as well as the movement and scale of debris flows, 6 groups of particle size distribution tests on the debris flow deposit were completed; these tests were conducted on samples from the areas of formation, circulation, and accumulation of debris flows to reveal the particle size distribution, superposition characteristics, and genetic characteristics of debris flow deposits.

3.2 Numerical analysis

Based on a gridded the DEM of before and after debris flow occurrence in Xiangbizui Gully, the modeling and numerical analysis of debris flow movement and accumulation processes were carried out by using the improved finite difference principal fluid dynamics method; important characteristic parameters, such as the fluid movement velocity, maximum accumulation thickness, accumulation range, and evolutionary process of the thickness, were obtained. As a result, the stages of debris flow movement in Xiangbizui Gully were identified and divided.

In the continuum model, the debris flow fluid is assumed to be an unstable and heterogeneous fluid that can be characterized by the

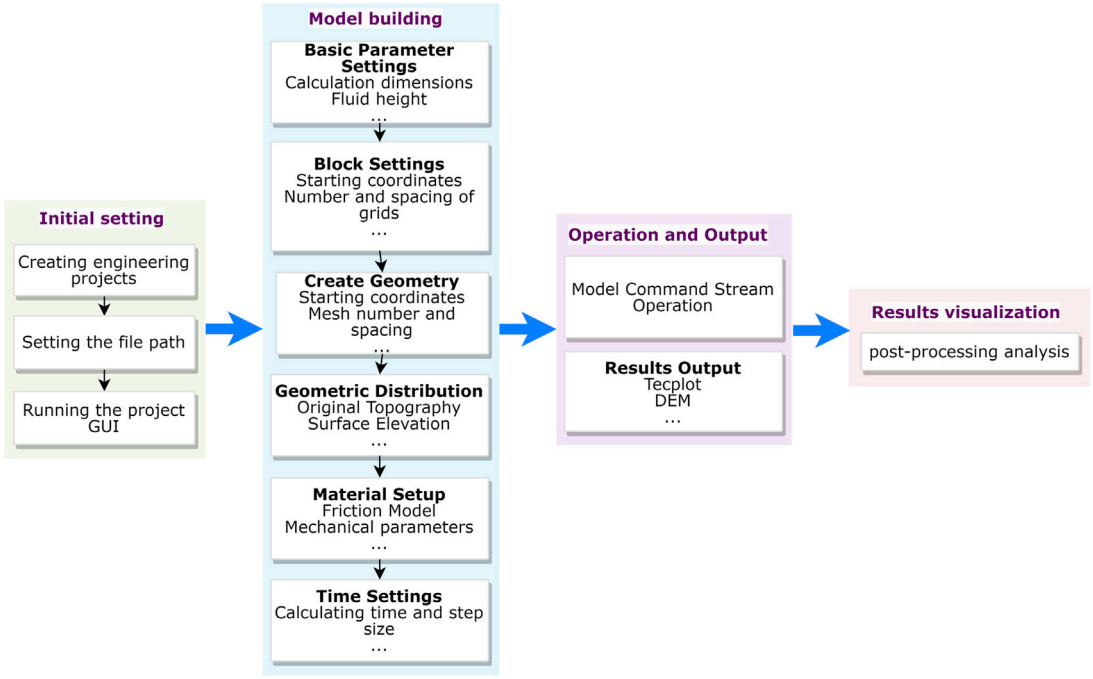

FIGURE 3
Construction and flow of the numerical simulation model of the study area.

average velocity U (x, y, t) (Savage and Hutter, 1989; Ouyang et al., 2015):

$$\mathrm{U}(x,y,t) = \left[U_x(x,y,t), U_y(x,y,t)\right]^T \tag{1}$$

where Ux and Uy are the velocities in the x and y directions, respectively. T is the transpose matrix of the average velocity. The magnitude of the speed can be defined as:

$$\|\mathrm{U}\| = \sqrt{U_x^2 + U_y^2} \tag{2}$$

where $\|\mathrm{U}\|$ indicates taking the absolute average of the velocity U, which ensures that U is strictly positive in vector space, and the direction of the fluid velocity can be defined by unit vector n_u:

$$n_u = \frac{1}{\|U\|} = \left(U_x, U_y\right)^T \tag{3}$$

The Voellmy rheological model is represented by the following mass balance formula:

$$\partial_t H + \partial_x (HU_x) + \partial_y \left(HU_y\right) = Q(x,y,t) \tag{4}$$

where $H(x, y, t)$ is the fluid height. $Q(x, y, t)$ represents the mass sources. When $Q = 0$, it means that no matter is deposited. The average fluid depth equilibrium equation in the x and y directions can be expressed as:

$$\partial_t (HU_x) + \partial_x \left(C_x HU_x^2 + g_z k_{a/p} \frac{H^2}{2}\right) + \partial_y \left(HU_x U_y\right) = S_{gx} - S_{fx} \tag{5}$$

where C_x and C_y are the cross-section coefficients and g_z is the acceleration of gravity in the vertical direction. In the Voellmy model, the vertical contact relationship can be defined as the heterogeneous Mohr–Coulomb relationship, and $k_{a/p}$ is the coefficient of the earth pressure, which is formulated by the following equation:

$$k_{a/p} = tan^2\left(45° \pm \frac{\varphi}{2}\right) \tag{6}$$

where φ is the internal friction angle of the debris flow fluid. Integrating the above equations, the Voellmy rheology equation can be derived as:

$$\frac{d(Uh)}{dt} = (z \cdot n)nh - k(\Delta h)h - \left[\mu(z \cdot n)h + \frac{1}{\xi}U^2\right]s \tag{7}$$

where the variables are measured by length L, speed $(gl)/2$, and time $(L/g)/2$ to obtain a unified Froude value. The gravity vector z = (0, 0, −1), and the perturbation coefficient is defined by the formula $\zeta'=\xi/g$ and has no dimension. The detailed operations and processes of the model are shown in Figure 3.

4 Research results

4.1 Flushing and siltation characteristics

The area of clear water in the upper reaches of Xiangbizui Gully and its branch ditches generally has a significant slope, mostly approximately 40°, and the longitudinal slope of valleys is steep (generally greater than 400‰) (Figure 4A). The characteristics of the movement of substantial uplift determine the regional crustal movement. In addition, the catchment area is large, the branches and shallow ditches are developed, and the channel is narrow. These

FIGURE 4
The circulation area in the upper **(A)** and lower **(B)** sections of the formation area and the accumulation fan at the outlet **(C)**.

characteristics make sediment in this area converge rapidly under rainfall, and the runoff that forms has a high velocity and scouring ability of solid material. Therefore, the features created by scouring and silting in areas where clear water converges are characterized by scouring.

The scouring and silting characteristics of the area where clear water converges have an overall longitudinal gradient in the circulation area formed by the Xiangbizui debris flow of approximately 438.24‰, with a slope of approximately 25° (Figure 4B). Therefore, a steep–gentle–steep terrain change appears in the channel. The terrain of the upper section of the circulation area from 2,531 m to 215 m is also steep, with a longitudinal gradient of more than 350‰; in this area, a large landslide is present, and it is the primary source of the debris flow that broke out on 18 May 2019. The middle section of the circulation area that formed lies in the middle reaches, where the terrain is gradual and the longitudinal gradient is approximately 220‰. The channel is bayonet-shaped, which leads to the accumulation of solid materials, so this channel has mainly siltation characteristics. The lower section of the flow area is narrow and steep, with a longitudinal gradient of the channel bed of 647‰. At the same time, multiple scarps are present in the channel, most of which are bedrock. Consequently, this terrain is conducive to the accelerated movement of debris flows, and this channel section has mainly erosional characteristics.

The height difference of the area with alluvial siltation in the accumulation area is approximately 350 m, with a 65.4 m channel length and only a 167.8‰ specific longitudinal drop. Its accumulation fan is developed, and much debris flow material is accumulated in it. Thus, the alluvial characteristics of this section of the channel are predominantly those of siltation. The debris flow formed a large alluvial fan at the beginning of the channel. The fan is 200 m long and 200 m wide, with an average thickness of approximately 7.0 m and a volume of approximately 28×10^4 m^3 (Figure 4C).

The analysis of the morphology of the debris flow accumulation fan and the characteristics of the extrusion of the main river indicate that Xiangbizui Gully is a relatively old debris flow trench. The topography of the debris flow accumulation area is trumpet-shaped, with the front edge directly reaching the Tiger River. The front edge is 150–200 m in width, and the back part is 30–50 m long, with a vertical length of 200 m (Figure 4C). The total area of the accumulation fan is approximately 0.04 km^2, and the mound thickness is approximately 7–10 m, accounting for approximately 28×10^4 m^3 of mounded material. Since the survey work is focused on the perspective of debris flow management, no special survey work has been arranged to explore the history of debris flow formation and development, and the changes in the mound fan structure are complex. More intense human farming activities make studying its mounded superposition relationship and analysis very difficult. Hence, the present investigation is based only on the ground survey and mapping, and some superficial speculations are proposed based on the relationship of stacking and superposition of the mounded fan body.

4.2 Compositional analysis of the particles in the deposit

To examine the particle size of sediments in the channel pile, the method is to collect soil samples from 0 to 50 cm in the surface layer for a field sieving test and obtain the weight and percentage of

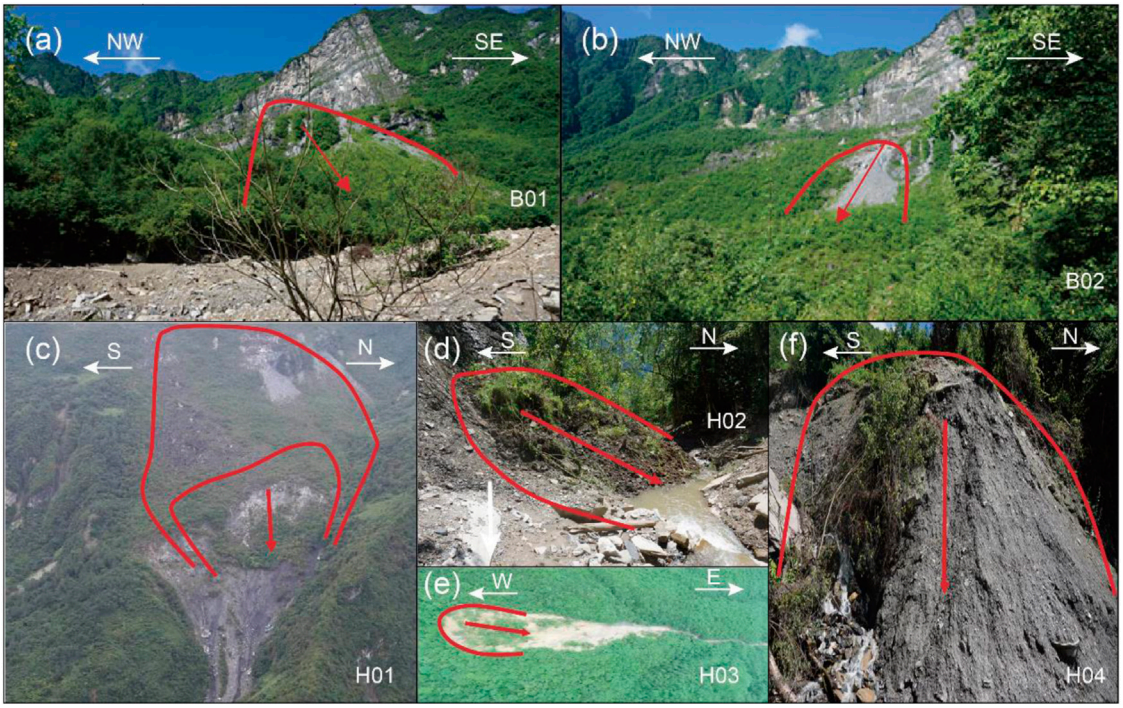

FIGURE 5
Main source types and distribution characteristics of debris flows in Xiangbizui Gully.

particles with sizes of <5 mm, 5–20 mm, 20–50 mm, 50–100 mm, 100–150 mm, 150–200 mm, and >200 mm, as well as those in other particle classes. Some of the sieved soil samples with particle sizes <5 mm were then sent to the laboratory for further sieve tests, and the results of field sieving and indoor tests were integrated to calculate the percentages of particles of different particle sizes, as shown in Table 1.

The chart shows that the grain size distribution of the debris flow reflects the hydrodynamic conditions and scouring and depositional characteristics of different gully sections, which is basically consistent with the field investigation results; this is mainly reflected in all the test results reflecting a large rock-to-soil ratio, with the maximum ratio of 84.4:15.6 being the result of the particle size analysis in the upper section of the accumulation area of Xiangbizui channel ditch 04. The lowest value is 78.5:21.5 in the midstream 05 region of the circulation area, with a sizeable rock-to-soil ratio; the further downstream the ditch is, the weaker the hydrodynamic conditions are, and the further upstream the ditch is, the stronger the hydrodynamic conditions are.

Xiangbizui Gully has abundant and reliable open source areas for debris flows. The distribution of sources is relatively concentrated, and they are mainly distributed in the 2,531–1,550 m section of the ditch and both sides of the ditch. There are 13 source points that were investigated in this research, and the source types mainly include landslides, collapse accumulations, slope erosion sources, and trench accumulation sources (Figure 5). Moreover, the areas where the channel does not have large avalanches and landslides were calculated as light erosion areas. According to the survey statistics, the total amount of accumulated solid material in the trench is 15.22×10^4 m^3, and the dynamic storage volume that may be involved in debris flow activities is 4.84×10^4 m^3. A total of 1521.81×10^4 m^3 of loose material was obtained from the avalanche slide, and the dynamic storage volume that may be involved in debris flow activity was approximately 386.91×10^4 m^3. The erosion sources on the slope surface totaled 13.58×10^4 m^3, and the dynamic storage volume that may be involved in debris flow activities was 4.6×10^4 m^3. Therefore, 1550.61×10^4 m^3 of loose solid material was available, and 396.41×10^4 m^3 of dynamic storage volume may be involved in debris flow activities.

4.3 Water source conditions

Regarding topography and geomorphology, the relative height differences in the Xiangbizui drainage basin are significant, the terrain is steep, and the longitudinal slope of the ditch is vast, which is conducive to the collection of debris flow materials and resulting disasters. For the material source conditions, the total accumulation of more material in the ditch, which is now the open ditch that houses a solid material amount of 439.68×10^4 m^3, may be involved in debris flow activities that fill a dynamic storage volume of 56.05×10^4 m^3; this is equivalent to 35 times the annual 20 debris flows per year; the critical rainfall intensity of debris flows may be reduced. Therefore, both the frequency and scale of debris flow outbreaks may increase. A future debris flow in the main ditch will occur once every 1–5 years. In the future, as vegetation recovers and some of the material sources stabilize, its frequency may gradually decrease. Accordingly, it is estimated that approximately 2 debris flow disasters may occur within 20 years of the designed lifespan, and the amount of solid material that washes out is approximately 4.62×10^4 m^3.

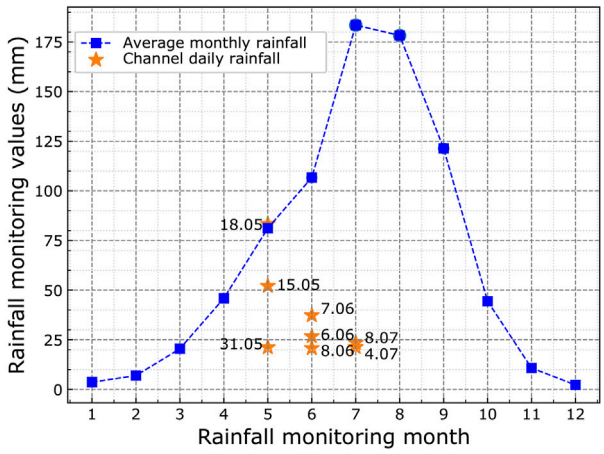

FIGURE 6
Annual rainfall and rainfall in the flood season in Xiangbizui Gully.

The primary water source for debris flows in Nose Mouth Gully is atmospheric precipitation. Since debris flows occur in the rainy season, snow and ice meltwater in spring generally do not become water sources for debris flows. In addition, the channel area is not enriched in groundwater; hence, it does not constitute the primary water source for debris flows, and no reservoirs, lakes, or other concentrated surface water bodies exist in the channel area. Therefore, surface runoff from heavy rainfall is the primary water source and stimulus for debris flows.

Precipitation statistics according to the 2019 rainfall data in the district show that the rainfall in the Xiangbuzui ditch is low but relatively concentrated, often occurring with localized geographically defined rainstorms and hail, and precipitation is concentrated in the rainy season (May to September) (Figure 6), which accounts for 80% of the annual rainfall. Based on the contour map attached to the "Manual for the Calculation of Storm Floods in Small- and Medium-sized Watersheds in Sichuan Province", the average values of 1/6, 1, 6, and 24 h multiyear maximum rainfall in the study area are 9.0, 12.5, 33, and 45 mm, respectively. Under the condition of p=2%, the rain intensities at 1/6, 1, 6, and 24 h can reach 22.32, 26.88, 59.4, and 86.4 mm, respectively. For p=5%, the 1/6, 1, 6, and 24 h rain intensities reach 18.27, 22.75, 52.47, and 75.15 mm, respectively, while the latest debris flow disaster in Xiangbuzui Gorge received 83.3 mm of rainfall, far exceeding the pre-disaster rainfall. However, the distribution is relatively sparse despite the seasonal snow accumulation in the upper reaches. Thus, snow and ice meltwater are used only as water conditions for forming debris flows, while heavy rainfall mobilizes mud. Moreover, the slopes of the upper part of the valley and each side of the valley accelerate the runoff and accumulation of surface precipitation, providing favorable water conditions for the formation of Xiangbizui Gully.

4.4 Dynamic numerical simulation

4.4.1 Process of flow movement at depth

This research simulated the debris flow movement in Xiangbizui Gully under actual rainfall frequencies using Massflow software and obtained the flow velocity, mud depth, and characteristics of mound fan movement of this debris flow ditch at this frequency. Three modes of topographic data in the Massflow model are z+h, z-h, and z+surface, and they are used for geometric assignment; this numerical simulation is based on the post-slide DEM of the landslide in Nixu village. Then, the topography raster data before the landslide are subtracted from the topography raster data after the landslide (the size and range of both raster elements should be kept the same) to obtain the topography raster data h within the slide area. However, the original topographic conditions were not input into the digital elevation model (DEM) and image data because the Xiangbigou debris flow trench is located in a high mountain canyon area, and many outbreaks of short-duration heavy rainfall-type debris flows occur in the trench. Therefore, a raster interpolation method is used to recover the undamaged terrain with a high-precision digital elevation model that shows the flow from UAV aerial photography. Finally, a raster image element size of 2 m*2 m is obtained for the preslippage terrain raster data. Due to the limitation of computational performance, the study resampled the numerical computation grid accuracy to 7 m×7 m, the number of computational grids ranks 335*212, giving a total of 71,020 grids, a time interval of 50 s, and a total computation time of approximately 6 h.

To select a suitable friction model and corresponding motion parameters for the numerical simulation of debris flows in Xiangbigou and to research and compare debris flow events with similar conditions for disasters in this area, the Voellmy base friction model and three parameters, namely, debris flow bulk density γ, friction coefficient μ and turbulence coefficient ξ, which are the most suitable for the actual situation, are selected. The paper used the debris flow deposits at the five locations in Table 1 to mix the debris flow slurry with the floodwater in the ditch, mix the slurry into the debris slurry consistency, weigh it, and measure the volume of the slurry on-site, and then calculating its gravity as the gravity of the debris flow fluid according to the "Specification for Debris flow Hazard Prevention and Control Engineering Investigation" (DZ/T0220--2006) (Varnes, 1958; Geological and Environmental Department of the Ministry of Land and Resources, 2006; Hungr et al., 2014). The friction coefficient (μ) and turbulence coefficients (ζ) were determined by preferential calibration of the model parameters using the methodology of Luna et al. (2011) and Liu et al. (2021) (Luna et al., 2011; Liu et al., 2021). The judgment was based on the iterative selection of the parameters until the simulation results matched the observed characteristics with the velocity and height of the debris flow along the channel (Luna et al., 2011). The debris flow γ = 1800 kg/m^3, μ = 0.25, and ζ= 200 (m/s^2); the total simulation time is 2,400 s, and different mud depths, flow intensities, and accumulation ranges of debris flows are obtained. The simulation results show that the maximum flow depth of the debris flow reaches 2.5 m in the first 100 s and 3 m within 300 s. The flow velocity is fast, the flow accumulates in front of the impact fan at the gully mouth, and then the accumulation velocity slows down. The final accumulation thickness is approximately 3.5 m. After 600 s of simulation, the source material is transformed into fluid, moves downstream along the channel, and accumulation accelerates at the accumulation fan at the groove mouth. At 900 s, the thicknesses of some fluids in the upper reaches of the debris flow channel gradually decrease, and the thickness of the fan accumulation gradually

TABLE 1 Statistical analysis of the particle composition of the deposit in Xiangbizui Gully.

Sample site	Particle size range (%) (mm)										Rock-to-soil ratio
	>60	60–40	40–20	20–10	10–2	2–0.5	0.5–0.25	0.25–0.075	0.075–0.005	<0.005	
Downstream of the accumulation area	41.1	10.2	13.1	11.3	8.5	4.7	5.2	3.1	2.7	0.1	84.2:15.8
Middle section of the accumulation area	31.7	15.2	19	10.2	7.7	5.1	4.7	3.9	2.4	0.1	83.8:16.2
Formation in the lower section of the circulation area	38.5	10.2	16.7	7.7	11.3	5.2	3.9	3.2	3.1	0.2	84.4:15.6
	39.1	9.4	14.2	13.6	7.5	7	5.5	2.8	0.8	0.1	83.8:16.2
Middle section of the formation circulation area	37.1	8.4	11.4	13.2	8.4	6.5	5.3	4.7	4.9	0.1	78.5:21.5
Upper section of the formation circulation area	38	10.4	16.3	13.5	6.2	5.7	4.4	3.8	1.5	0.2	84.4:15.6

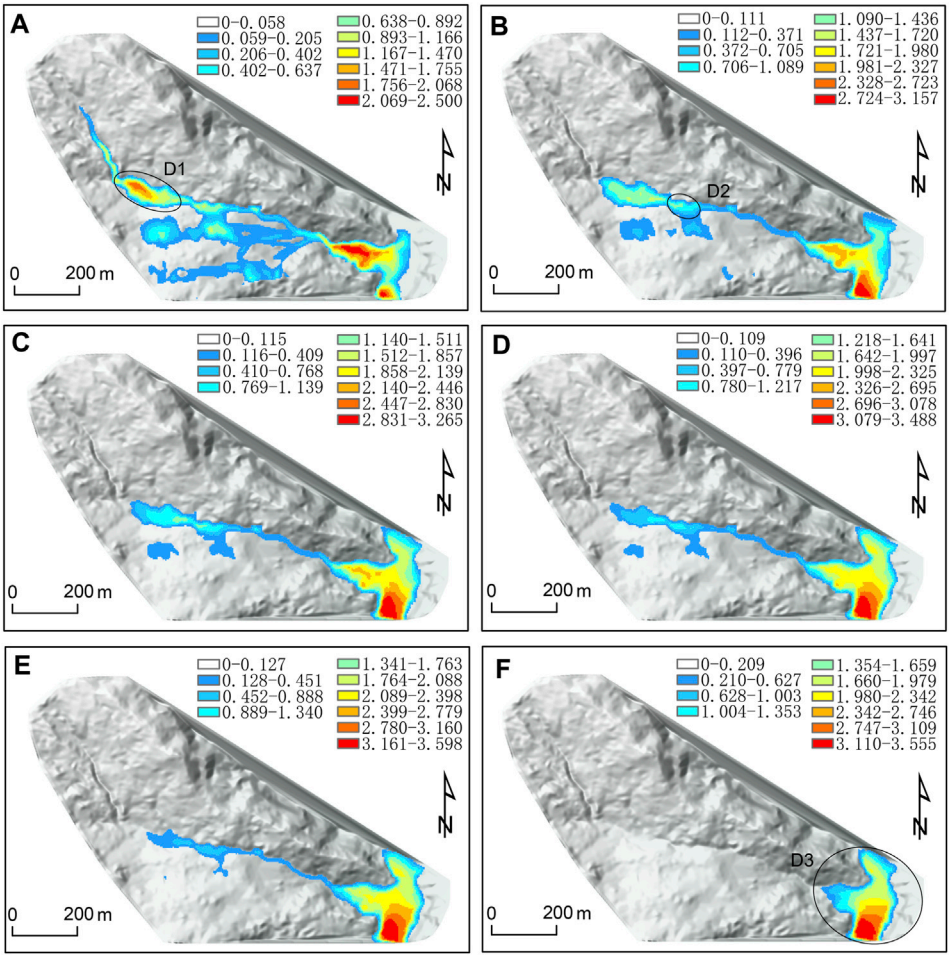

FIGURE 7
Variation in debris flow depth (m) in Xiangbizui Gully at different times.

increases and begins to progressively diffuse. At 1,200 s, most of the fluid accumulates in the channel mouth and slowly accumulates, and the maximum flow depth in the channel decreases to less than 1 m. At 2,400 s, debris flow movement ends, and the maximum flow depth of the accumulation fan diffuses outward and is reduced compared with that at 1,200 s. In this simulation, the maximum flow

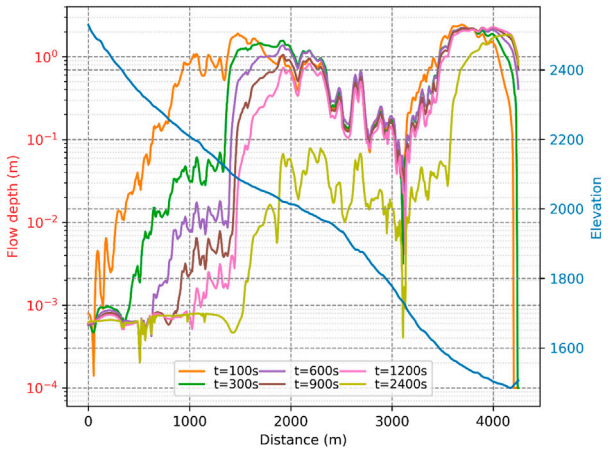

FIGURE 8
Evolutionary process of the fluid flow depth in the channel and response of topographic elevation during 6 monitoring periods along the channel.

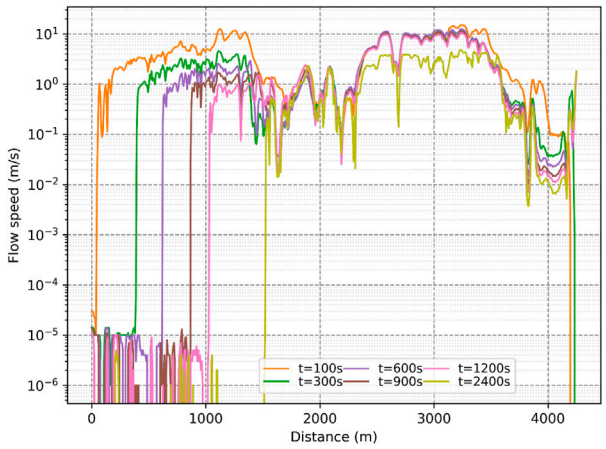

FIGURE 9
Evolutionary process of the flow velocity along the channel at different times.

depth in the debris flow movement is as high as 9. 6 m. In the process of fluid movement, the debris flow direction is consistent with the process of movement. From the starting point of the H03 landslide, the source material first flows into the formation area, forming initial accumulation area D1; from the starting point of the H02 landslide, material flows into the gully accumulation area, creating accumulation fan D2. After that, the material in accumulation area D1 and the landslide at starting point H02 further meet in the circulation–formation area in the middle of the debris flow gully, and the debris flow depth and velocity all show an enhancement effect based on superposition; this effect accelerates the speed (c-e) of debris flow movement in the lower section of the gully. After moving to the gully mouth, the open terrain causes the debris flow to stabilize and accumulate rapidly, forming the final typical fan-shaped accumulation area D3 (Figure 7). The measured area and volume of the deposition fan resulting from the latest debris flow event in Xiangbigou are compared with the numerical simulation results under actual rainfall frequencies. The results show that the measured area of the deposition fan is 0.04 km^2, the deposition fan's depth and numerical simulation area are 0.377 km^2, and the simulation accuracy of the stacking depth reaches 92%.

The curve showing the evolution of the accumulated thickness in the longitudinal section of the main gully obtained from the raster data of the fluid depth in the debris flow gully at different times shows that the accumulated thickness in the longitudinal section of the main gully changes most drastically within 0–100 s; the maximum thickness appears at distances of 0–1.5 and 3.2–3.6 km in the gully formation area, which occurs in the stage of rapid transformation of gravitational potential energy into kinetic energy of the sliding body. After t = 300 s the maximum accumulated thickness in the channel increases over time, its speed of decline slows down obviously, and its ability to move forward gradually weakens, but the accumulation depth deepens. When t=600–1200 s, the maximum accumulated thickness in the channel is approximately 1.3 m, and the change in the accumulated thickness in the source region of the channel decreases obviously, but the range of change is smaller than that in the whole front edge of the accumulation fan. When t=2,400 s, the comparison of the thickness evolution curves shows that the residual fluid in the front edge of the accumulation fan has stopped moving overall, the distance of horizontal movement has reached the maximum value of 4.45 km, and the accumulated thickness in the whole accumulation area no longer changes, reaching the final accumulation form (Figure 8).

4.4.2 Flow speed effects along the channel

To further study and compare the velocity change when the fluid moves to each position in the longitudinal section of the gully, the velocities at all monitoring points in the main gully in six periods are extracted along the main gully containing the debris flow, and the curve showing the velocity change (Figure 9) is generated. The results show that the overall velocities of the fluid are approximately 0–13 m/s within 0–100 s. The velocity is relatively high during the whole flow process, and the range of distance of the sliding body movement can be monitored at the upstream position of the corresponding source area as 0–1,300 m. During 100–300 s, the distribution begins to disperse and the velocity begins to decrease due to the expansion of the range of fluid accumulation in the channel and the synchronous expansion of the range of fluid velocity. The region with higher velocity is the transition between the upstream front edge of the channel and the source area, and the maximum velocity of the sliding body remains at 0–8 m/s during this period. From 300 to 600 s, the velocity of the fluid decreases obviously from the leading edge to the trailing edge, and the velocity of the leading edge decreases to approximately 5 m/s. At 600–1,200 s, the maximum velocity of the leading edge of the sliding body drops to less than 1 m/s. When t=2,400 s, the velocity at the stacking fan in the valley drops to zero, and only the residual sliding body in the source region maintains a certain flow velocity. During 300–6,000 s, the leading edge of the source region and the flow region upstream of the channel have the longest fluid movement time, and the peak velocities are 0–8 m/s. Moreover, there are oscillations in velocity in the distance range of 0–1,000 m, which may be related to the different phases of the flow of debris flow itself, which may show some instability during the initiation and acceleration of the debris flow.

Through the above analysis, the whole process of debris flow movement from initiation to stoppage can be divided into four stages: the starting and accelerating stage of the fluid body is in the range of 0–1,500 m upstream of the main channel, and the maximum velocity reaches 13 m/s in this period. During 1,500–22,200 m, the sliding body moves forward rapidly, the maximum velocity of the sliding body is approximately 1 m/s, and the horizontal movement distance reaches 700 m. At 2,200–3,400 m, the fluid accelerates to the middle and lower reaches of the channel, and the horizontal movement distance reaches the maximum of 1,200 m, which is the core stage of the long-distance movement of fluid. During 3,400–4,300 m, as the flow velocity gradually slows, the accumulated thickness in most areas of the accumulation fan continuously accumulates to 3.5 m, and the front edge of the debris flow stops moving and reaches the final accumulation state.

5 Discussion

The relative height difference in the upper reaches of the Xiangbizui Gully channel is approximately 1660.4 m, and the average gradient of the main channel is 358.9‰. The terrain is steep, and the longitudinal slope of the valley is large, which provides favorable topographic conditions for the development of debris flows. The regional structure has an area of strong uplift, and the undercutting valley and erosion of the side are strong, which increases the erosion of the debris flow gully. The vegetation coverage in the basin is generally high, with an average vegetation coverage rate of approximately 70%. The recent (2019 debris flow) range of debris flow scouring and silting in the valley is approximately 2 m, and the debris flow activity intensity is high. Metamorphic sandstone, phyllite, limestone, loose Quaternary residual slope deposits, colluvium, ice water deposits, etc., are mainly exposed in the area. The total reserves of loose materials along the ditch are abundant, and the average thicknesses of loose materials in the sand-producing area are 1–55 m. The slope of the gully bank is generally greater than 30, and the shape of the gully valley is V-shaped, which is beneficial to the convergence of source material and source water and the formation of debris flows. The degree of gully blockage is average. In addition, slippage in the area, side erosion of the gully bank, and re-transport of loose material at the bottom provide abundant solid source conditions for the occurrence of debris flows, while good catchment conditions and sufficient hydrodynamic forces in the gully provide better water source conditions for the development of debris flows, thereby providing basic requirements for the formation of debris flows.

According to a previous investigation, four large-scale debris flows occurred in Xiangbizui Gully on 23 October 2017, 26 June 2018, 11 July 2018, and 18 May 2019. Among them, the latest incident had an occurrence period of once in 50 years, with a 24-h rainfall of 83.3 mm, which caused a large-scale debris flow in the gully. The debris flow rushed out of the gully mouth and buried the highway for approximately 600 m, and the debris flow volume was approximately 5×10^4 m^3. The debris flow rushed into the Huya River, which is the main river, blocking the Huya River. According to the classification, i.e., high-frequency debris flows (multiple times a year to once every 5 years), medium-frequency debris flows (1 time/5–20 years), low-frequency debris flows (1 time/20–50 years), and extremely low-frequency debris flows (>1 time/50 years), the debris flows in this gully are classified as high-frequency debris flows. In the debris flow formation area, loose materials, such as mud and sand, are collected in valleys under the action of concentrated rainfall. Because the fluid contains much sediment, has a large specific gravity, and the relative height difference in the basin is large, the terrain is steep, the potential energy is converted into kinetic energy during collection, the flow velocity is fast, and the ability to impact erosion is strong. Because of its rapid erosion, the sediment forms the foot of the gully bank slope in the circulation area, which leads to a large area of gully bank slippage, and the loose source material quickly replenishes to the fluid. In addition, its downward erosion is intense, and the loose deposits at the original gully bottom also enter the debris flow, rapidly increasing the content of solid matter in the fluid (Ouyang et al., 2013).

The scale of a debris flow is mainly related to the accumulation and dynamic changes in loose solid source material in the gully and the rainstorm causing the debris flow. When loose solid source material accumulates more in gullies and encounters concentrated rainstorms, large-scale debris flow disasters often occur (Nettleton et al., 2005; Hungr and McDougall, 2009; Iverson and Ouyang, 2015; Wang et al., 2015; Wang et al., 2021). After the occurrence of a debris flow, some solid source material that can participate in a debris flow in the gully area are transported away by the debris flow. According to reconnaissance of the site, there is currently a large amount of loose solid source material that can participate in debris flow activities in the gully area. The solid source material in the gully area accumulates again and encounters heavy rain that can stimulate debris flows, which causes the loose solid materials that can participate in debris flow activities to rush into the accumulation area again. However, the shortening of the debris flow development and occurrence period are important factors influencing the increase in the scale of activity and destruction ability of Xiangbizui Gully.

6 Conclusion

This research adopts a field geological survey, low-altitude unmanned aerial survey (UAV), numerical simulation and other methodologies to explore the characteristics of the development conditions, surface accumulation, and kinematics of the Xiangbizui debris flow gully in southwestern China and mainly draws the following three conclusions:

1) The detailed field results showed that rainstorms and topographic conditions are the main conditions for debris flows, while the scale of the debris flows is primarily correlated with the accumulated volume of loose solid source material in the gully and the dynamics of the triggering conditions. At present, there are a total of 1550.61×10^4 m^3 of loose solid source material in Xiangbizui Gully and 396.41×10^4 m^3 of movable deposits that may be involved in debris flow events; thus, a large-scale debris flow hazard may occur in the case of heavy rainfall.
2) Numerical analysis revealed that the movement and accumulation processes of the Xiangbizui debris flow gully are characterized by remarkable phased flow and uneven

accumulation in the topographic domain. The maximum debris flow depth of approximately 3.5 m is mainly distributed in the gully channel and the accumulation fan at the outlet, and the maximum flow velocity of 13 m/s is concentrated in the middle and upper reaches of the channel where the topography is steep. The whole flow process consists of four stages: initial acceleration, fast forward movement, acceleration, deceleration and stopping.

3) This research was carried out to assess the geo-environmental conditions after the outbreak of debris flows, which were influenced by the variability of local heavy rainfall events in the middle–high zone, and it was hypothesized that new landslide bodies would be formed within the debris flow source area to further replenish the source material. Therefore, the monitoring of debris flows should be increased in the later stage of monitoring and control project operation, and it is necessary to supplement and update the research results according to the specific changing characteristics.

Data availability statement

The original contributions presented in the study are included in the article/Supplementary Material, further inquiries can be directed to the corresponding author.

Author contributions

JC: Investigation, Software, Writing–original draft. WH: Conceptualization, Funding acquisition, Methodology, Visualization, Writing–review and editing. QY: Investigation, Validation, Writing–original draft.

Funding

The author(s) declare financial support was received for the research, authorship, and/or publication of this article. This research was sponsored by the Sichuan Natural Science Foundation Project "Evaluation System of Debris flow Activity in Earthquake Zone Based on Spatial and Temporal Evolution Law" (No. 2023NSFSC0809). The Natural Resources Geological Survey Ministry Integrated Natural Resources Survey Project (Tibetan Plateau Lakes Survey) (No. DD20230509).

Acknowledgments

The authors would like to acknowledge the insightful comments and suggestions of the editor and anonymous referees that were very helpful for an earlier version of the manuscript.

Conflict of interest

Author WH was employed by Chengdu Huajian Geological Engineering Technology Co Ltd.; Author QY was employed by Sichuan Province Geological Engineering Co Ltd.

The remaining author declares that the research was conducted in the absence of any commercial or financial relationships that could be construed as a potential conflict of interest.

Publisher's note

All claims expressed in this article are solely those of the authors and do not necessarily represent those of their affiliated organizations, or those of the publisher, the editors and the reviewers. Any product that may be evaluated in this article, or claim that may be made by its manufacturer, is not guaranteed or endorsed by the publisher.

Supplementary material

The Supplementary Material for this article can be found online at: https://www.frontiersin.org/articles/10.3389/feart.2023.1257440/full#supplementary-material

References

Bao, Y., Su, L., Chen, J., Ouyang, C., Yang, T., Lei, Z., et al. (2023b). Dynamic process of a high-level landslide blocking river event in a deep valley area based on FDEM-SPH coupling approach. *Eng. Geol.* 319, 107108. doi:10.1016/j.enggeo.2023.107108

Bao, Y., Su, L., Chen, J., Zhang, C., Zhao, B., Zhang, W., et al. (2023a). Numerical investigation of debris flow–structure interactions in the Yarlung Zangbo River valley, north Himalaya, with a novel integrated approach considering structural damage. *Acta Geotech.* 18, 5859–5881. doi:10.1007/s11440-023-02079-w

Bao, Y., Sun, X., Zhou, X., Zhang, Y., and Liu, Y. (2021). Some numerical approaches for landslide river blocking: introduction, simulation, and discussion. *Landslides* 18, 3907–3922. doi:10.1007/s10346-021-01725-2

Canuti, P., Casagli, N., and Catani, F. (1999). "Successes and failures in fighting landslides: some experiences from Italy and elsewhere," in *Sub-forum on science and technology in support of natural disaster reduction* (World Meteorological Organization WMO), 89–110.

Chen, Z., and Song, D. (2021). Numerical investigation of the recent Chenhecun landslide (Gansu, China) using the discrete element method. *Nat. Hazards* 105, 717–733. doi:10.1007/s11069-020-04333-w

Chen, Z., and Song, D. (2023). Modeling landslide susceptibility based on convolutional neural network coupling with metaheuristic optimization algorithms. *Int. J. Digital Earth* 16 (1), 3384–3416. doi:10.1080/17538947.2023.2249863

Chen, Z., Song, D., and Dong, L. (2023). An innovative method for landslide susceptibility mapping supported by fractal theory, GeoDetector, and random forest: a case study in Sichuan Province, SW China. *Nat. Hazards* 118, 2543–2568. doi:10.1007/s11069-023-06104-9

Christen, M., Kowalski, J., and Bartelt, P. (2010). RAMMS: numerical simulation of dense snow avalanches in three-dimensional terrain. *Cold Regions Sci. Technol.* 63 (1-2), 1–14. doi:10.1016/j.coldregions.2010.04.005

Ciurean, R. L., Hussin, H., Van Westen, C. J., Jaboyedoff, M., Nicolet, P., Chen, L., et al. (2017). Multi-scale debris flow vulnerability assessment and direct loss estimation of buildings in the Eastern Italian Alps. *Nat. hazards* 85, 929–957. doi:10.1007/s11069-016-2612-6

Collins, T. K. (2008). Debris flows caused by failure of fill slopes: early detection, warning, and loss prevention. *Landslides* 5 (1), 107–120. doi:10.1007/s10346-007-0107-y

Fischer-Kowalski, M., Krausmann, F., Giljum, S., Lutter, S., Mayer, A., Bringezu, S., et al. (2011). Methodology and indicators of economy-wide material flow accounting: state of the art and reliability across sources. *J. Industrial Ecol.* 15 (6), 855–876. doi:10.1111/j.1530-9290.2011.00366.x

Gan, J., and Zhang, Y. S. (2019). Numerical simulation of debris flow runout using Ramms: a case study of Luzhuang Gully in China. *Comput. Model. Eng. Sci.* 121, 981–1009. doi:10.32604/cmes.2019.07337

Gao, J., and Sang, Y. (2017). Identification and estimation of landslide-debris flow disaster risk in primary and middle school campuses in a mountainous area of Southwest China. *Int. J. disaster risk Reduct.* 25, 60–71. doi:10.1016/j.ijdrr.2017.07.012

Geological and Environmental Department of the Ministry of Land and Resources (2006). *Specification for debris flow hazard prevention and control engineering investigation*. DZ/T0220–2006.

Harris, C., Arenson, L. U., Christiansen, H. H., Etzelmüller, B., Frauenfelder, R., Gruber, S., et al. (2009). Permafrost and climate in Europe: monitoring and modelling thermal, geomorphological and geotechnical responses. *Earth-Science Rev.* 92 (3-4), 117–171. doi:10.1016/j.earscirev.2008.12.002

Hu, W., Xu, Q., Van Asch, T. W. J., and Zhu, X. (2014). Flume tests to study the initiation of huge debris flows after the Wenchuan earthquake in SW China. *Eng. Geol.* 182, 121–129. doi:10.1016/j.enggeo.2014.04.006

Huang, G., Lv, G., Zhang, S., Huang, D., Zhao, L., Ni, X., et al. (2022). Numerical analysis of debris flows along the Sichuan-Tibet railway based on an improved 3D sphere DDA model and UAV-based photogrammetry. *Eng. Geol.* 305, 106722. doi:10.1016/j.enggeo.2022.106722

Hungr, O., Leroueil, S., and Picarelli, L. (2014). The Varnes classification of landslide types, an update. *Landslides* 11, 167–194. doi:10.1007/s10346-013-0436-y

Hungr, O., and McDougall, S. (2009). Two numerical models for landslide dynamic analysis. *Comput. geosciences* 35 (5), 978–992. doi:10.1016/j.cageo.2007.12.003

Hungr, O., Morgan, G. C., and Kellerhals, R. (1984). Quantitative analysis of debris torrent hazards for design of remedial measures. *Can. Geotechnical J.* 21 (4), 663–677. doi:10.1139/t84-073

Iverson, R. M., and Ouyang, C. (2015). Entrainment of bed material by Earth-surface mass flows: review and reformulation of depth-integrated theory. *Rev. Geophys.* 53 (1), 27–58. doi:10.1002/2013rg000447

Jakob, M., Stein, D., and Ulmi, M. (2012). Vulnerability of buildings to debris flow impact. *Nat. hazards* 60, 241–261. doi:10.1007/s11069-011-0007-2

Kang, T., Jang, C. L., Kimura, I., and Lee, N. (2022). Numerical simulation of debris flow and driftwood with entrainment of sediment. *Water* 14 (22), 3673. doi:10.3390/w14223673

Kong, Y., Guan, M., Li, X., Zhao, J., and Yan, H. (2022). How flexible, slit and rigid barriers mitigate two-phase geophysical mass flows: a numerical appraisal. *J. Geophys. Res. Earth Surf.* 127 (6), e2021JF006587. doi:10.1029/2021jf006587

Li, Y., Chen, J., Zhou, F., Li, Z., and Mehmood, Q. (2022). Stability evaluation and potential damage of a giant paleo-landslide deposit at the east himalayan tectonic junction on the southeastern margin of the qinghai–tibet plateau. *Nat. Hazards* 111, 2117–2140. doi:10.1007/s11069-021-05132-7

Liu, B., Hu, X., Ma, G., He, K., Wu, M., and Liu, D. (2021b). Back calculation and hazard prediction of a debris flow in Wenchuan meizoseismal area, China. *Bull. Eng. Geol. Environ.* 80, 3457–3474. doi:10.1007/s10064-021-02127-3

Liu, C., Yu, Z., and Zhao, S. (2021a). A coupled SPH-DEM-FEM model for fluid-particle-structure interaction and a case study of Wenjia gully debris flow impact estimation. *Landslides* 18, 2403–2425. doi:10.1007/s10346-021-01640-6

Liu, M., Zhang, Y., Tian, S., Chen, N. S., Mahfuzr, R., and Javed, I. (2020). Effects of loose deposits on debris flow processes in the Aizi Valley, southwest China. *J. Mt. Sci.* 17 (1), 156–172. doi:10.1007/s11629-019-5388-9

Luna, Q. B., Blahut, J., Van Westen, C. J., Sterlacchini, S., van Asch, T. W. J., and Akbas, S. O. (2011). The application of numerical debris flow modelling for the generation of physical vulnerability curves. *Nat. hazards earth Syst. Sci.* 11 (7), 2047–2060. doi:10.5194/nhess-11-2047-2011

Musumeci, R. E., Foti, E., Rosi, D. L., Sanfilippo, M., Stancanelli, L. M., Iuppa, C., et al. (2021). Debris-flow hazard assessment at the archaeological UNESCO world heritage site of Villa Romana del Casale (Sicily, Italy). *Int. J. Disaster Risk Reduct.* 64, 102509. doi:10.1016/j.ijdrr.2021.102509

Nettleton, I. M., Martin, S., and Hencher, S. (2005). *Debris flow types and mechanisms*. Scottish road network landslides study, 45–67.

Ni, H., Zheng, W., Song, Z., and Xu, W. (2014). Catastrophic debris flows triggered by a 4 July 2013 rainfall in Shimian, SW China: formation mechanism, disaster characteristics and the lessons learned. *Landslides* 11, 909–921. doi:10.1007/s10346-014-0514-9

Ouyang, C. (2021). "Massflow—a software for dynamic modeling and risk evaluation of earth-surfaced flow," in *EGU general assembly conference abstracts* (EGU General Assembly), EGU21–14914.

Ouyang, C., He, S., and Tang, C. (2015). Numerical analysis of dynamics of deb-ris flow over erodible beds in Wenchuan earthquake-induced area. *Eng. Geol.* 194, 62–72. doi:10.1016/j.enggeo.2014.07.012

Ouyang, C., He, S., Xu, Q., Luo, Y., and Zhang, W. (2013). A MacCormack-TVD finite difference method to simulate the mass flow in mountainous terrain with variable computational domain. *Comput. Geosciences* 52, 1–10. doi:10.1016/j.cageo.2012.08.024

Savage, S. B., and Hutter, K. (1989). The motion of a finite mass of granular material down a rough incline. *J. fluid Mech.* 199, 177–215. doi:10.1017/s0022112089000340

Tang, C., van Asch, T. W. J., Chang, M., Chen, G., Zhao, X., and Huang, X. (2012). Catastrophic debris flows on 13 August 2010 in the Qingping area, southwestern China: the combined effects of a strong earthquake and subsequent rainstorms. *Geomorphology* 139, 559–576. doi:10.1016/j.geomorph.2011.12.021

Tang, J., Liu, C., and Mao, J. (2023). Numerical simulation and hazard analysis of debris flows in guxiang gully, tibet, China. *Front. Rock avalanche, landslide debris flow hazards Mt. areas* 4, 16648714.

Thiebes, B. (2012). *Landslide analysis and early warning systems: local and regional case study in the Swabian Alb, Germany*. Springer Science and Business Media.

Thouret, J. C., Antoine, S., Magill, C., and Ollier, C. (2020). Lahars and debris flows: characteristics and impacts. *Earth-Science Rev.* 201, 103003. doi:10.1016/j.earscirev.2019.103003

Varnes, D. J. (1958). Landslide types and processe. *Landslides Eng. Pract.* 24, 20–47.

Wang, F., Wang, J., Chen, X., Zhang, S., Qiu, H., and Lou, C. (2022). Numerical simulation of boulder fluid–solid coupling in debris flow: a case study in zhouqu county, gansu Province, China. *Water* 14 (23), 3884. doi:10.3390/w14233884

Wang, Y., Nie, L., Liu, C., Zhang, M., Xu, Y., Teng, Y., et al. (2021). Rainfall warning model for rainfall-triggered channelized debris flow based on physical model test—a case study of laomao mountain debris flow in dalian city. *Water* 13 (8), 1083. doi:10.3390/w13081083

Wang, Z. Y., Lee, J. H. W., and Melching, C. S. (2015). *Debris flows and landslides*. River dynamics and integrated river management, 193–264.

Wu, Y., and Lan, H. (2020). Debris flow analyst (DA): a debris flow model considering kinematic uncertainties and using a GIS platform. *Eng. Geol.* 279, 105877. doi:10.1016/j.enggeo.2020.105877

Xu, W., Wang, S., Qi, W., Li, X., and Wang, C. (2021). Disaster chain analysis of landfill landslide: scenario simulation and chain-cutting modeling. *Sustainability* 13 (9), 5032. doi:10.3390/su13095032

Zhang, N., Matsushima, T., and Peng, N. (2019). Numerical investigation of post-seismic debris flows in the epicentral area of the Wenchuan earthquake. *Bull. Eng. Geol. Environ.* 78, 3253–3268. doi:10.1007/s10064-018-1359-6

Zhou, J., Cui, P., and Yang, X. (2013). Dynamic process analysis for the initiation and movement of the Donghekou landslide-debris flow triggered by the Wenchuan earthquake. *J. Asian Earth Sci.* 76, 70–84. doi:10.1016/j.jseaes.2013.08.007

Zhu, X., Yan, G., and Zhao, Y. (2023). "Disaster assessment and prediction of Gaojiayu landslide based on numerical method," in *Advances in Geology and Resources exploration* (CRC Press), 820–825.

frontiers | Frontiers in Earth Science

TYPE Original Research
PUBLISHED 16 January 2024
DOI 10.3389/feart.2023.1304969

OPEN ACCESS

EDITED BY
Jie Dou,
China University of Geosciences Wuhan, China

REVIEWED BY
Weile Li,
Chengdu University of Technology, China
Chaoying Zhao,
Chang'an University, China
Jian Fang,
Central China Normal University, China

*CORRESPONDENCE
Chong Xu,
xc11111111@126.com
Wentao Yang,
yang_wentao@bjfu.edu.cn

RECEIVED 30 September 2023
ACCEPTED 27 December 2023
PUBLISHED 16 January 2024

CITATION
Liu M, Yang W, Xu C, Yang Y, Taylor L and Shi P (2024), Impact of precipitation on Beishan landslide deformation from 1986 to 2023. *Front. Earth Sci.* 11:1304969. doi: 10.3389/feart.2023.1304969

Impact of precipitation on Beishan landslide deformation from 1986 to 2023

Meng Liu[1], Wentao Yang[1,2,3]*, Chong Xu[4]*, Yuting Yang[1], Liam Taylor[3] and Peijun Shi[5,6]

[1]Three-gorges reservoir area (Jinyun Mountain, Chongqing) Forest Ecosystem National Observation and Research Station, School of Soil and Water Conservation, Beijing Forestry University, Beijing, China, [2]Academy of Plateau Science and Sustainability, People's Government of Qinghai Province and Beijing Normal University, Xining, China, [3]School of Geography, University of Leeds, Leeds, United Kingdom, [4]National Institute of Natural Hazards, Ministry of Emergency Management of China, Beijing, China, [5]Academy of Disaster Reduction and Emergency Management, Ministry of Emergency Management and Ministry of Education, Beijing, China, [6]State Key Laboratory of Earth Surface Processes and Resource Ecology (ESPRE), Beijing Normal University, Beijing, China

Investigating the response of landslide activity to climate change is crucial for understanding the disastrous effects of climate change on high mountains. However, the lack of long-term, spatial–temporal consistent measurement of landslide activity prohibits the study of this relationship. In this work, we used two methods to derive the time series of a landslide's deformation and study its relationship with precipitation in the northeastern Tibetan Plateau. The small baseline subset-interferometric synthetic aperture radar (SBAS-InSAR) method with Sentinel-1A images is first applied to derive time series of the landslide's deformation from 2020 to 2021. A recently developed method to derive cumulative deformations of optical images was used with Landsat 5 and Sentinel-2 images to derive the long-term deformation time series from 1986 to 2023. Centimeter-scale deformations detected by using the InSAR method are mainly located in the upper and eastern parts of the landslide, whereas meter-scale deformations detected by using the optical method are in the middle of the landslide. Time-series results from both methods show that intra-annual initiations of the landslide's deformation occurred in rainy months (from July to October). Although there seems to be no direct relations between inter-annual deformations and precipitation, significant displacements since 2020 occurred after exceptionally wet years from 2018 (with a record-breaking precipitation year in 2020). With optical images, we found that the maximum cumulative deformation of the landslide has been >35 m since 1986 with major deformations (>20 m) found after 2020, which may indicate an imminent risk to the Lijie town near the toe of the landslide. With climate change, increased precipitation is expected in future, which may trigger more similar landslides in the vicinity of this region. This work demonstrates an executable framework to assess landslide hazard risk under climate change.

KEYWORDS

pixel offset tracking, small baseline subset-interferometric synthetic aperture radar, landslide deformation, climate change, landslide simulation

1 Introduction

Landslide hazards are major threats to mountain communities (Froude and Petley, 2018). Due to complex topography, landslides usually act as the initiators of mountain disaster chains (Cook et al., 2018; Qi et al., 2021). For example, the 2000 Yigong landslide in Tibet blocked the Yigong River, forming a giant lake, the dam-breaking flood of which affected downstream regions of hundred kilometers (Delaney and Evans, 2015). In July 2016, another landslide in Tibet triggered the collapse of a moraine lake, which led to a flood disaster of the Sunkoshi River in Nepal and damaged downstream infrastructures such as roads and hydropower plants (Cook et al., 2018). In October and November 2018, the two Baige landslides dammed the Jinsha River and resulted in two mega floods in Yunnan province (Fan et al., 2019; Ouyang et al., 2019; Zhang et al., 2020). In February 2021, the Chamoli ice–rock avalanche in Uttarakhand, India, scraped glacial moraine, triggered a landslide-glacial debris flow (mountain torrent) disaster chain, destroyed two hydropower stations, and caused nearly 200 casualties (Qi et al., 2021). With ongoing climate change and increased human activities in mountains, similar disasters may become common phenomena.

1.1 Studying the impacts of climate change on landslide activities is challenging

The topic of climate change's impact on landslide activities has long been recognized (Gruber et al., 2004; Crozier, 2010). More landslide activities have been expected with higher temperature and intense rainfall under climate change (Ozturk et al., 2022). Although theories have been formulated to explain the mechanisms of landslide due to climate change (Huggel et al., 2012; Ozturk et al., 2022), existing works mainly rely on statistics of regional landslide inventories of a few years (Pei et al., 2023). There are some limitations to use these landslide inventories: 1) most landslides are usually small in size and can only be recognized in very high spatial resolution (VHR) optical images (finer than 1 m), which became widely available in 2000s and not long enough to assess the impact of climate change (Deroin et al., 2012). In addition, frequent acquisitions (e.g., yearly) of VHR images for many years in remote mountains are expensive and very rare, and interpreting landslides from optical images of different spatial resolution could not generate temporally consistent landslide inventories. 2) Establishing regional landslide inventories is labor- and time-consuming. 3) Mapping of landslides is rather subjective depending on the interpreter's' personal experience (Galli et al., 2008; Van Westen et al., 2008). Therefore, there is a lack of long-term, temporally consistent observations of landslide activities that can be used to quantify the impacts of climate change (Patton et al., 2019).

In contrast, measurements of a slow, long-lasting, creeping landslide's deformation could result in more frequent, longer-term observations. In addition, landslide deformation is simpler to study, with all influencing variables being constant (e.g., local slope and lithology), except for climate.

1.2 Synthetic use of optical feature tracking and interferometric synthetic aperture radar (InSAR) has been rarely applied for the same landslide

Based on the principle of radar phase interference, the interferometric synthetic aperture radar (InSAR) algorithm can identify landslide deformation of a few millimeters to centimeters (Meng et al., 2015; Zhang et al., 2020). However, the radar phase interferometry method has the following problems: 1) it is greatly affected by vegetation, and it is difficult to find the same point in densely vegetated areas; 2) the temporal interval between two phase-coherent synthetic aperture radar (SAR) images cannot be too long; otherwise, coherent imaging cannot be obtained; 3) it has difficulty in detecting surface deformation that exceeds a single wavelength in image pairs; 4) the monitoring accuracy is significantly affected by atmosphere conditions, and it is necessary to find a stable area to remove the atmospheric effect (Yang et al., 2018). The small baseline subset (SBAS) technique with multi-SAR images is frequently used to overcome some of the drawbacks of InSAR and to derive time series of surface deformation (Intrieri et al., 2018). Despite this, the deformation detected by using the radar phase interferometry method is a one-dimensional deformation in the radar line of sight (LOS) direction, and it may lead to omissions in complex terrains with single-orbit data.

The sub-pixel offset tracking (POT) of optical images is another commonly used method to invert landslide deformation based on the brightness information of remote sensing images (Liu et al., 2020). POT is simpler to operate when compared to the InSAR method. It could use image pairs of longer time intervals and is better at extracting larger displacement deformation (Yang et al., 2020b). The monitoring accuracy of this method is related to the spatial resolution of the imagery used (Stumpf et al., 2017). In recent years, high spatial resolution remote sensing data have become easier to access, and applications of POT (such as the Co-registration of Optically Sensed Image and Correlation (COSI-Corr) and MicMac) have become more common (Leprince et al., 2007; Bradley et al., 2019; Lacroix et al., 2020). A time series inversion method has recently been proposed to reduce background noise in optical POT results (Bontemps et al., 2018). However, most previous works used either InSAR or optical POT to derive landslide deformation, and few works compared both methods.

In this work, we used SBAS-InSAR and optical POT to study the spatial and temporal deformation of the Beishan landslide in northeast Tibet. Synthetic use of both methods could unveil a holistic picture of the landslide's dynamics and its long-term deformation history and prompt a better understanding of its response to climate change. Our objectives are 1) to reveal and compare the surface deformations of the landslide with SBAS-InSAR and optical POT methods; 2) to analyze deformation dynamics in relation to climate drivers; and 3) to simulate potential disastrous scenarios for a nearby town.

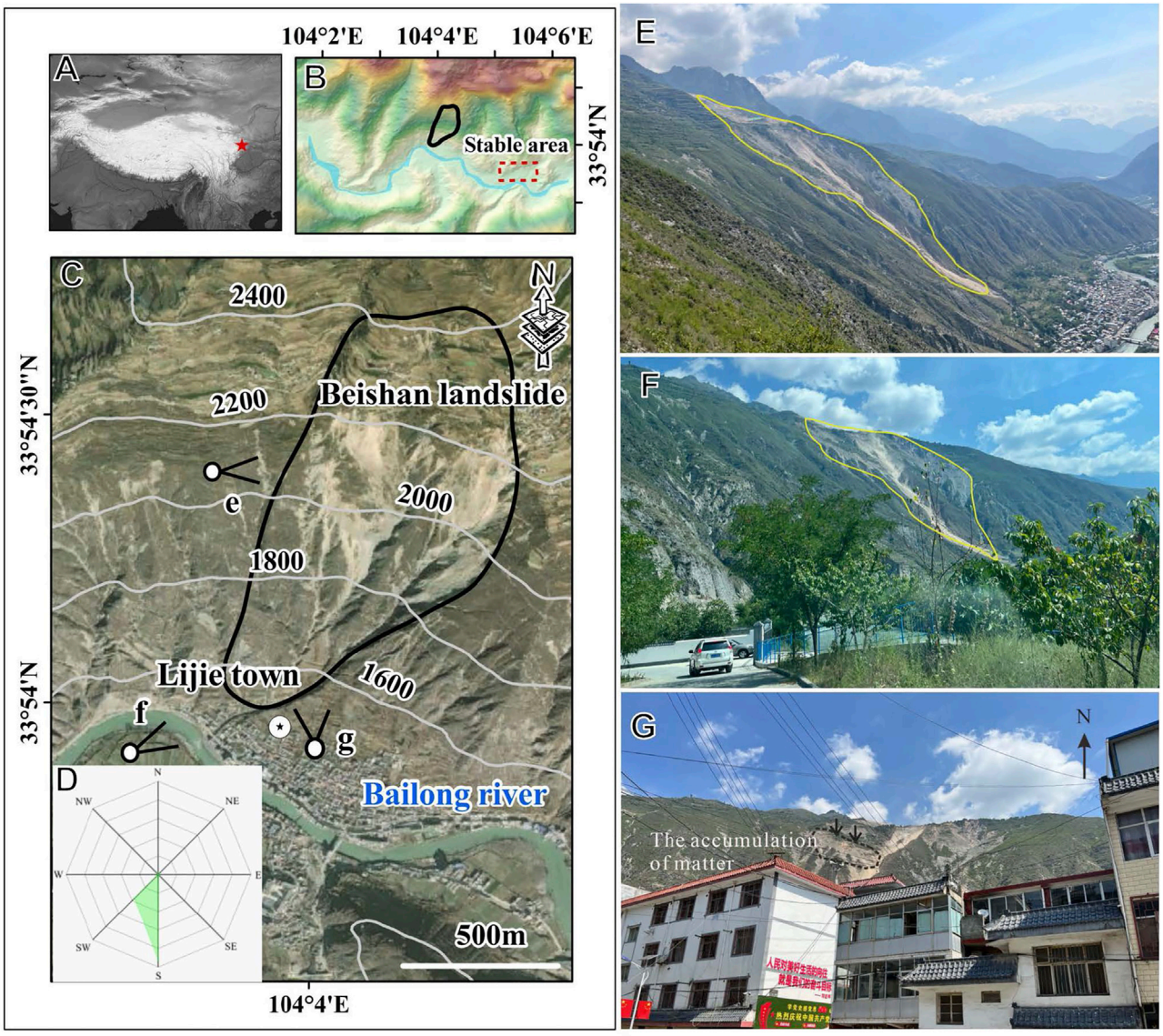

FIGURE 1
Study area **(A–C)**, the Beishan landslide aspect distribution **(D)**, and the field photos **(E–G)**.

2 Study area

In the eastern mountains of the Qinghai–Tibet Plateau, landslide hazards are very active because of the following reasons: 1) deep canyons incised by major rivers are pervasive; 2) tectonic activities are very active, and earthquakes occur frequently; and 3) local lithology is fragmented and fragile (Zhang et al., 2021). The study area is in the northeastern Tibetan Plateau. The study area has a monsoon climate, and the multi-year Global Precipitation Measurement (GPM) shows that the average annual precipitation of the study area is 598.5 mm.

The Beishan landslide in Zhouqu County, Gansu, China, is studied. The Bailong River runs through the study area, and the landslide occurred on the northern bank of the river. The Lijie town is located at the foot of the landslide along the Bailong River (Figure 1). The elevations of the landslide head and the toe are ~2,473 and ~1,582 m, respectively. The aspect of the landslide ranges from 135° to 219°, and the mean aspect is 178°. The landslide body has three major lithologies. The upper part of the landslide is Devonian limestone. The middle part of the landslide is Quaternary loess, and the lower part of the landslide is the Silurian slate and phyllite (Zhong et al., 2022). The surface of the landslide area is covered by sparse xerocolous grass and shrubs. Landslide scarps are clearly visible in optical images of earlier than 2017. The landslide had been reported in previous work, but its deformation was not well-studied (Zhong et al., 2022). The landslide has been slowly moving for a long time. In the past 40 years, it reactivated several times and transferred into debris flows during heavy rains in 1978, 1992, 2010, and 2018. In 1978, reactivation of the landslide damaged many cottages, and the local authorities displaced more than 100 threatened families (Wang et al., 2022). Since August 2020, the landslide has partly reactivated and caused some road collapses in Beishan village near the landslide head.

During 14–20 August 2022, we carried out field work in the study area and took some photos of the Beishan landslide. By interviewing residents, we found some people in the west part of the Lijie town had already moved to other places in awareness of the landslide hazard. Constructions have been implemented by the government at the landslide head to try to stabilize the slope since 2021.

3 Materials and methods

3.1 Rainfall data for 1986 to 2022 and the Mann–Kendall test

In this work, three sets of precipitation data were used. The first set of precipitation data is the GPM. It is a joint satellite mission by the National Aeronautics and Space Administration (NASA) and the Japanese Aerospace Exploration Agency (JAXA) to measure rain and snow every 3 hours globally. GPM data are produced with microwave and infrared precipitation estimates of satellite and precipitation gauge estimates. using the Integrated Multi-satellitE Retrievals for GPM (IMERG) algorithm (Fang et al., 2019). The monthly GPM v6 data used in this work are downloaded from Google Earth Engine, and the data have a spatial resolution of 11,132 m. The monthly GPM v6 data from June 2000 to September 2021 are available. Annual GPM data from 2001 to 2020 were summed from the monthly GPM v6 data.

The second set of precipitation data is the Climate Hazards Group InfraRed Precipitation with Station (CHIRPS) data. It is a quasi-global rainfall dataset from 1981 to the present day. CHIRPS combines 0.05° resolution satellite imagery with field station data to create gridded rainfall time series for trend analysis and seasonal drought monitoring. The CHIRPS rainfall data are daily rainfall data, and we obtained monthly rainfall data from 1986 to 2022 through the Google Earth Engine (GEE). The third set of precipitation data is from a meteorological station in the Zhouqu city, which is ~30 km east of the landslide area. Monthly precipitation data from 1986 to 2021 measured by this station are also used as a reference.

The Mann–Kendall (M-K) test is often used to analyze long-term, inter-annual, and seasonal trends and mutations in meteorology and hydrology (Pei et al., 2023). In this work, we mainly obtain the trend and *p*-value test of three sets of different sets of rainfall data through the trend analysis of the M-K test.

First, we defined time-series data as X1, X2, X3, . . . , Xn, where ni denotes the cumulative number of samples. Among them, Xj is greater than Xi in the time series (1≤i≤j). The statistic Sk is defined as follows:

$$Sk = \sum_{i=1}^{k} n_i. \tag{1}$$

Under the assumption that the time-series data are randomized and independent, the mean and variance of the statistic are expressed as E (Sk) and Var (Sk), respectively. They can be represented as follows:

$$E(Sk) = \frac{k(k-1)}{4}, \tag{2}$$

$$Var(Sk) = \frac{k(k-1)(2k+5)}{72}. \tag{3}$$

TABLE 1 Parameters of SAR images.

Radar satellite	Sentinel-1A	
Wavelength (m)	0.056	
Polarization mode	VV	
Orbital direction	Ascending	Descending
Path number	62	479
Frame number	55	107
Time span	April 2020–April 2022	
Spatial resolution (m)	5*20	
Number of images	59	46
Number of composing image pairs	261	219
Heading (°)	347.07	192.92

Then, we normalize the statistic Sk and obtain the U(Sk).

$$U(Sk) = \frac{S_K - E(Sk)}{\sqrt{Var(Sk)}}. \tag{4}$$

3.2 Surface deformation by SBAS-InSAR

We used a total of 46 scenes of Sentinel-1A single-look complex (SLC) images under the descending orbit and 59 scenes of ascending orbit data from April 2020 to April 2022 to derive surface deformation using SBAS-InSAR (https://search.asf.alaska.edu/), and the orbit correction is performed through the precise orbit file (https://scihub.copernicus.eu/) corresponding to the time. By setting a temporal baseline threshold of 60 days and a spatial baseline threshold of 20%, 261 and 219 interferometric pairs were generated for the ascending and descending track images, respectively. The image parameters are shown in Table 1. Among them, the maximum spatial thresholds in the descending track and ascending track image pairs are 228 and 218 m, respectively. Connections of SAR images are shown in Figure 2.

Adaptive filtering functions were used for improving interferogram quality, and unwrapping of the phase was done by using the minimum cost flow (MCF) algorithm (Werner et al., 2003; Pepe and Lanari, 2006). After these processes, we used SRTM-DEM (https://dwtkns.com/) data for terrain correction (Zhang et al., 2021). We set ground control points (GCPs) based on the selection of a relatively stable region. To estimate and remove the remnant constant phase, these points are used to do refinement and reflattening. We inverse the first deformation rate to flatten the resulting interferogram by selecting the linear model. Based on the result of the first deformation rate, we remove atmosphere phase delay by using a temporal high-pass filter and a spatial low-pass filter to separate the phase components. Finally, the singular value decomposition (SVD) method was used to obtain LOS deformation results from the unwrapped phase (Chen et al., 2021; Berardino et al., 2002). The SBAS-InSAR operation steps of this work are implemented in the ENVI/SARscape package. A 1:4 multi-look operation is used for

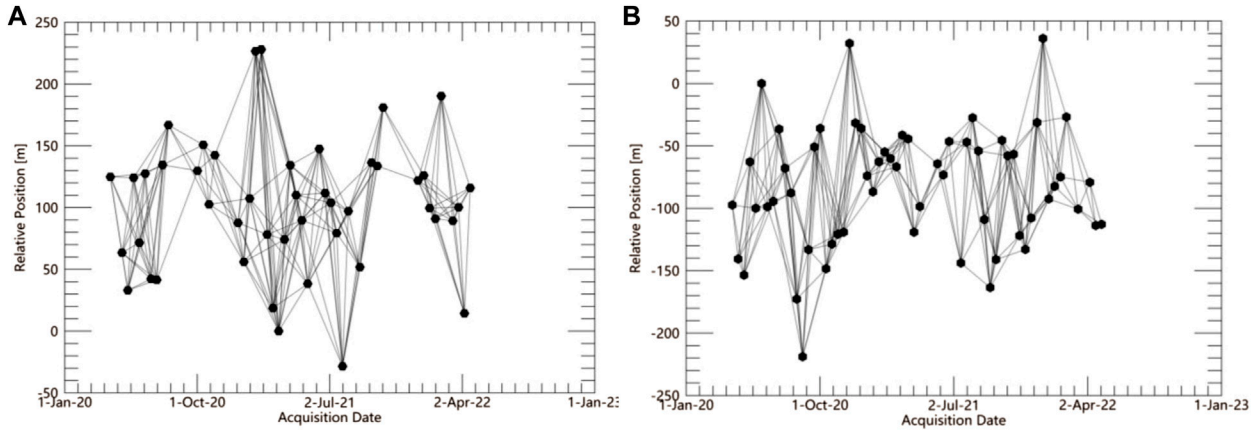

FIGURE 2
Descending **(A)** and ascending **(B)** InSAR pairs used in this work.

the range and azimuth direction, and the final output image resolution is 20*20 m.

3.3 Deformation derived by pixel offset tracking and time-series inversion

Sentinel-2 images with POT were first used to derive the surface deformation of the landslide. The Multi-Spectral Instrument (MSI) onboard Sentinel-2 images is a push-broom sensor. There are two Sentinel-2 satellites at space, 2A and 2B, both of which are phased at 180° to each other. For each satellite, the revisit time at the equator is 10 days. The constellation of two satellites can view the equator every 5 days. At mid to low latitude, the revisit time is even shorter (<5 days). There are 13 bands with a spatial resolution of 10, 20, and 60 m. Near-infrared (NIR), red, green, and blue are four bands with 10 m in spatial resolution. The 10-m red band is the most frequently used data to detect surface deformation (Yang et al., 2020a; Qi et al., 2021).

We downloaded 135 Sentinel-2 red band images (t0, t1, . . . t134) from 27 November 2015 to 24 May 2023 (Table 2) and 94 Landsat-5 red band images from 1986 to 2011 (Table 3). For this work, we selected images that were least affected by clouds. We used the COSI-Corr software, which was developed by a team in the California Institute of Technology (Leprince et al., 2007) and is a frequently used sub-pixel offset tracking method to derive surface deformation in Sentinel-2 images (Bontemps et al., 2018; Lacroix et al., 2018; 2020; Yang et al., 2020a; Qi et al., 2021). To derive surface deformation with the software, we must compose a pair of two images acquired at different dates. The principle of the COSI-Corr is to use sliding windows to find the difference between the earlier or the master image and the later image, also known as the slavery image. By taking the image of Sentinel-2 as an example, we composed 2069 image pairs with these 135 images.

$$\boldsymbol{A} = \begin{bmatrix} 1 & 0 & \cdots & & 0 & 0 & 0 \\ 0 & 0 & \cdots & & 0 & 0 & 0 \\ \cdots & \cdots & \cdots & \cdots & \cdots & \cdots & \cdots \\ 0 & 0 & \cdots & -1 & 0 & 1 & \\ 0 & 0 & \cdots & 0 & -1 & 1 & \end{bmatrix}. \quad (5)$$

Matrix $\boldsymbol{A}$ is a two-dimensional matrix. It has 2069 rows and 135 columns.

The rank of $\boldsymbol{A}$ is 135, which is the same as that of unknown variables.

$$X = [x_{0-1}\, x_{0-2}\, x_{0-3} \cdots x_{0-44}\, x_{0-142}\,]. \quad (6)$$

Vector $\boldsymbol{X}$ is a one-dimensional vector. It has 135 rows and one column. Elements in $\boldsymbol{X}$, such as x_{0-j} (j=1, 2, . . . 134), represent the cumulative displacement from the date of the first image (t_0). The vector $\boldsymbol{X}$ is the target of the function.

$$b = [b_{0-1}\, b_{0-2}\, b_{0-3} \cdots b_{0-143}]. \quad (7)$$

$$\mathrm{AX} = \mathrm{b}. \quad (8)$$

As we have 2069 equations and 135 unknowns, we used the singular value decomposition (SVD) method to find a solution. Because A is not a square matrix, it can be decomposed into three other matrices.

$$A = \mathrm{U}SV^T, \quad (9)$$

where U and V are square matrices. The columns of U are the eigenvectors of AA^{T}, and the columns of V are the eigenvectors of $\mathrm{A}^{\mathrm{T}}\mathrm{A}$. S is a diagonal matrix with singular values of A ([diag $(\sigma_1, \sigma_1, \ldots, \sigma_n)$]).

$$A^{-1} = V\left[diag\left(\sigma_1^{-1}, \sigma_2^{-1}, \ldots, \sigma_n^{-1}\right)\right]\mathrm{U}^T. \quad (10)$$

We also processed the inversion twice with a similar form of weights (Bontemps et al., 2018). In the first SVD inversion, we took the surface deformations within the stable area and calculated the reciprocal of the standard deviation as the weight. In the second inversion, we used the reciprocal of the residual error from the first SVD inversion as the weight.

3.4 Landslide simulation by MassFlow

MassFlow is a two-dimensional finite difference scheme developed to model mass movements in mountainous regions (Ouyang et al., 2013). The software has been used to simulate the collapse of the Beishan landslide (Zhong et al., 2020). In this work,

TABLE 2 Dates of all 135 Sentinel-2 optical images used in this work.

20151127	20171211	20181002	20190425	20200209	20200827	20210223	20211115	20220504	20221215
20151227	20171216	20181101	20190525	20200219	20201021	20210315	20211125	20220509	20221220
20160126	20171221	20181201	20190704	20200224	20201110	20210330	20211130	20220708	20221230
20161121	20180105	20181216	20190803	20200229	20201115	20210429	20211205	20220723	20230109
20161211	20180120	20181221	20190927	20200305	20201205	20210509	20211220	20220728	20230124
20170219	20180219	20181226	20191012	20200320	20201220	20210524	20220109	20220807	20230203
20170530	20180224	20190105	20191017	20200325	20201225	20210713	20220114	20220911	20230305
20170709	20180301	20190125	20191111	20200409	20201230	20210802	20220119	20221011	20230409
20170729	20180311	20190204	20191116	20200414	20210114	20210827	20220203	20221031	20230414
20170907	20180415	20190219	20191206	20200529	20210119	20210911	20220213	20221105	20230419
20171101	20180515	20190311	20191211	20200603	20210129	20210921	20220310	20221110	20230429
20171111	20180604	20190316	20191226	20200618	20210203	20211105	20220315	20221125	20230514
20171126	20180714	20190326	20200130	20200708	20210208	20211110	20220409	20221205	20230524
20171201	20180823	20190331	20200204	20200802					

10.3389/feart.2023.1304969

10.3389/feart.2023.1304969

TABLE 3 Dates of all 94 Landsat-5 optical images used in this work.

19860706	19901224	19930826	19980128	19990421	20010629	20030923	20060611	20080904	20110116
19870114	19910226	19931114	19980317	19990827	20011003	20031212	20060627	20081006	20110305
19870130	19911024	19931130	19980402	19991201	20011120	20040113	20060915	20081209	20110727
19870303	19920213	19940829	19980418	20000102	20011222	20040214	20061102	20090110	20110828
19870404	19920229	19960717	19980621	20000712	20020107	20040402	20061118	20090126	
19870725	19921111	19960802	19981128	20001101	20020224	20040520	20061220	20090211	
19871216	19921127	19961021	19981214	20010104	20020803	20041128	20070222	20100129	
19881202	19921213	19970109	19981230	20010120	20030110	20041214	20070918	20100318	
19891205	19930420	19970720	19990216	20010221	20030416	20050131	20080616	20100403	
19901208	19930709	19970906	19990405	20010613	20030721	20060424	20080718	20101231	

we used MassFlow to model the potential collapses of the main deformation area. The spatial extents of the simulated landslide were from displacement >5 m by POT. To better meet the conditions of field hydrogeology and other conditions, we used the same simulation parameters as in the previous paper (Zhong et al., 2020). The simulation parameters used in this paper are a friction coefficient of 0.65 and cohesion of 6 Kpa. The shear shrinkage effect of the sliding soil and the fragmentation of particles caused by shearing make the pores of the sliding soil smaller, generating pore water pressure, and the shear strength completely or partially disappears. The pore water pressure coefficient in this work (used by Zhong et al. (2020)) is 0.05. However, they were simulated during January 2021 (dry wintertime), when the pore water pressure coefficient was at its lowest condition, which means that the same value of the parameter cannot represent the situations throughout the year, especially in rainy months. So we set up three gradients (0.05, 0.1, and 0.15) for this parameter to simulate three scenarios for the landslide.

4 Results

4.1 Deformation results derived from optical POT and SBAS-InSAR

The optical POT method was used to inverse the deformation results of the slope for nearly 8 years from November 2015 to May 2023. It was found that the deformation in the middle part of the landslide has the largest deformation (Figure 3A). Maximum deformation of this part of the landslide is >15 m during the studied period. The white border represents the deformation area greater than 5 m, which has an area of ~196,094 m^2, accounting for 31% of the entire landslide (Figure 3C). Figure 3B shows the directions of landslide movement. The dominant moving directions of the landslide are from northeast to southwest along the slope.

Figures 4A, B show the spatial pattern of the surface deformation in the LOS direction of landslides monitored by SBAS-InSAR under the descending and ascending orbits. From the SBAS-InSAR results of the descending orbit, discernible larger surface deformations (<-20 mm ± 4.06 mm) are found to the east and upper parts of the landslide (Figure 4A). From the results of the ascending orbit, large surface deformations (<-20 mm ± 3.61 mm) are only discerned on the upper part of the landslide (Figure 4B). The maximum deformation in the LOS direction detected by the descending and ascending tracks is of the same magnitude (close to 50 ± 4 mm). In the detected deformation, the uncertainty of these displacements was assessed using standard deviations of the InSAR and POT displacement results in the stable area.

4.2 Relations between precipitation and deformations of the Beishan landslide

Figure 5 shows the deformation time series of three points on the middle (P1), upper (P2), and east (P3) parts of the landslide (P1, P2, and P3 are shown in Figures 3 and 4) derived from optical POT and

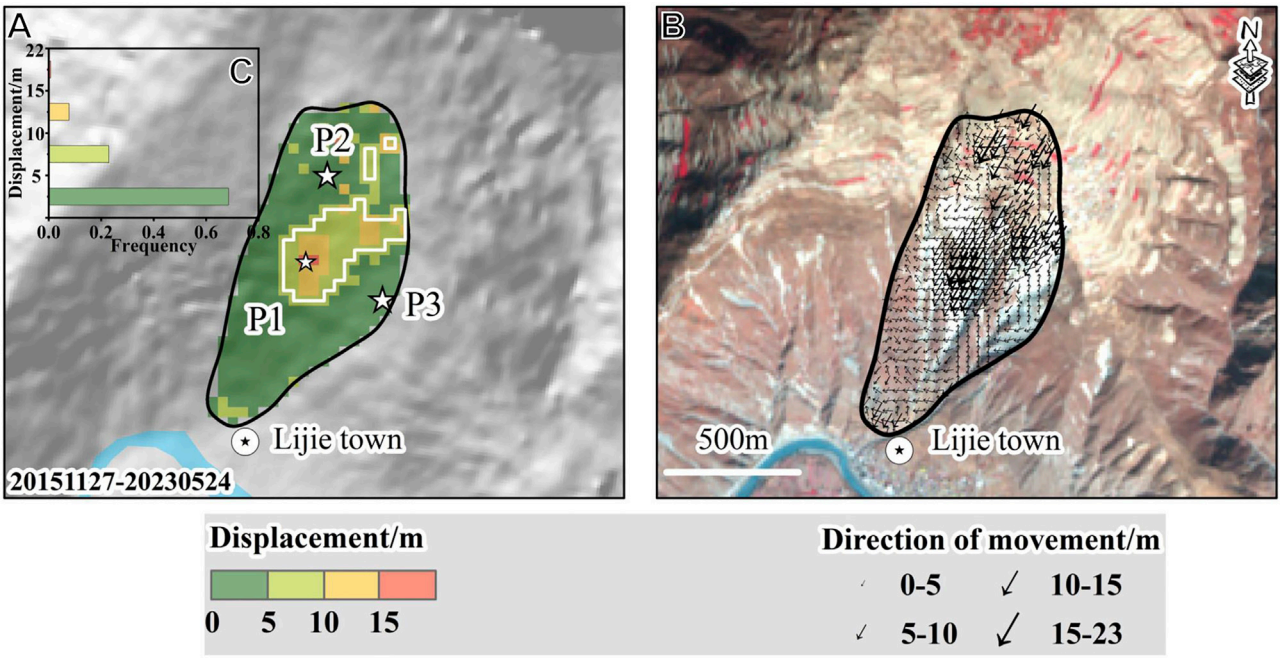

FIGURE 3
Derived displacement between 27 November 2015 and 24 May 2023 **(A)**, the directions of landslide movement derived from POT **(B)**, and the histogram of deformation distribution **(C)**.

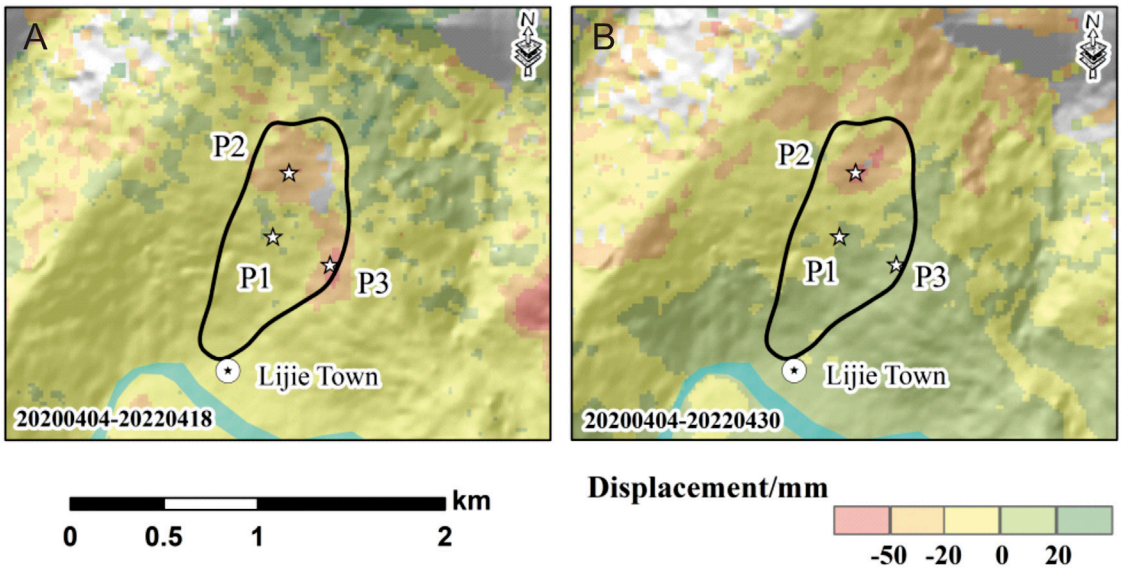

FIGURE 4
Slope deformation derived from descending and ascending SBAS-InSAR methods **(A, B)**. Selected points from the middle (P1), upper (P2), and east sides (P3) of the landslide.

ascending/descending InSAR from April 2020 to April 2022. The two vertical black dashed lines represent accelerated deformations of the landslide in the rainy months of 2020 and 2021. Figure 5A shows the cumulative deformation of P1 at the middle part of the landslide. For this point, only deformations measured by optical POT are valid because deformations of P1 derived from ascending/descending SBAS-InSAR are non-monotonic. Time series of its deformation increased rapidly by 4.76 m within 3 months from 8 July 2020 to 21 October 2020, with a deformation rate of 0.04 m/d, which is immediately after the rainy months of the year.

Deformation time series of P2 is valid for both ascending and descending SBAS-InSAR, but not for the optical POT. For the

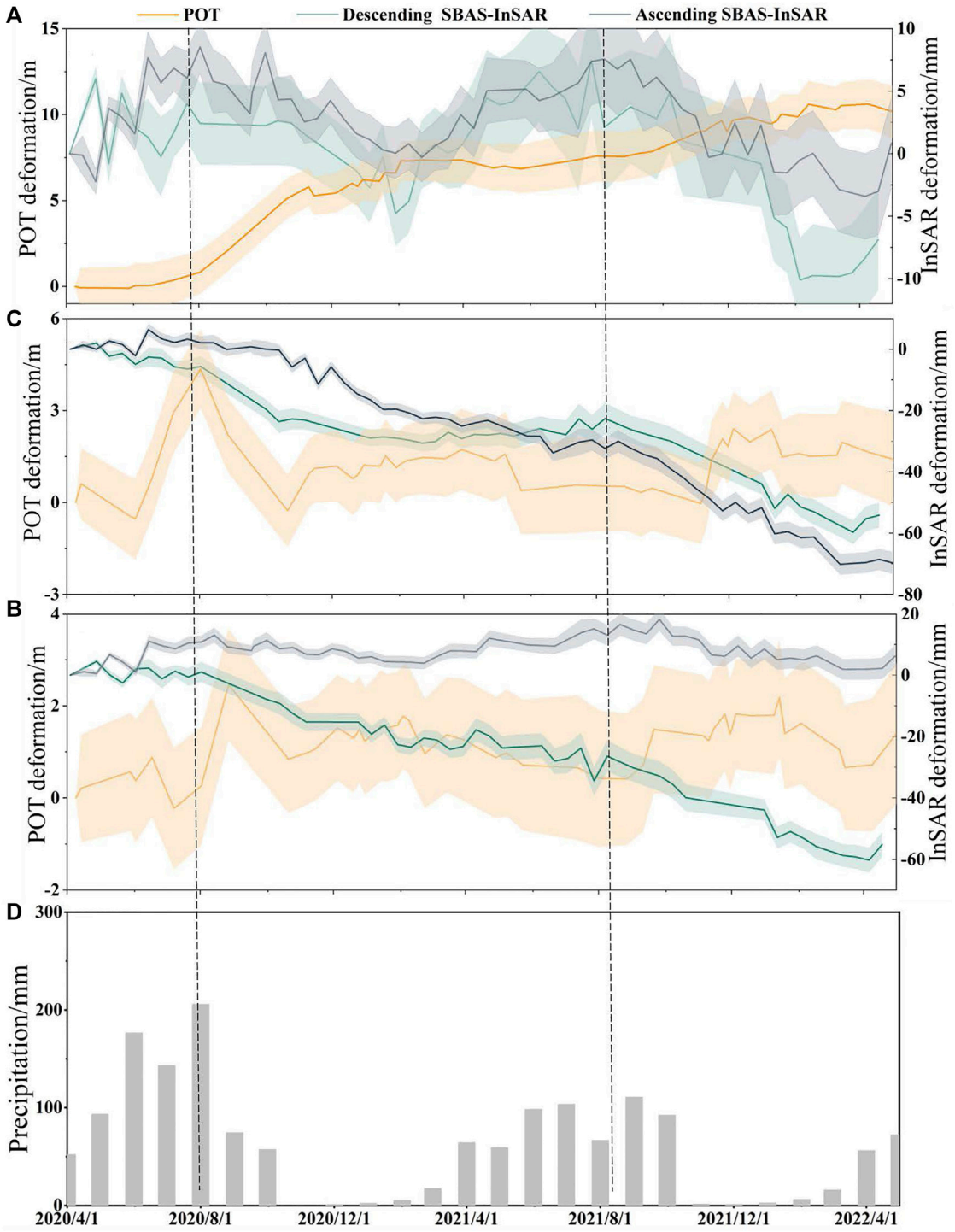

FIGURE 5
Optical POT- and SBAS-InSAR-derived cumulative displacements for P1 **(A)**, P2 **(B)**, and P3 **(C)** (labeled in Figures 3 and 4) and monthly rainfall from CHIRPS **(D)**. The shaded area is the standard deviation of the deformation monitored using the optical POT and InSAR methods within the stable zone. In Figure 6, the title of the figure was changed to: The deformation time-series in 35 years (1986–2023) **(A)**, precipitation change and distribution in 42 years (1981–2022) from three datasets, and the shadings are 95% confidence intervals for the linear models **(B)**.

descending result, the deformation rate from August to October 2021 reached nearly 0.3 mm/d, far exceeding the annual average deformation rate of 0.07 mm/d. Figure 5C shows that the deformation of P3 is valid only in the descending InSAR result. The deformation velocities from August to October in 2020 and 2021 are 0.14 mm/d and 0.15 mm/d, respectively, much larger than the annual average deformation velocity of 0.07 mm/d from April 2020 to April 2022. The fast-moving deformations for both ascending and descending SBAS-InSAR also occurred immediately after rainy months.

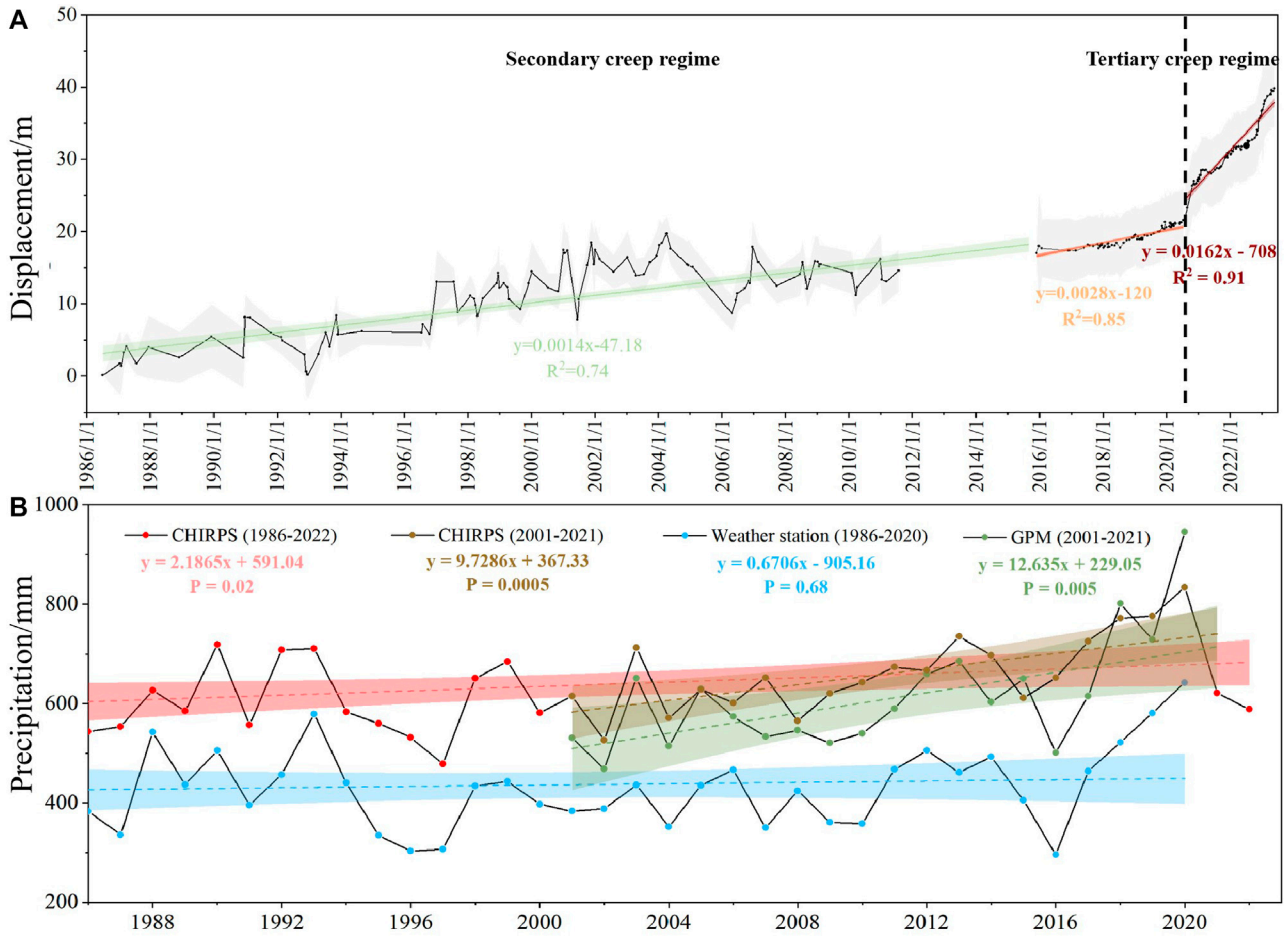

FIGURE 6
The deformation time-series in 35 years (1986–2023) (Figure 6A), precipitation change and distribution in 42 years (1981–2022) from three datasets, and the shadings are 95% confidence intervals for the linear models.

Figure 6A shows the deformation time-series curve from 1986 to 2023. It can be found that the displacement velocities in 1986–2011 (phase 1) and November 2015–July 2020 (phase 2) are 0.59 m/year and 0.96 m/year, respectively. The slope of the two-stage fitting curve is equivalent. It shows that the displacement velocities in the two phases are roughly the same, and the deformation is stable. After July 2020, the deformation suddenly accelerated. The displacement velocity of phase 3 (July 2020–May 2023) is 6.3 m/year, nearly 10 times that of the previous stages (phase 1 and phase 2).

To explore the relationship between the trend of deformation and rainfall, we fitted the trend graphs of three sets of rainfall data (Figure 6B). Different rainfall data show that the annual rainfall in the past 20–30 years has an upward trend (except for the weather station data, the *p*-values of all other data after Mk testing are less than 0.05). Although the rainfall data of the weather station are approximately 150 mm lower than those of the satellite rainfall (GPM and CHIRPS) on average, the rainfall trend of the two is consistent. This may be caused by differences in the locations of weather stations and monitoring methods. The two sets of satellite rainfall data (GPM and CHIRPS) agree well with each other in the 20 years from 2001 to 2021. In addition, all three datasets show that the rainfall increased sharply after 2018 and peaked in 2020, which is very likely to be the reason for the sudden accelerated deformation in summer 2020.

4.3 Potential risks of the Beishan landslide

We simulated the collapse of the pore water pressure at three different intensities. The houses and buildings in the Lijie town (the white area is the interpreted building area) will be possibly damaged with landslide collapse. The collapse of the landslide gradually increases with the increase in the pore water pressure (Figure 7). When the pore water pressure is 0.05, the collapse of the landslide has a less impact on the built-up area (Figure 7A). When the pore water pressure is 0.1, the collapsed material of the landslide begins to affect the northwest part of the urban area (Figure 7B).

When the pore water pressure is 0.15, the buried area of the landslide accumulation core is the largest (partial area>20 m). The buried area above 1 m reaches 39,664 m^2, accounting for 18% of the construction area (the total construction area of the north and south areas of the river reaches 224,503 m^2). In addition, the average buried depth of this area reaches 9.54 m (Figure 7C).

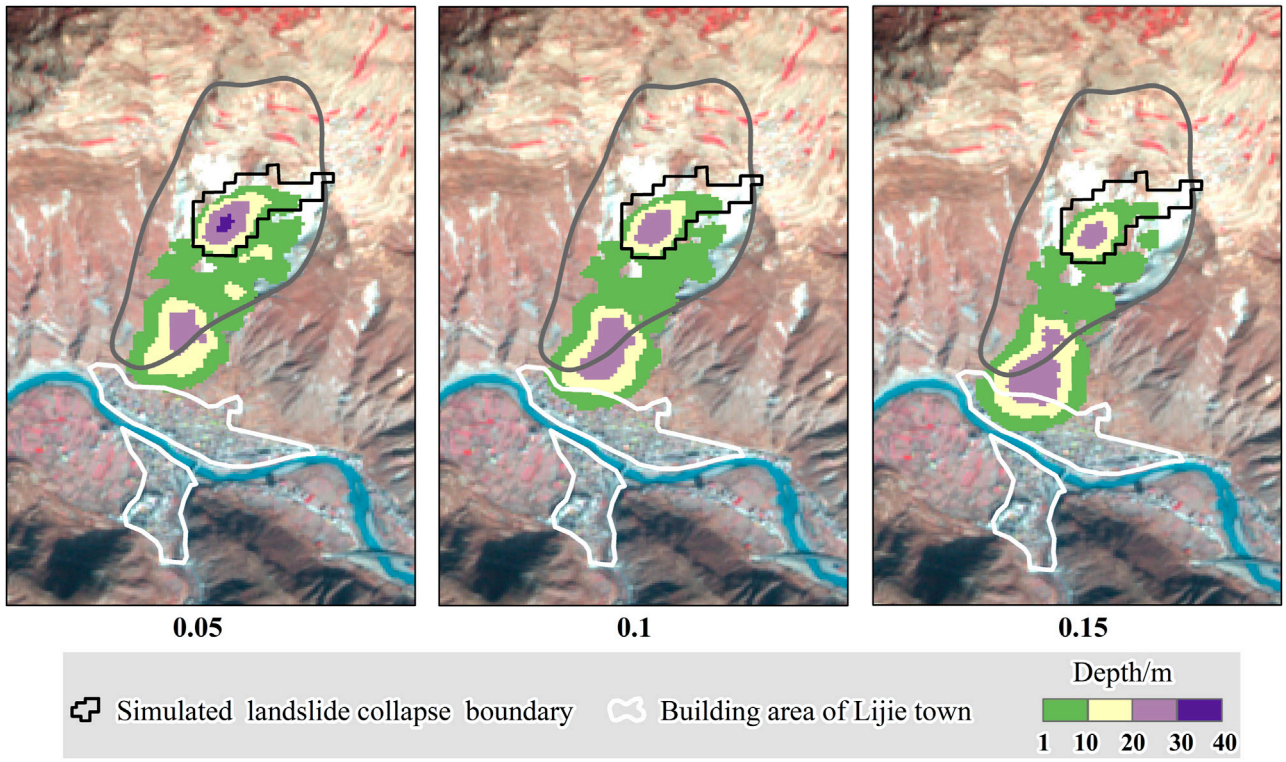

FIGURE 7
Collapse simulations for the main deformation area of the Beishan landslide.

5 Discussion

5.1 What are the differences between SBAS-InSAR and optical POT in measuring landslide deformation?

The SBAS-InSAR and optical POT techniques are two commonly used remote sensing methods to extract regional landslide deformation (Hu et al., 2018; Handwerger et al., 2019). Although one recent work compared InSAR and optical POT results, they did not derive time series of landslide deformation (Kuang et al., 2023). The recently developed time-series inversion model can significantly remove spatial noises and is indispensable to uncover landslide dynamics over time (Bontemps et al., 2018). Our work is the first to compare time series of deformations between SBAS-InSAR and optical POT for the same landslide.

Our results show that spatial deformation patterns of both methods are distinct from each other (Figures 3 and 4). This is because the POT is excellent in detecting larger deformations (>1 m) in the horizontal direction (Yang et al., 2021), whereas InSAR is better in detecting smaller deformations (centimeter scale) in the LOS direction of the satellite (Zhang et al., 2020). The smallest deformation that POT can detect relies upon the spatial resolution of the used optical images (Stumpf et al., 2017; Bontemps et al., 2018). With time series of POT results from 10-m resolution images, we are confident to say that we detected deformation signals of >1 m. These distinct results from both methods indicate that the onefold use of either InSAR or optical POT would underestimate the extent of the landslide's spatial deformation. The spatial pattern of a landslide's deformation is an important reference to assess the magnitude (e.g., detaching volume, moving speed, potential deposition area, and depositing depth) of a landslide hazard, which is the most important part for quantifying landslide risks. The complete spatial pattern of the landslide's deformation unveiled by integration of both methods is also crucial for assessing the risks of other similar slow-moving landslides.

In this work, the maximum deformation detected by SBAS-InSAR is ~50 mm, whereas the POT-derived deformation is >20 m. This is consistent with the findings of previous works that POT is excellent in detecting larger deformation (>1 m) in the horizontal direction (Yang et al., 2021) and InSAR is better in detecting smaller deformation (centimeter scale) (Zhang et al., 2020). In addition, InSAR detects deformation in the LOS direction (Zhang et al., 2020), which explains different performances between the ascending and descending track results shown in Figure 4. Deforming slopes with the west and east aspects are easier to detect by Sentinel-1A SAR images of ascending and descending orbits, respectively. The InSAR method is sensitive to the vertical deformation but not sensitive to the north–south deformation (Chen et al., 2023; Tian et al., 2023). In theory, InSAR cannot detect moving slopes with aspects to SAR tracks. This may have caused the SBAS-InSAR method to fail to effectively monitor the deformation in the central part of the landslide.

TABLE 4 The 10 days with the highest daily rainfall (CHIRPS) from 1 November 2016 to 30 August 2023.

Date	Precipitation (mm)	Date	Precipitation (mm)
20190728	75.899	20210709	48.028
20170607	75.006	20200713	46.077
20180710	56.075	20180701	44.748
20210725	55.475	20170505	42.333
20190721	54.556	20200710	41.39

5.2 How dangerous is the Beishan landslide?

Deformations of a landslide can be used to help issue early warnings. Laboratory experiments and numerical models show that there are three creeping regimes before the collapse of a landslide: primary creep with decreasing velocity, secondary creep with constant slow velocity, and tertiary creep with accelerations (Main, 2000; Amitrano and Helmstetter, 2006). The last two schemes are frequently reported before paroxysmal collapses of some famous landslides (Intrieri et al., 2018; Liu et al., 2020). Our results of the deformation time series from 1981 to 2023 seem to follow those of the secondary creep and early stage of the tertiary creep. The landslide seems to be deforming with constant velocity, whereas accelerations were observed since 2020. Although the deforming velocity in 2022 is slower than that in 2020 and 2021, it is still larger than velocities before 2019. Similar to the famous Baige landslide (Liu et al., 2020), long-term deformation time series indicates that the middle part of this landslide is highly active and that it could be susceptible to collapse in the future.

A previous work simulated the collapse of the landslide and found that it had little influence on the nearby Lijie town (Zhong et al., 2022). However, their model used the pore water pressure parameter in wintertime, during which it was at its lowest level. Our results show that major deformations of the landslide occur in rainy months when pore water pressure is at its maximum. The most conservative scenarios in this work serve a baseline for the landslide's impact. Our modeling indicates that collapse of the middle part of the landslide may cause destructions to the Lijie town.

5.3 What is the relationship between landslide deformation and precipitation?

Our results that deformation time series from both methods of SBAS-InSAR and Sentinel-2 POT shows accelerations in rainy months indicate that precipitation is likely to be the major driver for intra-annual landslide dynamics. Although measurements of Landsat 5 are very coarse and sparse with high uncertainties, it is possible that intra-annual landslide deformations from 1986 to 2011 also followed similar temporal patterns. During our study period, there is no seismicity with Modified Mercalli Intensity (MMI) larger than IV, and the deformation correlates well with precipitation. Consistent with others, these findings indicate that intra-annual acceleration of this landslide is initiated by precipitation (Handwerger et al., 2022; Liu et al., 2022). As the slope continues to slide down, the threshold to accelerate the moving of the slope may continue to decrease.

On an inter-annual time scale, our findings indicate that the relation between the landslide's deformations and annual precipitation since 1986 has been complex. All precipitation data show that annual precipitations are among the highest in record from 2018 to 2020, overlying with significant acceleration of the landslide in 2020. These abnormally high precipitation years may cause the transition of the landslide from the second creep regime to the tertiary creep regime, indicating the impact of climate warming on landslide stability.

To investigate the correlation between rainfall and deformation, we conducted analysis of daily rainfall spanning from 1 November 2016 to 30 August 2023. During this period, we identified the

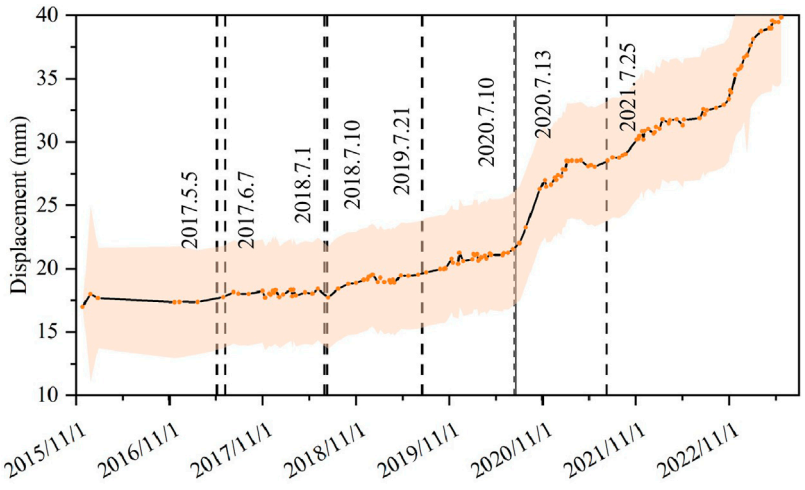

FIGURE 8
Deformation time series from 27 November 2015 to 24 May 2023 obtained by Sentinel-2 inversion and dates of the 10 wettest days from 1 November 2016 to 30 August 2023.

10 days with the highest recorded rainfall. Notably, a significant majority of these extreme rainfall events were observed in the month of July each year, constituting 80% of the total dates under consideration (Table 4). In July 2020, there were 2 days of extremely intense rainfall, which is highly likely to be associated with the substantial deformation observed during the summer of 2020 (Figure 8). An escalation in the occurrence of extreme rainfall events in alpine regions can intensify the occurrence of landslides (Shah et al., 2023). Beyond the direct erosive impact of rainfall, extreme precipitation can also induce landslides by influencing the hydrology of the watershed (Zhu et al., 2021).

Most landslides in this part of the plateau are triggered by rainfall (Li et al., 2023; Peng et al., 2015). Based on the >40 years (1981–2022) of annual precipitation record, the climate in this region found getting wetter. In addition, as estimated in Coupled Model Intercomparison Project Phase 6, precipitation in this region will continue to increase with more extremity (Thackeray et al., 2022). Increasing annual precipitations may lead to more landslide activities in this part of the plateau in future. With ongoing climate change, there may be more similar landslides as this area becomes unstable. Frequent landslides will provide erosive loose materials in this semi-arid region of poor vegetation cover, potentially feeding more debris flows during extreme precipitations.

6 Conclusion

In this work, we studied deformations of a landslide in northeast Tibetan Plateau with SBAS-InSAR and optical POT. Deformations detected using both the methods are very different. Optical POT is sensitive to meter-scale deformations in the middle part of the landslide, where SBAS-InSAR is invalid. From 1986 to 2023, the middle part of the landslide moved >35 m. In contrast, SBAS-InSAR is more sensitive to centimeter-scale deformations in upper and east parts of the landslide, which is ineffective for optical POT to monitor. It is possible that sections of landslides with centimeter-scale deformations may be at its earlier stage toward meter-scale deformations in future. Based on theoretical landslide deformation regime and previous collapsing landslides, we speculate that the landslide may be at its final tertiary creep regime, meaning a partial collapse is susceptible in future.

Time series of deformations from both SBAS-InSAR and POT with Sentinel-2 images can detect seasonal deformation signals related to rainy months every year. However, inter-annual landslide deformation is not directly related to multiyear precipitations. The significant acceleration of the middle part of the landslide in 2020 may be related to the extraordinary wetting years from 2018 to 2020. With climate change, precipitation in this region will continue to increase, potentially posing more slopes unstable in future.

Data availability statement

The original contributions presented in the study are included in the article/Supplementary material; further inquiries can be directed to the corresponding author.

Author contributions

ML: data curation, formal analysis, investigation, methodology, software, writing–original draft, and writing–review and editing. WY: resources, supervision, visualization, writing–review and editing, and writing–original draft. CX: supervision and writing–review and editing. YY: visualization, validation, and writing–review and editing. LT: writing–review and editing. PS: writing–review and editing and validation.

Funding

The author(s) declare financial support was received for the research, authorship, and/or publication of this article. This work is supported by the Second Tibetan Plateau Scientific Expedition and Research Program (STEP, Grant No. 2019QZKK0906).

Acknowledgments

The authors are grateful for the scholarship from the China Scholarships Council (No. 202006515016). The authors would like to thank Mr. Jiaxin Gao for his help in screening and downloading all optical images.

Conflict of interest

The authors declare that the research was conducted in the absence of any commercial or financial relationships that could be construed as a potential conflict of interest.

The author(s) declared that they were an editorial board member of Frontiers, at the time of submission. This had no impact on the peer review process and the final decision.

Publisher's note

References

Amitrano, D., and Helmstetter, A. (2006). Brittle creep, damage, and time to failure in rocks. *J. Geophys. Res.* 111, n/a–n. doi:10.1029/2005JB004252

Berardino, P., Fornaro, G., Lanari, R., and Sansosti, E. (2002). A new algorithm for surface deformation monitoring based on small baseline differential SAR interferograms. *IEEE Trans. Geosci. Remote Sens.* 40, 2375–2383. doi:10.1109/TGRS.2002.803792

Bontemps, N., Lacroix, P., and Doin, M.-P. (2018). Inversion of deformation fields time-series from optical images, and application to the long term kinematics of slow-

moving landslides in Peru. *Remote Sens. Environ.* 210, 144–158. doi:10.1016/j.rse.2018.02.023

Bradley, K., Mallick, R., Andikagumi, H., Hubbard, J., Meilianda, E., Switzer, A., et al. (2019). Earthquake-triggered 2018 Palu Valley landslides enabled by wet rice cultivation. *Nat. Geosci.* 12, 935–939. doi:10.1038/s41561-019-0444-1

Chen, M. K., Xu, G. Y., Zhang, T. X., Xie, X. W., and Chen, Z. P. (2023). A novel method for inverting coseismic 3D surface deformation using InSAR considering the weight influence of the spatial distribution of GNSS points. *Adv. Space Res.* 0273, 585–596. doi:10.1016/j.asr.2023.11.013

Chen, Y., Yu, S. W., Tao, Q. X., Liu, G. L., Wang, L. Y., and Wang, F. Y. (2021). Accuracy verification and correction of D-InSAR and SBAS-InSAR in monitoring mining surface subsidence. *Remote Sens.* 13, 4365. doi:10.3390/rs13214365

Cook, K. L., Andermann, C., Gimbert, F., Adhikari, B. R., and Hovius, N. (2018). Glacial lake outburst floods as drivers of fluvial erosion in the Himalaya. *Science* 362, 53–57. doi:10.1126/science.aat4981

Crozier, M. J. (2010). Deciphering the effect of climate change on landslide activity: a review. *Geomorphology* 124, 260–267. doi:10.1016/j.geomorph.2010.04.009

Delaney, K. B., and Evans, S. G. (2015). The 2000 Yigong landslide (Tibetan Plateau), rockslide-dammed lake and outburst flood: review, remote sensing analysis, and process modelling. *Geomorphology* 246, 377–393. doi:10.1016/j.geomorph.2015.06.020

Deroin, J.-P., Téreygeol, F., Cruz, P., Guillot, I., and Méaudre, J.-C. (2012). Integrated non-invasive remote-sensing techniques and field survey for the geoarchaeological study of the Sud Lípez mining district, Bolivia. *Geophys Eng.* 9, S40–S52. doi:10.1088/1742-2132/9/4/S40

Fan, X. M., Xu, Q., Alonso-Rodriguez, A., Subramanian, S. S., Li, W. L., Zheng, G., et al. (2019). Successive landsliding and damming of the Jinsha River in eastern Tibet, China: prime investigation, early warning, and emergency response. *Landslides* 16, 1003–1020. doi:10.1007/s10346-019-01159-x

Fang, J., Yang, W. T., Luan, Y. B., Du, J., Lin, A. W., and Zhao, L. (2019). Evaluation of the TRMM 3B42 and GPM IMERG products for extreme precipitation analysis over China. *Atmos. Res.* 223, 24–38. doi:10.1016/j.atmosres.2019.03.001

Froude, M. J., and Petley, D. N. (2018). Global fatal landslide occurrence from 2004 to 2016. *Nat. Hazards Earth Syst. Sci.* 18, 2161–2181. doi:10.5194/nhess-18-2161-2018

Galli, M., Ardizzone, F., Cardinali, M., Guzzetti, F., and Reichenbach, P. (2008). Comparing landslide inventory maps. *Geomorphology* 94, 268–289. doi:10.1016/j.geomorph.2006.09.023

Gruber, S., Hoelzle, M., and Haeberli, W. (2004). Permafrost thaw and destabilization of Alpine rock walls in the hot summer of 2003. *Geophys. Res. Lett.* 31, n/a. doi:10.1029/2004GL020051

Handwerger, A. L., Fielding, E. J., Huang, M. H., Bennett, G. L., Liang, C. R., and Schulz, W. H. (2019). Widespread initiation, reactivation, and acceleration of landslides in the northern California coast ranges due to extreme rainfall. *J. Geophys. Res. Earth Surf.* 124, 1782–1797. doi:10.1029/2019JF005035

Handwerger, A. L., Fielding, E. J., Sangha, S. S., and Bekaert, D. P. S. (2022). Landslide sensitivity and response to precipitation changes in wet and dry climates. *Geophys. Res. Lett.* 49, e2022GL099499. doi:10.1029/2022GL099499

Hu, K. H., Wu, C. H., Tang, J. B., Pasuto, A., Li, Y. J., and Yan, S. X. (2018). New understandings of the June 24th 2017 xinmo landslide, maoxian, sichuan, China. *Landslides* 15, 2465–2474. doi:10.1007/s10346-018-1073-2

Huggel, C., Clague, J. J., and Korup, O. (2012). Is climate change responsible for changing landslide activity in high mountains? *Earth Surf. Process Landf.* 37, 77–91. doi:10.1002/esp.2223

Intrieri, E., Raspini, F., Fumagalli, A., Lu, P., Del Conte, S., Farina, P., et al. (2018). The Maoxian landslide as seen from space: detecting precursors of failure with Sentinel-1 data. *Landslides* 15, 123–133. doi:10.1007/s10346-017-0915-7

Kuang, J. M., Ng, A. H.-M., Ge, L. L., Metternicht, G. I., and Clark, S. R. (2023). Joint use of optical and radar remote sensing data for characterizing the 2020 aniangzhai landslide post-failure displacement. *Remote Sens.* 15, 369. doi:10.3390/rs15020369

Lacroix, P., Bièvre, G., Pathier, E., Kniess, U., and Jongmans, D. (2018). Use of Sentinel-2 images for the detection of precursory motions before landslide failures. *Remote Sens. Environ.* 215, 507–516. doi:10.1016/j.rse.2018.03.042

Lacroix, P., Dehecq, A., and Taipe, E. (2020). Irrigation-triggered landslides in a Peruvian desert caused by modern intensive farming. *Nat. Geosci.* 13, 56–60. doi:10.1038/s41561-019-0500-x

Leprince, S., Barbot, S., Ayoub, F., and Avouac, J.-P. (2007). Automatic and precise orthorectification, coregistration, and subpixel correlation of satellite images, application to ground deformation measurements. *IEEE Trans. Geosci. Remote Sens.* 45, 1529–1558. doi:10.1109/TGRS.2006.888937

Liu, X. J., Zhao, C. Y., Zhang, Q., Lu, Z., and Li, Z. H. (2020). Deformation of the Baige landslide, Tibet, China, revealed through the integration of cross-platform ALOS/PALSAR-1 and ALOS/PALSAR-2 SAR observations. *Geophys. Res. Lett.* 47. doi:10.1029/2019GL086142

Liu, Y., Qiu, H. J., Yang, D. D., Liu, Z. J., Ma, S. Y., Pei, Y. Q., et al. (2022). Deformation responses of landslides to seasonal rainfall based on InSAR and wavelet analysis. *Landslides* 19, 199–210. doi:10.1007/s10346-021-01785-4

Main, I. G. (2000). A damage mechanics model for power-law creep and earthquake aftershock and foreshock sequences. *Geophys. J. Int.* 142, 151–161. doi:10.1046/j.1365-246x.2000.00136.x

Meng, Y. S., Lan, H. X., Li, L. P., Wu, Y. M., and Li, Q. W. (2015). Characteristics of surface deformation detected by X-band SAR interferometry over sichuan-tibet grid connection project area, China. *Remote Sens.* 7, 12265–12281. doi:10.3390/rs70912265

Ouyang, C. J., He, S. M., Xu, Q., Luo, Y., and Zhang, W. C. (2013). A MacCormack-TVD finite difference method to simulate the mass flow in mountainous terrain with variable computational domain. *Comput. Geosci.* 52, 1–10. doi:10.1016/j.cageo.2012.08.024

Ouyang, C. J., Zhao, W., An, H. C., Zhou, S., Wang, D. P., Xu, Q., et al. (2019). Early identification and dynamic processes of ridge-top rockslides: implications from the Su Village landslide in Suichang County, Zhejiang Province, China. *Landslides* 16, 799–813. doi:10.1007/s10346-018-01128-w

Ozturk, U., Bozzolan, E., Holcombe, E. A., Shukla, R., Pianosi, F., and Wagener, T. (2022). How climate change and unplanned urban sprawl bring more landslides. *Nature* 608, 262–265. doi:10.1038/d41586-022-02141-9

Patton, A. I., Rathburn, S. L., and Capps, D. M. (2019). Landslide response to climate change in permafrost regions. *Geomorphology* 340, 116–128. doi:10.1016/j.geomorph.2019.04.029

Pei, Y. Q., Qiu, H. J., Yang, D. D., Liu, Z. J., Ma, S. Y., Li, J. Y., et al. (2023). Increasing landslide activity in the Taxkorgan River Basin (eastern Pamirs Plateau, China) driven by climate change. *Catena* 223, 106911. doi:10.1016/j.catena.2023.106911

Pepe, A., and Lanari, R. (2006). On the extension of the minimum cost flow algorithm for phase unwrapping of multitemporal differential SAR interferograms. *IEEE Trans. Geosci. Remote Sens.* 44, 2374–2383. doi:10.1109/TGRS.2006.873207

Qi, W. W., Yang, W. T., He, X. L., and Xu, C. (2021). Detecting Chamoli landslide precursors in the southern Himalayas using remote sensing data. *Landslides* 18, 3449–3456. doi:10.1007/s10346-021-01753-y

Shah, B., Alam, A., Bhat, M. S., Ahsan, S., Ali, N., and Sheikh, H. A. (2023). Extreme precipitation events and landslide activity in the Kashmir Himalaya. *Bull. Eng. Geol. Environ.* 82, 328. doi:10.1007/s10064-023-03350-w

Stumpf, A., Malet, J.-P., and Delacourt, C. (2017). Correlation of satellite image time-series for the detection and monitoring of slow-moving landslides. *Remote Sens. Environ.* 189, 40–55. doi:10.1016/j.rse.2016.11.007

Thackeray, C. W., Hall, A., Norris, J., and Chen, D. (2022). Constraining the increased frequency of global precipitation extremes under warming. *Nat. Clim. Chang.* 12, 441–448. doi:10.1038/s41558-022-01329-1

Tian, Q. H., Zhang, W. T., and Zhu, W. (2023). Characterizing crustal deformation of the weihe fault, weihe basin (Central China), using InSAR and GNSS observations. *Appl. Sci.* 13 (11), 6835. doi:10.3390/app13116835

Van Westen, C. J., Castellanos, E., and Kuriakose, S. L. (2008). Spatial data for landslide susceptibility, hazard, and vulnerability assessment: an overview. *Eng. Geol.* 102, 112–131. doi:10.1016/j.enggeo.2008.03.010

Wang, Y. J., Cui, X. M., Che, Y. H., Li, P. X., Jiang, Y., and Peng, X. Z. (2022). Automatic identification of slope active deformation areas in the Zhouqu region of China with DS-InSAR results. *Front. Environ. Sci.* 10, 883427. doi:10.3389/fenvs.2022.883427

Werner, C., Wegmuller, U., Strozzi, T., and Wiesmann, A. (2003). "Interferometric point target analysis for deformation mapping," in *Igarss 2003. 2003 IEEE international geoscience and remote sensing symposium. Proceedings (IEEE cat. No.03CH37477)* (Toulouse, France: IEEE), 4362–4364. doi:10.1109/IGARSS.2003.1295516

Yang, W. T., Fang, J., and Liu-Zeng, J. (2021). Landslide-lake outburst floods accelerate downstream hillslope slippage. *Earth Surf. Dynam.* 9, 1251–1262. doi:10.5194/esurf-9-1251-2021

Yang, W. T., Liu, L. Y., and Shi, P. J. (2020a). Detecting precursors of an imminent landslide along the Jinsha River. *Nat. Hazards Earth Syst. Sci.* 20, 3215–3224. doi:10.5194/nhess-20-3215-2020

Yang, W. T., Wang, Y. J., Wang, Y. Q., Ma, C., and Ma, Y. H. (2020b). Retrospective deformation of the Baige landslide using optical remote sensing images. *Landslides* 17, 659–668. doi:10.1007/s10346-019-01311-7

Yang, Z. F., Li, Z. W., Zhu, J. J., Preusse, A., Hu, J., Feng, G. C., et al. (2018). Time-series 3-D mining-induced large displacement modeling and robust estimation from a single-geometry SAR amplitude data set. *IEEE Trans. Geosci. Remote Sens.* 56, 3600–3610. doi:10.1109/TGRS.2018.2802919

Zhang, J. M., Zhu, W., Cheng, Y. Q., and Li, Z. H. (2021). Landslide detection in the linzhi–ya'an section along the sichuan–tibet railway based on InSAR and hot spot analysis methods. *Remote Sens.* 13, 3566. doi:10.3390/rs13183566

Zhang, S. L., Yin, Y. P., Hu, X. W., Wang, W. P., Zhang, N., Zhu, S. N., et al. (2020a). Dynamics and emplacement mechanisms of the successive Baige landslides on the upper reaches of the Jinsha River, China. *Eng. Geol.* 278, 105819. doi:10.1016/j.enggeo.2020.105819

Zhang, Y., Meng, X. M., Dijkstra, T. A., Jordan, C. J., Chen, G., Zeng, R. Q., et al. (2020b). Forecasting the magnitude of potential landslides based on InSAR techniques. *Remote Sens. Environ.* 241, 111738. doi:10.1016/j.rse.2020.111738

Zhong, Y., Chen, G., Meng, X. M., Yue, D. X., Zhang, Y., Guo, F. Y., et al. (2022). Analysis of the transformation mechanism and prediction of a landslide debris flow multi-hazards chain in an alpine canyon area: a case study in Zhouqu. *J. Lanzhou Univ. Nat. Sci.* 58 (3). doi:10.13885/j.issn.0455-2059.2022.03.012

Zhu, D. F., Song, K., Mu, J. C., Huang, H. F., Du, H. J., Fanzhe, X. Z., et al. (2021). Effect of climate change induced extreme precipitation on landslide activity in the Three Gorges Reservoir, China. *Bull. Eng. Geol. Environ.* 80, 781–794. doi:10.1007/s10064-020-01948-y

frontiers | Frontiers in Earth Science

TYPE Original Research
PUBLISHED 26 March 2024
DOI 10.3389/feart.2024.1302553

OPEN ACCESS

EDITED BY
Hans-Balder Havenith,
University of Liège, Belgium

REVIEWED BY
Danny Love Wamba Djukem,
Chengdu University of Technology, China
Maheshreddy Gade,
Indian Institute of Technology Mandi, India

*CORRESPONDENCE
Guoliang Du,
✉ 756591925@qq.com

RECEIVED 26 September 2023
ACCEPTED 26 February 2024
PUBLISHED 26 March 2024

CITATION
Yang Z, Du G, Zhang Y, Xu C, Yu P, Shao W and Mai X (2024), Seismic landslide hazard assessment using improved seismic motion parameters of the 2017 Ms 7.0 Jiuzhaigou earthquake, Tibetan Plateau.
Front. Earth Sci. 12:1302553.
doi: 10.3389/feart.2024.1302553

Seismic landslide hazard assessment using improved seismic motion parameters of the 2017 Ms 7.0 Jiuzhaigou earthquake, Tibetan Plateau

Zhihua Yang[1,2], Guoliang Du[3]*, Yangshuang Zhang[4], Chong Xu[5], Pengfei Yu[4], Weiwei Shao[1,6] and Ximao Mai[1,6]

[1]Institute of Geomechanics, Chinese Academy of Geological Sciences, Beijing, China, [2]Key Laboratory of Active Tectonics and Geological Safety, Ministry of Natural Resources, Beijing, China, [3]School of Urban Geology and Engineering, Hebei GEO University, Shijiazhuang, China, [4]School of Engineering and Technology, China University of Geosciences (Beijing), Beijing, China, [5]National Institute of Natural Hazards, Ministry of Emergency Management of China, Beijing, China, [6]Faculty of Engineering, China University of Geosciences, Wuhan, China

Seismic landslide hazard assessment plays a very important guiding role during urgent earthquake relief. In August 2017, an Ms 7.0 earthquake in Jiuzhaigou County, Sichuan Province, China, triggered thousands of landslides. Based on the analysis of geological settings and coseismic landslide characteristics, the Newmark model is used to complete the seismic landslide hazard assessment. Three seismic motion parameters, namely, peak ground acceleration (PGA), traditional Arias intensity (Arias_P), and improved Arias intensity (Arias_C), are adopted. A publicly published coseismic landslide catalog is used as the validation samples. The results show that the coseismic landslides are mainly distributed in the deep gullies and steep mountainous slopes on the north and south sides of the epicenter. The seismic landslide hazard accuracy based on Arias_C is the best, followed by that based on PGA and Arias_P. The spatial distribution of seismic landslide hazards based on Arias_C shows an almost standard elliptical ring and is in good agreement with that of coseismic landslides. These results fully reflect the combined influence of the epicenter and seismogenic fault on landslide development. The middle seismic landslide hazard and over are mainly located at areas with seismic intensity of VII degree and above. The Arias intensity is very suitable for rapid seismic landslide hazard assessment in emergency situations. The study results can provide scientific and technological support for rapid earthquake relief and have reference significance for future seismic landslide hazard assessment.

KEYWORDS

seismic landslide, Jiuzhaigou earthquake, landslide hazard assessment, Newmark model, peak ground acceleration and Arias

Introduction

The seismic landslide is one of the important geo-hazard types, which seriously enhances the damaging effect of earthquake-induced disasters. The spatial distribution characteristics, formation mechanism, and causative factor sensitivity of a lot of seismic landslide cases

have been analyzed in depth. Many valuable methods and models have been established and widely used in the seismic landslide hazard assessment at a regional scale, such as the multi-criteria evaluation method (Kamp et al., 2008), artificial neural network (Yilmaz, 2010; Nayek and Gade, 2022), support vector machine (Yao et al., 2008), Bayesian network (Song et al., 2012), logistic regression (Nefeslioglu et al., 2006), and transfer learning (Ai et al., 2022). Based on the limit equilibrium theory of infinite slope, the Newmark displacement model was developed to conduct seismic landslide hazard assessment (Wilson and Keefer, 1983; Miles and Ho, 1999). Based on many research results of the statistical laws of seismic landslides, the simplified regression-based Newmark displacement model (Jibson, 2007; Chousianitis et al., 2014; Pareek et al., 2014; Gade et al., 2021; Nayek and Gade, 2022; Cheng et al., 2023) and various statistical probability models (Rathje and Saygili, 2008; Du and Wang, 2014; Nowicki et al., 2014; Du and Wang, 2016) were established. The simplified regression-based Newmark displacement model is applicable and can quickly conduct the seismic landslide hazard assessment at a regional scale, and has been widely used all over the world (Liu et al., 2018; Ma and Xu, 2019; Nayek and Gade, 2021; Zeng et al., 2023).

On 8 August 2017, an Ms 7.0 earthquake occurred in Jiuzhaigou County, Sichuan Province, China, with the epicenter at E103.82° and N33.20° and a focal depth of 20 km. The maximum seismic intensity was IX degree. The area with seismic intensity of VII degree and above covers approximately 4,294.81 km^2, and the major axis of the isoseismal line generally shows an NW direction. As of 14 August 2017, a total of 3,704 aftershocks were recorded, which included three aftershocks with magnitudes 4.0–4.9 and 27 aftershocks with magnitudes 3.0–3.9. The largest aftershock with magnitude 4.8 occurred in Jiuzhaigou County on 9 August 2017 (National Earthquake Data Center, https://data.earthquake.cn/gxdt/info/2017/39880.html). The Jiuzhaigou earthquake had triggered thousands of collapses and landslides (Li et al., 2019; Ling et al., 2021; Cai et al., 2022), which resulted in heavy casualties and damage to transportation, power, communications, buildings, and other infrastructures. After the earthquake, studies on landslide investigation and assessment were carried out in time (Fan et al., 2018; Tian et al., 2019), which effectively guided the emergency relief and reduced earthquake disaster losses.

In the existing studies on deterministic seismic landslide hazard assessment using Newmark displacement, the adopted seismic motion parameters rarely consider the influence of seismogenic faults (Nayek and Gade, 2021; Zeng et al., 2023), and it only has fewer applications in probabilistic seismic landslide hazard assessment (Zhang et al., 2017; Liu et al., 2018). However, the seismogenic fault has a significant control effect on coseismic landslide development (Gorum and Carranza, 2015; Fan et al., 2018). So, taking the Jiuzhaigou earthquake as a typical example, the simplified regression-based Newmark displacement model and three kinds of seismic motion parameters are used to carry out the seismic landslide hazard assessment. The assessment results are validated by taking the coseismic landslide as test samples. The result accuracy based on three kinds of seismic motion parameters [peak ground acceleration (PGA), traditional Arias intensity (Arias_P), and improved Arias intensity (Arias_C)] is compared and analyzed to elaborate the significant effect of the seismogenic fault on seismic landslide development. The study ideas and results have significant reference for promoting rapid seismic landslide hazard assessment during emergency earthquake relief.

Study area

The eastern margin of the Qinghai–Tibet Plateau is characterized by strong tectonic and fault activities, extremely complex stress fields, and frequent strong earthquakes, such as the Ms 8.0 Wenchuan earthquake in 2008 (Dai et al., 2011), the Ms 7.0 Lushan earthquake in 2013 (Zhang et al., 2013), and the Ms 6.8 Luding earthquake in 2023 (Dai et al., 2023). These strong earthquakes have triggered many landslides and their chain hazards. The Jiuzhaigou earthquake occurred in the northeast margin of the Bayankela block and the middle of the famous North–South (NS) seismic tectonic belt, where the developed active faults mainly include the Minjiang fault, Tazang fault, and Huya fault (Figures 1, 2). The Minjiang fault is a Quaternary thrust and strike-slip fault with a total length of approximately 170 km, with a general NS trend and NW dip direction (Deng et al., 1994). It has been highly active since the late Pleistocene, with a strike-slip rate of approximately 1 mm/y. The Zhenjiangguan–Lianghekou section of the Minjiang fault is the most active since the late Quaternary and even the Holocene, where the most recent event was the Ms 7.5 Diexi earthquake in 1933. The Tazang fault is the east branch of the East Kunlun fault zone, with a total length of 170 km and a general NW trend, and is the northeast boundary of the Bayankela block. The late Quaternary activities of the Tazang fault are segmented and multiphase, with dominated horizontal shear movement in the west section and gradually decreasing strike-slip movement and an increasing vertical component in the east section (Ren et al., 2013). The Huya fault is a Quaternary thrust and left strike-slip fault, with a general NNW trend and a vertical slip rate of approximately 0.5 mm/y and left strike-slip rate of approximately 1.4 mm/y (Qi et al., 2018). There have been many strong historical earthquakes in the Huya fault zone, such as the Ms 6¾ Xiaohe earthquake in 1630 and the Ms 7.2 earthquake between Songpan County and Pingwu County in 1976.

The seismogenic fault of the Jiuzhaigou earthquake is the northern section of the Huya fault. The direction of the maximum principal stress around the Jiuzhaigou earthquake is NWW-SEE, which is consistent with the direction of the regional stress field, indicating that the Jiuzhaigou earthquake is mainly controlled by regional stress (Sun et al., 2018). The Jiuzhaigou earthquake is in the Pingwu potential seismic-prone area in western China, which has the seismic geological conditions for the occurrence of large earthquakes, with the upper limit of magnitude 7.5. The Jiuzhaigou earthquake is in the transition zone from the Sichuan Basin to west Sichuan Plateau, which belongs to the middle–high mountainous erosion landform. Its regional terrain is high in the northwest and low in the southeast, with an average altitude of more than 4,000 m.

Here, the Jiuzhaigou earthquake area mainly includes areas with seismic intensity of VI and above (Figure 2), which extends to the Diebu County in the north, Pingwu County in the south, Wenxian County in the east, and Ruoergai County in the west. The black

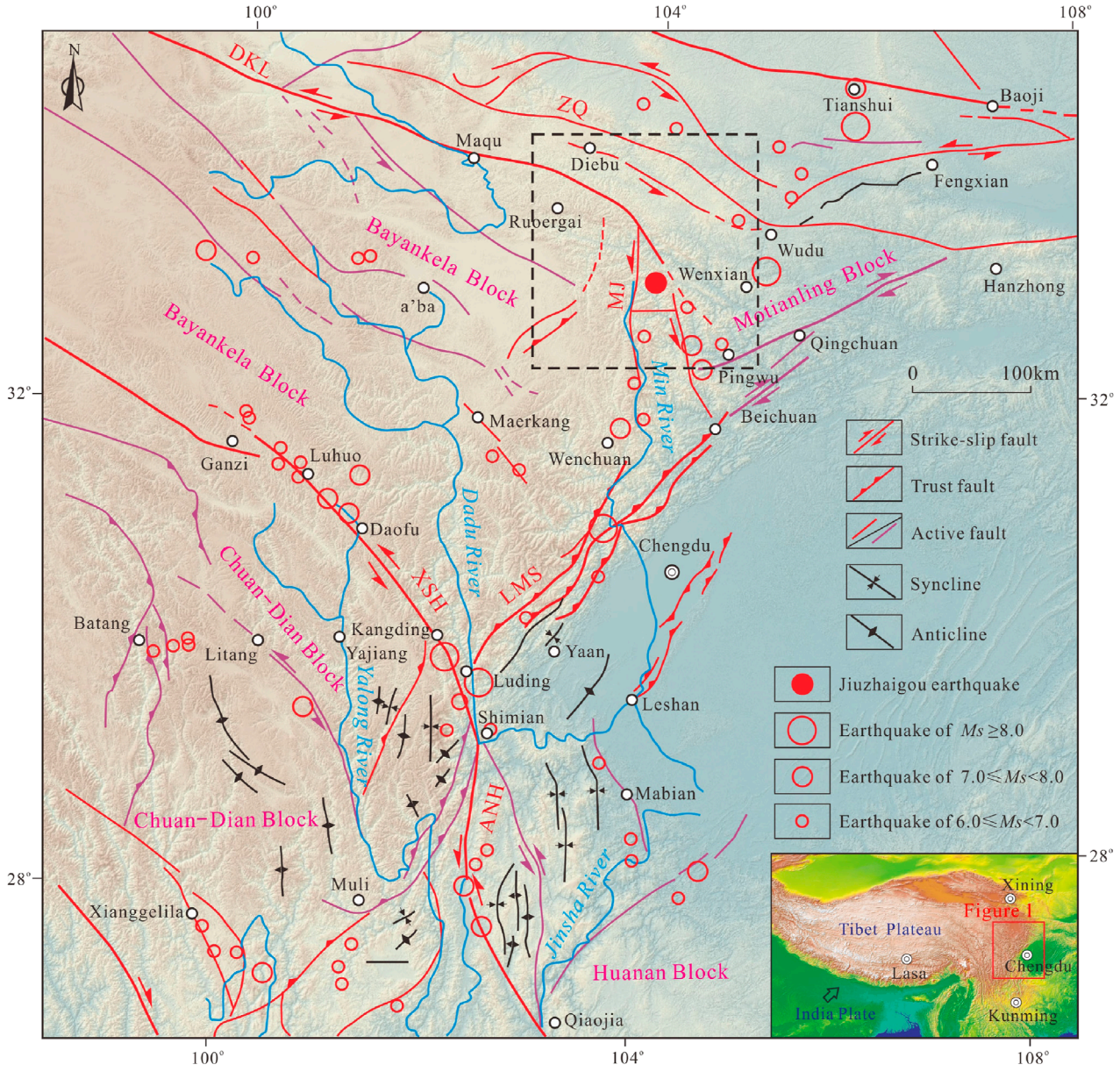

FIGURE 1
Schematic diagram of regional major active structures in the eastern Qinghai–Tibet Plateau. The black dashed rectangular box is the scope of Figure 2. DKL is the Dongkunlun fault zone, ZQ is the Zhouqu fault zone, MJ is the Minjiang fault zone, XSH is the Xianshuihe fault zone, LMS is the Longmenshan fault zone, and ANH is the Anninghe fault zone. The fault data are obtained from the 1:500,000 geological maps.

dashed rectangular box shown in Figure 2 was selected as the main assessment area to conduct seismic landslide hazard assessment, which is the scope of Figures 5–13 and extends to the Yuwa town in the north, Huanglong town in the south, Shuanghe town in the east, and the Baozuo town in the west.

Data and methods

Basic data such as seismic motion parameters, geology, topography, and coseismic landslides and the simplified Newmark model are used to carry out the landslide hazard assessment for the Jiuzhaigou earthquake.

Data

The geographical, geological, and surveying data are used to realize the presented study work. The regional tectonic and active fault data are obtained from the geological cloud website of the China Geological Survey (https://geocloud.cgs.gov.cn/#/home). The regional historical earthquake data and

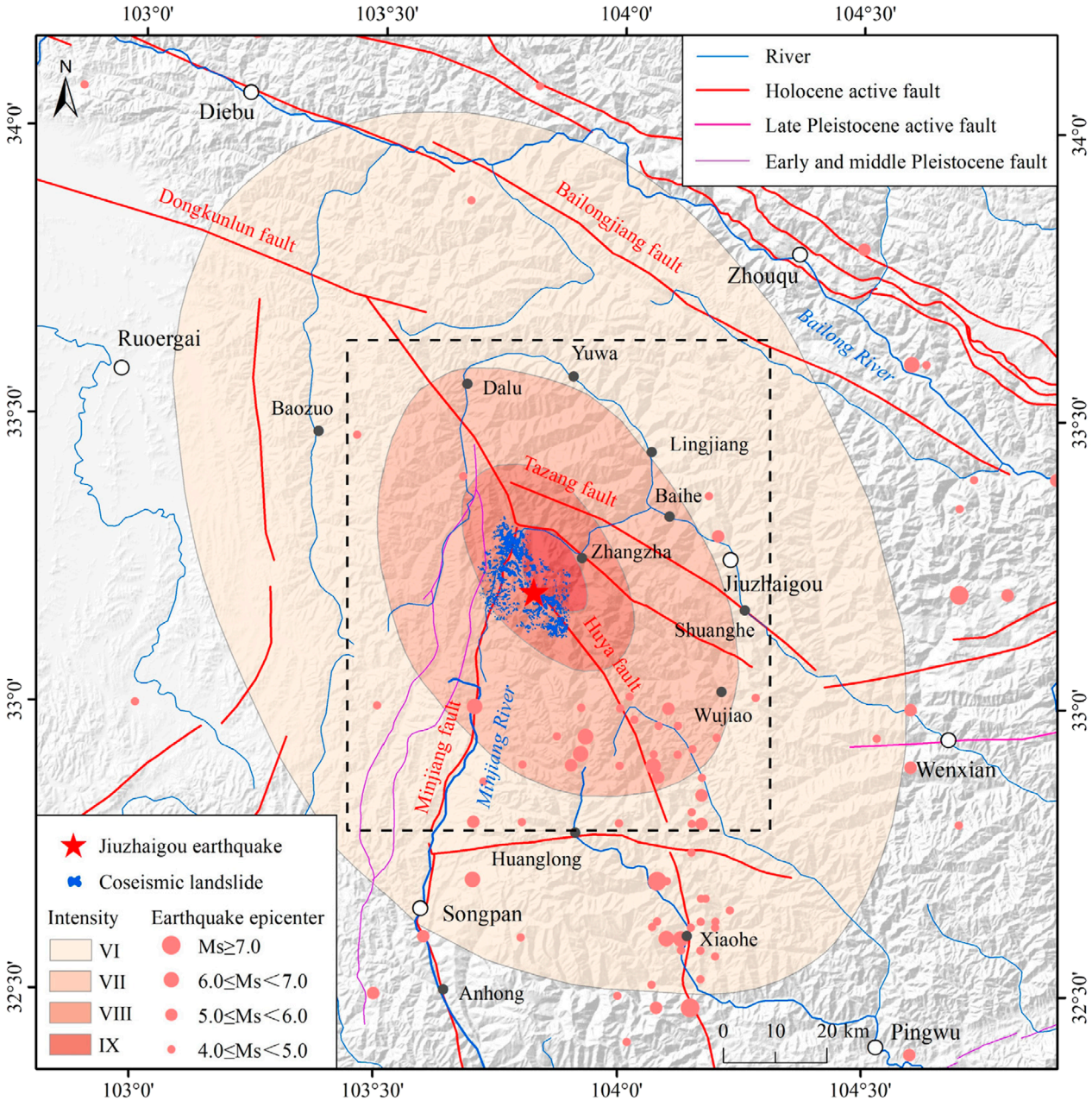

FIGURE 2
Seismic intensity, epicenter, and coseismic landslides of the Ms 7.0 Jiuzhaigou earthquake. The black dashed rectangular box indicates the main assessment area and is the scope of Figures 5–13. The fault data are obtained from the 1:200,000 geological maps.

Jiuzhaigou earthquake parameters (epicenter, seismic intensity, and aftershock) are obtained from the National Earthquake Data Center (https://data.earthquake.cn/index.html). The stratigraphic lithology data used to divide the engineering geological units are obtained from the 1:200,000 geological maps. The PGA data of the Jiuzhaigou earthquake are obtained from the Strong Motion Observation Data Subcenter of the National Earthquake Data Center and related references (Yue et al., 2018). The terrain elevation data [digital elevation model (DEM)] adopt the ASTER GDEM V3 with a spatial resolution of 30 m (https://search.asf.alaska.edu/#/), from which the terrain slope data can be calculated. The publicly published coseismic landslide data triggered by the Jiuzhaigou earthquake are obtained from Tian et al. (2019), whose acquisition methods are mainly remote sensing interpretation and field verification. The vector data (such as polygon data) are converted into raster data for use in the algebraic calculations of the spatial layer, and the resolution of the raster data is 30 m. All vector and raster data operations and calculations are implemented on the ArcGIS Platform.

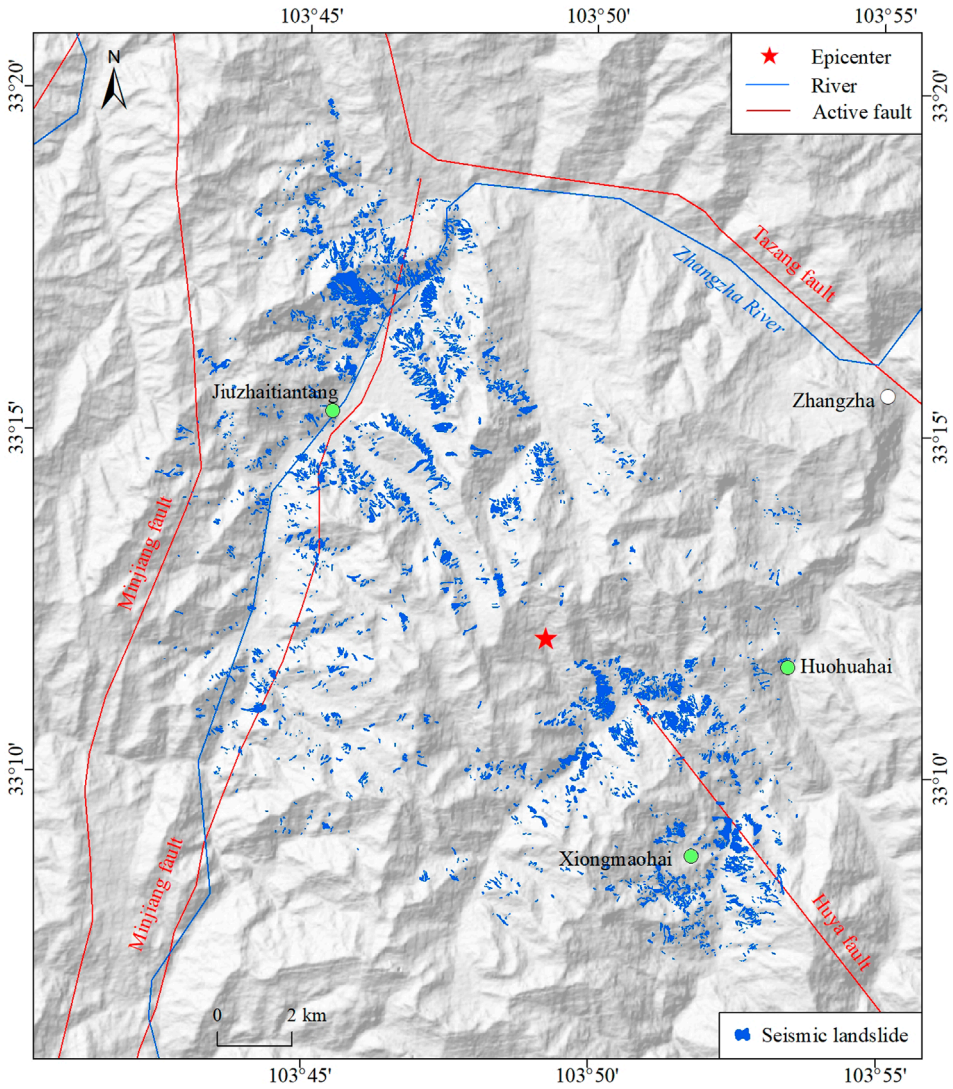

FIGURE 3
Spatial distribution of coseismic landslides triggered by the Ms 7.0 Jiuzhaigou earthquake. Landslide data are obtained from Tian et al. (2019).

Methods

The Newmark model can predict seismic landslide hazards by calculating the slope displacement under seismic loading (Newmark, 1965). Its theoretical basis is the limit equilibrium theory of infinite slope. The Newmark model regards the sliding body as a rigid body and mainly considers the critical acceleration and safety factor of the sliding body itself. When the external force is greater than the critical acceleration, the finite displacement of the sliding body occurs, which accumulates continuously to produce permanent displacement (Jibson, 1993; Roberto, 2000). Based on many statistical analysis results of seismic landslides, a simplified Newmark displacement model based on statistical laws was developed (Miles and Ho, 1999; Jibson et al., 2000) and has been widely used in seismic landslide hazard assessment at the regional scale (Maharjan et al., 2021). Referring to the existing study results, the general calculation steps of the simplified Newmark model are sorted out.

Firstly, the static safety factor is calculated. The static safety factor represents the safety situation of a slope body without internal and external dynamic effects, which can be calculated by the traditional slope stability factor formula (Eq. 1) based on the limit equilibrium theory (Miles and Ho, 1999; Jibson et al., 2000). In Eq. 1, F_s is the slope static safety factor, c' is the effective cohesion of rock and soil mass (kPa), φ' is the effective internal friction angle of rock and soil mass (°), γ is the unit weight of rock and soil mass (kN/m^3), γ_w is the unit weight of groundwater (kN/m^3), t is the thickness of the potential sliding body (m), α is the inclination angle of the potential sliding surface (°), and m is the proportion of the saturated part of the total potential sliding body.

FIGURE 4
Typical landslides triggered by the Ms 7.0 Jiuzhaigou earthquake. Landslide figures are obtained from the web and from Fan et al. (2018) and Ling et al. (2021).

$$F_s = \frac{c'}{\gamma t \sin\alpha} + \frac{\tan\varphi'}{\tan\alpha} - \frac{m\gamma_w \tan\varphi'}{\gamma \tan\alpha} = \frac{c'}{\gamma t \sin\alpha} + \left(1 - \frac{m\gamma_w}{\gamma}\right) \times \frac{\tan\varphi'}{\tan\alpha}. \quad (1)$$

Secondly, the critical acceleration is calculated. The slope critical acceleration refers to the seismic motion acceleration corresponding to the sliding force of the slider equal to the anti-sliding force. The calculation formula (Eq. 2) of the slope critical acceleration was derived from the limit equilibrium state equation of the potential slider (Wilson and Keefer, 1983). In Eq. 2, a_c is the critical acceleration (m/s^2), g is the gravity acceleration (m/s^2), and α is the inclination angle of the sliding surface (°).

$$a_c = (F_s - 1)g \sin\alpha. \quad (2)$$

Finally, the seismic slope displacement and seismic landslide hazard are calculated. The seismic slope displacement can be calculated by the slope critical acceleration and PGA (Eq. 3) proposed by Jibson (2007). Based on the statistical analysis of a large number of existing study results, the seismic slope displacement can also be expressed as a functional relationship between the slope critical acceleration and the Arias intensity (Eq. 4) (Jibson et al., 2000; Jibson, 2007). The seismic slope displacement is positively correlated with the PGA and Arias intensity and negatively correlated with the slope critical acceleration. There are no precise conditions for using either the PGA or Arias intensity. The seismic motion parameters can be selected based on their accessibility. In Eqs 3, 4, D_n is the slope displacement, a_{max} is the PGA, and I_a is the Arias intensity.

$$\log D_n = 0.215 + \log\left[\left(1 - \frac{a_c}{a_{max}}\right)^{2.341}\left(\frac{a_c}{a_{max}}\right)^{-1.438}\right] \pm 0.510, \quad (3)$$

$$\lg D_n = 2.401 \lg I_a - 3.481 \lg a_c - 3.230. \quad (4)$$

The slope displacement does not mean that there will be a significant landslide. Only when the slope displacement accumulates to a certain extent, do the slope masses lose their stability and slide along the sliding surface to cause a landslide. Therefore, the landslide occurrence is a probability problem. The seismic landslide probability can be calculated using the statistical relationship formula (Eq. 5) proposed by Jibson et al. (2000). In Eq. 5, $P(f)$ is the seismic landslide probability.

$$P(f) = 0.335\left[1 - \exp\left(-0.048 D_n^{1.565}\right)\right]. \quad (5)$$

10.3389/feart.2024.1302553

TABLE 1 Physical and mechanical parameters of engineering geological units in the main assessment area.

ID	Engineering geological units	c′ (KPa)	φ' (°)	γ (KN/m^3)
1	Relatively hard to hard, medium-thick-bedded sandstone interbedded with conglomerate, mudstone, and slate	35	36	23
2	Alternate of soft and hard, medium-thick-bedded sandstone and mudstone interbedded with limestone	32	34	21
3	Soft to relatively hard and thin-bedded to medium-thick-bedded sandstone and mudstone	31	33	20
4	Soft thin-bedded mudstone and shale	30	32	18
5	Hard medium-thick-bedded limestone and dolomite	35	37	25
6	Relatively hard, thin-bedded to medium-thick-bedded limestone and argillaceous limestone	34	36	23
7	Alternate of soft and hard, medium-thick-bedded limestone and dolomite interbedded with sandstone and mudstone	32	34	20
8	Relatively hard to hard, thin-bedded to medium-thick-bedded slate, phyllite, and metamorphic sandstone	30	33	19
9	Soft to relatively hard, thin-bedded to medium-thick-bedded phyllite and schist interbedded limestone, sandstone, and volcanic rocks	29	32	18
10	Hard blocky granite, andesite, and diorite	36	38	28
11	Soft loose sediments and deposits	27	30	16

Note: ID is the corresponding number of engineering geological units in Figure 5, c′ is the effective internal cohesion, φ' is the effective internal friction angle, and γ is the weight of rock masses.

Seismic landslide characteristics

Remote sensing interpretation and field investigation reveal that there are 4,834 coseismic landslides in the Jiuzhaigou earthquake area (Figures 2, 3). The total landslide area is 9.64 km^2, and the largest landslide area is 0.24 km^2 (Tian et al., 2019). The coseismic landslides are mainly distributed in areas with seismic intensity of VII degree and above. These landslides are mainly composed of small- and medium-sized shallow fractured landslides, collapses, rockfalls, and rock/debris slides (Figure 4). Many shallow coseismic landslides are mostly developed in the Quaternary deposits such as residual slope deposits. The instability of rock masses occurs at the slope shoulders, forming the landslide–debris flow disaster chain. The coseismic landslides mainly develop along roads and gullies. The landslide density is relatively high in the two NE-SW-oriented valleys close to the epicenter (Fan et al., 2018; Tian et al., 2019). The

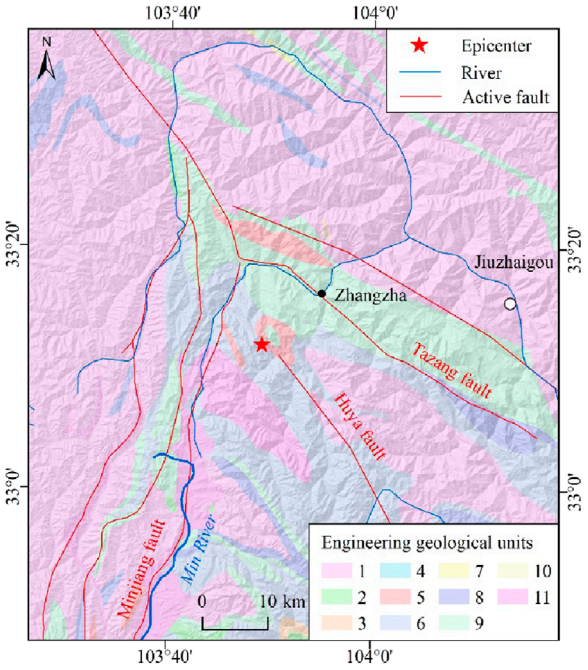

FIGURE 5
Engineering geological units in the main assessment area. The number of engineering geological units in the legend corresponds to ID in Table 1.

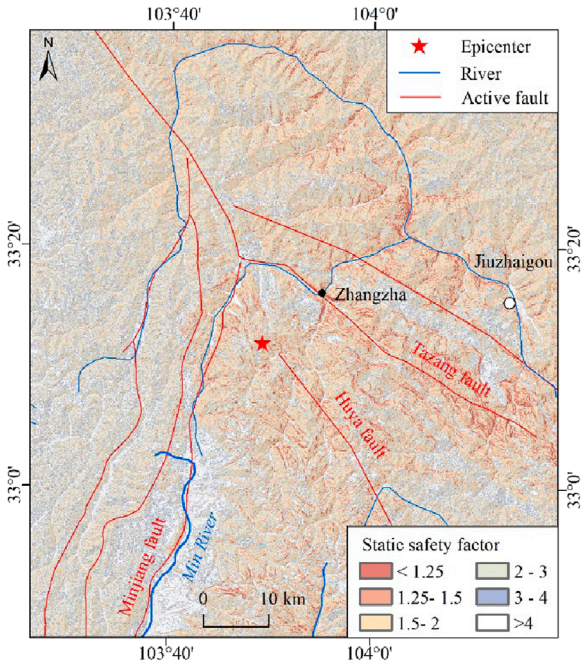

FIGURE 6
Slope static safety factor in the main assessment area.

highest coseismic landslide density was found at special locations where the valley shape evolves from the U-shape to V-shape, with an inclination between 20° and 50° (Chang et al., 2021). The

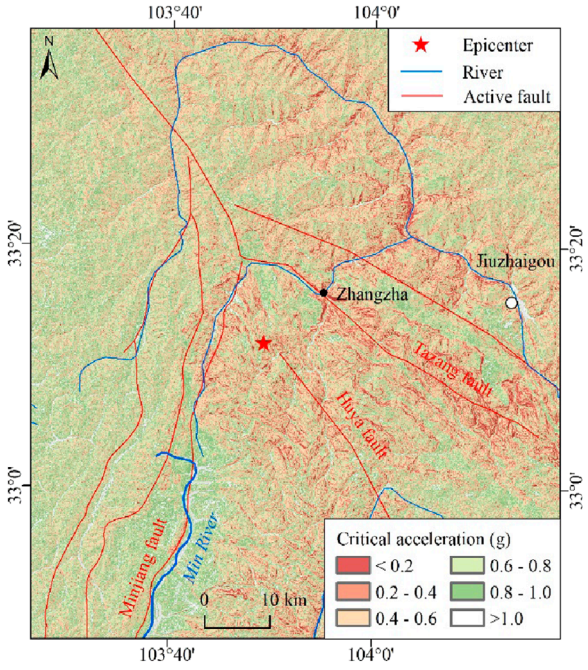

FIGURE 7
Slope critical acceleration in the main assessment area.

coseismic landslides are mainly distributed in a strip area with NW-SE trending. The spatial distribution pattern of coseismic landslides has revealed that a previously unknown blind fault segment (which is possibly the north-western extension of the Huya fault) is the plausible seismogenic fault (Fan et al., 2018). The inferred result of the seismogenic fault suggests that seismic energy is released concentratedly near the epicenter and along the fault.

Results and analysis

Based on the presented data, model, and seismic landslide characteristics, the seismic landslide hazard can be calculated, validated, and analyzed.

Result calculation

The seismic motion parameters such as the PGA and two types of Arias intensity are obtained to calculate seismic landslide hazard in the main assessment area.

Static safety factor

The physical and mechanical parameters of the rock and soil mass and terrain parameters are crucial for calculating the slop static safety factor. Comprehensively considering the geological structure, stratigraphic lithology, rock and soil type, and rock mass weathering degree, the engineering geological units in the main assessment area were divided into 11 types (Figure 5; Table 1). With reference to

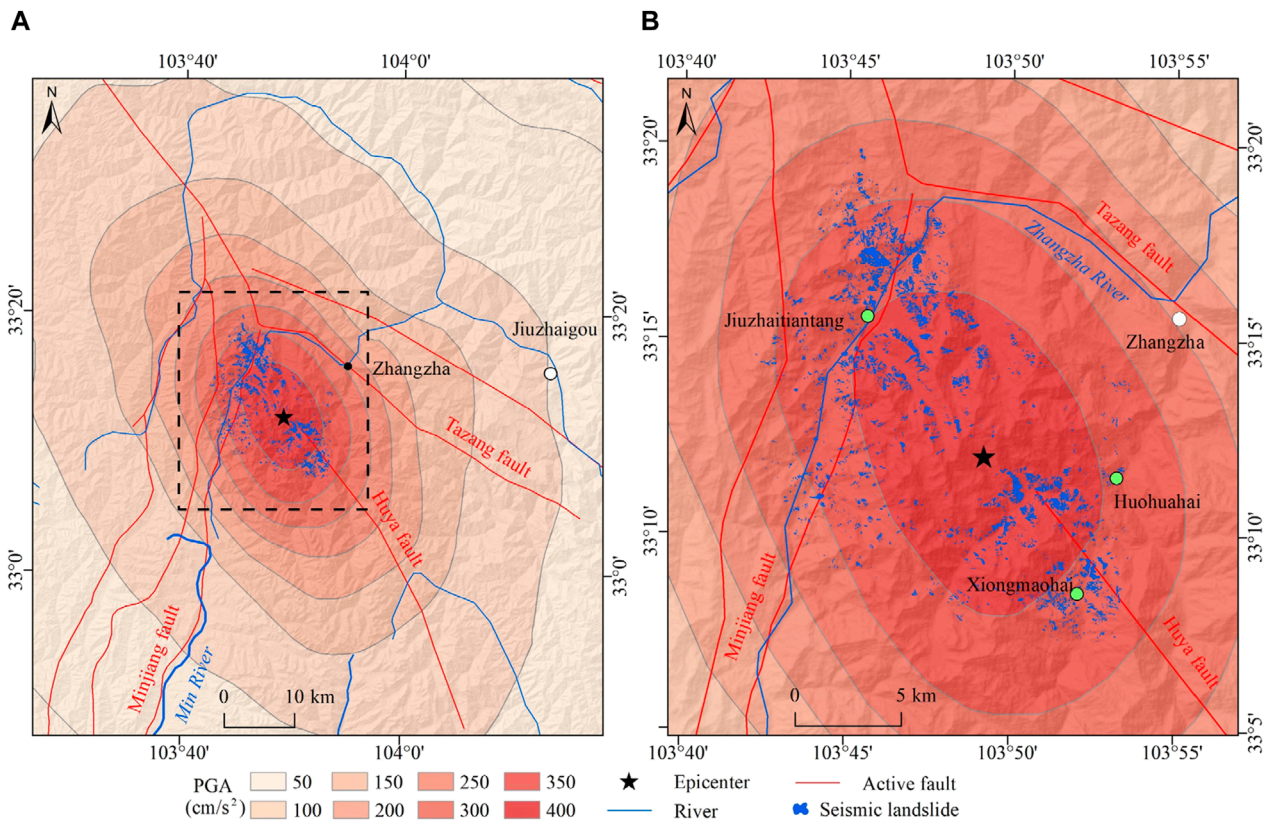

FIGURE 8
Peak ground acceleration in the main assessment area. The black dashed rectangular box in **(A)** is the scope of **(B)**.

the existing literature (Jibson et al., 2000; Jibson, 2007; Hua et al., 2018; Yang et al., 2023), the physical and mechanical parameters for all engineering geological units were carefully initialized (Table 1). The terrain slope angle (α) was calculated from the DEM data. The thickness of the potential sliding body (t) was approximately set to 3 m for shallow landslides. The parameter γ_w was approximately 10 kN/m^3. Considering the local climate and geological conditions, as well as the existing research results on seismic landslide hazards in the Xianshuihe fault zone (Zhang et al., 2017), the parameter m was approximately 0.3. The slope static safety factor was finally calculated using Eq. 1, as shown in Figure 6. The slope static safety factor in the western plateau region with a relatively flat terrain is larger, while it is smaller in the central and eastern mountainous regions with a relatively large topographic relief.

Critical acceleration

The critical acceleration can represent the landslide sensitivity, and the smaller the static safety factor, the greater the landslide sensitivity. According to the slope static safety factor and terrain slope angle obtained above, the slope critical acceleration in the Jiuzhaigou earthquake area is calculated using Eq. 2, as shown in Figure 7. The smaller the slope static safety factor is, the smaller is the critical acceleration and the more unstable is the slope.

Seismic motion parameters

The Newmark model is compatible with a variety of seismic motion parameters (Jibson et al., 2000; Jibson, 2007; Zeng et al., 2023). The seismic motion parameters should be comprehensively selected according to seismic geological settings and seismogenic mechanisms. Here, the PGA and two types of Arias intensity parameters are adopted.

During the Jiuzhaigou earthquake, the China Earthquake Administration recorded the strong motion observation data. For example, the Baihe strong motion station in the Jiuzhaigou county is 30.5 km away from the epicenter, and its maximum PGA values in the east–west, north–south, and vertical directions are 129.5, 185.0, and 124.7 cm/s^2, respectively (National Earthquake Data Center, https://data.earthquake.cn/). Using these valuable strong motion observation data, the PGA contour of the Jiuzhaigou earthquake area is fitted (Figure 8) (Yue et al., 2018).

The Arias intensity (I_a) is a meaningful physical quantity to measure seismic intensity, which is determined by integrating the square of seismic acceleration within the duration of a strong earthquake and multiplying by a constant (Arias, 1970). At the regional scale, several complex empirical attenuation equations are developed to calculate the Arias intensity with the rupture distance parameter (Travasarou et al., 2003; Fulser-Piggott and Stafford, 2012). However, these equations require complex conditions and parameters, such as fictitious hypocentral depth, indicator variables

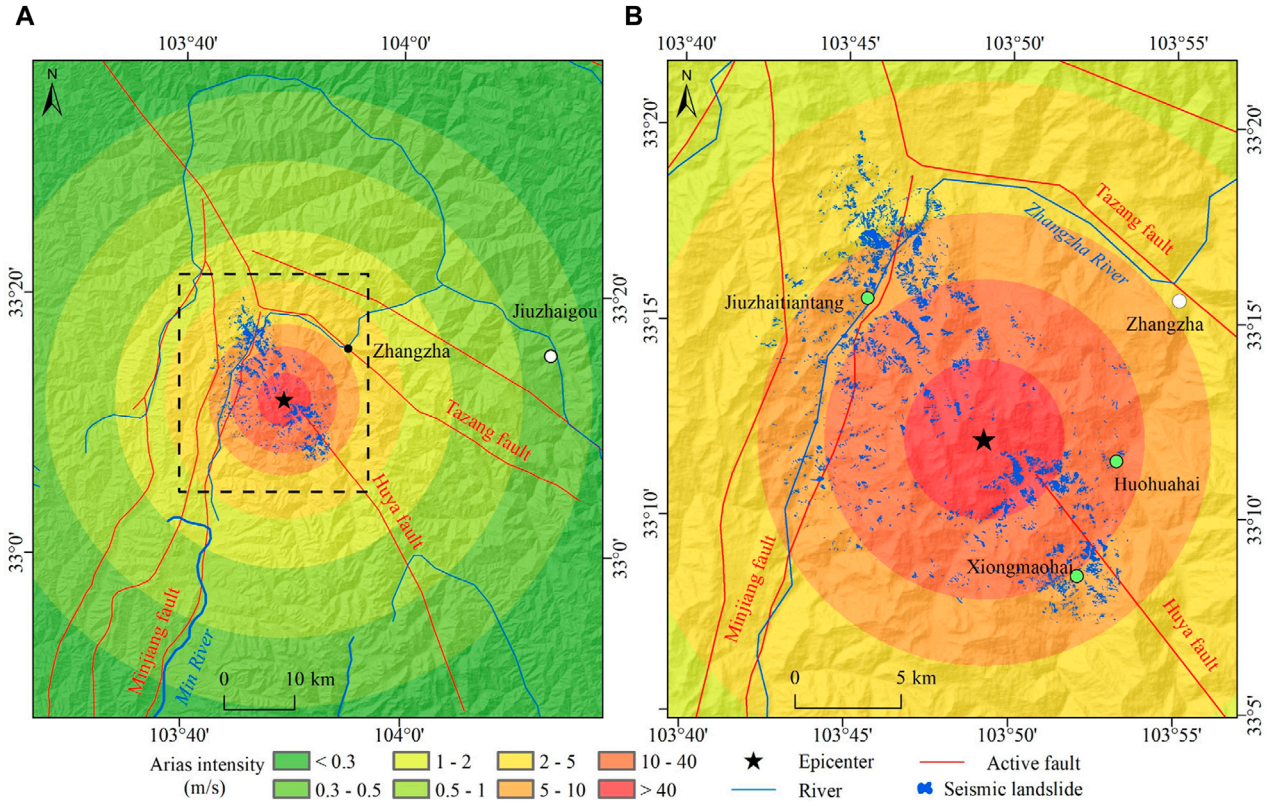

FIGURE 9
Arias intensity in the main assessment area (point focal source). The black dashed rectangular box in **(A)** is the scope of **(B)**.

for the soil types, indicator variables for the fault types, and average shear wave velocity. It is difficult to obtain these complex parameters in the process of urgent and rapid coseismic landslide hazard assessment. Here, the simplest empirical equation (Eq. 6) based on statistical laws is adopted, which only requires the seismic moment magnitude (M_w) and focal distance (R) (Wilson and Keefer, 1985). The focal distance is the closest distance from a particular site to the seismic source. The seismic moment magnitude can be obtained by converting the surface wave magnitude (Ms) (Eq. 7).

$$\lg I_a = \begin{cases} M_w - 2\lg R - 4.1 & M_w \le 7.0 \\ 0.75M_w - 2\lg R - 2.35 & M_w > 7.0 \end{cases}, \quad (6)$$

$$M_w = 0.884M_s + 0.951. \quad (7)$$

The epicenter of the Jiuzhaigou earthquake is used as the point focal source to calculate the focal distance using the buffer analysis method. The surface wave magnitude of the Jiuzhaigou earthquake is M_s 7.0, so the corresponding moment magnitude is M_w 6.9 using Eq. 7. The traditional Arias intensity with a point focal source (abbreviated as Arias_P) is calculated using Eq. 6, which is distributed in a circular shape in space (Figure 9). The seismic intensity, PGA, and landslides of the Jiuzhaigou earthquake all show a NW trending distribution. So, it can be inferred that the macroscopic seismic action is determined by both the epicenter and seismogenic fault. The existing study results suggest that the seismogenic fault of the Jiuzhaigou earthquake is the northern section of the Huya fault with left-lateral strike-slip characteristics. The rupture length of the seismogenic fault is approximately 33–35 km, and the rupture depth is approximately 23–26 km (Qi et al., 2018; Wang and Mao, 2022). The ground projection of the seismogenic fault is used as the linear focal source (Figure 10). The comprehensive focal distance, a kind of virtual focal distance that considers the combined influence of the point focal source (epicenter) and linear focal source (seismogenic fault), can be calculated by Eq. 8 (Zhang et al., 2017). In Eq. 8, R is the comprehensive focal distance, R_p is the point focal distance, and R_l is the linear focal distance. The Arias intensity with a comprehensive focal source (abbreviated as Arias_C) is calculated using the comprehensive focal distance (Figure 10), showing a NW trending elliptical distribution in space.

$$R = \frac{R_l\left(R_p + 1\right)R_{l\min}}{\left(R_l\left(R_p + 1\right)\right)_{\max}}. \quad (8)$$

Seismic landslide hazard

The seismic landslide hazard can be represented by seismic landslide probability. The seismic slope displacement was calculated using the slope critical acceleration (Figure 7) and PGA (Figure 8)

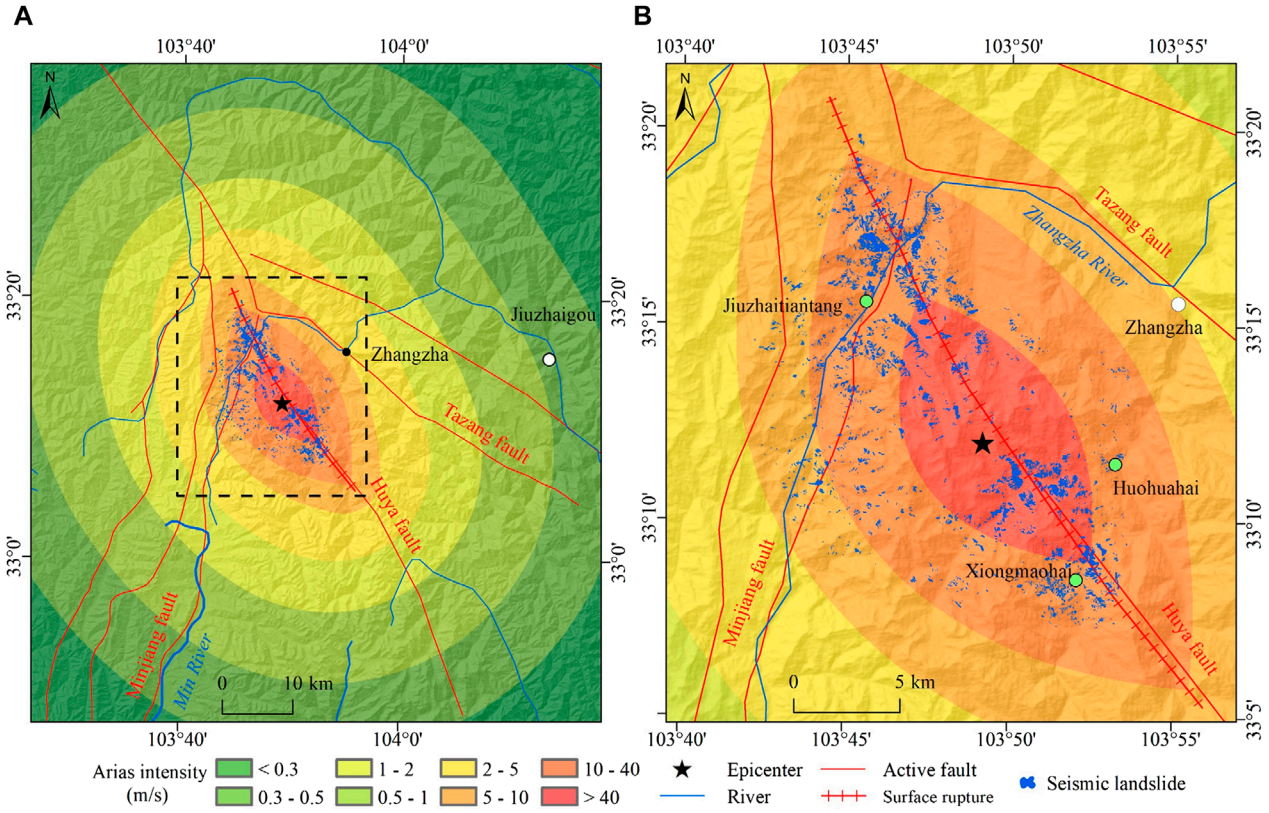

FIGURE 10
Arias intensity in the main assessment area (comprehensive focal source). The black dashed rectangular box in **(A)** is the scope of **(B)**.

in the main assessment area. Similarly, the slope critical acceleration (Figure 7), Arias_P (Figure 9), and Arias_C (Figure 10) were used to calculate the seismic slope displacement in the main assessment area. Then, the seismic landslide probability was calculated according to the seismic slope displacement. The natural break method in the ArcGIS and field experiences are used to divide the seismic landslide hazard into 5 grades: very high (seismic landslide probability ≥25%), high (seismic landslide probability 15%–25%), middle (seismic landslide probability 5%–15%), low (seismic landslide probability 1%–5%), and very low (seismic landslide probability <1%) (Figures 11–13).

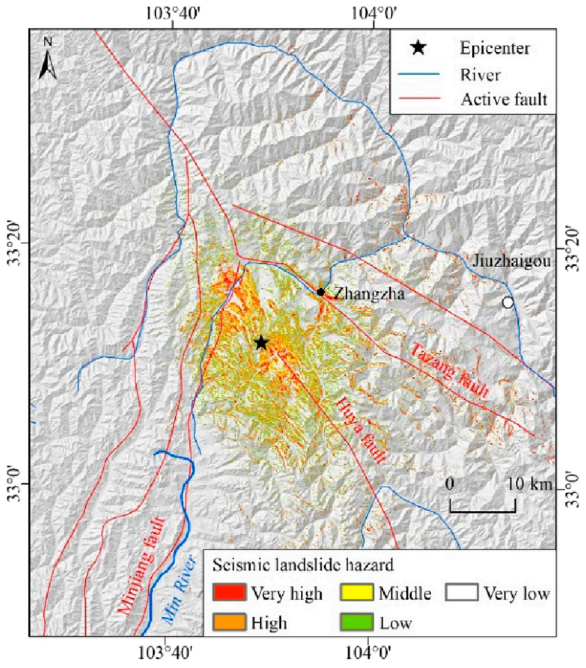

FIGURE 11
Seismic landslide hazard using peak ground acceleration (PGA) in the main assessment area.

Result validation

The receiver operating characteristic (ROC) curve method and the coseismic landslide samples (Figure 3) are adopted to validate the results of seismic landslide hazards. The area under the curve (AUC) is used to characterize the accuracy of the mathematical model (Yilmaz, 2010; Guo et al., 2015). It is generally believed that the closer the AUC is to 1, the better the model accuracy is. When the AUC is 0.5–0.7, the model accuracy is poor; when the AUC is 0.7–0.9, the model accuracy is good; and when the AUC is above 0.9, the model accuracy is excellent.

Based on the spatial statistical correlation between seismic landslide hazards and coseismic landslide samples, the seismic

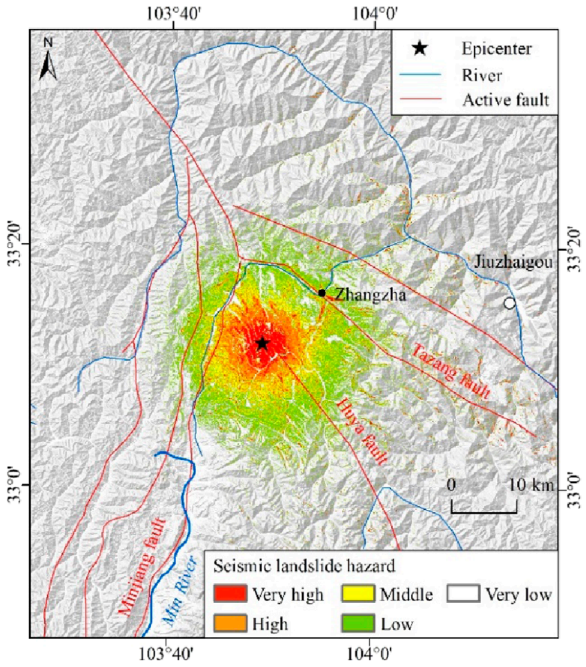

FIGURE 12
Seismic landslide hazard using the Arias intensity in the main assessment area (point focal source).

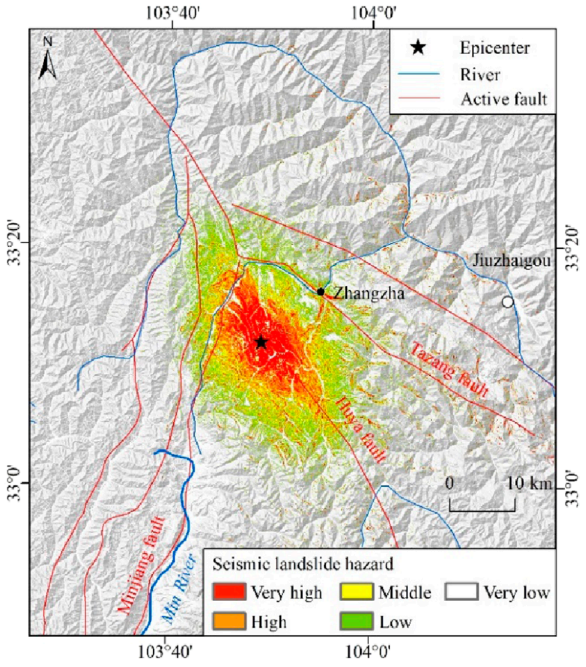

FIGURE 13
Seismic landslide hazard using the Arias intensity in the main assessment area (comprehensive focal source).

landslide hazard indexes were arranged in the descending order and divided into 50 bins. The accumulative area percentage with respect to 50 bins (as the horizontal coordinate) and their corresponding accumulative area percentage of coseismic landslide samples (as the vertical coordinate) were calculated. These values of the accumulative area percentage were used to draw the desired ROC curve and calculate the AUC (Figure 14) (Chung and Fabbri, 1999). With the increase in the accumulative area percentage, the corresponding accumulative area percentage of coseismic landslides increased rapidly at a faster rate, then increased slowly, and finally reached 100%. The accuracies of seismic landslide hazard results based on the PGA, Arias_P, and Arias_C are 0.79, 0.73, and 0.82, respectively. The accuracy of seismic landslide hazard results based on Arias_C is the highest, followed by that based on PGA and Arias_P.

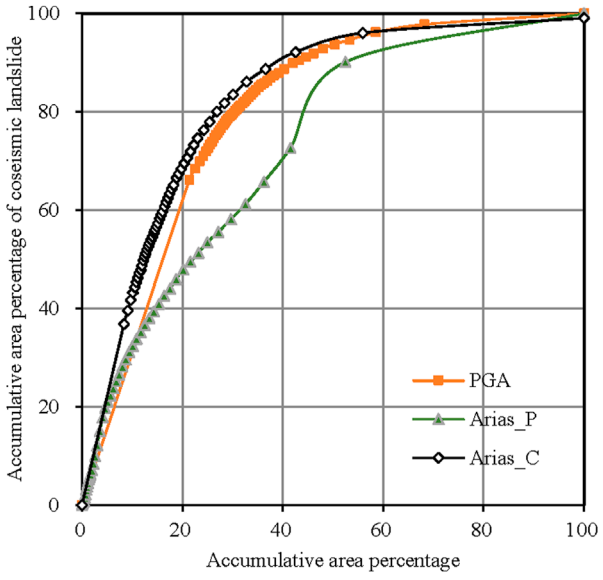

FIGURE 14
Receiver operating characteristic (ROC) curve of the seismic landslide hazard in the main assessment area (Arias_P indicates the Arias intensity with point focal source, and Arias_C indicates the Arias intensity with comprehensive focal source).

Result analysis

By analyzing the spatial distribution characteristics of seismic landslide hazards, it can be found that the seismic landslide hazard based on the PGA presents an approximate elliptical ring distribution. The seismic landslide hazard based on Arias_P presents a circular ring distribution. The seismic landslide hazard based on Arias_C presents an almost standard elliptical ring distribution with a major axis in the NW trend, which is more significantly affected by the seismogenic fault.

The coseismic landslides are mainly distributed in the area with seismic intensity of VII degree and above. The number of coseismic landslides with seismic intensity of VII, VIII, and IX is 47, 3,612, and 1,175, respectively. In this area, the spatial distribution characteristics of seismic landslide hazards are statistically analyzed (Table 2; Figure 15). Areas with very high and high seismic landslide hazards based on Arias_C, PGA, and Arias_P are 323 km^2, 317 km^2, and 586 km^2, accounting for 7.51%, 7.38%, and 13.64% of the

TABLE 2 Result analysis of seismic landslide hazard in the Jiuzhaigou earthquake area.

Seismic landslide hazard		Very high	High	Middle	Low	Very low
Arias_C	Area (km^2)	177	146	148	300	3,525
	Area percentage (%)	4.11	3.40	3.44	6.98	82.07
	Landslide percentage (%)	71.37	18.82	6.19	2.77	0.84
PGA	Area (km^2)	120	197	251	719	3,008
	Area percentage (%)	2.80	4.58	5.84	16.75	70.03
	Landslide percentage (%)	44.43	36.00	13.71	5.09	0.77
Arias_P	Area (km^2)	253	332	442	952	2,315
	Area percentage (%)	5.90	7.74	10.28	22.18	53.90
	Landslide percentage (%)	37.46	26.61	17.22	11.19	7.52

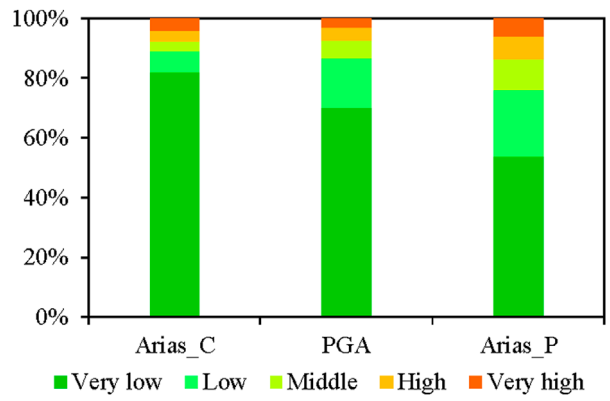

FIGURE 15
Statistical area proportion of the seismic landslide hazard zone in the main assessment area.

total area, respectively. In these areas, the corresponding coseismic landslide proportion is 90.19%, 80.43%, and 64.07%, respectively. The results show that the seismic landslide hazard zone can be well identified based on the presented Arias_C parameter. The middle seismic landslide hazard and over are mainly located at areas with seismic intensity of VII degree and above, which is also the concentrated area of the coseismic landslides. The coseismic landslides are mainly distributed in the deep gullies and steep mountainous slopes on the north and south sides of the epicenter. The spatial distribution of seismic landslide hazards is in good agreement with that of the coseismic landslides.

Discussion

The accuracy of seismic landslide hazard assessment is significantly affected by various factors such as seismic geological data, modeling methods, and landslide data set size and type (Comert, 2021). Many studies on seismic landslide hazard assessment have been carried out in the 2017 Jiuzhaigou earthquake area (Yue et al., 2018; Ai et al., 2022), the 2008 Wenchuan earthquake area (Li et al., 2013; Wang et al., 2016), and the 2005 Kashmir earthquake area (Kamp et al., 2008). In these studies, the Newmark model mostly used the PGA parameter and traditional point focal source, while the fault parameter (such as distance to the fault) has often been used in statistical models, such as in the transfer learning and logistic regression model (Li et al., 2013; Ai et al., 2022). Most of these results have an accuracy of above 0.80, indicating that the fault is an important parameter for seismic landslide hazard assessment (Li et al., 2013; Ai et al., 2022). It also shows the effectiveness of the proposed calculation method of the comprehensive focal distance.

The seismic energy is released concentratedly near the epicenter and along the plausible seismogenic fault, which has seriously affected the spatial distribution characteristics of coseismic landslides, that is, the elliptic distribution in the NW-SE direction. Where the fault passes through, valleys, gullies, and summit landforms are often formed, which are geographical environments prone to landslides. In particular, the coseismic landslide intensity is relatively high in the intersection area of the seismogenic fault and the Minjiang fault in the northwest of the epicenter. Among the three presented seismic motion parameters, the spatial distribution characteristics of Arias_C are more similar to those of coseismic landslides, followed by those of PGA and Arias_P. So, the newly proposed Arias intensity showed better results.

The Jiuzhaigou earthquake area presents mountainous and canyon landforms, and the number of seismic stations deployed is limited, which does not completely cover the seismic area, especially the zones along the seismogenic fault. Therefore, the simulated PGA results based on the seismic station data are biased. The PGA requires a certain number of seismic stations and simulation analyses, and so takes a long time after strong earthquakes.

However, the Arias intensity can be calculated only by knowing the focal location and magnitude parameters so that the general seismic landslide hazard situation can be obtained more quickly, and it is very suitable for emergency seismic landslide hazard assessment.

The slope displacement does not necessarily mean landslide occurrence, and there is a probability problem between them. This work adopts the worldwide formula between slope displacement and landslide probability, which are obtained from the statistical analyses of many seismic landslide data (Jibson et al., 2000). However, for different seismic areas, there exit many differences in complicated geological environmental conditions such as landforms, stratigraphic lithology, and hydrogeology. So, it is necessary to further analyze coseismic landslide samples and propose a new formula between slope displacement and landslide probability, which is more suitable for the geological environmental settings in the Jiuzhaigou earthquake area.

The high and steep mountain has an obvious topographic amplification effect on seismic ground motion, and it is more significant at the mountain top. Here, the seismic landslide hazard assessment is carried out on a regional scale, and the topographic amplification effect of seismic ground motion is not considered. So, from this aspect, the current presented results are relatively conservative.

After strong earthquakes, the trend of increasing landslide development intensity lasts for several decades (Wasowski et al., 2011; Fan et al., 2019; Wu et al., 2019; Tanyas et al., 2021). This work only completes a preliminary study on the Jiuzhaigou coseismic landslide hazard. It is necessary to analyze the duration period of increasing landslide development intensity. Moreover, the long-term seismic influence should be carefully considered for the post-earthquake rainfall-triggered landslide hazard.

Conclusion

The 2017 Ms 7.0 Jiuzhaigou earthquake in the Tibetan Plateau is a valuable case because of its complex topography, landform, geological settings, and developed coseismic landslides. Based on the analysis of the geological settings and coseismic landslide development characteristics, the simplified Newmark model is used to complete the seismic landslide hazard assessment in the Jiuzhaigou earthquake area, which effectively enriches the valuable case study of seismic landslide hazard assessment.

Considering the combined effect of the point focal source (epicenter) and linear focal source (seismogenic fault), the improved calculation method is used to determine the Arias_C parameter under the constraint of seismogenic fault. A better seismic landslide hazard result has been obtained using the new Arias_C parameter. It embodies the advanced nature, precision, and practicability of the seismic landslide hazard assessment model. The Arias intensity is very suitable for rapid seismic landslide hazard assessment under emergency situations.

The seismic landslide hazard based on the Arias_C parameter shows a spatial distribution pattern with a clear elliptical ring, which indicates a significant impact of the seismogenic fault on seismic landslide development and can better identify seismic landslide hazard areas. The high and very high seismic landslide hazard is mainly distributed in the areas with seismic intensity of VIII degree. The spatial distribution pattern of seismic landslide hazards is highly consistent with that of coseismic landslides.

Data availability statement

The raw data supporting the conclusion of this article will be made available by the authors, without undue reservation.

Author contributions

ZY: Manuscript writing–original draft, review, and editing; methodology, investigation, and funding acquisition. GD: Manuscript writing–original draft, review, and editing; validation, software, and formal analysis. YZ: Manuscript writing–review and editing, methodology, and formal analysis. CX: Manuscript writing–review and editing, supervision, formal analysis, and data curation. PY: Manuscript writing–review and editing, investigation, and data curation. WS: Manuscript writing–review and editing, methodology, and investigation. XM: Manuscript writing–review and editing, validation, and investigation.

Funding

The authors declare that financial support was received for the research, authorship, and/or publication of this article. This research was supported by the National Natural Science Foundation of China (42277180), State Key Laboratory of Resources and Environmental Information System, and the China Geological Survey Project (DD20221816).

Conflict of interest

The authors declare that the research was conducted in the absence of any commercial or financial relationships that could be construed as a potential conflict of interest.

Publisher's note

References

Ai, X., Sun, B. T., and Chen, X. Z. (2022). Construction of small sample seismic landslide susceptibility evaluation model based on Transfer Learning: a case study of Jiuzhaigou earthquake. *B. Eng. Geol. Environ.* 81, 116. doi:10.1007/s10064-022-02601-6

Arias, A. (1970). *A measure of earthquake intensity. Seismic design for nuclear power plants*. Cambridge, MA: Massachussetts Institute of Technology Press, 438–483.

Cai, J. H., Zhang, L., Dong, J., Dong, X. J., Li, M. H., Xu, Q., et al. (2022). Detection and characterization of slow-moving landslides in the 2017 Jiuzhaigou earthquake area by combining satellite SAR observations and airborne lidar DSM. *Eng. Geol.* 305, 106730. doi:10.1016/j.enggeo.2022.106730

Chang, M., Cui, P., Xu, L., and Zhou, Y. (2021). The spatial distribution characteristics of coseismic landslides triggered by the Ms7.0 lushan earthquake and Ms7.0 Jiuzhaigou earthquake in southwest China. *Environ. Sci. Pollut. Res.* 28, 20549–20569. doi:10.1007/s11356-020-11826-5

Cheng, Y., Wang, J., and He, Y. (2023). Prediction models of newmark sliding displacement of slopes using deep neural network and mixed-effect regression. *Comput. Geotech.* 156, 105264. doi:10.1016/j.compgeo.2023.105264

Chousianitis, K., Del, G. V., and Kalogeras, I. (2014). Predictive model of Arias intensity and Newmark displacement for regional scale evaluation of earthquake-induced landslide hazard in Greece. *Soil Dyn. Earthq. Eng.* 65, 11–29. doi:10.1016/j.soildyn.2014.05.009

Chung, C. J. F., and Fabbri, A. G. (1999). Probabilistic prediction models for landslide hazard mapping. *Photogramm. Eng. Rem. S.* 65 (12), 1389–1399. doi:10.1016/S0924-2716(99)00030-1

Comert, R. (2021). Investigation of the effect of the dataset size and type in the earthquake-triggered landslides mapping: a case study for the 2018 hokkaido iburu landslides. *Front. Earth Sci.* 9, 633665. doi:10.3389/feart.2021.633665

Dai, F. C., Xu, C., Yao, X., Xu, L., Tu, X. B., and Gong, Q. M. (2011). Spatial distribution of landslides triggered by the 2008 Ms8.0 wenchuan earthquake, China. *J. Asian Earth Sci.* 40 (4), 883–895. doi:10.1016/j.jseaes.2010.04.010

Dai, L. X., Fan, X. M., Wang, X., Fang, C. Y., Zou, C. B., Tang, X. C., et al. (2023). Coseismic landslides triggered by the 2022 luding Ms6.8 earthquake, China. *Landslides* 20, 1277–1292. doi:10.1007/s10346-023-02061-3

Deng, Q. D., Chen, S. F., and Zhao, X. L. (1994). Tectonics, scismisity and dynamics of longmenshan mountains and its adjacent regions. *Seismol. Geol.* 16 (4), 389–403. (in Chinese with English abstract).

Du, W., and Wang, G. (2014). Fully probabilistic seismic displacement analysis of spatially distributed slopes using spatially correlated vector intensity measures. *Earthq. Engng Struct. Dyn.* 43, 661–679. doi:10.1002/eqe.2365

Du, W., and Wang, G. (2016). A one-step Newmark displacement model for probabilistic seismic slope displacement hazard analysis. *Eng. Geol.* 205, 12–23. doi:10.1016/j.enggeo.2016.02.011

Fan, X. M., Scaringi, G., Korup, O., West, A. J., Westen Cees, J. V., Tanyas, H., et al. (2019). Earthquake-induced chains of geologic hazards: patterns, mechanisms, and impacts. *Rev. Geophys.* 57 (2), 421–503. doi:10.1029/2018RG000626

Fan, X. M., Scaringi, G., Xu, Q., Zhan, W. W., Dai, L. X., Li, Y. S., et al. (2018). Coseismic landslides triggered by the 8th August 2017 Ms 7.0 Jiuzhaigou earthquake (sichuan, China): factors controlling their spatial distribution and implications for the seismogenic blind fault identification. *Landslides* 15 (5), 967–983. doi:10.1007/s10346-018-0960-x

Foulser-Piggott, R., and Stafford, P. J. (2012). A predictive model for Arias intensity at multiple sites and consideration of spatial correlations. *Earthq. Engng. Struct. Dyn.* 41 (3), 431–451. doi:10.1002/eqe.1137

Gade, M., Nayek, P. S., and Dhanya, J. (2021). A new neural network–based prediction model for Newmark's sliding displacements. *B. Eng. Geol. Environ.* 80, 385–397. doi:10.1007/s10064-020-01923-7

Gorum, T., and Carranza, E. G. M. (2015). Control of style-of-faulting on spatial pattern of earthquake-triggered landslides. *Int. J. Environ. Sci. Technol.* 12, 3189–3212. doi:10.1007/s13762-015-0752-y

Guo, C., Montgomery, D. R., Zhang, Y., Wang, K., and Yang, Z. H. (2015). Quantitative assessment of landslide susceptibility along the Xianshuihe fault zone, Tibetan plateau, China. *Geomorphology* 248, 93–110. doi:10.1016/j.geomorph.2015.07.012

Hua, J. X., Zheng, J. G., and Wang, D. L. (2018). *Engineering geology handbook (fifth edition) of China*. Beijing: China architecture and building press. in Chinese.

Jibson, R. W. (1993). Predicting earthquake-induced landslide displacements using newmark's sliding block analysis. *Transp. Res. Rec.* 1411, 9–17.

Jibson, R. W. (2007). Regression models for estimating coseismic landslide displacement. *Eng. Geol.* 91 (2-3), 209–218. doi:10.1016/j.enggeo.2007.01.013

Jibson, R. W., Harp, E. L., and Michael, J. A. (2000). A method for producing digital probabilistic seismic landslide hazard maps. *Eng. Geol.* 58 (3–4), 271–289. doi:10.1016/S0013-7952(00)00039-9

Kamp, U., Growley, B. J., Khattak, G. A., and Owen, L. A. (2008). GIS-based landslide susceptibility mapping for the 2005 Kashmir earthquake region. *Geomorphology* 101 (4), 631–642. doi:10.1016/j.geomorph.2008.03.003

Li, W. L., Huang, R. Q., Tang, C., Xu, Q., and Westen, C. V. (2013). Co-Seismic landslide inventory and susceptibility mapping in the 2008 wenchuan earthquake disaster area, China. *J. Mt. Sci.* 10 (3), 339–354. doi:10.1007/s11629-013-2471-5

Li, X. N., Ling, S. X., Sun, C. W., Xu, J. X., and Huang, T. (2019). Integrated rockfall hazard and risk assessment along highways: an example for Jiuzhaigou area after the 2017 Ms 7.0 Jiuzhaigou earthquake, China. *J. Mt. Sci.* 16 (6), 1318–1335. doi:10.1007/s11629-018-5355-x

Ling, S. X., Sun, C. W., Li, X. N., Ren, Y., Xu, J. X., and Huang, T. (2021). Characterizing the distribution pattern and geologic and geomorphic controls on earthquake-triggered landslide occurrence during the 2017 Ms 7.0 Jiuzhaigou earthquake, sichuan, China. *Landslides* 18, 1275–1291. doi:10.1007/s10346-020-01549-6

Liu, J., Shi, J., Wang, T., and Wu, S. (2018). Seismic landslide hazard assessment in the Tianshui area, China, based on scenario earthquakes. *B. Eng. Geol. Environ.* 77, 1263–1272. doi:10.1007/s10064-016-0998-8

Ma, S., and Xu, C. (2019). Assessment of co-seismic landslide hazard using the Newmark model and statistical analyses: a case study of the 2013 Lushan, China, Mw6.6 earthquake. *Nat. Hazards* 96, 389–412. doi:10.1007/s11069-018-3548-9

Maharjan, S., Gnyawali, K. R., Tannant, D. D., Xu, C., and Lacroix, P. (2021). Rapid terrain assessment for earthquake-triggered landslide susceptibility with high-resolution DEM and critical acceleration. *Front. Earth Sci.* 9, 689303. doi:10.3389/feart.2021.689303

Miles, S. B., and Ho, C. L. (1999). Rigorous landslide hazard zonation using newmark's method and stochastic ground motion simulation. *Soil Dyn. Earthq. Eng.* 18, 305–323. doi:10.1016/S0267-7261(98)00048-7

Nayek, P. S., and Gade, M. (2021). Seismic landslide hazard assessment of central seismic gap region of Himalaya for a Mw 8.5 scenario event. *Acta geophys.* 69, 747–759. doi:10.1007/s11600-021-00572-y

Nayek, P. S., and Gade, M. (2022). Artificial neural network-based fully data-driven models for prediction of newmark sliding displacement of slopes. *Neural comput. Appl.* 34 (11), 9191–9203. doi:10.1007/s00521-022-06945-8

Nefeslioglu, H. A., Duman, T. Y., and Durmaz, S. (2006). Landslide susceptibility mapping for A part of tectonic kelkit valley (eastern black sea region of Turkey). *Geomorphology* 94 (3–4), 401–418. doi:10.1016/j.geomorph.2006.10.036

Newmark, N. M. (1965). Effects of earthquakes on dams and embankments. *Geotechnique* 15 (2), 139–160. doi:10.1680/geot.1965.15.2.139

Nowicki, M. A., Wald, D. J., Hamburger, M. W., Hearne, M., and Thompson, E. M. (2014). Development of A Globally applicable model for near real-time prediction of seismically induced landslides. *Eng. Geol.* 173, 54–65. doi:10.1016/j.enggeo.2014.02.002

Pareek, N., Pal, S., Kaynia, A. M., and Sharma, M. L. (2014). Empirical-based seismically induced slope displacements in A geographic information System environment: a case study. *Georisk Assess. Manage. Risk Eng. Syst. Geohazards.* 8 (4), 258–268. doi:10.1080/17499518.2014.980273

Qi, Y. P., Long, F., Xiao, B. F., Lu, Q., and Jiang, P. (2018). Focal mechanism solutions and tectonic stress field characteristics of the 2017 Ms7.0 Jiuzhaigou earthquake sequence. *Acta. geo. Sin.* 39 (5), 622–634. (in Chinese with English abstract). doi:10.3975/cagsb.2018.061901

Rathje, E. M., and Saygili, G. (2008). Probabilistic seismic hazard analysis for the sliding displacement of slopes: scalar and vector approaches. *J. Geotech. Geoenviron. Eng.* 134 (6), 804–814. doi:10.1061/(ASCE)1090-0241(2008)134:6(804)

Ren, J. J., Xu, X. W., Yeats, R. S., and Zhang, S. M. (2013). Millennial slip rates of the Tazang fault, the eastern termination of Kunlun fault: implications for strain partitioning in eastern tibet. *Tectonophysics* 608, 1180–1200. doi:10.1016/j.tecto.2013.06.026

Roberto, R. (2000). Seismically induced landslide displacements: a predictive model. *Eng. Geol.* 58 (3–4), 337–351. doi:10.1016/S0013-7952(00)00042-9

Song, Y. Q., Gong, J. H., Gao, S., Wang, D. C., Cui, T. J., Li, Y., et al. (2012). Susceptibility assessment of earthquake-induced landslides using bayesian network: a case study in beichuan, China. *Comput. Geosci.* 42, 189–199. doi:10.1016/j.cageo.2011.09.011

Sun, J. B., Yue, H., Shen, Z. K., Fang, L. H., Zhan, Y., and Sun, X. Y. (2018). The 2017 Jiuzhaigou earthquake: a complicated event occurred in A young fault System. *Geophys. Res. Lett.* 45 (5), 2230–2240. doi:10.1002/2017GL076421

Tanyas, H., Kirschbaum, D., Gorum, T., van Westen, C. J., and Lombardo, L. (2021). New insight into post-seismic landslide evolution processes in the tropics. *Front. Earth Sci.* 9, 700546. doi:10.3389/feart.2021.700546

Tian, Y. Y., Xu, C., Ma, S. Y., Xu, X. W., Wang, S. Y., and Zhang, H. (2019). Inventory and spatial distribution of landslides triggered by the 8th August 2017 MW 6.5 Jiuzhaigou earthquake, China. *J. Earth Sci.* 30, 206–217. doi:10.1007/s12583-018-0869-2

Travasarou, T., Bray, J. D., and Abrahamson, N. A. (2003). Empirical attenuation relationship for Arias intensity. *Earthq. Engng. Struct. Dyn.* 32 (7), 1133–1155. doi:10.1002/eqe.270

Wang, X. M., and Mao, H. (2022). Spatio-temporal evolution of post-seismic landslides and debris flows: 2017 Ms 7.0 Jiuzhaigou earthquake. *Environ. Sci. Pollut. Res.* 29, 15681–15702. doi:10.1007/s11356-021-16789-9

Wang, Y., Song, C. Z., Lin, Q. G., and Li, J. (2016). Occurrence probability assessment of earthquake-triggered landslides with Newmark displacement values and logistic regression: the Wenchuan earthquake, China. *Geomorphology* 258, 108–119. doi:10.1016/j.geomorph.2016.01.004

Wasowski, J., Keefer, D. K., and Lee, C. (2011). Toward the next generation of research on earthquake-induced landslides: current issues and future challenges. *Eng. Geol.* 122 (1-2), 1–8. doi:10.1016/j.enggeo.2011.06.001

Wilson, R. C., and Keefer, D. K. (1983). Dynamic analysis of A slope failure from the 6 August 1979 coyote lake, California, earthquake. *B. Eng. Geol. Environ.* 73 (3), 863–877. doi:10.1785/bssa0730030863

Wilson, R. C., and Keefer, D. K. (1985). Predicting areal limits of earthquake induced landsliding. *Geol. Surv. Prof. Pap.* 1360, 317–345.

Wu, Z. H., Barosh, P. J., Ha, G. H., Yao, X., Xu, Y. Q., and Liu, J. (2019). Damage induced by the 25 april 2015 Nepal earthquake in the Tibetan border region of China and increased post-seismic hazards. *Nat. Hazard. Earth Syst. Sci.* 19 (4), 873–888. doi:10.5194/nhess-19-873-2019

Yang, Z. H., Guo, C. B., Wu, R. A., Shao, W. W., Yu, P. F., and Li, C. H. (2023). Potential seismic landslide hazard and engineering effect in the ya'an-linzhi section of the sichuan-tibet transportation corridor, China. *China Geol.* 6, 1–13. doi:10.31035/cg2023032

Yao, X., Tham, L. G., and Dai, F. C. (2008). Landslide susceptibility mapping based on support vector machine: a case study on natural slopes of Hong Kong, China. *Geomorphology* 101, 572–582. doi:10.1016/j.geomorph.2008.02.011

Yilmaz, I. (2010). Comparison of landslide susceptibility mapping methodologies for koyulhisar, Turkey: conditional probability, logistic regression, artificial neural networks, and support vector machine. *Environ. Earth Sci.* 61 (4), 821–836. doi:10.1007/s12665-009-0394-9

Yue, X. L., Wu, S. H., Yin, Y. H., Gao, J. B., and Zheng, J. Y. (2018). Risk identification of seismic landslides by joint newmark and rockfall analyst models: a case study of roads affected by the Jiuzhaigou earthquake. *Int. J. Disast. Risk Sci.* 9, 392–406. doi:10.1007/s13753-018-0182-9

Zeng, Y., Zhang, Y., Liu, J., Wang, Q., and Zhu, H. (2023). Rapid emergency response assessment of earthquake-induced landslides driven by fusion of InSAR deformation data and newmark physical models. *Remote Sens.* 15, 4605. doi:10.3390/rs15184605

Zhang, Y. S., Dong, S. W., Hou, C. T., Guo, C. B., Yao, X., Li, B., et al. (2013). Geohazards induced by the lushan Ms7.0 earthquake in sichuan province, southwest China: typical examples, types and distributional characteristics. *Acta. geo. Sin.* 87 (3), 646–657. doi:10.1111/1755-6724.12076

Zhang, Y. S., Yang, Z. H., Guo, C. B., Wang, T., Wang, D. H., and Du, G. L. (2017). Predicting landslide scenes under potential earthquake scenarios in the Xianshuihe fault zone, southwest China. *J. Mt. Sci.* 14 (7), 1262–1278. doi:10.1007/s11629-017-4363-6

frontiers | Frontiers in Earth Science

TYPE Original Research
PUBLISHED 05 April 2024
DOI 10.3389/feart.2024.1370992

OPEN ACCESS

EDITED BY
Paul Sestras,
Technical University of Cluj-Napoca, Romania

REVIEWED BY
Mohammad Azarafza,
University of Tabriz, Iran
Huajin Li,
Chengdu University, China
Sanda Rosca,
Babeș-Bolyai University, Romania

*CORRESPONDENCE
Chong Xu,
xc11111111@126.com

RECEIVED 15 January 2024
ACCEPTED 19 March 2024
PUBLISHED 05 April 2024

CITATION
Li T, Xu C, Li L and Xu J (2024), The landslide traces inventory in the transition zone between the Qinghai-Tibet Plateau and the Loess Plateau: a case study of Jianzha County, China.
Front. Earth Sci. 12:1370992.
doi: 10.3389/feart.2024.1370992

The landslide traces inventory in the transition zone between the Qinghai-Tibet Plateau and the Loess Plateau: a case study of Jianzha County, China

Tao Li[1,2], Chong Xu[1,2]*, Lei Li[3] and Jixiang Xu[4]

[1]National Institute of Natural Hazards, Ministry of Emergency Management of China, Beijing, China, [2]Key Laboratory of Compound and Chained Natural Hazards Dynamics, Ministry of Emergency Management of China, Beijing, China, [3]Key Laboratory of Shale Gas and Geoengineering, Institute of Geology and Geophysics, Chinese Academy of Sciences, Beijing, China, [4]Institute of Geology, China Earthquake Administration, Beijing, China

The upper reaches of the Yellow River in China, influenced by erosion of the Yellow River and tectonic activities, are prone to landslides. Therefore, it is necessary to investigate the existing landslide traces. Based on visual interpretation on high-resolution satellite images and terrain data, supplemented and validated by existing landslide records, this paper prepared the most complete and detailed landslide traces inventory in Jianzha County, Huangnan Tibetan Autonomous Prefecture, Qinghai Province, to date. The results indicate that within the study area of 1714 km^2, there are at least 713 landslide traces, ranging in scale from 3,556 m^2 to 11.13 km^2, with a total area of 134.46 km^2. The total landslide area excluding the overlap area is 126.30 km^2. The overall landslide point density and area density in the study area are 0.42 km^{-2} and 7.37% respectively. The maximum point density and maximum area density of landslide traces in the area are as high as 5.69 km^{-2} and 98.0% respectively. The landslides are primarily distributed in the relatively low-elevation northeastern part of Jianzha County, characterized mainly by large-scale loess landslides, with 14 landslides exceeding 1×10^6 m^2. This inventory not only supplements the landslide trace data in the transition zone between the Qinghai-Tibet Plateau and the Loess Plateau, but also provides an important basis for subsequent landslide risk zoning, response to climate change, and landscape evolution. Additionally, it holds significant reference value for compiling landslide inventories in similar geological environments.

KEYWORDS

landslide traces inventory, upper reaches of the yellow river, loess landslides, Jianzha County, visual interpretation

1 Introduction

Worldwide, mass movements such as landslides are prevalent geological hazards, causing heavy casualties (Petley, 2012; Froude and Petley, 2018). As far as landslide hazards are concerned, China ranks among the regions with the very frequency of landslide hazards globally (Kirschbaum et al., 2015; Xu and Xu, 2021). According to statistics from 2004 to 2016, China experienced 463

fatal landslides not induced by earthquakes, resulting in 4,718 deaths and causing economic losses exceeding 900 million dollars (Zhang and Huang, 2018). Therefore, the prevention and control of landslide hazards is crucial for people's lives. As a key step in hazard prevention and mitigation, including the analysis of regional landslide distribution patterns, hazard assessments, and risk assessment, the construction of a regional landslide inventory is fundamental and essential. A complete and accurate inventory ensures the objectivity and precision of subsequent work (Xu, 2015; Piacentini et al., 2018).

In the construction of China's landslide traces inventory, many scholars have carried out a lot of work and made certain progress (Chen et al., 2016; Qiu et al., 2019; Zhao et al., 2019; Zhang et al., 2020). In northwestern China, Huang et al. (2022) compiled a landslide traces inventory for Hualong County, Qinghai Province, consisting of 3,517 landslides through visual interpretation of high-resolution optical images. Furthermore, an in-depth study on the spatial distribution patterns of landslides was conducted based on this inventory. In central China, Li et al. (2022a) primarily utilized visual interpretation, supplemented by existing literature and hazard records, to improve and supplement the landslide traces inventory for Baoji City, Shaanxi Province. The inventory contains a total of 3,422 landslides, providing foundational data for subsequent exploration of the distribution characteristics of large-scale landslides in the region. In the western part of the Qinghai-Tibet Plateau, Cui et al. (2023) employed the Google Earth platform and visual interpretation method to identify landslide traces in the Western Himalayan Syntaxis. They established a landslide traces inventory containing 7,947 landslides. This inventory serves as a support for subsequent landslide hazard assessments. Wu et al. (2016) collected landslide data based on aerial photographs at a scale of 1:50,000 under the conditions of existing data and field survey. They mapped 328 landslides in Gangu County, Gansu Province, providing a crucial foundation for subsequent research. Lan et al. (2004) combined aerial photographs, previous landslide investigation data, and on-site verification to compile a landslide inventory for the Xiaojiang River Basin, including 574 landslide records. They conducted spatial analysis and prediction of landslide based on this inventory. The landslide data sets constructed by these studies, supported by various methods, demonstrate the ability to facilitate subsequent study on landslide in terms of accuracy and completeness. Nevertheless, accurate and complete landslide trace data are still lacking for the entire region of China.

In studies covering Jianzha County, many scholars have carried out identification work on regional landslides, or conducted research on landslide failure patterns, InSAR deformation analysis, geomorphic effects, and other aspects based on landslide data (Ma et al., 2008; Guo et al., 2020a; Wang et al., 2022; Tu et al., 2023). Yin et al. (2014) primarily utilized visual interpretation to identify 508 landslides from Sigou Gorge to Lagan Gorge in the upper reaches of the Yellow River, with many landslides distributed in Jianzha County. Tu et al. (2023) conducted landslide detection in the upper reaches of the Yellow River based on InSAR technology, and carried out detailed deformation analysis of the Lijia Gorge landslides group in Jianzha County. Du et al. (2023) combined InSAR deformation monitoring and optical images to identify 597 landslides in the upper reaches of the Yellow River. Landslides are mainly distributed in Jianzha County and its surrounding areas. Wang et al. (2022) conducted deformation analysis on the Simencun landslide in Jianzha County to explore the relationship between the failure patterns before and after the landslide occurrence. Currently, although many studies have been carried out in Jianzha County based on landslide data. However, the landslide inventory maps produced do not cover the entire Jianzha County, or the landslide data are not complete and detailed enough. Therefore, by combining the visual interpretation of high-resolution optical images with the comparison of existing literature, this study compiled a landslide traces inventory for Jianzha County, Qinghai Province. Additionally, a spatial analysis was performed on the inventory. Finally, the completeness and importance of the landslide inventory are discussed.

2 Study area

Jianzha County has a total area of approximately 1714 km^2 and is located in the transitional zone from the upper reaches of the Yellow River on the northeastern edge of the Qinghai-Tibet Plateau to the Loess Plateau (Figure 1) (Ma et al., 2008). For a long time, the landscape evolution of this region has been influenced by the northeastward compression of the Qinghai-Tibet Plateau, resulting in the formation of basin and mountainous topography (Guo et al., 2020a; Peng et al., 2020). The overall terrain in the region is high in the southwest and low in the northeast. The northeastern part is the Qunke-Jianzha Basin, characterized by relatively low elevations and crossed by the main trunk of the Yellow River. On either side, there are two basins, namely, the Guide Basin and the Xunhua Basin. The Yellow River and its tributaries exert strong erosion and incision along the edges of the basins, with cutting depths exceeding 500 m. This has resulted in the formation of numerous erosion and accumulation terraces, as well as steep and rugged slopes, providing favorable conditions for landslide occurrence (Craddock et al., 2010; Guo et al., 2020a; Du et al., 2023).

The study area exhibits undulating and rugged topography with well-developed valleys and gullies. The surrounding active tectonics are developed, with the north part of the area having the Lajishanbeiyuan Fault (LJSBYF) and the Lijishannanyuan Fault (LJSNYF). The NWW-SEE trending Daotanghe-Linxia Fault (DTH-LXF) and NNW-SSE trending Riyueshan Fault (RYSF) pass through the study area. Tectonic activity and climate change contribute to the frequent geological hazards (Yin et al., 2014). The large, extra-large, and giant landslides in the region are typical and representative in China (Guo et al., 2020b; Yin et al., 2021). Some studies suggest that the tectonic uplift of the Qinghai-Tibet Plateau, as an internal dynamic factor, has led to the episodic incision of the Yellow River main and tributary channels, serving as the underlying cause for the formation of giant landslides (Li et al., 2011). As shown in Figure 1, there are several historical earthquakes with Ms greater than 5.0 around Jianzha County. The occurrence of landslides may be related to seismic activity or may be the result of landscape evolution, such as river erosion and high groundwater levels (Guo et al., 2016; Guo et al., 2018).

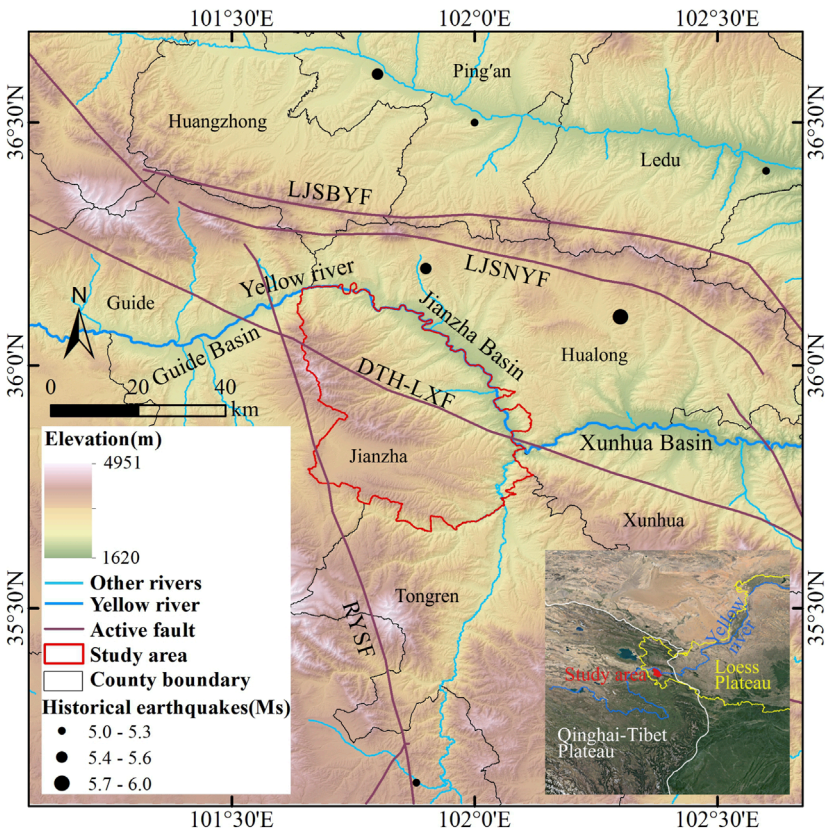

FIGURE 1
Location of the study area. Surface wave magnitude (Ms) is a measure of the strength of an earthquake, calculated from surface wave. The larger the value, the stronger the earthquake. Active fault data from Deng (2007).

3 Methods

With the advancement of remote sensing technology and improved transportation accessibility, the main methods for compiling regional landslide inventories currently include field investigation, visual interpretation of satellite images combined with computer, and automatic identification technology. Table 1 summarizes the advantages and disadvantages of the three landslide identification methods. Detailed field investigation can ensure high accuracy for landslide investigations in small-scale areas (Huangfu et al., 2021). However, for large-scale regional landslide investigations, the feasibility of extensive field investigation decreases. This is primarily due to the substantial cost and time required (Peng et al., 2016), as well as the difficulty in accessing rugged landslide sites. With the development of automatic identification technology, it has a significant advantage in quickly obtaining regional landslide data. However, its accuracy may be not very good (Fayne et al., 2019; Zhang et al., 2020; Piralilou et al., 2021; Vecchiotti et al., 2021; Milledge et al., 2022). Combining the strengths of both approaches, the human-computer interaction visual interpretation of satellite images has gradually become an important method for constructing landslide inventory (Xu et al., 2015; Shao et al., 2020; Li et al., 2021; Cui et al., 2022a). This approach requires interpreters to have certain professional background knowledge. Compared to detailed field survey, it sacrifices a small portion of accuracy but significantly improves the efficiency of constructing landslide inventory (Xu et al., 2014b; Cui et al., 2022b; Cui et al., 2022c).

This article primarily employed high-resolution optical images overlayed on terrain data for human-computer interactive visual interpretation, and combined existing landslide records in literature for validation and supplementation to construct a landslide traces inventory for Jianzha County. Google Earth Pro platform integrates a vast amount of high-resolution optical satellite image data and allows for the three-dimensional, multi-angle display of landscape by overlaying terrain data (Crosby et al., 2012; Rabby and Li, 2019). This provides extremely convenient conditions for landslide identification. Focusing on the Jianzha County, the image quality is exceptionally high, with 100% satellite image coverage and 0% cloud coverage. Therefore, we performed repetitive basic work on landslide interpretation based on the Google Earth Pro for inventory construction. First of all, the shape and boundary of the landslide can be easily determined based on the differences between the texture, tone, shadow and vegetation development on the satellite images and the surrounding environment, combined with terrain differences and multi-angle observation. Secondly, many existing literature findings on landslides in the region will be conducted to check and supplement the inventory for ensuring the completeness and objectivity. Because different landslides have different topographic and geomorphic characteristics, there is no

TABLE 1 Advantages and disadvantages of three landslide identification methods.

Methods	Advantages	Disadvantages	Scope of application
Detailed field investigation	Precision, accurate landslide parameter measurement	High cost, high time consumption, difficult to access in rugged terrain	High-precision landslide investigation in a small area with convenient transportation
Automatic identification technology	Low cost, less time consumption, rapid mapping, emergency response	Low accuracy, prone to omissions	Emergency response to landslides induced by earthquake or rainfall
human-computer interactive visual interpretation	Balancing efficiency and quality, high accuracy	Professional background required	Construction of inventories for large area event-based landslides and landslide traces

TABLE 2 Selected recorded landslides in Jianzha County.

No.	Name	Longitude	Latitude	Citation
1	Simencun Landslide	101.94°	36.04°	Wang et al. (2022)
2	Xiazangtan landslide	102.00°	35.98°	Guo et al. (2020b)
3	Lijia Gorge landslide group	101.75°	36.14°	Tu et al. (2023)
4	Kangyang landslide	101.96°	36.00°	Yin et al. (2013a)
5	Lannitan landslide	101.98°	36.00°	Yin et al. (2013a)
6	Tangse landslide	101.82°	36.09°	Yin et al. (2013b)
7	Quhetankou landslide	101.94°	36.01°	Yin et al. (2013b)
8	Gurisi landslide	102.02°	35.97°	Ma et al. (2008)

uniform standard applicable to the interpretation of all landslide traces. Here, some common landslide features used in landslide interpretation are listed: 1) Having an obvious armchair-shaped back wall and the phenomenon of double grooves homologous; 2) Depression in the source area, prominent topography in the accumulation area, accompanied by a distinct landslide boundary; 3) Obvious displacement between the landslide body and the surrounding environment, accompanied by cracks or differences in elevation; 4) The source area shows a brighter color, and the accumulation has transverse fissures and appears tongue-shaped; 5) Irregular stepped appearance in the accumulation body, with the terraces possibly transformed into residential areas or farmland.

4 Results and analysis

4.1 Landslide traces inventory

The landslide inventory serves as a crucial foundation for regional landslide risk assessment and prevention. Many scholars have conducted regional or individual landslide studies in Jianzha County (Yin et al., 2014; Guo et al., 2020b; Du et al., 2023; Tu et al., 2023). Although the study areas of these studies cover or partially cover Jianzha County, most have not established a complete landslide traces inventory that fully encompasses Jianzha County. Table 2 presents selected existing landslide records in Jianzha County. After objectively supplemented and validated by these records, the landslide inventory constructed in this study contains a total of 713 landslide traces (Figure 2). The total area of these landslides is 134.46 km^2. The total landslide area excluding the overlap area is 126.30 km^2, accounting for 7.37% of the study area. The average landslide area is approximately 0.19 km^2, with a minimum of 3,556 m^2 and a maximum of 11.13 km^2. It can be found that landslides mainly occur on the slopes of the relatively low-elevation ridges in the northeastern part of Jianzha County. These landslides are widely distributed in towns such as Kanbula, Jiajia, Cuozhou, Maketang, and Angla, with a predominance of large-scale landslides. In the southwest, where the altitude is relatively high, landslides are sparsely distributed.

4.2 Typical landslide display

In order to more intuitively display the landslides, several typical landslides were selected within the study area for display (Figure 3). It can be found that the predominant landslide type is loess landslide. The landslide boundary is easily identified based on the discontinuity in texture and shape between the deposits and the surrounding environment. The material movement along the slope is evident. The displacement between the landslide deposits and the boundary visually demonstrates the movement direction and shape of the landslide. Over time, traces of human activity become visible on the deposits. After reconstruction, roads and buildings of various sizes are distributed across the deposits. These typical landslide examples can clearly capture the landslide morphology and material movement traces, which is of great value for the study of regional landslide failure mechanisms.

4.3 Landslide density statistics

In order to quantitatively analyze the spatial distribution of landslides, landslide point density and area density are used to characterize the distribution and aggregation of landslides. After kernel density calculation with the search radius set to 2 km, the

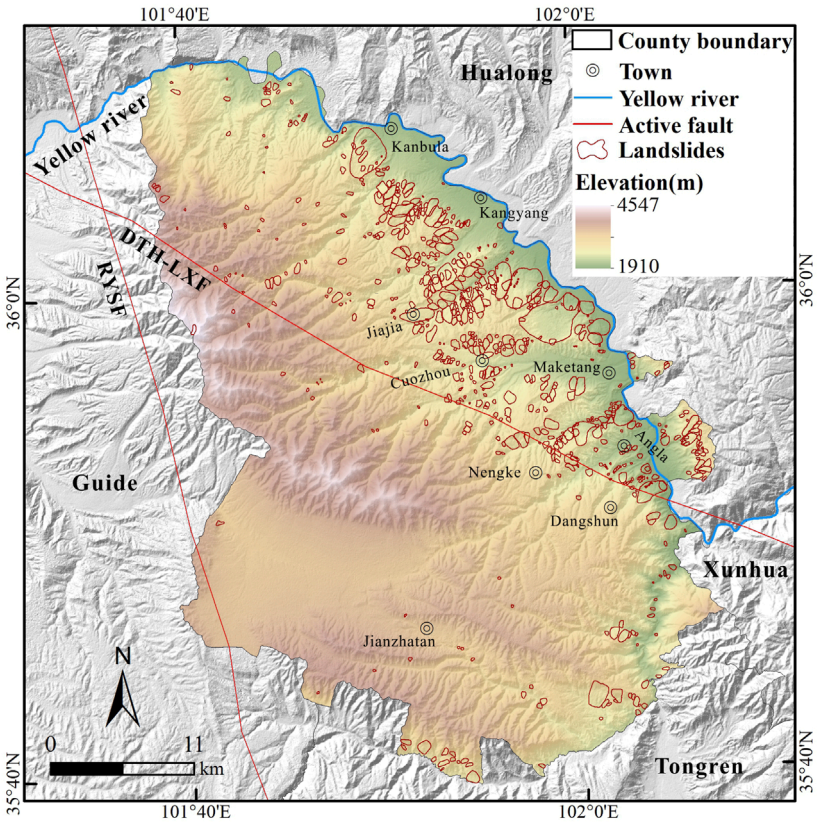

FIGURE 2
Spatial distribution map of landslide traces.

results are shown in Figure 4. High point density areas are primarily concentrated in the northeastern part of the study area (Figure 4A), with the maximum density reaching 5.69 km^{-2}. This indicates that landslides in these areas are numerically dominant. The maximum landslide area density is 98.0% (Figure 4B). High area density areas are different from high point density areas in distribution. For instance, landslide area density is more significant relative to point density in areas close to the Kanbula Town. This indicates that the landslides in this area tend to be larger in scale.

5 Discussion

5.1 Landslide scale and the completeness analysis

To explore the scale of landslides in Jianzha County, the cumulative landslide number was plotted against the landslide area in a double logarithmic coordinate system to show the relationship between them (Figure 5). Where N represents the number of landslides exceeding a given area, A. It can be observed that the majority of landslides have a scale smaller than 1×10^6 m^2, with only 14 landslides exceeding 1×10^6 m^2 in scale. The fitting formula for all landslides is $lgN(A) = -0.728\,lgA + 5.957$, with R^2=0.882. For landslides with an area larger than 1×10^5 m^2, the fitting formula is $lgN(A) = -1.210\,lgA + 8.552$, with R^2=0.99, indicating that these data are relatively complete. For landslides with an area smaller than 1×10^4 m^2, the curve exhibits a smoother trend, possibly due to the less distinct image change characteristics in the exposed loess areas, making them difficult to identify.

As shown in Figure 5, landslides with an area greater than 1×10^5 m^2 are fitted as $lgN(A) = -1.210\,lgA + 8.552$. In previous studies, this formula was often used in the statistics of coseismic landslide inventories to evaluate the completeness. For example, in the nearly complete coseismic landslide inventory established by Xu et al. (2014a) after the Wenchuan earthquake, landslides within a certain area are defined by the equation $lgN(A) = -2.0745\,lgA + 13$, and the landslides exhibit a rolling trend. Similarly, coseismic landslide inventories for the Minxian-Zhangxian earthquake (Xu et al., 2014b) and Maerkang earthquake (Chen et al., 2023) also show a similar trend, with the slopes and intercepts of the corresponding fitting equations are −1.341 and 6.02 (Minxian-Zhangxian earthquake) and −1.1052 and 5.7839 (Maerkang earthquake), respectively. Although the scale of landslides may vary due to different environmental conditions. However, it can be observed that whether it is the landslide traces inventory of this article or the coseismic landslide inventory, the landslides show a similar trend of change. In particular, in the work of establishing a landslide inventory with similar landslide scales, Li et al. (2022b) constructed a landslide traces inventory containing 3,757 landslides around the Baihetan Hydropower Station reservoir in China. The

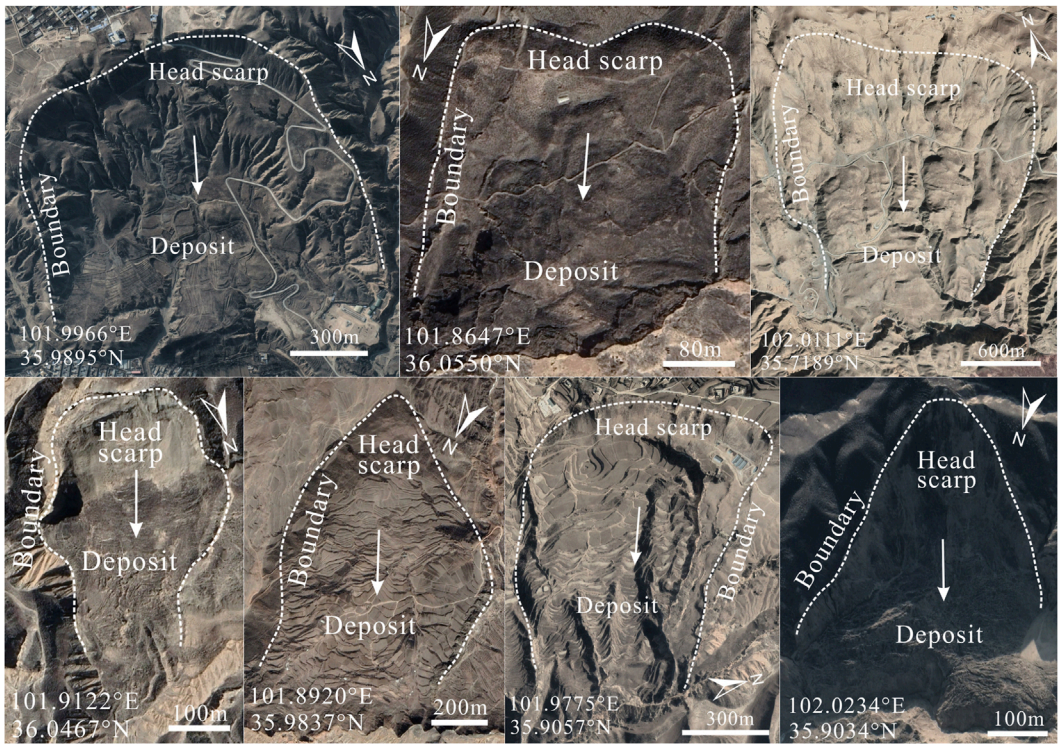

FIGURE 3
Display of seven typical landslide traces in the study area.

relationship between the cumulative number and area of landslides with an area greater than 1×10^5 m^2 is $lgN(A) = -1.275\,lgA + 6.26$. Upon comparison, this is very close to the results of this article, which also proves the completeness of our inventory to a certain extent. By comparing the completeness of landslide inventories in different categories, it is concluded that landslide inventories of the same category have more reference value than those of different categories.

5.2 Objective assessment of methods

A complete and detailed landslide inventory is of great significance for regional landslide research and risk management. The human-computer interaction visual interpretation method, as one of the primary approaches for establishing regional landslide inventory, possesses advantages that are irreplaceable by field investigation and automatic identification techniques (Guzzetti et al., 2012; Tian et al., 2019; Xu et al., 2020). While this study primarily relied on such a method to construct a relatively objective landslide traces inventory for Jianzha County, there are still some limitations. For small-scale landslides, due to the resolution limitations of satellite images, the coverage of topographic and geomorphic features, and the subjective factors from interpreters, it is inevitable that landslides with unclear identification characteristics will be missed. Compared with detailed field investigation, the visual interpretation method consumes less cost and time. Compared with automatic identification method, it is superior in accuracy and is currently a widely used method for identifying regional landslides (Cui et al., 2021; Li et al., 2022a; Sun et al., 2024). This method sacrifices some accuracy compared to field investigation, but greatly improves efficiency. Balancing the efficiency of automatic identification and the accuracy of field investigation is an exploratory and challenging task.

5.3 The importance of the landslide inventory

Landslide susceptibility refers to the probability of slope failure in a specific geological environment without considering triggering factors (Akgun, 2012; Nikoobakht et al., 2022). As a fundamental component, landslide inventory plays an indispensable role in landslide susceptibility assessment. It provides essential information about landslides, including the number, scale, location. Based on landslide inventory, one can select a single assessment method and specific influencing factors for landslide susceptibility assessment (Huangfu et al., 2021; Nanehkaran et al., 2021; Cemiloglu et al., 2023). Alternatively, one can choose several different assessment methods for comparative analysis to find the optimal results (Azarafza et al., 2021; Nanehkaran et al., 2022; Mao et al., 2024). With the development of landslide assessment, machine learning has demonstrated outstanding performance among many methods, gradually becoming the preferred approach for assessment (Nanehkaran et al., 2023). Based on susceptibility

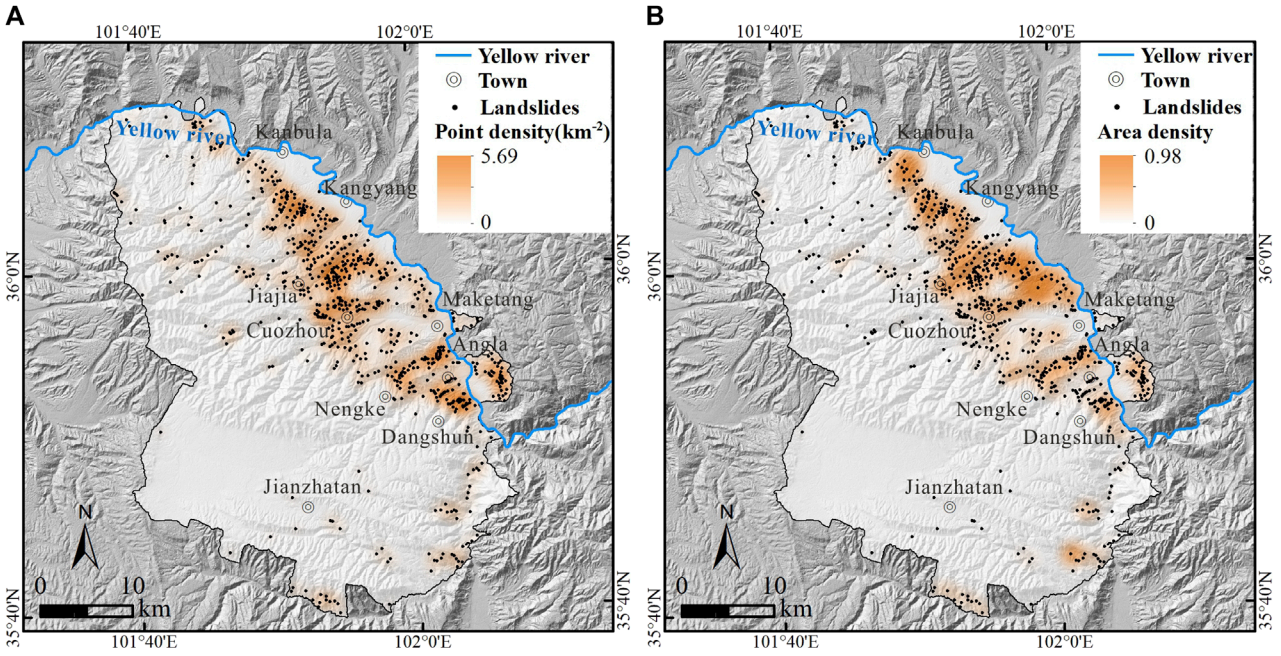

FIGURE 4
Landslide density map. **(A)** point density map; **(B)** area density map.

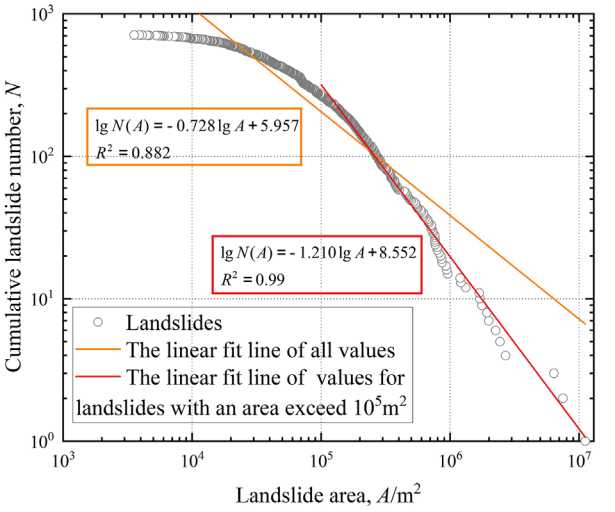

FIGURE 5
Curve depicting correlation between the cumulative landslide number and the landslide area.

assessment, triggering factors are added to evaluate landslide hazard, while carrier indicators are added for vulnerability assessment. Risk assessment is then performed by overlaying hazard and vulnerability. However, regardless of which assessment method is chosen and which landslide influencing factors are considered, the susceptibility assessment, hazard assessment, vulnerability assessment, and risk assessment all need to be based on landslide data. The landslide inventory can not only be used to validate the results obtained through predictive modeling, but also provide an important reference for exploring factors involved in the occurrence of new landslides. Many studies have been carried out on incomplete landslide inventories and updated the inventories, effectively enhancing the understanding of subsequent landslide development and assessment research. For example, the Hokkaido earthquake (Kasai and Yamada, 2019; Cui et al., 2021), Wenchuan earthquake (Dai et al., 2011; Xu et al., 2014a), and Jiuzhaigou earthquake (Tian et al., 2019; Sun et al., 2024). The work of compiling a complete and detailed landslide inventory is not only of great value and significance, but also has important supporting value for subsequent research on landslide failure mechanisms, landscape evolution, especially landslide susceptibility assessment.

6 Conclusion

This study established a landslide traces inventory in Jianzha County, Qinghai Province, China, and conducted a statistical analysis of their number, area, and density. A total of 713 landslides were identified, mainly loess landslides. The total area of landslides is 134.46 km^2, ranging in scale from 3556 m^2 to 11.13 km^2. The landslides are primarily concentrated in the low-elevation regions of the northeastern part of the study area. This inventory is more similar in scale and completeness to other loess landslide inventories. Furthermore, it is more complete and detailed than previous landslide traces records in Jianzha County. The study compiled the most complete and detailed landslide traces inventory in Jianzha County so far, which is of great significance to landslide scientific research. In future, relevant research on loess landslide development characteristics, failure mechanisms, susceptibility

assessment and risk zoning can be conducted based on this landslide inventory.

Data availability statement

The raw data supporting the conclusion of this article will be made available by the authors, without undue reservation.

Author contributions

TL: Investigation, Visualization, Writing–original draft. CX: Conceptualization, Resources, Writing–review and editing. LL: Investigation, Writing–review and editing. JX: Investigation, Writing–review and editing.

Funding

The author(s) declare financial support was received for the research, authorship, and/or publication of this article. This work was supported by the National Institute of Natural Hazards, Ministry of Emergency Management of China (2023-JBKY-57) and the National Natural Science Foundation of China (42077259).

Acknowledgments

Deep thanks are extended to the reviewers for their beneficial review and valuable comments.

Conflict of interest

The authors declare that the research was conducted in the absence of any commercial or financial relationships that could be construed as a potential conflict of interest.

The author(s) declared that they were an editorial board member of Frontiers, at the time of submission. This had no impact on the peer review process and the final decision.

Publisher's note

References

Akgun, A. (2012). A comparison of landslide susceptibility maps produced by logistic regression, multi-criteria decision, and likelihood ratio methods: a case study at İzmir, Turkey. *Landslides* 9 (1), 93–106. doi:10.1007/s10346-011-0283-7

Azarafza, M., Azarafza, M., Akgün, H., Atkinson, P. M., and Derakhshani, R. (2021). Deep learning-based landslide susceptibility mapping. *Sci. Rep.* 11 (1), 24112. doi:10.1038/s41598-021-03585-1

Cemiloglu, A., Zhu, L., Mohammednour, A. B., Azarafza, M., and Nanehkaran, Y. A. (2023). Landslide susceptibility assessment for Maragheh County, Iran, using the logistic regression algorithm. *Land* 12 (7), 1397. doi:10.3390/land12071397

Chen, W., Chai, H., Zhao, Z., Wang, Q., and Hong, H. (2016). Landslide susceptibility mapping based on GIS and support vector machine models for the Qianyang county, China. *Environ. Earth Sci.* 75, 474. doi:10.1007/s12665-015-5093-0

Chen, Z., Huang, Y., He, X., Shao, X., Li, L., Xu, C., et al. (2023). Landslides triggered by the 10 June 2022 Maerkang earthquake swarm, Sichuan, China: spatial distribution and tectonic significance. *Landslides* 20, 2155–2169. doi:10.1007/s10346-023-02080-0

Craddock, W. H., Kirby, E., Harkins, N. W., Zhang, H., Shi, X., and Liu, J. (2010). Rapid fluvial incision along the Yellow River during headward basin integration. *Nat. Geosci.* 3 (3), 209–213. doi:10.1038/ngeo777

Crosby, C. J., Whitmeyer, S. J., De Paor, D. G., Bailey, J., and Ornduff, T. (2012). Lidar and Google Earth: simplifying access to high-resolution topography data. *Spec. Pap. Geol. Soc. Am.* 492, 37–47. doi:10.1130/2012.2492(03)

Cui, Y., Bao, P., Xu, C., Ma, S., Zheng, J., and Fu, G. (2021). Landslides triggered by the 6 September 2018 Mw6.6 Hokkaido, Japan: an updated inventory and retrospective hazard assessment. *Earth Sci. Inf.* 14, 247–258. doi:10.1007/s12145-020-00544-8

Cui, Y., Hu, J., Xu, C., Miao, H., and Zheng, J. (2022b). Landslides triggered by the 1970 Ms7.7 Tonghai earthquake in Yunnan, China: an inventory, distribution characteristics, and tectonic significance. *J. Mt. Sci.* 19 (6), 1633–1649. doi:10.1007/s11629-022-7321-x

Cui, Y., Hu, J., Zheng, J., Fu, G., and Xu, C. (2022a). Susceptibility assessment of landslides caused by snowmelt in a typical loess area in the Yining County, Xinjiang, China. *Q. J. Eng. Geol. Hydrogeology* 55 (1), qjegh2021–2024. doi:10.1144/qjegh2021-024

Cui, Y., Jin, J., Huang, Q., Yuan, K., and Xu, C. (2022c). A data-driven model for spatial shallow landslide probability of occurrence due to a typhoon in Ningguo City, Anhui Province, China. *Forests* 13 (5), 732. doi:10.3390/f13050732

Cui, Y., Yang, W., Xu, C., and Wu, S. (2023). Distribution of ancient landslides and landslide hazard assessment in the Western Himalayan Syntaxis area. *Front. Earth Sci.* 11, 1135018. doi:10.3389/feart.2023.1135018

Dai, F., Xu, C., Yao, X., Xu, L., Tu, X., and Gong, Q. (2011). Spatial distribution of landslides triggered by the 2008 Ms8.0 Wenchuan earthquake, China. *J. Asian Earth Sci.* 40 (4), 883–895. doi:10.1016/j.jseaes.2010.04.010

Deng, Q. (2007). *Map of active tectonics in China*. Beijing: Seismological Press. (In Chinese)

Du, J., Li, Z., Song, C., Zhu, W., Ji, Y., Zhang, C., et al. (2023). InSAR-based active landslide detection and characterization along the upper reaches of the Yellow River. *IEEE J. Sel. Top. Appl. Earth Observations Remote Sens.* 16, 3819–3830. doi:10.1109/jstars.2023.3263003

Fayne, J. V., Ahamed, A., Roberts-Pierel, J., Rumsey, A. C., and Kirschbaum, D. (2019). Automated satellite-based landslide identification product for Nepal. *Earth Interact.* 23 (3), 1–21. doi:10.1175/ei-d-17-0022.1

Froude, M. J., and Petley, D. N. (2018). Global fatal landslide occurrence from 2004 to 2016. *Nat. Hazards Earth Syst. Sci.* 18 (8), 2161–2181. doi:10.5194/nhess-18-2161-2018

Guo, X., Forman, S. L., Marin, L., and Li, X. (2018). Assessing tectonic and climatic controls for late quaternary fluvial terraces in Guide, Jianzha, and Xunhua basins along the Yellow River on the northeastern Tibetan plateau. *Quat. Sci. Rev.* 195, 109–121. doi:10.1016/j.quascirev.2018.07.005

Guo, X., Sun, Z., Lai, Z., Lu, Y., and Li, X. (2016). Optical dating of landslide-dammed lake deposits in the upper Yellow River, Qinghai-Tibetan Plateau, China. *Quat. Int.* 392, 233–238. doi:10.1016/j.quaint.2015.06.021

Guo, X., Wei, J., Lu, Y., Song, Z., and Liu, H. (2020a). Geomorphic effects of a dammed pleistocene lake formed by landslides along the upper Yellow River. *Water* 12 (5), 1350. doi:10.3390/w12051350

Guo, X., Wei, J., Song, Z., Lai, Z., and Yu, L. (2020b). Optically stimulated luminescence chronology and geomorphic imprint of Xiazangtan landslide upon the upper Yellow River valley on the northeastern Tibetan Plateau. *Geol. J.* 55 (7), 5498–5507. doi:10.1002/gj.3754

Guzzetti, F., Mondini, A. C., Cardinali, M., Fiorucci, F., Santangelo, M., and Chang, K.-T. (2012). Landslide inventory maps: new tools for an old problem. *Earth-Science Rev.* 112 (1-2), 42–66. doi:10.1016/j.earscirev.2012.02.001

Huang, Y., Xu, C., Li, L., He, X., Cheng, J., Xu, X., et al. (2022). Inventory and spatial distribution of ancient landslides in Hualong county, China. *Land* 12 (1), 136. doi:10.3390/land12010136

Huangfu, W., Wu, W., Zhou, X., Lin, Z., Zhang, G., Chen, R., et al. (2021). Landslide geo-hazard risk mapping using logistic regression modeling in Guixi, Jiangxi, China. *Sustainability* 13 (9), 4830. doi:10.3390/su13094830

Kasai, M., and Yamada, T. (2019). Topographic effects on frequency-size distribution of landslides triggered by the Hokkaido Eastern Iburi Earthquake in 2018. *Earth, Planets Space* 71 (1), 89–12. doi:10.1186/s40623-019-1069-8

Kirschbaum, D., Stanley, T., and Zhou, Y. (2015). Spatial and temporal analysis of a global landslide catalog. *Geomorphology* 249, 4–15. doi:10.1016/j.geomorph.2015.03.016

Lan, H. X., Zhou, C. H., Wang, L. J., Zhang, H. Y., and Li, R. H. (2004). Landslide hazard spatial analysis and prediction using GIS in the Xiaojiang watershed, Yunnan, China. *Eng. Geol.* 76 (1), 109–128. doi:10.1016/j.enggeo.2004.06.009

Li, L., Xu, C., Xu, X., Zhang, Z., and Cheng, J. (2021). Inventory and distribution characteristics of large-scale landslides in Baoji city, Shaanxi province, China. *ISPRS Int. J. Geo-Information* 11 (1), 10. doi:10.3390/ijgi11010010

Li, L., Xu, C., Yang, Z., Zhang, Z., and Lv, M. (2022a). An inventory of large-scale landslides in Baoji city, Shaanxi province, China. *Data* 7 (8), 114. doi:10.3390/data7080114

Li, L., Xu, C., Yao, X., Shao, B., Ouyang, J., Zhang, Z., et al. (2022b). Large-scale landslides around the reservoir area of Baihetan hydropower station in Southwest China: analysis of the spatial distribution. *Nat. Hazards Res.* 2 (3), 218–229. doi:10.1016/j.nhres.2022.07.002

Li, X., Guo, X., and Li, W. (2011). Mechanism of giant landslides from Longyangxia valley to Liujiaxia valley along upper Yellow River. *J. Eng. Geol.* 19 (4), 516–529 [in Chinese, with English summary].

Ma, X., Wang, L., Lv, B., and Ju, S. (2008). An investigation of geological hazards based on IRS-P^6 remote sensing data, Jianzha county, Qinghai province. *Northwest. Geol.* 41 (2), 93–100 [in Chinese, with English summary].

Mao, Y., Li, Y., Teng, F., Sabonchi, A. K. S., Azarafza, M., and Zhang, M. (2024). Utilizing hybrid machine learning and soft computing techniques for landslide susceptibility mapping in a Drainage Basin. *Water* 16 (3), 380. doi:10.3390/w16030380

Milledge, D. G., Bellugi, D. G., Watt, J., and Densmore, A. L. (2022). Automated determination of landslide locations after large trigger events: advantages and disadvantages compared to manual mapping. *Nat. Hazards Earth Syst. Sci.* 22 (2), 481–508. doi:10.5194/nhess-22-481-2022

Nanehkaran, Y. A., Chen, B., Cemiloglu, A., Chen, J., Anwar, S., Azarafza, M., et al. (2023). Riverside landslide susceptibility overview: leveraging artificial neural networks and machine learning in accordance with the United Nations (UN) sustainable development goals. *Water* 15 (15), 2707. doi:10.3390/w15152707

Nanehkaran, Y. A., Licai, Z., Chen, J., Azarafza, M., and Yimin, M. (2022). Application of artificial neural networks and geographic information system to provide hazard susceptibility maps for rockfall failures. *Environ. Earth Sci.* 81 (19), 475. doi:10.1007/s12665-022-10603-6

Nanehkaran, Y. A., Mao, Y., Azarafza, M., Kockar, M. K., and Zhu, H.-H. (2021). Fuzzy-based multiple decision method for landslide susceptibility and hazard assessment: a case study of Tabriz, Iran. *Geomechanics Eng.* 24 (5), 407–418. doi:10.12989/gae.2021.24.5.407

Nikoobakht, S., Azarafza, M., Akgün, H., and Derakhshani, R. (2022). Landslide susceptibility assessment by using convolutional neural network. *Appl. Sci.* 12 (12), 5992. doi:10.3390/app12125992

Peng, D., Xu, Q., Qi, X., Fan, X., Dong, X., Li, S., et al. (2016). Study on early recognition of loess landslides based on field investigation. *Int. J. Georesources Environment-IJGE Former. Int'l J Geohazards Environ.* 2 (2), 35–52. doi:10.15273/ijge.2016.02.006

Peng, J., Lan, H., Qian, H., Wang, W., Li, R., Li, Z., et al. (2020). Scientific research framework of livable Yellow River. *J. Eng. Geol.* 28 (2), 189–201 [in Chinese, with English summary].

Petley, D. (2012). Global patterns of loss of life from landslides. *Geology* 40 (10), 927–930. doi:10.1130/g33217.1

Piacentini, D., Troiani, F., Daniele, G., and Pizziolo, M. (2018). Historical geospatial database for landslide analysis: the catalogue of landslide occurrences in the Emilia-Romagna region (CLOCkER). *Landslides* 15 (4), 811–822. doi:10.1007/s10346-018-0962-8

Piralilou, S. T., Shahabi, H., and Pazur, R. (2021). Automatic landslide detection using bi-temporal sentinel 2 imagery. *GI_Forum* 9, 39–45. doi:10.1553/giscience2021_01_s39

Qiu, H., Cui, Y., Yang, D., Pei, Y., Hu, S., Ma, S., et al. (2019). Spatiotemporal distribution of nonseismic landslides during the last 22 years in Shaanxi province, China. *ISPRS Int. J. Geo-Information* 8 (11), 505. doi:10.3390/ijgi8110505

Rabby, Y. W., and Li, Y. (2019). An integrated approach to map landslides in Chittagong Hilly Areas, Bangladesh, using Google Earth and field mapping. *Landslides* 16 (3), 633–645. doi:10.1007/s10346-018-1107-9

Shao, X., Ma, S., Xu, C., Shen, L., and Lu, Y. (2020). Inventory, distribution and geometric characteristics of landslides in Baoshan city, Yunnan province, China. *Sustainability* 12 (6), 2433. doi:10.3390/su12062433

Sun, J., Shao, X., Feng, L., Xu, C., Huang, Y., and Yang, W. (2024). An essential update on the inventory of landslides triggered by the Jiuzhaigou Mw6. 5 earthquake in China on 8 August 2017, with their spatial distribution analyses. *Heliyon* 10 (2), e24787. doi:10.1016/j.heliyon.2024.e24787

Tian, Y., Xu, C., Ma, S., Xu, X., Wang, S., and Zhang, H. (2019). Inventory and spatial distribution of landslides triggered by the 8th August 2017 Mw 6.5 Jiuzhaigou earthquake, China. *J. Earth Sci.* 30 (1), 206–217. doi:10.1007/s12583-018-0869-2

Tu, K., Ye, S., Zou, J., Hua, C., and Guo, J. (2023). InSAR displacement with high-resolution optical remote sensing for the early detection and deformation analysis of active landslides in the upper Yellow River. *Water* 15 (4), 769. doi:10.3390/w15040769

Vecchiotti, F., Tilch, N., and Kociu, A. (2021). The use of TERRA-ASTER satellite for landslide detection. *Geosciences* 11 (6), 258. doi:10.3390/geosciences11060258

Wang, L., Qiu, H., Zhou, W., Zhu, Y., Liu, Z., Ma, S., et al. (2022). The post-failure spatiotemporal deformation of certain translational landslides may follow the pre-failure pattern. *Remote Sens.* 14 (10), 2333. doi:10.3390/rs14102333

Wu, Y., Li, W., Liu, P., Bai, H., Wang, Q., He, J., et al. (2016). Application of analytic hierarchy process model for landslide susceptibility mapping in the Gangu County, Gansu Province, China. *Environ. Earth Sci.* 75, 422. doi:10.1007/s12665-015-5194-9

Xu, C. (2015). Preparation of earthquake-triggered landslide inventory maps using remote sensing and GIS technologies: principles and case studies. *Geosci. Front.* 6 (6), 825–836. doi:10.1016/j.gsf.2014.03.004

Xu, C., Xu, X., and Shyu, J. B. H. (2015). Database and spatial distribution of landslides triggered by the Lushan, China Mw6.6 earthquake of 20 April 2013. *Geomorphology* 248, 77–92. doi:10.1016/j.geomorph.2015.07.002

Xu, C., Xu, X., Shyu, J. B. H., Zheng, W., and Min, W. (2014b). Landslides triggered by the 22 July 2013 Minxian–Zhangxian, China, Mw5.9 earthquake: inventory compiling and spatial distribution analysis. *J. Asian Earth Sci.* 92, 125–142. doi:10.1016/j.jseaes.2014.06.014

Xu, C., Xu, X., Yao, X., and Dai, F. (2014a). Three (nearly) complete inventories of landslides triggered by the May 12, 2008 Wenchuan Mw7.9 earthquake of China and their spatial distribution statistical analysis. *Landslides* 11, 441–461. doi:10.1007/s10346-013-0404-6

Xu, X., and Xu, C. (2021). Natural Hazards Research: an eternal subject of human survival and development. *Nat. Hazards Res.* 1 (1), 1–3. doi:10.1016/j.nhres.2020.12.003

Xu, Y., Allen, M. B., Zhang, W., Li, W., and He, H. (2020). Landslide characteristics in the Loess Plateau, northern China. *Geomorphology* 359, 107150. doi:10.1016/j.geomorph.2020.107150

Yin, Z., Qin, X., and Zhao, W. (2014). "Characteristics of landslides from sigou gorge to lagan gorge in the upper reaches of Yellow River. Landslide Science for a Safer Geoenvironment: vol. 1," in *The international programme on landslides (IPL)* (Springer).

Yin, Z., Qin, X., Zhao, W., and Wei, G. (2013a). Characteristics of landslides in upper reaches of Yellow River with multiple data of remote sensing. *J. Eng. Geol.* 21 (5), 779–787 [in Chinese, with English summary].

Yin, Z., Wei, G., Qi, X., and Zhou, C. (2013b). Spatial and temporal characteristics of landslides and there response to climatic change from Sigou to Lagan gorges in upper reaches of Yellow River. *J. Eng. Geol.* 21 (1), 129–137 [in Chinese, with English summary].

Yin, Z., Wei, G., Qin, X., Li, W., and Zhao, W. (2021). Research progress on landslides and dammed lakes in the upper reaches of the Yellow River, northeastern Tibetan Plateau. *Earth Sci. Front.* 28 (2), 46–57 [in Chinese, with English summary].

Zhang, F., and Huang, X. (2018). Trend and spatiotemporal distribution of fatal landslides triggered by non-seismic effects in China. *Landslides* 15 (8), 1663–1674. doi:10.1007/s10346-018-1007-z

Zhang, P., Xu, C., Ma, S., Shao, X., Tian, Y., and Wen, B. (2020a). Automatic extraction of seismic landslides in large areas with complex environments based on deep learning: an example of the 2018 Iburi earthquake, Japan. *Remote Sens.* 12 (23), 3992. doi:10.3390/rs12233992

Zhang, Z., Wang, T., and Wu, S. (2020b). Distribution and features of landslides in the tianshui basin, northwest China. *J. Mt. Sci.* 17 (3), 686–708. doi:10.1007/s11629-019-5595-4

Zhao, B., Wang, Y., Chen, M., Luo, Y., Liang, R., and Li, J. (2019). Typical characteristics of large-scale landslides in the transition belt between the Qinghai-Tibet Plateau and the Loess Plateau. *Arabian J. Geosciences* 12, 470. doi:10.1007/s12517-019-4612-9

frontiers | Frontiers in Earth Science

TYPE Original Research
PUBLISHED 11 April 2024
DOI 10.3389/feart.2024.1376900

OPEN ACCESS

EDITED BY
Xiaoli Liu,
Tsinghua University, China

REVIEWED BY
Yaohui Liu,
Shandong Jianzhu University, China
Amod Mani Dixit,
Universal Engineering and Science College (UESC), Nepal

*CORRESPONDENCE
Jia Cheng,
jiacheng@cugb.edu.cn

RECEIVED 26 January 2024
ACCEPTED 11 March 2024
PUBLISHED 11 April 2024

CITATION
Wang Z, Cheng J and Xu C (2024), Earthquake scenario-specific framework for spatial accessibility analysis (SAA) of emergency shelters: a case study in Xichang City, Sichuan Province, China.
Front. Earth Sci. 12:1376900.
doi: 10.3389/feart.2024.1376900

Earthquake scenario-specific framework for spatial accessibility analysis (SAA) of emergency shelters: a case study in Xichang City, Sichuan Province, China

Ziyue Wang[1,2], Jia Cheng[3]* and Chong Xu[1,2]

[1]National Institute of Natural Hazards, Ministry of Emergency Management of China, Beijing, China, [2]Key Laboratory of Compound and Chained Natural Hazards Dynamics, Ministry of Emergency Management of China, Beijing, China, [3]School of Earth Sciences and Resources, China University of Geosciences (Beijing), Beijing, China

The spatial accessibility of emergency shelters, indicating the difficulty of evacuation and rescue, is crucial for disaster mitigation and emergency management. To analyze accessibility, an effective approach is to evaluate the service capacity of emergency shelters. Multifaceted factors were employed to enhance the quantitative accuracy of accessibility indicators. However, scenario-specific analysis has not been emphasized. Considering the devastating potential of great earthquake disasters, we cannot ignore the impact of these scenarios on emergency shelter accessibility, especially in areas with high seismic risk. In this study, we developed an earthquake scenario-specific framework for spatial accessibility analysis (SAA), which integrates the service capacity of emergency shelters and the impact of strong ground motion and fault rupturing. We applied this framework to the urban area of Xichang City in Sichuan Province, western China. Xichang City, located in the linked area of the Anninghe fault and Zemuhe fault with many extreme historical earthquake disaster records, is prone to high seismic risk. We firstly collected emergency shelter and road network data in Xichang City. We then applied SAA based on the road network, using the network analysis method. After that, we analyzed the impact of strong ground motion on accessibility and generated the setback zone of fault rupturing. We integrated the effect of strong ground motion on accessibility within the setback zone of active faults. Finally, we generated a comprehensive accessibility map, considering both the predicted strong ground motion and potential fault rupturing. Our results show that the accessibility level changed in several towns of urban Xichang City due to strong ground motion and fault rupturing. The accessibility level decreased in Lizhou, Xingsheng, and Anning Towns. For areas with mapped fault lines, the accessibility level is Very-Low. Our results demonstrate the impact of earthquake damage on the accessibility of emergency shelters and the complexity of evacuation in earthquake scenarios. In general, we added earthquake rupturing

and ground motion characteristics into the SAA framework. This framework will help us enhance the reliability of SAA and the feasibility of seismic vulnerability evaluation.

KEYWORDS

earthquake disasters, spatial accessibility, emergency shelter, emergency management, risk assessment, Xichang City

1 Introduction

Earthquake disasters rank as the most destructive natural disasters in the world (Albulescu, 2023). With the rapid development of urbanization, the growing exposure of populations and structures aggravates the seismic risk in urban areas (Zou et al., 2023). Such unpromising circumstances necessitate the optimization of earthquake disaster mitigation. The foundation of an optimal formulation lies in knowledge about the location, capacity, and spatial accessibility of critical emergency facilities (Albulescu, 2023). Emergency shelters are one of the most essential emergency facilities, providing temporary resettlement, medical services, and emergency command centers for residents. The spatial accessibility of emergency shelters depends on the complexity of evacuation in an emergency and reflects the effectiveness of mitigation strategies and emergency management. The SAA of emergency shelters can also assist in formulating strategies to optimize disaster mitigation for high seismic risk areas.

Once an earthquake occurs, taking shelter is the very first instinct of residents, which demands mobility and accessibility (Zou et al., 2023). Exploring the spatial distribution of emergency shelters is an effective approach for identifying their accessibility to refugees (Gall, 2004; Chang and Liao, 2015). A map of spatial accessibility distribution could visualize the ease of reaching emergency shelters and evaluate the rationality of their allocation.

The methods used for the SAA of urban facilities mainly encompass typical spatial analysis methods such as buffer analysis (Zhang, 2020) and network analysis (Hou and Jiang, 2014; Albulescu, 2023; Yan, 2023). Methods are constantly developing, with advanced methods combined with GIS technology. The gravity model, which considers the relationship between supply- and demand-sides, can be an essential companion to GIS spatial analysis technology to distinguish the radiation coverage of different-sized areas (Zhang, 2020). As a special form of the gravity model, the two-step floating catchment area (2SFCA) method can assist in the study of urban emergency facilities. For example, the Gaussian two-step mobile search method, which is an improved 2SFCA method, introduces a Gaussian function with an excellent fit for distance decay. This function can help obtain a more accurate accessibility indicator (Tong et al., 2021; Jiang et al., 2023). In addition, a 2SFCA method with a variable service radius and evacuation radius was proposed to deal with the differences in emergency shelter service capacities and population distribution (Su, Chen, and Cheng, 2022a). Moreover, typical map applications (e.g., Google Map and Baidu Map) also stimulate accessibility evaluation. For instance, the application programming interface (API) can provide automatic time cost calculations for real-time travel (Wang et al., 2019) and navigation data (Shen et al., 2020). As the accuracy of the accessibility index constantly improves, the quantitative assessment of spatial accessibility continues to evolve.

However, qualitative analysis involving particular scenarios has not been much emphasized, although multiple scenarios can affect the accessibility of emergency shelters. For example, demographic density, evacuation capacity across age groups, population spatial temporal distribution, and even topographic factors can lead to differences in evacuation time (Su, Chen, and Zhang, 2022b; Zou et al., 2023). Moreover, the accessibility of emergency shelters in disaster scenarios is of great concern (Zhang and Yun, 2019). The accessibility might be undermined at different levels due to severe damage. Earthquake damage can be distinguished into direct damage (e.g., shaking or failure of over-bridges and roads) and indirect damage (e.g., street blockages due to debris from collapsed buildings) (Anastassiadis and Argyroudis, 2007). Strong ground motion and fault rupturing can cause catastrophic damage to buildings and road surfaces. During the 2008 *M*8 Wenchuan earthquake, the buildings along the fault-ruptured area were all significantly destroyed because of sudden fault rupturing (Xu et al., 2009). Moreover, open space damage caused by shaking and collapsed buildings can indirectly impede evacuation and rescue in the immediate aftermath (Francini et al., 2020; Bernardini and Ferreira, 2022). Dramatic destruction due to fault rupturing and strong ground motion can significantly impede emergency evacuations. In such situations, accessibility to emergency shelters would be impaired. To better assist in emergency management, we must explore the reasonable SAA of emergency shelters for earthquake scenarios.

In this study, we developed an earthquake scenario-specific framework for SAA. This framework integrated the service capacity of urban facilities with the characteristics of earthquake scenarios. Except for the spatial distribution of emergency shelters, we were able to gain an insight into the fault rupturing and strong ground motion caused by earthquake disasters. First, we operated the spatial service area of emergency shelters through network analysis. Based on the service area distribution, we generated the impact of strong ground motion and fault rupturing on the level of accessibility. Finally, we generated a comprehensive distribution map of the level of accessibility to emergency shelters in earthquake scenarios.

We employed this framework in the urban area of Xichang City in western China. After analyzing the impact of strong ground motion and fault rupturing characteristics, we determined the changes in the accessibility level in several towns of Xichang City. We also identified the practical service area of emergency shelters in earthquake scenarios. Our results are reasonable as we considered the potential effects caused by earthquake disaster characteristics.

In the subsequent sections, we introduce the historical earthquake records and the extent of the study area in Section 2. Then, in Section 3, we illustrate the framework combined with the case study in Xichang City. We display the results in Section 4

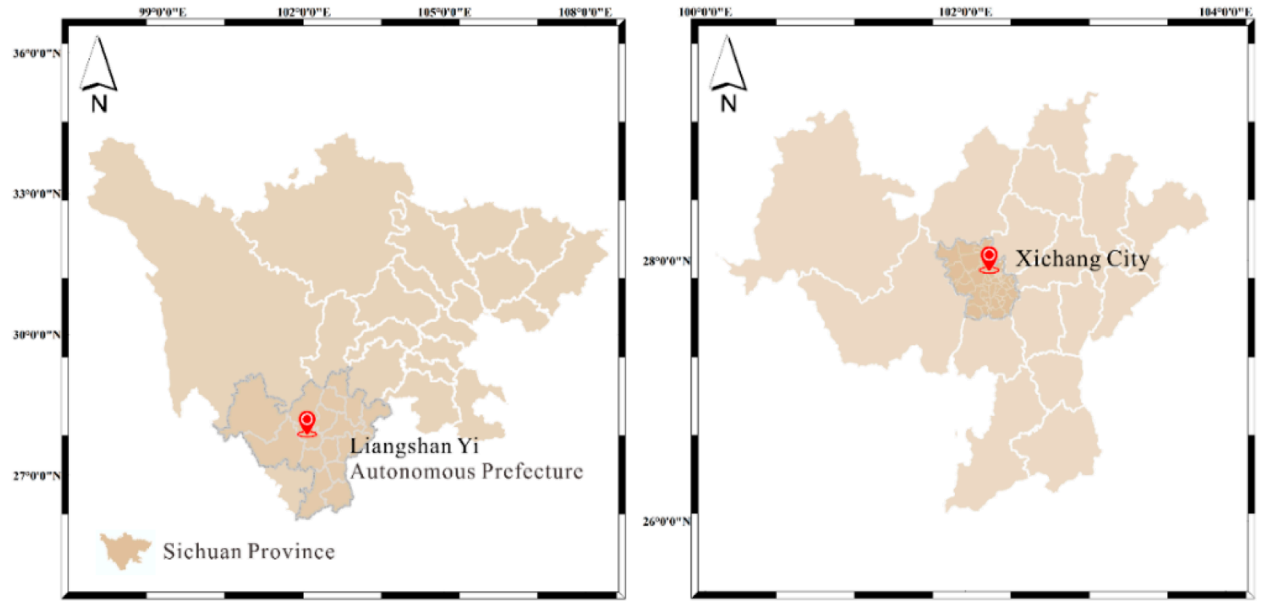

FIGURE 1
Geological location of Xichang City.

and discuss them in Section 5. The last section draws conclusions for this study.

2 Study area

Xichang City, located in southwestern Sichuan Province, China, is the capital of the Liangshan Yi Autonomous Prefecture (Figure 1). Xichang City's population has increased from 700,000 to 966,000 in the past 10 years. Infrastructure construction there has expanded ~ four times, with an urbanization rate of 68.48% (http://www.xichang.gov.cn/zfxxgk/zfxxgknr/tjsj_31356/202305/t20230526_2487868.html, last accessed in January 2024). The increased population and expanded inhabited structures can raise issues of natural disaster prevention, especially in high seismic risk zones. To cope with emergency evacuation issues in earthquake-prone areas, the construction of a reasonable SAA framework for emergency shelters is particularly important.

Xichang City is in an area with frequent earthquake occurrences. Due to the collision between the Indian and Eurasian plates, the eastern Tibetan plateau exhibits active crustal extrusion at a rate of approximately 10 mm/yr, resulting in frequent historical earthquakes. This pattern is particularly evident on large-scale boundary faults such as the Xianshuihe fault, the Anninghe fault, the Zemuhe fault and the Xiaojiang fault. Xichang City is located at the link of the Anninghe fault and the Zemuhe fault (Figure 2), both with high left-lateral strike–slip rates of ~6.5 mm/yr (Ren et al., 1990; Xu et al., 2003; Shen et al., 2005; Cheng et al., 2012).

Historically, Xichang City has suffered significantly from devastating earthquakes—the 814 *M*7 earthquake, the 1489 *M*6.8 earthquake, the 1536 *M*7.5 earthquake, the 1732 *M*6.8 earthquake, and the 1850 *M*7.8 earthquake (Ren et al., 1993; Wen, 2000; Jia Cheng et al., 2021; Jia Cheng, 2023). These historical earthquakes and their damage (Liu, 1989; Zhang et al., 1998; Min et al., 2005) are illustrated in Supplementary Table S1.

In the 1489 *M*6.8 earthquake, Xichang City was near the assumed VIII or VIII+ intensity zone. The seismic intensity for cities situated about 100 km from Xichang (e.g., Mianning and Yuexi) also reached VIII or VIII+. Cities located approximately 600 km–700 km from Xichang (e.g., Suining, Yingshan, and Lingshui) are near the IV-intensity zone (Supplementary Figure S1). In the 1536 *M*7.5 earthquake, Xichang City was in the IX intensity zone. Cities situated approximately 400 km from Xichang (e.g., Dayi, Chengdu, Chongqing, and Ziyang) were near the assumed VI or VI+ intensity zone (Supplementary Figure S2A). In the 1732 *M*6.8 earthquake, Xichang City was in the IX intensity zone (Supplementary Figure S2B). In the 1850 *M*7.8 earthquake, Xichang City was in the region where seismic intensity is assumed to be X (Supplementary Figure S2C).

Xichang City is still in a high-risk zone for earthquakes. Recent studies have proposed a sizable seismic gap in the Anninghe–Zemuhe–Daliangshan region, both from the lengthy intervals between historical earthquakes and the scarcity of M_L2.5 earthquakes since 1980 (Yi et al., 2004; Wen et al., 2008; Yi, Wen, and Su, 2008). The expansion of the population and the number of high buildings make the evacuation of residents difficult in large earthquake events. Hence, we applied our SAA methodology to emergency shelters in Xichang City.

Prompt evacuation and rescue are crucial for preventing fatalities and severe injuries in residential buildings in an emergency (Chen et al., 2023). Increasingly large populations in urban areas also increase exposure to natural disasters. This situation should be emphasized in disaster mitigation research (Huang et al., 2019;

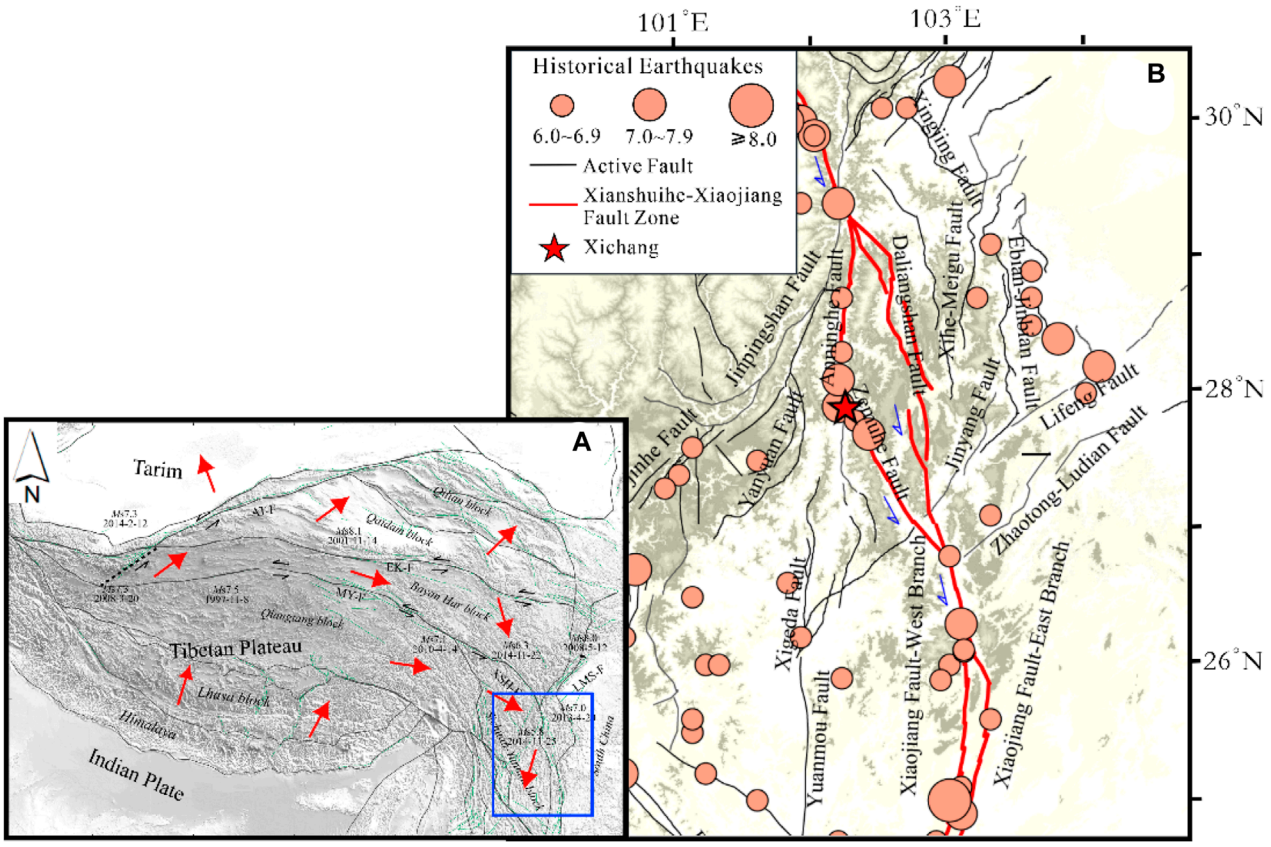

FIGURE 2
(A) Tectonic background in Fang et al. (2015). Red arrows show the present crustal deformation direction; AT-F: the Altyn Tagh fault; EK-F: eastern Kunlun fault; MY-F: Manyi fault; XSH-F: Xianshuihe fault; LMS-F: Longmenshan fault; black lines show the boundaries of the tectonic blocks (Zhang et al., 2003). Green lines are active faults. The blue rectangle marks the region of Figure 2B; **(B)** Active faults and historical earthquakes around Xichang City (Cheng et al., 2015).

Elliott, 2020; Iglesias et al., 2021; Albulescu, 2023). In this case, we employed SAA on emergency shelters in urban Xichang City, which is in a high seismic risk area. Using its population density data and remote sensing images, we extracted an area with an obviously high population density in Xichang City. Here, we analyzed raster data from Grid Population of the World Version 4 (GPW v4) in 2020 (https://sedac.ciesin. Columbia. edu/data/collection/gpw_v4, last accessed November 2023) and divided them into different categories according to the attribute values of each raster. Finally, we clipped out the areas with significant population density as the study area (Figure 3).

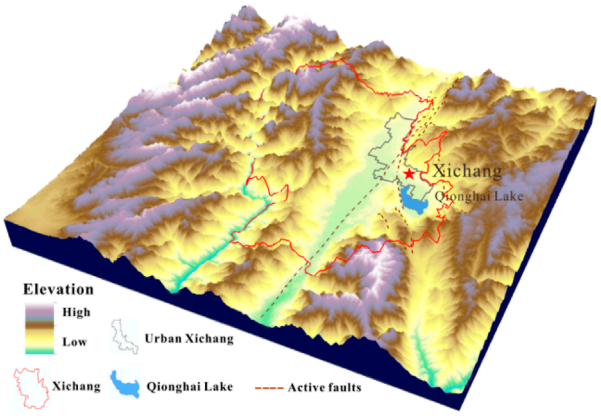

FIGURE 3
3D terrain model of Xichang City.

3 Methodology

Here, we develop an earthquake scenario-specific SAA framework for cities with high seismic risks, such as Xichang City. Based on quantitative analysis with the network analysis method, we focus on the characteristics of earthquake scenarios (e.g., strong ground motion and fault rupturing). The procedure in this framework contains three main steps. First, we analyzed the accessibility of emergency shelters based on road network data using network analysis. Next, we assessed the impact of strong ground motion on accessibility. Finally, we calculated the impact of fault rupturing on accessibility and generated a comprehensive accessibility distribution map. We illustrate the workflow in Figure 4.

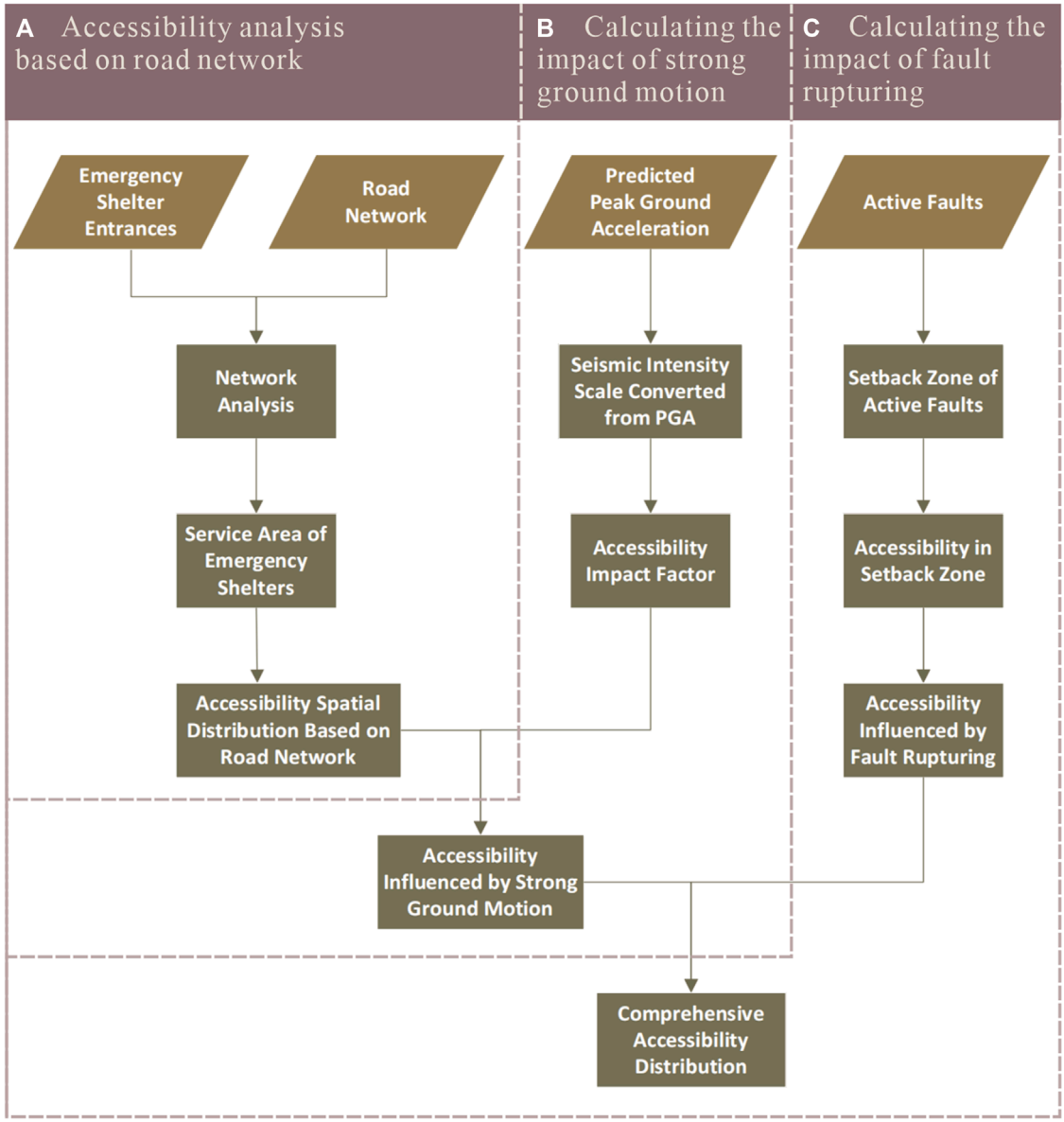

FIGURE 4
Workflow of the earthquake scenario-specific framework for SAA.

3.1 Data

In this study, datasets for analysis included emergency shelters, the urban road network, predicted peak ground motion, and the active faults. We illustrate the detailed information and source of these data in Table 1.

Urban emergency shelters refer to sites with certain functional facilities which can protect people from direct or indirect damage in disasters and provide essential life support after disasters (Qian, 2010). The local government makes some improvements and modifications to extend emergency evacuation functions on public open spaces (e.g., parks and squares). In the event of a disaster, these improved facilities can supply temporary resettlement and fundamental medical services for injuries (Li et al., 2023). Evacuation efficiency relies on the reasonability of emergency shelter spatial distribution. Here, we applied SAA to emergency shelters in Xichang City to analyze the reasonability of their distribution.

We used remote sensing images from Google Earth Pro to select proper sites as emergency shelters. In urban areas with congregations of tall buildings, a qualified emergency shelter requires the following conditions: flat terrain, open areas, and no tall buildings around to ensure safety (Amini Hosseini, Asadzadeh Tarebari, and Mirhakimi, 2022). According to these conditions, we selected some spacious and flat sites, such as playgrounds, parks, squares, sizeable open-air parking lots, and stadiums (Figures 5A–E). Among the selected sites, we found some large open spaces covered with green dust cloth on remote sensing images (Figure 5F), which may be alternate building

TABLE 1 Data source and details.

Dataset	Source	Details and processing
Emergency shelters	Manual selection	Reference for selection: GB 21734-2008 (General Administration of Quality Supervision, Inspection and Quarantine of the People's Republic of China, 2008), GB/T 33744-2017 (General Administration of Quality Supervision, Inspection and Quarantine of the People's Republic of China, 2017), and GB/T 35624-2017 (General Administration of Quality Supervision, Inspection and Quarantine of the People's Republic of China, 2017). General principles: i. Being flat and spacious; ii. Away from high buildings and structures.
Urban road network	Open Street Map	Extraction via Open Street Map. Manual pre-procession via QGIS.
Predicted Peak Ground Acceleration (PGA)	475-year PGA values (Jia Cheng et al., 2021)	Calculation of PGA values using a compatible fault model from geological slip rates and geodetic slip rates inverted in an elastic block model
Active faults	Updated and integrated active faults dataset (Wu et al., 2023)	Update and integration of the dataset based on the most recent 20-year region-scale active fault survey data (1:250,000–1:50,000), including geophysical probing, drill logging, offset landform measuring, and sample dating, as well as geometric and kinematic parameters of exposed and blind faults, paleo-earthquake sequences, and recurrence intervals

sites. Although they meet the basic requirements of being flat with no tall buildings around, we still excluded these sites due to the possibility of construction in the short term.

Since every second in an earthquake emergency evacuation is essential for minimizing casualties (Chen et al., 2023), we identified accurate locations of selected emergency shelters for subsequent calculations. Most emergency shelters are sizeable and open while people's running speed is limited, so we directly labeled the location of entrances instead of the emergency shelter center in our SAA. Residents from different directions can reach the shelters from shorter distances through multiple entrances. Our approach used the time to the entrances of available emergency shelters other than the time to the center. This procedure makes our results more reasonable.

We employed Open Street Map (OSM) data for the urban road network data and preprocessed them through QGIS. After extracting and clipping the road network vector data for the urban areas of Xichang, we simplified the road network to ensure the efficiency and rationality of subsequent analysis. We removed the line elements unsuitable for emergency evacuation from the attribute table, such as track, rail, river, stream, administrative, and boundary. Moreover, we determined the anomalies in the road network vector data, such as unreasonable dangles, pseudo-nodes, and self-intersections. Dangles are not allowed in the road network topology, except for dead ends (Liu et al., 2017). The pseudo-nodes indicate that the complete lines are separated into discrete segments by the unconnected nodes (Qin, 2010). We also examined them using the error inspector and corrected them to ensure the implementation of subsequent network analysis.

We used active fault data from the updated and integrated database of Wu et al. (2023). In their database, region-scale active fault survey data (1:250,000–1:50,000) for the past 20 years are used to update and integrate the active fault data in the Seismotectonic Map of China and its Adjacent Regions (1:4,000,000).

We used predicted PGA to represent strong ground motion. The 475-year PGA results are from Jia Cheng et al. (2021). Two sets of the results were supplied in their work: a compatible fault model from geological slip rates and geodetic slip rates inverted in an elastic block model. Their results are reasonable, as they considered both the fault slip rate and multi-segment rupture events in their PGA results.

3.2 Spatial accessibility analysis based on the road network

In this process, we operated the SAA via the Network Analysis Tool. Network analysis allows for the optimal investigation of network structure and resources by analyzing the network state. This method can also simulate the resource flow and distribution of the network (Liu et al., 2017). The positioning and allocation of resources in the network system is one of the main application scenarios of network analysis (Qin, 2010). The generation of a service area includes the components of a road network located within a specified impedance. The service area distribution of facilities can represent the accessibility of urban facilities for residents in different locations without a specific travel direction. Therefore, network analysis is an effective method for facility SAA.

We used the following steps for SAA based on the road network. First, we calculated the time cost and added it to the attribute table of road network vector data. Next, we established a new network dataset. We set the impedance to the value of the Time Cost field and did not assign a specific direction of travel. We chose these selected emergency shelters as the facilities in our dataset. Then, we started to generate the service area based on road network data. We created a new service area in the network analysis tool and loaded the emergency shelter entrances into the facility point layer. In analysis settings, we input the break value of impedance. Here, we set the break value at 5-min intervals for the former and 15-min intervals for the last two (0–5 min, 5–10 min, 10–15 min, 15–30 min, and ≥30 min). Finally, we chose to merge by break value in multiple facilities options and set rings as overlay types.

After all the setup work, we obtained the time cost distribution circles as the accessibility to emergency shelters. Time cost indicates the complexity of evacuation routes, so we set the accessibility level based on different time circles (Table 2). Five accessibility levels were used in our results: Very-High, High, Medium, Low, and Very-Low.

FIGURE 5
Examples of selected emergency shelters and excluded sites: **(A)** playground; **(B)** park; **(C)** square; **(D)** sizeable open-air parking lots; **(E)** open-air stadium; **(F)** space covered with green dust cloth which might be used for future engineering and construction.

TABLE 2 Relationship between time cost for evacuation and corresponding accessibility level.

Time cost for evacuation (min)	Accessibility level
≤5	Very-High
5–10	High
10–15	Medium
15–30	Low
≥30	Very-Low

3.3 Influence from strong ground motion

In an earthquake event, fault rupturing and its ground motion will cause severe earthquake disasters, especially for cities with large populations and high buildings. Strong ground motion can cause violent shudders and ground shaking (Anastassiadis and Argyroudis, 2007), which would severely affect the evacuation of residents. In that case, people will change their routes, times, and escape modes of evacuation (Nakanishi, Matsuo, and Black, 2013). Therefore, we analyzed the influence from the predicted strong ground motion data to improve the reliability of the SAA results.

The intensity of earthquakes (e.g., Modified Mercalli intensity scale) is often used to measure the effects of an earthquake at given locations. Here, we converted the predicted PGA data to seismic intensity levels according to the statistical relationship between peak ground acceleration and seismic intensity according to the Chinese national standard China Seismic Intensity Scale (GB_T 17742-2020). The PGA data are those predicted as 10% in the next 50 years (Jia Cheng et al., 2021), based on the inverted geodetic and geological fault slip rates. In the intensity maps both from the geodetic and geological fault slip rates, the urban area of Xichang City is located in the VIII+ intensity zone (Figure 6). According to the China Seismic Intensity Scale (GB_T 17742-2020), most people will be shaken, bumped, and have difficulty walking in intensity VIII areas. When the intensity reaches IX degrees, people walking or running will fall. According to these conditions, we established three sets of impact factors on the accessibility level. Here, we employed different impact factor sets to identify the most suitable set to represent the impacted accessibility distribution in the predicted strong ground motion field (Table 3).

The accessibility level decreases when the time cost for evacuation increases. Hence, we multiplied the time by the inverse of the impact factors (Eq. (1)).

$$T_2 = T_1 \times \frac{1}{I}(1), \tag{1}$$

where T_2 is the time cost for evacuation impacted by strong ground motion, T_1 is the time cost for evacuation based on road network analysis, and I refers to the impact factor on the accessibility level.

After this, we obtained the distribution of time-cost circles under each impact factor set. We employed the impact factor set with

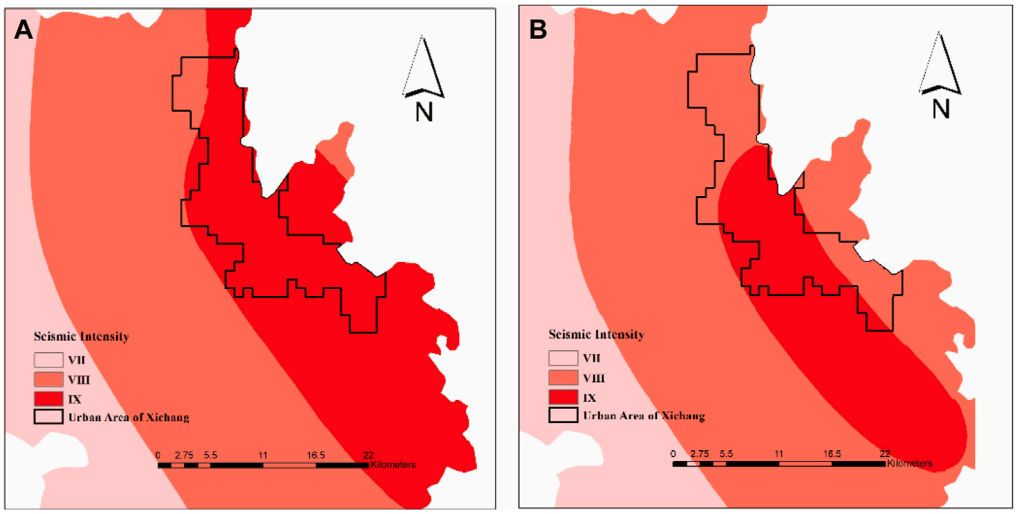

FIGURE 6
(A) Seismic intensity converted from predicted PGA data with the geodetic slip rate. **(B)** Seismic intensity converted from predicted PGA data with geological slip rate (Jia Cheng et al., 2021; GB_T 17742-2020).

TABLE 3 Impact factors on accessibility in different seismic intensity zones.

Seismic intensity degree	Impact factor on accessibility level (I)		
	a	b	c
VIII (8)	0.5	0.6	0.7
IX (9)	0.3	0.4	0.5

clearest demonstration and generated the accessibility level based on the time cost for evacuation (T_2) (Table 2).

3.4 Influence from fault rupturing

Surface rupturing by strong earthquakes can destroy any inhabited structure along the fault lines. On-site investigations and experimental research show that buildings within a rupture zone usually suffer the most severe damage, causing the heaviest disaster (Xu et al., 2016; He et al., 2022). Therefore, we added the effect of surface potential rupturing on the mapped surface lines of the Anninghe fault and the Zemuhe fault from Wu et al. (2023).

The primary setback distance between buildings and the boundary of the active fault rupture zone is set to 15 m (Xu et al., 2016; He et al., 2022). The road surface and the surrounding buildings or structures will probably be damaged within this region, which would significantly impede the evacuation of residents. We generated a buffer zone of linear features with a distance of 15 m around the faults as the setback zone. We set the accessibility level in this region to Very-Low due to the high probability of severe damage.

We then integrated the accessibility level in the setback zone into that affected by the strong ground motion layer, obtaining a comprehensive accessibility distribution map.

4 Results

In this section, we present the result of each procedure (Figure 4).

For data collection, we selected 59 emergency shelter entrances in the urban area of Xichang City (Table 4). Table 4 shows that Xiaomiao Town, Xijiao Town, and Beicheng Block are the top three regarding emergency shelter quantity. Regarding density, emergency shelters are the most densely distributed in Beicheng, Changning, and Changan Blocks. Figure 7A illustrates the spatial distribution of selected emergency shelters and road networks. Our results show that Xichang City has more emergency shelters in the south but fewer in the north (Figure 7A). Emergency shelter distribution is consistent with the spatial distribution of population density. However, on both sides of the Dong River (the area linking Xicheng Block and Dongcheng Block), the number of emergency shelters is not proportional to the large population there. Lizhou and Xisheng Towns, with sparse populations and undeveloped road networks, have no proper emergency shelters according to the remote sensing imagery.

Figure 7B shows the road network-based accessibility distribution map. In this figure, we found that, in areas with dense emergency shelters and well-developed road networks, residents had faster access to emergency shelters (e.g., Beicheng, Xicheng, Dongcheng, and Changning Blocks, eastern Sihe and southern Anning Towns). In rural areas far from emergency shelters, residents have to spend more time accessing emergency shelters (e.g., Lizhou, Xingsheng, northern Anning, Xixiang, Chuanxing, and western Sihe Towns). For example, people living in Xingsheng Town need >20 min to access the nearest shelter, while people in Lizhou and Chuanxing Towns will spend more than 30 min escaping to selected emergency shelters. Figure 9A shows the accessibility level distribution based on road network analysis. In Lizhou, Xingsheng, western Anning, and Chuanxing Towns, the accessibility level is

TABLE 4 Information about selected emergency shelters.

Towns/ blocks	Area (km^2)	Number of emergency shelters	Emergency shelter density (per km^2)	Ranking by quantity	Ranking by density
Xiaomiao Town	45.85	14	0.31	1	7
Xijiao Town	29.25	12	0.41	2	5
Beicheng Block	2.16	7	3.24	3	1
Anning Town	52.64	6	0.11	4	10
Xixiang Town	30.08	4	0.13	5	9
Gaoba Town	22.04	4	0.18	5	8
Xicheng Block	3.92	3	0.77	6	4
Changning Block	1.15	2	1.74	7	2
Changan Block	3.63	2	0.83	7	3
Chuanxing Town	67.17	2	0.03	7	12
Dongcheng Block	2.61	1	0.38	8	6
Sihe Town	80.59	1	0.01	8	13
Xincun Block	14.84	1	0.07	8	11
Xingsheng Town	37.07	0	0	9	14
Lizhou Town	35.32	0	0	9	14

at Very-Low and Low levels, while for towns or blocks with a density of emergency shelters, accessibility presents Very-High and High levels.

After analyzing the impact of strong ground motion based on values of impact factors, we can see that the time cost escaping to emergency shelters increased in general (Supplementary Figure S3). In Figure 7B, we see five grades of classification based on the road network with clear accessibility distribution for different levels. For accessibility levels under the impact of ground motion, some of the time circle distributions are not clearly demonstrated (Figure 8). Figure 8C shows four grades of time-cost circle, while Figures 8A and 8B only display three distinct grades. This phenomenon might be caused by the increasing time cost in an earthquake scenario. Hence, we chose set C for the impact factors to analyze the influences from strong ground motion.

Based on the results in Figure 8C, we generated accessibility level distribution under the effect of strong ground motion. Our results show that the accessibility level in most areas changed after analyzing the influence from the predicted strong ground motion. Figure 9 shows the accessibility level distribution based on different sources. Figure 9A shows different accessibility levels only based on road networks, while Figures 9B and 9C show influence from predicted ground motion data calculated from the geodetic slip rates of the faults and those from geological fieldwork. Figure 9Bs and 9C show the accessibility of Low-level areas diminished to Very-Low (e.g., southern Lizhou, western Xingsheng, and central Chuanxing Towns). We also noted that the accessibility of Medium- and High-level areas in Figure 9A decreased to Low and Medium levels, as given in Figures 9B and 9C, respectively, such as the area in northeastern, northwestern, and southwestern Anning Town, central Xixiang Town, and the linked area of northeastern Xiaomiao Town, western Xijiao Town, and southwestern Sihe Town. For areas with a Very-High level in Figure 9A, the accessibility level is almost unchanged, such as the areas in Beicheng, Dongcheng, Xicheng, Changning and, Changan Blocks, and northern Gaoba, eastern Xiaomiao, and south-central Anning Towns. In Figures 9B and 9C, the accessibility levels of some specific towns or blocks, such as Anning and Xixiang Towns, cover four levels, including Very-High, Medium, Low, and Very-Low. There are three accessibility levels in Chuanxing Town: Very-High, Medium, and Very-Low. In the towns above, the accessibility level decreases with increasing distance from emergency shelters. While for the Beicheng Block, Dongcheng Block, Xicheng Block, and Changan Block, the accessibility level presents only the type of Very-High level. However, the accessibility level of the entirety of Lizhou Town (within the scope of our study) is only Very-Low.

Considering the fault rupturing effects in an earthquake, we also added the fault surface lines and generated the setback zone of regional mapped active faults. Two large-scale N–S trending faults spread across the urban areas of Xichang City,

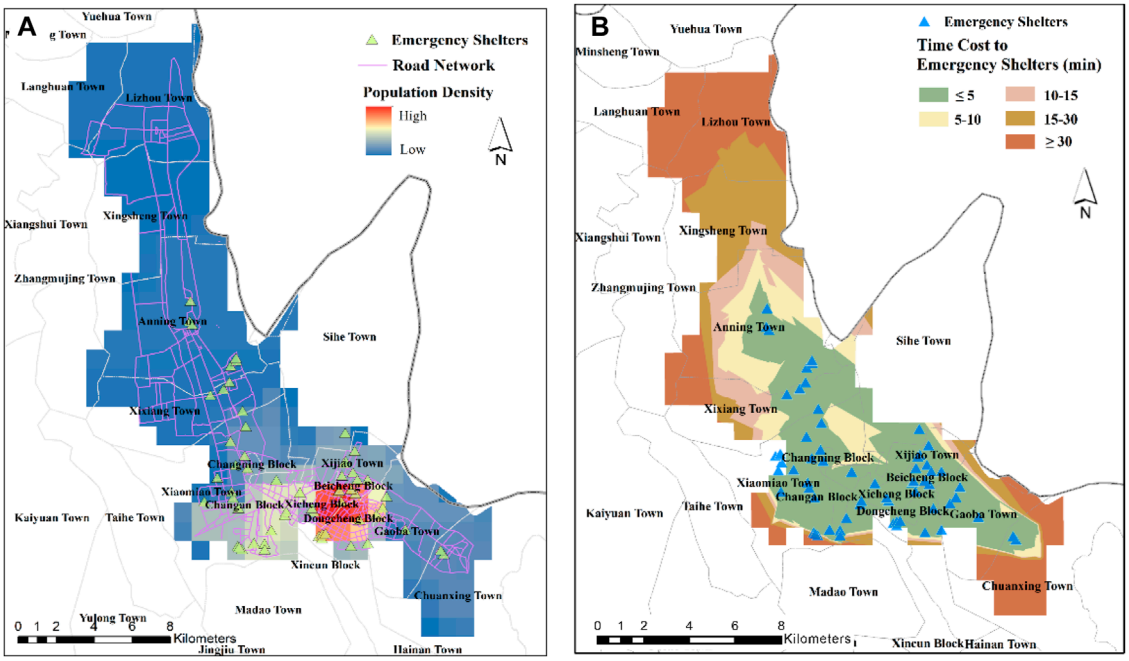

FIGURE 7
(A) Spatial distribution of population density, selected emergency shelters, and simplified road network in the urban area of Xichang City. **(B)** Accessibility to emergency shelters based on road network analysis. We used a network analysis tool, in which the facilities are emergency shelters and the impedance is the time cost for evacuation. Gray lines show the boundary of the towns.

such as Anning, Xixiang, and Xiaomiao Towns (Figure 10). After reassigning the raster value of the setback zone, the accessibility level there is Very-Low. We found the apparent change in the accessibility level in towns or blocks crossed by setback zones, such as the Changan and Xicheng Blocks, at Very-High level decreased to Very-Low.

5 Discussion

In this study, we developed an earthquake scenario-specific framework for SAA. We applied this framework to analyze the practical accessibility of emergency shelters in earthquakes for urban Xichang City. We employed active fault data and predicted strong ground motion data from geodetic and geological slip rates to explore the impact of earthquake damage.

Our results show that the areas with high accessibility to emergency shelters are in the middle of Xichang City, where emergency facilities are densely distributed, such as Beicheng, Dongcheng, Xicheng, Changan and Changning Blocks and Xijiao Town. Low accessibility levels are mainly distributed on the outskirts with few emergency shelters, such as in Lizhou, Xingsheng, central Chuanxing and, and western Anning Towns. Our results show that the spatial variation of accessibility level distribution decreases gradually with increasing distance from emergency shelters. It is worth noting that the accessibility level for Very-High areas almost did not change after adding the effect of potentially strong ground motion (see Figure 9), implying that people living in these areas can escape to emergency shelters in 5 min, even under strong ground motion from a sudden earthquake. We believed that the dense emergency shelters in urban areas can help residents evacuate in emergencies, even in earthquake scenarios.

Nevertheless, we also found that some areas with few emergency shelters still had a Very-High accessibility level, such as west Dongcheng Block and east Xicheng Block (Figure 11A). These areas have few emergency shelters but large populations and dense residential buildings. Our results show that their accessibility level is Very-High instead of Low. We considered this a result of their well-developed road networks. Thus, a developed road network can improve the accessibility level even in an area with few emergency shelters.

In contrast, an undeveloped road network can diminish accessibility, such as the linked area of northeastern Xiaomiao, western Xijiao, and southwestern Sihe Towns, which have plenty of emergency shelters. Their accessibility level is still Medium rather than Very High. In these areas, the hills (e.g., Panying, Wangjia, Macao, and Majingzi Hills) result in undeveloped road networks (Figure 11B), making evacuation more difficult. Hence, the role of road networks is also crucial to SAA.

We also demonstrated that the impact of potentially strong ground motion and fault rupturing on accessibility to emergency shelters should not be ignored. After analyzing potentially strong ground motion, the accessibility level in most areas declined due to the increasing time cost to access emergency shelters. In areas with mapped faults, the accessibility level decreased as far as Very-Low due to impedance from ruptured surfaces and damaged inhabited structures. These changes in the accessibility level to emergency shelters indicate that SAA should also consider the significant

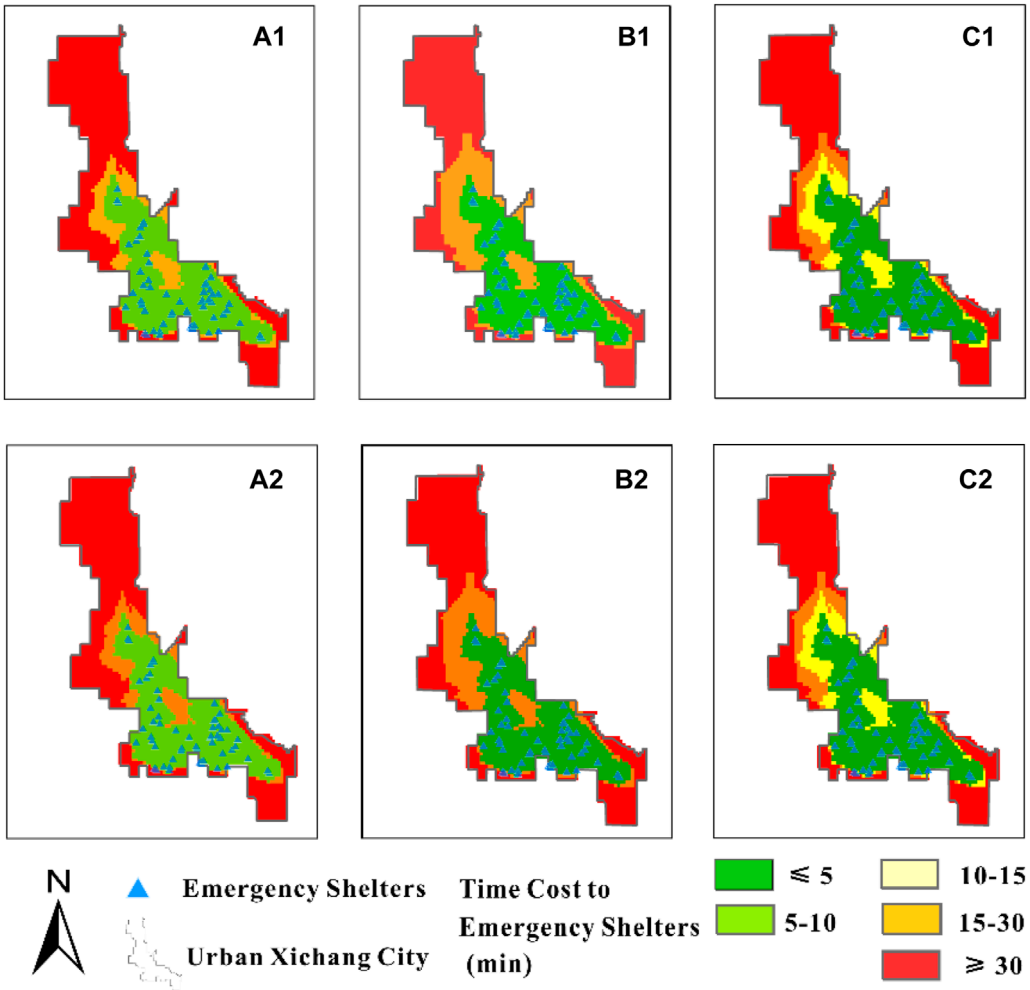

FIGURE 8
Accessibility to emergency shelters under three sets of strong ground motion impact factor (Table 3). **(A1, A2)** Results from impact factor set a. **(B1, B2)** Results from impact factor set b. **(C1, C2)** Results from impact factor set c. Pictures of the first and second row respectively show the results based on geodetic and geological slip rates.

influence of extreme situations, such as strong earthquake scenarios. To cope with such an pessimistic emergency relief situation, the government should take action to refine emergency management. For areas with decreased levels of emergency shelter accessibility, the government should formulate an emergency evacuation plan and guidebook targeted at earthquake scenarios. For towns with multiple accessibility levels, the government should customize emergency evacuation work based on different accessibility levels (e.g., Anning, Xixiang, and Chuanxing Towns).

Our results indicate that people living on urban outskirts have difficulty escaping to emergency shelters. This does not directly mean that residents living there are more vulnerable to an earthquake. For these areas, we only analyzed the spatial accessibility of emergency shelters using the 59 selected emergency shelters, road network data, potential strong ground motion data, and active fault data, but we neglected the role of spaces for shelters, such as farmland and other open fields. In addition, it is easier for residents to exit structures via the lower height of rural residences and in lower populations than urban areas.

In summary, we developed an earthquake scenario-specific framework in the regional SAA for emergency shelters from the following aspects:

1. We developed an earthquake scenario-specific framework to generate a reasonable SAA for emergency shelters. Our framework is reasonable as it integrates the service capacity of urban emergency facilities with earthquake characteristics (strong ground motion and fault rupturing). We also added insights into earthquake scenario characteristics, which contribute to a reasonable simulation of emergency evacuation in earthquakes.
2. We applied this framework in Xichang City. We operated the analysis only in an urban area with an obviously high population density rather than all of Xichang City to obtain more targeted results. We directly labeled the location of entrances instead of the center of emergency shelters to improve the accuracy of accessibility analysis. We referred to the national standard Chinese Seismic Intensity Scale in

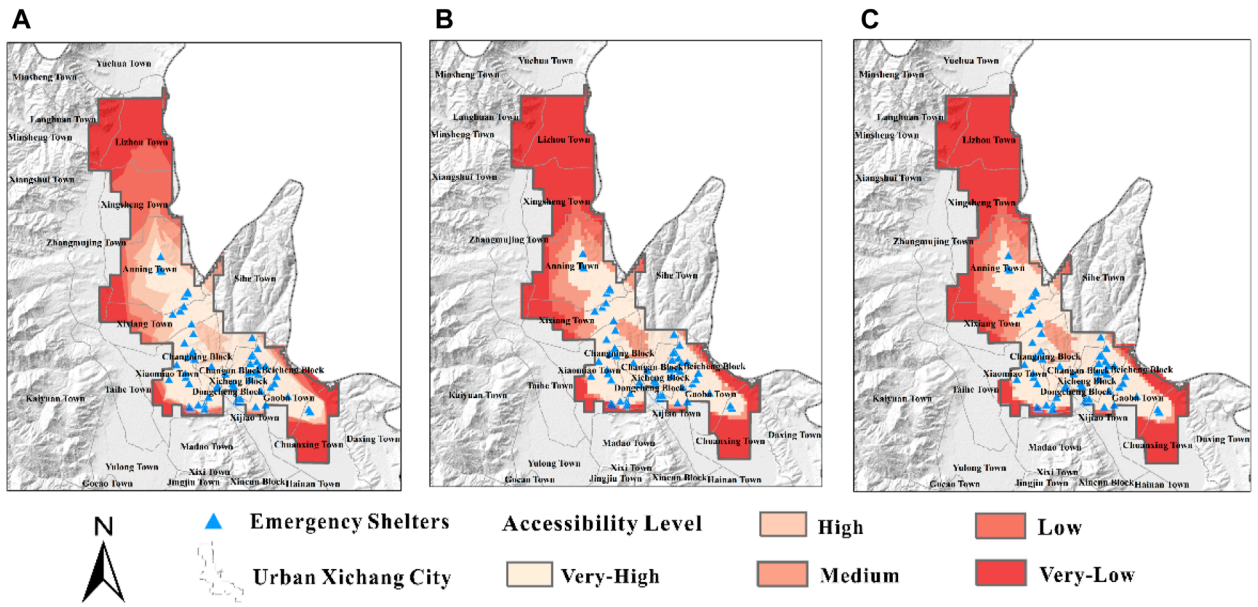

FIGURE 9
(A) Accessibility level based on road network analysis. **(B)** Accessibility level impacted by predicted strong ground motion based on the geodetic slip rate. **(C)** Accessibility level impacted by predicted strong ground motion based on the geological slip rate.

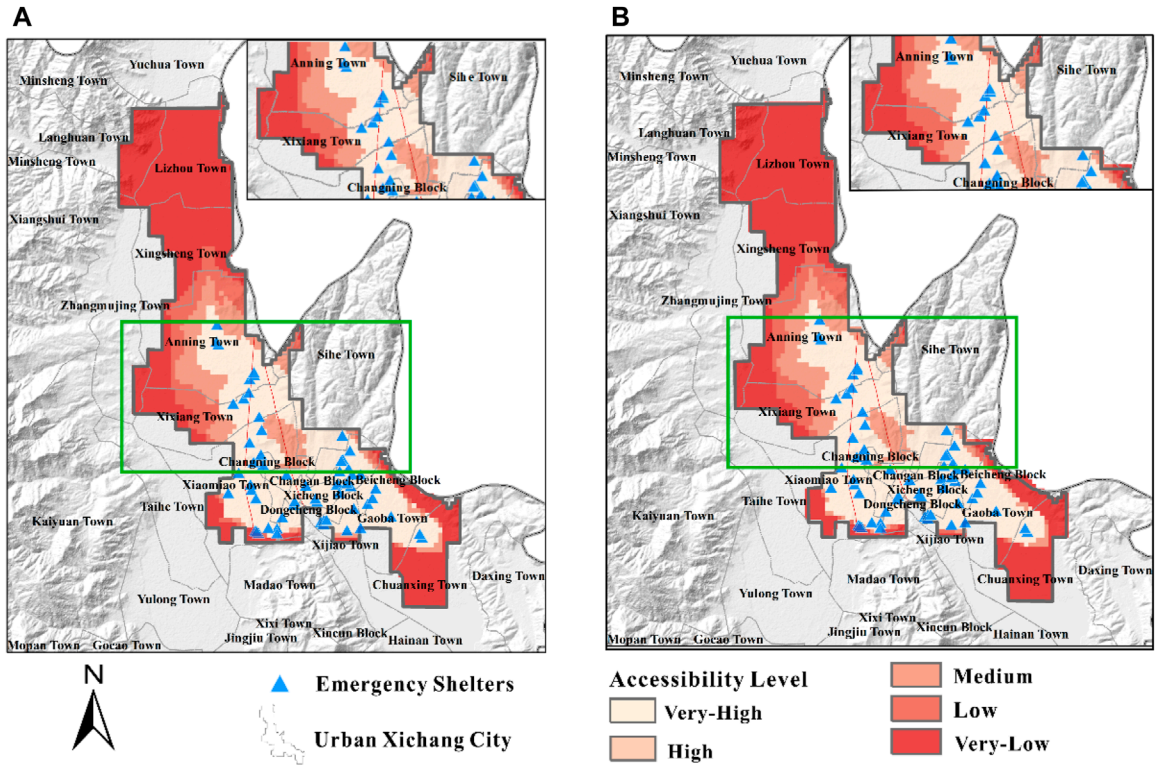

FIGURE 10
Comprehensive accessibility distribution map. **(A)** The accessibility was calculated based on predicted PGA data from the geodetic slip rate; **(B)** The accessibility was calculated based on predicted PGA data from the geological slip rate.

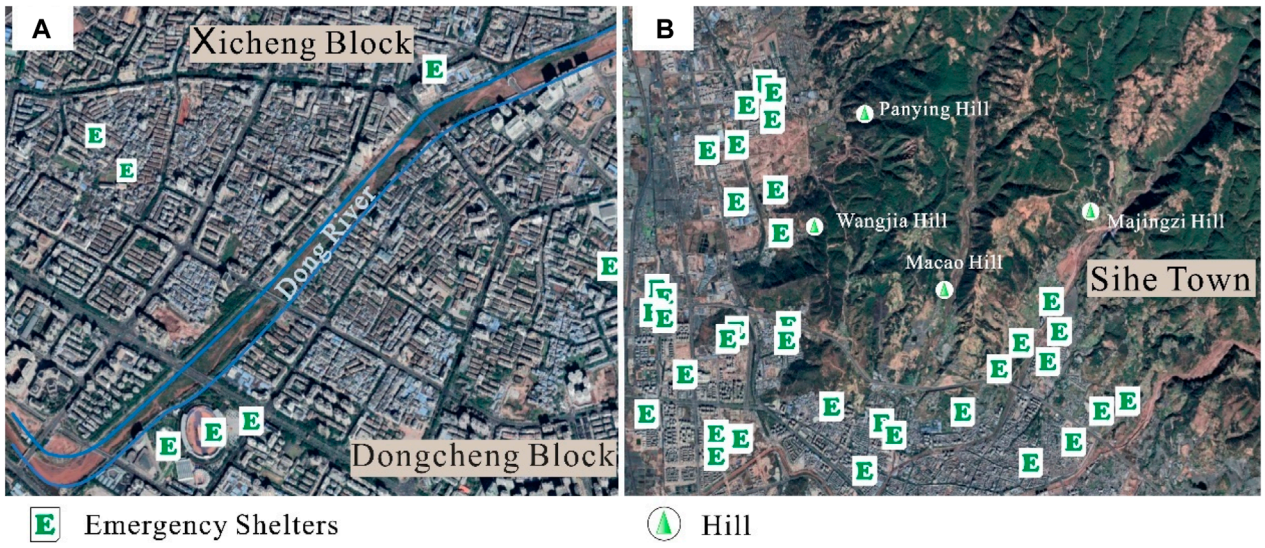

FIGURE 11
(A) Linked area of Xicheng and Dongcheng Blocks with few emergency shelters but developed road network. **(B)** Western Sihe Town with hills (e.g., Panying, Wangjia, Macao, and Majingzi Hills).

analyzing the impact of strong ground motion to make the result reliable.

3. Our results can help us understand evacuation to emergency shelters, especially in earthquake scenarios. We identified the practical service area of emergency shelters by analyzing the impact of potentially strong ground motion and fault rupturing. We identified the changes in the accessibility level of emergency shelters in several towns of Xichang City. These results are reasonable because we consider the potential impedance caused by earthquakes in this study.
4. The framework and results of this study can provide a reference for future planning of emergency shelters. Our analysis can assist in the evaluation of seismic vulnerability in terms of casualties and can further support research into the seismic risk of Xichang City.

However, this framework still requires some improvements. 1) We did not consider the relationship between population density and the capacity of emergency shelters. Among the 59 selected emergency shelters, the area varies from 994 m^2 to 2,789 m^2. Considering 2 m^2 per person to avoid overcrowding (Bernardini and Ferreira, 2022), the population capacity of emergency shelters ranges from 497 to 1,394, with a difference of nearly three times as significant.

2) We did not analyze the influence of the performance of buildings. The resistance of buildings can affect emergency evacuations. Building collapse will significantly impede emergency evacuation and even threaten the safety of residents (Guo et al., 2023; Magapu and Setia, 2023). The evacuation performance of buildings (e.g., distribution of separate stairs, maximum density, and vision time) is also related to evacuation efficiency (Chen et al., 2023).

3) In emergency evacuations, various responses to the surrounding environment can lead to multiple ways to avoid damage. For example, in a tunnel emergency evacuation, people's behavior may be influenced by variables such as the best location to install the board, variable message signs (VMS) contents, and formats and how they interact (Ilkhani et al., 2023).

6 Conclusion

In this study, we proposed an earthquake scenario-specific framework to analyze spatial accessibility to emergency shelters. We applied this framework in urban Xichang City and achieved a comprehensive distribution of accessibility to emergency shelters by adding the impact of strong ground motion and fault rupturing.

Our results show that areas with dense emergency shelters and developed road networks present high accessibility levels (e.g., Beicheng, Dongcheng, and Xicheng Blocks). In contrast, areas far from emergency shelters with undeveloped road networks present low accessibility levels (e.g., Lizhou, Xisheng, Chuanxing, and western Xixiang Towns). As impacted by strong ground motion, the accessibility level decreases in several particular towns (Lizhou, Xingsheng, and Anning). For areas with mapped fault lines, residents and buildings would suffer most damage in earthquakes. The accessibility level to emergency shelters presents a Very-Low level.

Therefore, the SAA of emergency shelters is crucial for efficient evacuation, especially in complex earthquake scenarios. The blocks and towns with few emergency shelters and low accessibility levels must receive greatest attention. The seismic performance of buildings within the setback zone of active faults needs to be emphasized.

Data availability statement

The original contributions presented in the study are included in the article/Supplementary Material; further inquiries can be directed to the corresponding author.

Author contributions

ZW: data curation, formal analysis, software, writing–original draft, and writing–review and editing. JC: funding acquisition, methodology, project administration, supervision, and writing–review and editing. CX: methodology, supervision, and writing–review and editing.

Funding

The author(s) declare financial support was received for the research, authorship, and/or publication of this article. This study receives funds from the National Natural Science Foundation of China (Grant Nos 42074064 and U2039201) and National Institute of Natural Hazards, Ministry of Emergency Management of China (Grant NO. ZDJ 2020-14).

Conflict of interest

The authors declare that the research was conducted in the absence of any commercial or financial relationships that could be construed as a potential conflict of interest.

The author(s) declared that they were an editorial board member of Frontiers at the time of submission. This had no impact on the peer review process and the final decision.

Publisher's note

Supplementary material

The Supplementary Material for this article can be found online at https://www.frontiersin.org/articles/10.3389/feart.2024.1376900/full#supplementary-material

References

Albulescu, A.-C. (2023). Open source data-based solutions for identifying patterns of urban earthquake systemic vulnerability in high-seismicity areas. *Remote Sens.* 15 (5), 1453. doi:10.3390/rs15051453

Amini Hosseini, K., Asadzadeh Tarebari, S., and Mirhakimi, S. A. (2022). A new index-based model for site selection of emergency shelters after an earthquake for Iran. *Int. J. Disaster Risk Reduct.* 77, 103110. July. doi:10.1016/j.ijdrr.2022.103110

Anastassiadis, A. J., and Argyroudis, S. A. (2007). Seismic vulnerability analysis in urban systems and road networks. Application to the city of thessaloniki, Greece. *Int. J. Sustain. Dev. Plan.* 2 (3), 287–301. doi:10.2495/SDP-V2-N3-287-301

Bernardini, G., and Ferreira, T. M. (2022). "Emergency and evacuation management strategies in earthquakes: towards holistic and user-centered methodologies for their design and evaluation," in *Seismic vulnerability assessment of civil engineering structures at multiple scales* (Elsevier), 275–321. doi:10.1016/B978-0-12-824071-7.00002-0

Chang, H.-S., and Liao, C.-H. (2015). Planning emergency shelter locations based on evacuation behavior. *Nat. Hazards* 76 (3), 1551–1571. doi:10.1007/s11069-014-1557-x

Chen, Y., Wang, C., Du, X., Shen, Y., and Hu, B. (2023). An agent-based simulation framework for developing the optimal rescue plan for older adults during the emergency evacuation. *Simul. Model. Pract. Theory* 128, 102797. November. doi:10.1016/j.simpat.2023.102797

Cheng, J., Wu, Z., Liu, J., Jiang, C., Xu, X., Fang, L., et al. (2015). Preliminary report on the 3 august 2014, mw 6.2/ms 6.5 ludian, yunnan-sichuan border, southwest China, earthquake. *Seismol. Res. Lett.* 86 (3), 750–763. doi:10.1785/0220140208

Cheng, J., Xu, C., Ma, J., Xu, X., and Zhu, P. (2023). From active fault segmentation to risks of earthquake Hazards and property and life losses—a case study from the xianshuihe-xiaojiang fault zone. *Sci. China Earth Sci.* 66 (6), 1345–1364. doi:10.1007/s11430-022-1076-y

Cheng, J., Xu, X., Gan, W., Ma, W., Chen, W., and Zhang, Y. (2012). Block model and dynamic implication from the earthquake activities and crustal motion in the southeastern margin of Tibetan plateau. *Chin. J. Geophys* 55 (4), 1198–1212. (in Chinese). doi:10.6038/j.issn.0001-5733.2012.04.016

Cheng, J., Xu, X., Qi, Y., Yang, X., and Chen, H. (2021). Seismic hazard of multi-segment rupturing for the anninghe–zemuhe–daliangshan fault region, southeastern Tibetan plateau: constraints from geological and geodetic slip rates. *Nat. Hazards* 107 (2), 1501–1525. doi:10.1007/s11069-021-04643-7

Elliott, J. R. (2020). Earth observation for the assessment of earthquake hazard, risk and disaster management. *Surv. Geophys.* 41 (6), 1323–1354. doi:10.1007/s10712-020-09606-4

Fang, L., Wu, J., Liu, J., Jia, C., Jiang, C., Han, L., et al. (2015). Preliminary report on the 22 november 2014 M_w 6.1/M_s 6.3 kangding earthquake, western sichuan, China. *Seismol. Res. Lett.* 86 (6), 1603–1613. doi:10.1785/0220150006

Francini, M., Gaudio, S., Palermo, A., and Viapiana, M. F. (2020). A performance-based approach for innovative emergency planning. *Sustain. Cities Soc.* 53, 101906. February. doi:10.1016/j.scs.2019.101906

Gall, M. (2004). Where to go? Strategic modelling of access to emergency shelters in Mozambique. *Disasters* 28 (1), 82–97. doi:10.1111/j.0361-3666.2004.00244.x

General Administration of Quality Supervision, Inspection and Quarantine of the People's Republic of China (2008). GB 21734_2008. *Emergency shelter for earthquake disasters-Site and its facilities (in Chinese)*. Standardization Administration of the People's Republic of China (SAC): Beijing, China.

General Administration of Quality Supervision, Inspection and Quarantine of the People's Republic of China (2020). GB/T 17742-2020. *The Chinese seismic intensity scale (in Chinese)*. Standardization Administration of the People's Republic of China (SAC): Beijing, China.

General Administration of Quality Supervision, Inspection and Quarantine of the People's Republic of China (2017). GBT 33744_2017. *Emergency shelter for earthquake disasters-Guidelines on the operation and management (in Chinese)*. Standardization Administration of the People's Republic of China (SAC): Beijing, China.

General Administration of Quality Supervision, Inspection and Quarantine of the People's Republic of China (2017). GBT 35624_2017. *General technical requirements of urban emergency shelter (in Chinese)*. Standardization Administration of the People's Republic of China (SAC): Beijing, China.

Gui-Xi, Yi, Wen, X.-Ze, and Su, Y.-J. (2008). Study on the potential strong-earthquake risk for the eastern boundary of the sichuan-yunnan active faulted-block, China. *Chin. J. Geophys.* 51 (6), 1151–1158. doi:10.1002/cjg2.1311

Guo, L., Wang, J., Wang, W., and Wang, H. (2023). Performance-based seismic design and vulnerability assessment of concrete frame retrofitted by metallic dampers. *Structures* 57, 105073. November. doi:10.1016/j.istruc.2023.105073

He, X., Xu, C., Xu, X., and Yang, Y. (2022). Advances on the avoidance zone and buffer zone of active faults. *Nat. Hazards Res.* 2 (2), 62–74. doi:10.1016/j.nhres.2022.05.001

Hou, S., and Jiang, H. (2014). An analysis on accessibility of hospitals in Changchun based on urban public transportation. *Geogr. Res.* 33, 915–925. doi:10.11821/dlyj201405010

Huang, Q., Meng, S., He, C., Dou, Y., and Zhang, Q. (2019). Rapid urban land expansion in earthquake-prone areas of China. *Int. J. Disaster Risk Sci.* 10 (1), 43–56. doi:10.1007/s13753-018-0207-4

Iglesias, V., Braswell, A. E., Rossi, M. W., Joseph, M. B., McShane, C., Cattau, M., et al. (2021). Risky development: increasing exposure to natural Hazards in the United States. *Earth's Future* 9 (7), e2020EF001795. doi:10.1029/2020EF001795

Ilkhani, I., Yazdanpanah, M., and Ali, D. (2023). Analysis of drivers' preferences toward content and message format of variable message signs during tunnel emergency evacuation: a case study of niayesh tunnel in tehran. *Int. J. Disaster Risk Reduct.* 93, 103744. July. doi:10.1016/j.ijdrr.2023.103744

Jiang, L., Sang, Q., Jian, W., and Kang, B. (2023). Research on accessibility of park green space in Xicheng district of Beijing based on Gaussian two-step mobile search method. *J. Beijing Univ. Civ. Eng. Archit.* 39, 41–47. (in Chinese). doi:10.19740/j.2096-9872.2023.04.06

Li, W., Sun, J., Zhou, D., and Huang, L. (2023). Dynamics of a diffusion epidemic SIRI system in heterogeneous environment. *South China J. Seismol.* 43 (2), 104–114. (in Chinese). doi:10.1007/s00033-023-02002-z

Liu, C. (1989). Historical materials and preliminary analysis of the 1489 Xichang earthquake. *Sichuan Earthq.* 1, 51–54. (in Chinese).

Liu, X., Wang, p., Guan, L., Lu, H., and Zhang, C. (2017). *GIS spatial analysis*. 3. Beijing, China: Science Press, 89–107. ISBN 978-7-03-051643-5. (in Chinese).

Magapu, S., and Setia, S. (2023). Seismic vulnerability assessment of rc frame structures subjected to seismic excitation: a review. *Mater. Today Proc.* 93, 196–200. July, S2214785323039883. doi:10.1016/j.matpr.2023.07.118

Min, Z., Wu, G., Jiang, Z., Liu, C., and Yang, Y. (2005). *The Catalogue of Chinese historical strong earthquakes (B.C. 2300–A.D. 1911)*. Beijing, China: Seismological Publishing House. (in Chinese).

Nakanishi, H., Matsuo, K., and Black, J. (2013). Transportation planning methodologies for post-disaster recovery in regional communities: the east Japan earthquake and tsunami 2011. *J. Transp. Geogr.* 31, 181–191. July. doi:10.1016/j.jtrangeo.2013.07.005

Qian, H. (2010). Study of environmental assessmental theories and application in city emergency shelters. *Urgent Rescue* 2 (19), 59–63. [in Chinese, with English abstract].

Qin, K. (2010). *Theories and methods of spatial analysis in GIS*. 2. Wuhan, China: Wuhan University Press. ISBN 978-7-307-07576-4. (in Chinese).

Ren, J. (1990). Preliminary study on the recurrence period of strong earthquakes on the fracture zone of Zemuhe, west of sichuan. *Inland Earthq.* 4, 107–115. doi:10.16256/j.issn.1001-8956.1990.02.003

Ren, J., and Li, P. (1993). The characteristics of surface faulting of 1850 earthquake in Xichang, sichuan. *Seismol. Geol.* 15, 97–108. [in Chinese, with English abstract].

Shen, C., Zhou, Z., Lai, S., Lu, Li, Dong, W., Su, M., et al. (2020). Measuring spatial accessibility and within-province disparities in accessibility to county hospitals in shaanxi Province of western China based on web mapping navigation data. *Int. J. Equity Health* 19 (1), 99. doi:10.1186/s12939-020-01217-0

Shen, Z.-K., Jiangning, Lü, Wang, M., and Roland, B. (2005). Contemporary crustal deformation around the southeast borderland of the Tibetan plateau: TIBET SOUTHWEST BORDERLAND DEFORMATION. *J. Geophys. Res. Solid Earth* 110. B11. doi:10.1029/2004JB003421

Su, H., Chen, W., and Cheng, M. (2022a). Using the variable two-step floating catchment area method to measure the potential spatial accessibility of urban emergency shelters. *GeoJournal* 87 (4), 2625–2639. doi:10.1007/s10708-021-10389-3

Su, H., Chen, W., and Zhang, C. (2022b). Evaluating the effectiveness of emergency shelters by applying an age-integrated method. *GeoJournal* 88 (1), 951–969. doi:10.1007/s10708-022-10669-6

Tong, De, Sun, Y., and Xie, M. (2021). Evaluation of green space accessibility based on improved Gaussian two-step floating catchment area method: a case study of Shenzhen City, China. *Prog. Geogr.* 40 (7), 1113–1126. doi:10.18306/dlkxjz.2021.07.004

Wang, Li, Cao, X., Li, T., and Gao, X. (2019). Accessibility comparison and spatial differentiation of xi'an scenic spots with different modes based on Baidu real-time travel. *Chin. Geogr. Sci.* 29 (5), 848–860. doi:10.1007/s11769-019-1073-8

Wen, X. (2000). Character of rupture segmentation of the xianshuihe-anninghe-zemuhe fault zone, western sichuan. *Seismol. Geol.* 22, 239–249. [in Chinese, with English abstract].

Wen, X.-ze, Ma, S.-li, Xu, X.-wei, and Yong-nian, He (2008). Historical pattern and behavior of earthquake ruptures along the eastern boundary of the sichuan-yunnan faulted-block, southwestern China. *Phys. Earth Planet. Interiors* 168 (1–2), 16–36. doi:10.1016/j.pepi.2008.04.013

Wu, X., Xu, X., Yu, G., Ren, J., Yang, X., Chen, G., et al. (2023). China active faults database and its web system. *Prepr. ESSD – Land/Geology Geochem*. doi:10.5194/essd-2023-119

Xu, X., Guo, T., Liu, S., Yu, G., Chen, G., and Wu, X. (2016). Discussion on issues associated with setback distance from active fault. *Seismol. Geol.* 38 (3), 477–502. [in Chinese, with English abstract]. doi:10.3969/j.issn.0253-4967.2016.03.001

Xu, X., Wen, X., Yu, G., Chen, G., Klinger, Y., Hubbard, J., et al. (2009). Coseismic reverse- and oblique-slip surface faulting generated by the 2008 Mw 7.9 wenchuan earthquake, China. *Geology* 37 (6), 515–518. doi:10.1130/G25462A.1

Xu, X., Wen, X., Zheng, R., Ma, W., Song, F., and Yu, G. (2003). Recent patterns of tectonic deformation and dynamics sources of active blocks in the sichuan-yunnan area. *Sci. China* 33, 151–162. (S1) (in Chinese).

Yan, Z. (2023). Analysis of regional traffic accessibility based on ArcGIS. *Stand. Surv. Mapp.* 39, 120–123. doi:10.20007/j.cnki.61-1275/P.2023.02.25

Yi, G., Wen, X., Fan, J., and Wang, S. (2004). Assessing current faulting behaviors and seismic risk of the anninghe-zemuhe fault zone from seismicity parameters. *ACTA Seismol. Sin.* 26, 294–303. [in Chinese, with English abstract].

Zhang, C., Wang, X., and Pei, X. (1998). Strong earthquake in 1536 and newly found surface rupture along Anninghe Fault. *Sichuan Earthq.* 4, 34–50. [in Chinese, with English abstract].

Zhang, P., Deng, Q., Zhang, G., Jin, Ma, Gan, W., Min, W., et al. (2003). Active tectonic blocks and strong earthquakes in the continent of China. *Sci. China Ser. D Earth Sci.* 46, 13–24. S2. doi:10.1360/03dz0002

Zhang, W., and Yun., Y. (2019). Multi-scale accessibility performance of shelters types with diversity layout in coastal port cities: a case study in nagoya city, Japan. *Habitat Int.* 83, 55–64. January. doi:10.1016/j.habitatint.2018.11.002

Zhang, Y. (2020). Research on accessibility of urban parks based on GIS and gravity model: taking the main city of zhengzhou as an example. *Henan Sci.* 38, 733–739. [in Chinese, with English abstract].

Zhao, X., Zheng, Q., Liu, X., and Jin, M. (2018). Study on the planning and allocation of urban park green space based on 2SFCA improved model—a case study of futian district, shenzhen. *Chin. Landsc. Archit.* 34, 95–99. [in Chinese, with English abstract].

Zou, F., Jiang, H., Che, E., Wang, J., and Wu, X. (2023). Quantitative evaluation of emergency shelters in mountainous areas among multiple scenarios: evidence from biancheng, China. *Int. J. Disaster Risk Reduct.* 90, 103665. May. doi:10.1016/j.ijdrr.2023.103665

Frontiers in Earth Science

Investigates the processes operating within the major spheres of our planet

Advances our understanding across the earth sciences, providing a theoretical background for better use of our planet's resources and equipping us to face major environmental challenges.

Discover the latest Research Topics

See more →

Frontiers

Avenue du Tribunal-Fédéral 34
1005 Lausanne, Switzerland
frontiersin.org

Contact us

+41 (0)21 510 17 00
frontiersin.org/about/contact